CARNEGIE MELLON UNIVERSITY

CONSTRUCTION AND EVALUATION OF A HIGH RESOLUTION SILICON MICROSTRIP TRACKING DETECTOR AND UTILIZATION TO DETERMINE INTERACTION VERTICES

THESIS

Presented to the Department of Physics,
Mellon College of Science,
In partial fulfilment of requirements for the degree
Doctor of Philosophy

Prakash Parayil Mathew

Pittsburgh, Pennsylvania
September 4, 1997

Abstract

A 20 plane, 47K channel silicon microstrip vertex detector was built for the charm baryon experiment 781(SELEX) at Fermilab. The detector is taking data with an average vertex transverse resolution of 6 microns. The measurement and multiple scattering errors are well understood and have been parametrized. The mass resolution of reconstructed Σ^+ and Σ^- hyperons produced at 540-640 GeV/c is consistent with silicon detector resolutions. The vertex detector has been used to resolve primary and secondary vertices and this high precision information is being used in the experiment's real-time online trigger. Flawless operation over 14 months and the long-term stability of the efficiency, alignment and accuracy demonstrates successful integration of hardware and software.

Acknowledgements

"In the beginning God created the heavens and the earth."
-Genesis 1:1, The Bible

This work is only a feeble attempt at uncovering the work of the Master.

I am grateful to my parents for all the patience, support and love they have given me.

I am indebted to Prof. James Russ for his impeccable role as teacher and advisor.

Thanks are due to all my colleagues at CMU and Fermilab for their collaborative help.

To all my friends from Bombay, Pittsburgh and Chicago-land, "Thank-you for being around".

Fermilab Experiment 781
February 5, 1997

-SELEX-
Segmented Large-x Baryon Spectrometer

R.Edelstein, E.Gottschalk, A.Kushnirenko, Dongning Mao, P.Mathew, M.Mattson, M.Procario, J.Russ
Carnegie-Mellon University, Pittsburgh, PA 15213

P. S. Cooper, J. Engelfried, J. Kilmer, S. Kwan, J. Lach, G. Oleynik, E. Ramberg, D. Skow, L. Stutte
Fermilab, Batavia, Illinois 60510

N.Akchurin, M.Aykac, M.Kaya, D.Magarrel, E.McCliment, K.Nelson, C.Newsom, Y.Onel, E.Ozel, S.Ozkorucuklu, P.Pogodin
University of Iowa, Iowa City, Iowa 52242

T. Ferbel, G. Ginther, C. Hammer, P. Slattery, M. Zielinski
University of Rochester, Rochester, NY 14627

C. Kenney, S. Parker
University of Hawaii, Honolulu, HI 96822

V.Andreev, A.G.Atamantchouk, N.F.Bondar, V.L.Golovtsov, V.T.Grachev, A.V.Khanzadeev, V.T.Kim, L.M.Kochenda, A.G.Krivshich, N.P.Kuropatkin, V.P.Maleev, P.V.Neoustroev, S.Patrichev, B.Razmyslovich, V.M.Samsonov, V.Stepanov, M.Svoiski, N.K.Terentyev, L.N.Uvarov, A.A.Vorobyov
Petersburg Nuclear Physics Institute, St. Petersburg, Russia

M.Ya.Balatz, G.V.Davidenko, A.G.Dolgolenko, G.B.Dzyubenko, A.G.Evdokimov, A.D.Kamenskii, M.A.Kubantsev, V.S.Lakaev, A.P.Nilov, V.A.Prutskoi, V.K.Semyatchkin, A.I.Sitnikov, V.S.Verebryusov, V.E.Vishnyakov
Institute of Theoretical and Experimental Physics, Moscow, Russia

Yu.M.Goncharenko, O.A.Grachev, V.P.Kubarovsky, A.I.Kulyavtzev, V.F.Kurshetsov, A.A.Kozhevnikov, L.G.Landsberg, V.V.Molchanov, V.A.Mukhin, S.B.Nurushev, A.N.Vasiliev, D.V.Vavilov, V.A.Victorov
Institute For High Energy Physics, Protvino, Russia

I. S. Filimonov, E. M. Leikin, A. V. Nemitkin, V. I. Rud
Moscow State University, Moscow, Russia

L. Emediato, C. Escobar, F. Garcia, P. Gouffon, T. Lungov, M. Srivastava, R. F. Zukanovich
University of São Paulo, Brazil

A.M.F.Endler
Centro Brasileiro de Pesquisas Fisicas, Rio de Janeiro, Brazil

M. Luksys
Universidade Federal da Paraiba, Paraiba, Brazil

Li Yunshan, Li Zhigang, Mao Chensheng, Zhao Wenheng, He Kangling, Zheng Shuchen, Mao Zhenlin
Institute of High Energy Physics, Beijing, PRC

S.L.McKenna, V.J.Smith
H. H. Wills Physics Laboratory, University of Bristol, BS8 1TL, United Kingdom

I.Giller, M.A.Moinester, A.Ocherashvili, V.Steiner
Tel Aviv University, Ramat Aviv, Israel

U.Dersch, I.Eschrich, I.Konorov, H.Krüger S.Masciocchi, B.Povh, J.Simon, K.Vorwalter
Max-Planck-Institute for Nuclear Physics, Heidelberg, Germany

A. Bravar, D. Dreossi, A. Lamberto, A. Penzo, G. F. Rappazzo, P. Schiavon
University of Trieste and INFN, Trieste, Italy

M. Gaspero, M. Iori
University of Rome "La Sapienza" and INFN , Rome, Italy

Antonio Morelos
Universidad Autonoma de San Luis Potosi, San Luis Potosi, Mexico

Erhan Gülmez
Bogazici University, Istanbul, Turkey

Spokesperson: **J. Russ** - 630/840-3600,2409 office - 630/262-0908 home

Contents

1 Introduction **16**

1.1 The scope of the problem 16

1.2 Overview of the thesis 18

2 Semiconductor charged particle detectors **20**

2.1 Introduction 20

2.2 Silicon Radiation Detectors 20

2.2.1 Semiconducting properties of Silicon 20

2.2.2 A p-n junction 22

2.2.3 Position sensitive strip diode 24

2.2.4 Readout and signals 26

2.3 SELEX-The Charm Baryon Experiment 27

2.3.1 Overview of Particle Physics 27

2.3.2 SELEX physics goals 28

2.3.3 SELEX Design 29

2.3.4 SELEX hyperon beam and target 32

2.3.5 SELEX Trigger 32

2.3.6 Data Acquisition System 33

2.3.7 Need for vertex resolution 34

3 Vertex detector construction and testing **35**

3.1 VSSD system components 35

3.1.1 Silicon Detector 35

3.1.2 SVX Silicon Readout Chip 38
3.1.3 Assembly of VSSD planes 41
3.1.4 Silicon Readout Sequencer 43
3.1.5 Driver Card 46
3.1.6 Fastbus FSDA Data Acquisition 47
3.1.7 Trigger Handling and read out Sequence 50
3.2 Software infrastructure development 53
3.3 Bench Testing of VSSD planes 55
3.3.1 Pedestal and Noise in planes 55
3.3.2 Sparsification and Calibration 58
3.3.3 Calibration Charge Injection 61
3.3.4 LED testing 62
3.3.5 Backplane pulsing 66
3.3.6 Source testing 69
3.4 Installation in the experiment hall(PC4) 70
3.4.1 Hardware Alignment on Monument blocks 70
3.4.2 Power Supply and Wiring layout 76
3.4.3 Cooling and shielding 77
3.4.4 Cabling to Fastbus Readout 79
3.5 Final System Checkout 79

4 Analysis of vertex silicon data 86
4.1 On-spill and off-spill data 87
4.2 Hits and Clustering 88
4.2.1 Tracking and Errors 89
4.2.2 Residuals 91
4.2.3 Hit and plane efficiency 92
4.2.4 Pulse Height ADC 97
4.2.5 Software Alignment 97
4.2.6 Detector plane resolution 103
4.3 Momentum dependent Multiple Coulomb Scattering 112

4.3.1 A model for scattering in the VSSD 113
4.3.2 Simulation and Parametrizing scattering 114
4.3.3 Agreement of Model with data 115
4.3.4 Track resolution at the vertex 116
4.4 Stability of the vertex detector 123
4.4.1 Monitoring detector performance 123
4.4.2 Stability of operating parameters 126

5 Hyperon mass resolution 137
5.1 Apparatus description 137
5.1.1 Hyperon beam 137
5.1.2 Beam silicon 138
5.1.3 M1 magnet chambers 141
5.1.4 M2 magnet chambers 141
5.1.5 Analyzing Magnets 141
5.1.6 Trigger 142
5.1.7 Incoming beam profiles 142
5.2 Two-body hyperon decays 143
5.2.1 Missing mass reconstruction 146
5.2.2 Tracking and reconstruction code 148
5.3 Reconstructed Hyperon decays 148
5.3.1 Discussion of the mass resolution 149
5.3.2 Embedded Monte Carlo 158

6 Vertex finding with the silicon vertex detector 162
6.1 Introduction 162
6.2 Silicon-M2 matched vertex segments 163
6.3 Vertexing algorithm 165
6.3.1 The general idea 165
6.3.2 The initial seed vertex 167
6.3.3 Track error matrix 167
6.3.4 Track errors and weights 168

6.3.5 A definition of a vertex χ^2 169
6.3.6 Successive iteration to find the vertex 170
6.3.7 Vertex refining using χ^2 criterion 171
6.4 Vertex chi squares and the definition of an outlier 172
6.5 Vertex reconstruction from embedded events 173
6.6 Discussion of χ^2 in real data 179
6.6.1 Detector and target alignments 179
6.6.2 Vertex plane combinations and track fitting 181
6.6.3 Degrees of freedom in the vertex fit 183
6.6.4 Different vertexing algorithm 185
6.7 Discrepancies from a purely normal distribution 185
6.8 Interpretation of the observed χ^2/dof 185

7 Conclusions **190**
7.1 Hardware performance and evaluation 190
7.2 Tracking errors in silicon detectors 194
7.3 Vertex reconstruction 196
7.4 Future developments 198

List of Figures

2.1 A p-n junction 23
2.2 A planar semiconductor device 25
2.3 Silicon microstrip device 26
2.4 The particles according to the Standard Model 28
2.5 Layout of the SELEX spectrometer(not to scale) 30

3.1 The layout of the vertex planes in the vertex region 36
3.2 A monument block showing 2 detectors on a side 37
3.3 a)signal from Back plane pulsing in ADC counts, in a single channel b)The signal to noise ratio for the same channel.(This channel is typical of all channels) 39
3.4 Schematic of a single SVX channel 40
3.5 Detail of the Detector and SVX chip region 42
3.6 Exploded view of a vertex detector 42
3.7 Schematic layout of the SRS module 45
3.8 Schematic of one channel of the FSDA 49
3.9 Arrangement of data flow in the vertex system 51
3.10 Flow chart showing the trigger-readout interaction 54
3.11 The pedestal distribution of a single channel(500events) . . . 57
3.12 Mean pedestal and noise for 512 channels in 4 SVX chips . . 58
3.13 The waterfall plot for a typical set of channels. The average noise occupancy is plotted as a function of the threshold setting. 59

3.14 Average noise occupancy of 5_cms and mosaic detectors (Note the log scale on the Y axis) 60
3.15 a)The gain of the SVX channels is a plot of the output ADC response to the input charge via threshold setting b)pedestal and noise of a few channels illuminated by an LED via a thin fiber c)The signal seen in the detector from an LED pulse d)The sparse occupancy response of the channels(note the full occupancy for a charge above 1.8fC) 63
3.16 a,b) The gains in 128 channels in each of two typical SVX chips c)The gains for all the SVX chips in the vertex system(ADC units/DAC units from calibration signals averaged over all 128 channels in a chip) 64
3.17 ADC output response to the integration time in one SVX channel.(This yields the characteristic risetime of the charge to voltage amplifier) 65
3.18 a)Schematic of the LED test setup b)Schematic of the Back Plane pulse setup 65
3.19 a)Mean LED pulse profile with a broad fiber on a mosaic detector(wire map from the REV side only) with plucked channels b) Same profile from the interleaved REV side, showing higher signal gain on channels adjacent to plucked channels. 67
3.20 The pedestal subtracted signal seen with a back bias pulse to a mosaic detector 68
3.21 Schematic of the radioactive source setup 69
3.22 The ADC pulse height spectrum in two VSSDs for a Ru radioactive source. Notice the well separated noise background. 71
3.23 Formation of the coodinate origin on a monument block . . . 73
3.24 Layout of surveyed points on vertex planes 73
3.25 Schematic of power supply to the vertex planes 78
3.26 Schematic of power supply to the driver cards 78

3.27 Typical Back-bias Pulse(BBP) signals seen in the detectors as installed.(The DAQ pathway was the same as that for runtime conditions) 81

4.1 Typical histograms showing hit wire maps, cluster size, hit multiplicity and ADC level in the raw data 90
4.2 Typical residuals in vertex planes 93
4.3 Hit efficiency and "fake"(noise) hit efficiency of vertex planes using beam tracks 95
4.4 a)Efficiency for correctly associating hits to all tracks in an event for a typical 5_cm plane b)The same efficiency for a typical mosaic plane c)The residuals from the correctly assigned hits on a 5_cm plane d)The same residual distribution for a mosaic plane e)The track multiplicity within the events analyzed e)The momentum distribution of the tracks analyzed . . 96
4.5 Variation of vertex plane hit efficiencies with thresholds . . . 98
4.6 a)Relative cluster size distributions, b) Fitted ADC spectrum of cluster charge, c)Single strip cluster residuals, d)Two strip cluster residuals 99
4.7 a)Relative cluster size distributions, b) Fitted ADC spectrum of cluster charge, c)Single strip cluster residuals, d)Two strip cluster residuals 100
4.8 Illustration of the determination of angular mis-alignments a)Scatter plot of residuals with coordinate of track position in the orthogonal view, for a typical detector, b)linear fit to the mean of the same distribution, c)Observed mis-rotations of all vertex planes 102
4.9 Illustration of the determination of z position shifts a)Scatter plot of residuals with the angle of the track for a typical detector, b)linear fit to the mean of the same distribution, c)Observed z position deviation of all vertex planes 104

4.10 a)Scatter plot of the observed and predicted(from ADC charge weighting) positions of tracks, from a strip center for a 20μm pitch 5_cm detector, b) The same plot for a 25μm pitch mosaic detector 108
4.11 Resolutions of all the vertex plane(Errors are $\pm 1\mu$m). 109
4.12 a)Momentum spectrum of sample of large angle tracks in the vertex b)Residuals seen in the central(every strip read out region)panel c)Residuals in the outer(alternate strip read out region)panels 111
4.13 The simulation model predicted error on each vertex plane from multiple scattering 117
4.14 χ^2/dof of fitted tracks in various momentum bins using the multiple scattering model predicted plane weights 118
4.15 The momentum distribution of tracks that were fitted a)high momentum beam b)low momentum interactions 119
4.16 A comparison of the χ^2/dof distributions for momentum dependent and momentum independent track weights 119
4.17 Mean χ^2/dof and vertex track resolution at different momenta 120
4.18 Variation of the 10 independent terms of the matrix of errors due to multiple scattering, with momentum 124
4.19 A example of the fit of the ER(1,1) term(i.e. the squared error in the X intercept) a)the computed value in 0.2Gev/c bins, b) fit to a third order polynomial in 1/p, c)relative error between the function and the fit (Note: The function values are displayed with a multiplicative factor) 125
4.20 Pedestal and rms deviation output from an offspill monitoring job. Displayed are the direct sides of a 5_cm(vx_ssd_2y) and mosaic(vx_msd_1x) detectors 127
4.21 The sparse noise occupancy output from an offspill monitoring job. Displayed are a 5_cm(vx_ssd_2y) and mosaic(vx_msd_2v) detector 128

4.22 The output from the onspill monitoring job for a mosaic detector 129
4.23 A single beam event display using the SEED package (Corresponding U and V views are not shown, but similar) 130
4.24 A typical interaction event (using the SEED display package) (Corresponding U and V views are not shown, but similar) . 131
4.25 Pedestal(and noise) variation of a single channel and average over an SVX chip, over 9 weeks 132
4.26 Typical hit efficiencies for 5_cm and mosaic detectors over 9 weeks 133
4.27 The ratio of two-strip to one-strip clusters in typical 5_cm and mosaic planes 133
4.28 a)The typical alignment drifts of 5_cm and mosaic planes w.r.t. the SELEX alignment reference(This reference contains points outside of the vertex system) b)The same alignment drift w.r.t. a reference within the vertex system. 134
4.29 The typical noise level in beam runs for 5_cm and mosaic planes seen over a period of 9 weeks 135
4.30 The typical resolution seen in beam runs for 5_cm and mosaic planes seen over a period of 9 weeks 135

5.1 Hyperon target and momentum selecting tungsten channel and target 139
5.2 Layout of the detector apparatus(as relevant to hyperon reconstruction) 140
5.3 Beam phase space in X and Y views at the exit of the hyperon channel 144
5.4 Beam momentum for positive and negative beam 145
5.5 Typical dominant hyperon decay topology 147
5.6 Σ^+ mass plots from positive beam data 150
5.7 Σ^- mass plot from negative beam data 151
5.8 Ξ^- mass from the negative beam data ($\Xi^- \rightarrow \Lambda + \pi^-$) 152

5.9 R-Θ plot for the positive hyperon reconstruction.(The angle of the kink at the hyperon decay plotted against the momentum fraction of the secondary daughter to the beam) 153
5.10 An exponential fit to the z distribution of the hyperon decay point. (The expected and observed decay lengths(1/slopes) are within one sigma) 154
5.11 The contribution to the total hyperon mass width vs. the secondary momentum from a) The beam momentum magnitude, b)The secondary particle momentum, c) The beam angular resolution(in 3-D) d) The secondary particle angular resolution(in 3-D) 159
5.12 Comparision of the estimated mass width and the actual mass width seen in the data (both plotted against the secondary momentum) 160
5.13 Monte-Carlo embedded data mass plots for the Σ^+ decay modes 161

6.1 χ^2 for reconstructed vertex tracks 164
6.2 General layout of the apparatus appropriate to the charm vertex reconstruction. The target area is shown in greater detail(fig not to scale). 166
6.3 A transverse slice at a fixed z of the primary vertex region. . 169
6.4 Overall χ^2/dof for vertex reconstructed data. 174
6.5 a)track multiplicity distribution, b)χ^2/dof versus vertex z position, and c) the reconstructed z position of the vertex for the interaction data 175
6.6 Illustration of a "modified" Chauvenet's criterion. Occurences with $\chi^2 > 11.5$ in a 2-dof distribution are considered outliers. 176
6.7 Overall χ^2/dof in reconstructed embedded data. 177
6.8 a) χ^2/dof versus vertex z position and b) reconstructed vertex z position in embedded data. 178

6.9 Residuals plotted in the last 4 vertex detectors(These planes are not used in the track fit). 182
6.10 Track parameter differences between two different track fitting packages. 184
6.11 The χ^2 distributions for different degrees of freedom in interaction data. 186
6.12 Track χ^2/dof distributions. (The bold curve is real data and the dashed curve is from purely normal simulated data) 187
6.13 Track χ^2/dof distributions(log y scale). (The bold curve is real data and the dashed curve is from purely normal simulated data) 188

7.1 The long term alignment stability seen in typical 5_cm detectors. 192
7.2 The long term alignment stability seen in typical mosaic detectors. 193
7.3 The track χ^2 probability distributions(bold) seen over different momentum bins. (The dotted histogram is the same for a pure normal distribution) 195
7.4 The distance from tracks in a vertex to the fitted vertex position 197
7.5 The online filter data-rejection fraction seen over 7 weeks of operation. This uses the vertex detector information. 198

List of Tables

2.1 Properties of silicon. 22

3.1 8-bit Amplitude format Data word 50
3.2 Normal format Data word 50
3.3 Nomenclature and readout orientation of the VSSD planes. . 74
3.4 Aligned Strip locations(in mm) on the Mosaic detectors . . . 82
3.5 Aligned Strip locations(in mm) on the 5_cm detectors 83
3.6 z positions(in mm) for all vertex detector planes.(Origin chosen to be at the upstream face of the first monument block) (** is with origin on the upstream face of that particular monument block.) 84
3.7 Detector hookup to FSDAs 85

4.1 Alignment deviations from the expected positions 105
4.2 Beam segment fit error(μm) at vertex planes 107
4.3 Position resolution(μm) at vertex planes 110
4.4 Description of material associated with multiple scattering simulations. 136

5.1 Analyzing magnet characteristics 142
5.2 Reconstructed hyperons 149

6.1 Properties of the segmented charm targets and other scattering material 165
6.2 Criterion used to select the vertex 172

6.3 Embedded vertex track characteristics 176
6.4 χ^2/dof dependence on transverse BM-VX system alignment offsets 180
6.5 χ^2/dof dependence on BM-VX system angular alignment offsets 180
6.6 Segmented target positions as surveyed and calculated from vertexing 181
6.7 Vertexing χ^2/dof after removing detectors(in sets of 4). . . . 183

Chapter 1

Introduction

The area of particle physics has time and again, shed light on the innermost workings of the atom. The "simple" atom of yesterday has been linked to a "complicated" cast of particles, each seemingly more exotic than the last. It stands to reason to assume that the tools employed by the particle physicist are also complicated and exotic. In a different sense they are quite simple. Each class of detector picks a single function and endeavours to do it extremely well. Hence tracking chambers only track the flight of particles, and calorimeters only measure particle energy. The particle physicist is constantly pushing the performance limits of his hardware, in his quest for answers.

1.1 The scope of the problem

This thesis seeks to describe the design and implementation of a solution, to the problem at hand. The problem is to design a vertex detector capable of detecting decay vertices from short lived secondary products in the environment of high-multiplicity primary interactions. The experiment 781(SELEX) at Fermilab, proposes to study the production and decay characteristics of charm baryons through the primary interaction of a beam of hyperons and a Cu(or C) target. It is expected that an average of 13 charged tracks origi-

nate from the primary vertex. Charm particles produced in this interaction, decay into 2 or 3 tracks within a distance of 1-20mm. The angle any of the products makes with the beam track is generally < 30mrad. The vertex detector should be capable of resolving vertices in this "noisy" background of tracks. It should make high precision track measurements to precisely determine their initial trajectory and subsequently reconstruct vertices at high resolution. A 20 plane silicon vertex detector was developed with this functionality in mind. The average interaction track(with momentum 15-300 GeV/c) will Multiple Coulomb Scatter(MCS) in the silicon detector. An understanding of the detector accuracy will have to include this momentum dependent correction in the software algorithm which reconstructs tracks.

This kind of a precise measurement requires the detector to have a high density of active read out channels. The event acquisition rate, dictated by physics cross-sections is 5kHz. All active strips must be integrated into the data acquisition system with uniform read out response at this rate. This must be done within the constraints of available physical space and maximum allowable noise pick-up. As the detector is radiation sensitive, it must be shielded from light and other radio frequency noise sources. Power supplies must be clean and the detector must be calibrated so that the signal to noise is consistently optimized.

As the average transvere track resolution at the vertex is expected to be about 6μm, the composite detector is highly sensitive to micron level relative misalignments in individual planes. This requires the mechanical installation to be capable of controlling and retaining alignment on this scale. It should also be robust enough to handle transportation into the experimental area and the effects of sag due to its own weight.

Cooling the closely packed active semiconductor electronics is another important issue. Higher temperatures during the operation could damage the electronics, introduce thermal noise into the silicon system and distort the alignment through thermal expansion of the hardware. Any cooling system designed, must be careful not to interfere with the normal operation of the

detector(by forming condensation etc.).

The detector is also expected to operate in a hazardous radiation area, for about 15 months. This requires that all the support systems operate in a stand alone manner with minimum manual intervention. The safety of the vertex hardware is also of prime consideration and all the associated systems must be made fail-safe. Long term stablity of all operating parameters of the detector is an important issue. This is because data from the vertex detector is designed to be included at an online physics trigger level. The stability of the noise, efficiency and alignment in the detector is hence directly related to the stored physics data. Elaborate care must be taken to monitor and study all these parameters.

1.2 Overview of the thesis

The characteristics of semiconductors and recent developments in silicon detectors will be explained in Chapter 2. The choice of silicon vertex detector as opposed to a different vertex detector for SELEX will hopefully become evident. An overall description of the experiment and the physics of interest to SELEX is also introduced.

Chapter 3 launches into the description of constructing the individual detector planes that make up the vertex detector. Individual detector planes were prototyped, fabricated, tested and characterized. The readout sequencing and the detector noise response were studied in detail. The detectors were then assembled into the composite vertex unit and integrated into the rest of the experiment. All along the way, lessons were learned and the design was constantly adapting to accomodate changes. The execution of the hardware design with respect to testing, mounting, cooling, alignment and check-out are described in Chapter 3.

A fully built detector only meant that our job had gotten off to a good start. It still had to prove its worth as a detector of particles. Hence, once the beam arrived in the experimental hall, we busied ourselves in trying to

understand the hardware. Its response to a minimum ionizing particle was studied and particle trajectories were reconstructed in the detector. Track residuals were examined in detail to derive the alignment accuracy of the detectors. The vertex detector was compared with the Beam silicon detector to gauge its resolution. Chapter 4 describes the answers to questions on the alignment, accuracy, efficiency and stability of the detector.

Once the design specifications of the detector in the real beam environment were verified, we began to explore the impact of this class of high precision detectors on measurable physics quantities. The masses of Σ^+, Σ^- and Ξ^- hyperons in the SELEX beam were reconstructed, using silicon detectors in the beamline. These observations of hyperons at 540-650 GeV/c, at a Feynman x_F of 0.72-0.78, were quite possibly a first. A careful analysis of the factors contributing to the mass width of the hyperons can give a quantitative understanding of the inherent resolution of silicon detectors. Chapter 5 analyzes the reconstructed hyperon mass width through contributions from tracking parameters(slopes, intercepts, curvature in a magnetic field).

Finally we examined the vertex detectors performance with regard to the main purpose it was built for - that of vertex finding. One of the biggest considerations was to properly account for Multiple Coulomb Scattering(MCS) in the detector. Experimental science not only makes careful observations, but also uses them to develop "models" that have some predictive power. One such model for momentum dependent Multiple Coulomb Scattering in the vertex detector was formulated(initially introduced in Chapter 4) . Chapter 6 describes how the vertex is resolved using the vertex detector and then goes on to compare our MCS model with observations on real data.

It is hoped that this thesis would provide an exhaustive description of the SELEX vertex detector. Furthermore, its goal is to demonstrate that all relevant aspects of the detector were scrutinized and that a satisfactory level of understanding was reached. However, let the reader read on and be the final judge of this.

Chapter 2

Semiconductor charged particle detectors

2.1 Introduction

Energy measurements in nuclear physics were made using semiconductor detectors as far back as 1951[1]. Starting in the seventies, high energy physics experiments have used semiconductor detectors for detecting charged particles and interactions. In 1980, J. Kemmer[2] devised the planar technique for silicon to make possible position measurements of particle trajectories. Using this technique, silicon microstrip detectors were developed and these could now be used to perform charged particle tracking. The good position and energy resolution[3, 4] afforded by these detectors make their use widespread among both collider and fixed target experiments[5].

2.2 Silicon Radiation Detectors

2.2.1 Semiconducting properties of Silicon

Silicon[6, 7] is a group IV element with a half filled valence shell. When gaseous silicon condenses, its atomic levels form valence and conduction energy bands. The valence band comprises the bound valence electrons. Above

this level, lies the conduction band with its unfilled levels. The separation between the valence and conduction band, or bandgap is 1.1eV. In conductors, the conduction and valence bands overlap and in insulators the band gap is large(e.g. 9eV in SiO_2). It takes 3.6eV of energy to free a bound electron and excite it into the conduction band(and the corresponding hole into the valence band). This is referred to as the formation of an electron-hole pair. Pure silicon(intrinsic materials) at room temperature has a number "n_i" of thermally excited(dictated by Maxwell-Boltzmann statistics)free carriers and the hole concentration "p", is equal to the electron concentration "n". When pentavalent(trivalent) element atoms are substituted for some of the crystalline silicon atoms there is now an excess of electron(hole) "majority" concentration. This is called doping and may be achieved by techniques such as diffusion, ion implantation etc. Doped materials(n-type or p-type) also have thermally generated carriers of the opposite kind called "minority carriers" but this relative concentration is usually small. In both doped and pure material, the following relation holds

$$n_p = n_i^2 = N_c N_v e^{-E_g/kT} \tag{2.1}$$

where E_g is the bandgap and N_c and N_v are the density of states in the conduction and valence band.

The free carrier concentrations contribute to the bulk resistivity (conductivity) of the material. Under an applied electric field the drift velocity of electrons and holes is proportional to the field. The constant of proportionality is called the mobility(μ_0). Table 2.1 lists the physical properties of silicon[8] at room temperature.

When an ionizing particle traverses the silicon crystal, it Coulomb scatters with the electrons in the solid to create free electrons and holes. These free electrons and holes will produce a forward peaked cascade of secondary and tertiary etc. electron - hole pairs until their kinetic energy drops below 3.6eV. For a minimum ionizing charged particle in 300μm thick silicon, the electron hole pairs generated will be about 3.2×10^4(dE/dx about 3.8MeV/cm). In

Atomic number	14
Atomic weight	28.08
Atom number density	$4.99 \times 10^{22} cm^{-3}$
Density	$2.33 g/cm^{-3}$
Dielectric constant	11.7
Bandgap	1.11eV
N_c	$2.80 \times 10^{19} cm^{-3}$
N_v	$1.04 \times 10^{19} cm^{-3}$
Electron mobility	$1350 cm^2/(V\ s)$
Hole mobility	$480 cm^2/(V\ s)$
Electron Diffusion const	$34.6 cm^2/s$
Hole Diffusion const	$12.3 cm^2/s$
Intrinsic carrier density	$1.45 \times 10^{10} cm^{-3}$
Intrinsic resistivity	235kΩcm
Melting point	1415^oC
Thermal expansion coefficient	$2.5\times 10^{-6} cm^{-3}\ /^o$C
Breakdown field	30 V/μm

Table 2.1: Properties of silicon.

order to observe this signal, we need to suppress the charge generated from thermal excitations which at room temperature will be 4 orders of magnitude higher. This may be done, by cooling the detector, by choosing a larger bandgap material(but small enough to produce sufficient e-h pairs) or by depleting the bulk material of free carriers in the quiescent state.

2.2.2 A p-n junction

The method of depleting the bulk of free carriers is achieved by implementing a p-n junction as shown in Fig 2.1. When doped p-type and n-type materials are brought into contact, the majority carriers from either side diffuse across the interface and recombine. This leaves exposed negatively charged immobile ions in the p-type material and positive ions in the n-type region. An electric field is set up across the interface due to this space charge which

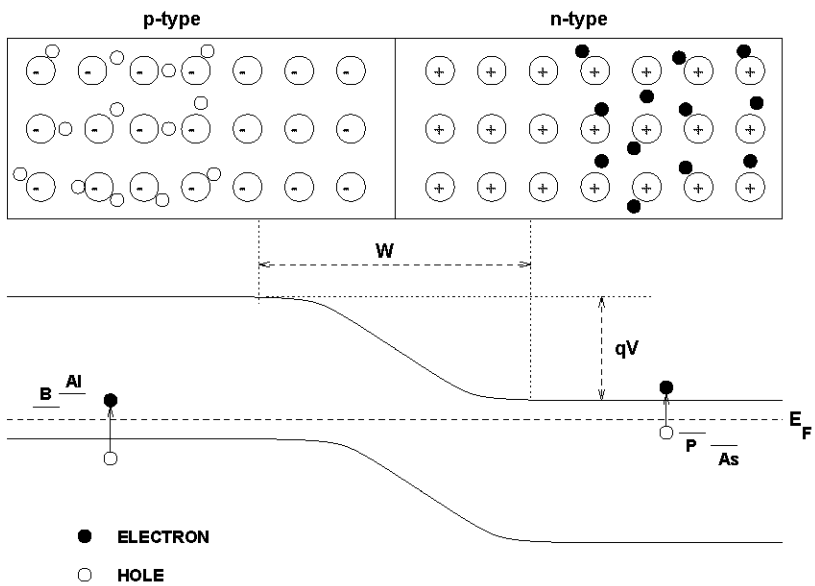

Figure 2.1: A p-n junction

prevents further free carrier diffusion and recombination. The region without any free carriers is the depletion width. Thermally generated carriers in this width are immediately swept away by the electric field in this region. The potential barrier developed is the built in junction potential V_d given by

$$V_d = \frac{kT}{q} ln \frac{N_a N_d}{n_i^2} \tag{2.2}$$

Furthermore, applying a reverse bias potential V_a to the junction will increase the barrier height and extend the depletion region widths in both materials.

Now consider the planar semiconductor device shown in Fig 2.2. The bulk is high resistivity n-type material with the junction formed by a thin heavily doped p-type layer on the leading edge. The rear contact with an n^+ layer to a metal layer ensures an ohmic contact on the back surface. The assymetric doping strengths implies that the depletion region will be almost entirely in the n-type bulk. Using electrical neutrality of the crystal and

solving Poisson's equations we get,

$$W^2 = 2K\epsilon_o(V_d + V_a)q^{-1} \mid N_d - N_a \mid^{-1} \tag{2.3}$$

where W is the thickness of the space charge region, q is the charge on the electron, K is the dielectric constant of the semiconductor(12 for Si), ϵ_o is the permittivity of vacuum, N_d is the density of donor states and N_a is the density of acceptor states.

For charged particle detection, the depletion region represents the active volume of charge production. We may increase the bias potential V_a until the entire n-type bulk of the detector is depleted. A higher resisitivity material ensures a lower V_a for depletion. The noise in such a depleted junction arises from the reverse bias leakage current. This is due to minority charge carriers generated thermally as well as diffusion of carriers from outside the depletion region. The thermal component is temperature sensitive(i.e. $\propto$ exp(-E_g/kT)) and is lower for cooler temperatures. This argues for keeping the junction at a cooled stable temperature. The capacitance of a depleted junction is another important variable as it affects the signal-to-noise ratio (SNR) as well as the response time of the detector. For a partially depleted planar detector with no edge effects, the capacitance per unit area is given by

$$C = \sqrt{\frac{qK\epsilon_o N}{2(V_a + V_d)}} \tag{2.4}$$

where N $\equiv \mid N_d - N_a \mid$.

This adds to the noise (V $\propto \sqrt{C}$) and a preamplifier risetime component of about $2.2R_sC_d$ where R_s is any series resistance associated with the detector readout circuit and C_d is the detector capacitance.

2.2.3 Position sensitive strip diode

In order to incorporate position sensitivity into silicon detectors, planar technology is used to fabricate multiple p-n junctions on a silicon wafer(typical

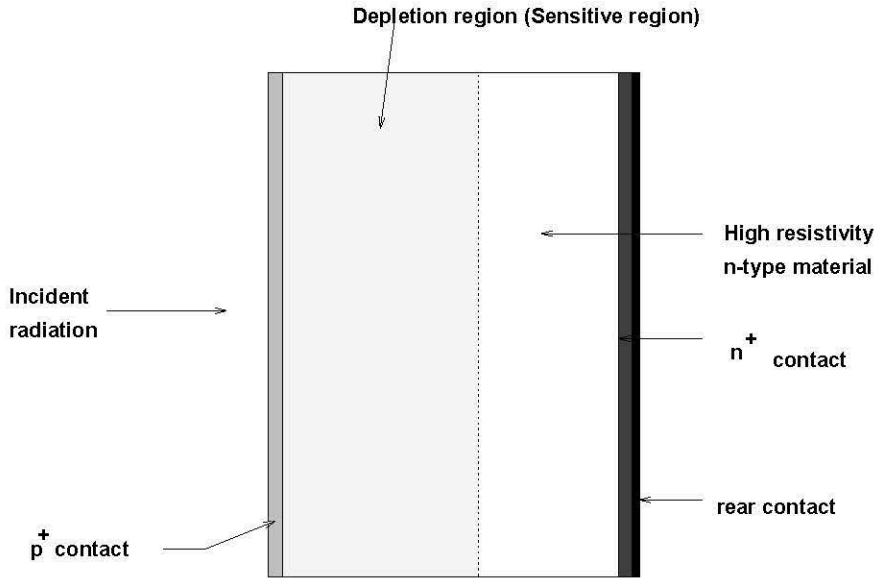

Figure 2.2: A planar semiconductor device

size 5cm x 5cm) in the form of strip diodes along one dimension. The typical strip pitch is 50μm. A cross section of such a structure is shown in Fig 2.3. The fabrication techniques are all routinely used processes in the semiconductor industry. High resistivity(>10Kohm) 300μm n-type silicon is the substrate and its back plane is doped n^+ and a 10μm Al deposited on it. An oxide layer is grown on the top layer, windows are opened(using photolithography)and p^+ strips formed by ion implantation. The lower surface is ion implanted with an n-type dopant. The oxide over a p^+ strip maybe regrown to achieve an AC coupled detector structure. The buried strips are usually grounded through large value($\geq$1MΩ) polysilicon resistors. After standard annealing stages, the top and backplane metallization layers are deposited. The finished detector may be encapsulated in a polyimide film and has the strip metallization leading to pads along the edges of the detector. These pads are wire-bonded to the readout amplifier.

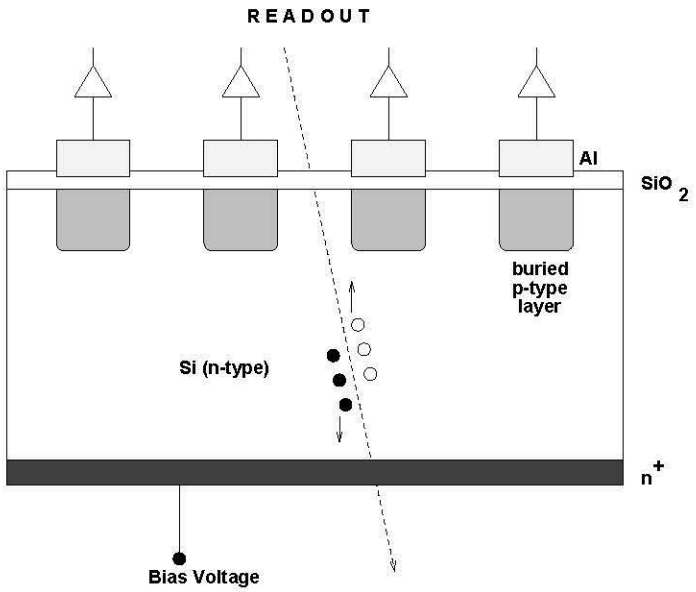

Figure 2.3: Silicon microstrip device

2.2.4 Readout and signals

The detector strips are usually wire-bonded to a low noise charge to voltage amplifier. The signal may pass through a discriminator stage and may be shaped before being digitized by an ADC. Position resolution depends on the pitch of the strips and on the amount of charge sharing across strips. A particle passing in between 2 strips deposits charge on the two adjacent strips. A charge weighted centroid algorithm will give the position of the particle typically with a resolution of pitch/5. If the interstrip capacitance is higher than the junction capacitance, more charge sharing occurs and better charge weighted resolution is obtained. But then the average charge on a strip falls and noise contributions from load capacitances dominate. Low noise readout systems are hence essential to maintain high resolution tracking.

Typical depletion voltages required are 40-65V for 300μm thick silicon. Pulse height SNRs(signal to noise ratios) exceed 6 and position resolutions are 5-10μm . Radiation damage to the detector starts to become important

when the fluences seen by the detector exceed 5×10^{12} cm^{-2}. These are evidenced as crystal bulk damage leading to space charge inversion, depletion voltage and noise increases, until the device fails to function.

2.3 SELEX-The Charm Baryon Experiment

SELEX[9] is a particle physics experiment, currently running at Fermilab Hyperon Hall at Fermilab,(Batavia IL). The collaboration comprises about 115 physicists from 20 institutions worldwide. It was proposed in 1987 and the E781T(test run) was conducted in 1991. It has been running(at the time of this writing) since June 1996 and gathering charm data during the fixed target operation period.

2.3.1 Overview of Particle Physics

Particle physics deals with the continuing quest to understand the basic constituents of matter and their interactions. Over the last few decades, a variety of sub-atomic particles have been discovered, studied and grouped. The Standard Model[10](see Fig 2.4) has been quite successful(so far) in describing the relations between these elementary particles. Elementary particles can be broadly subdivided into quarks, leptons and the interaction "mediators". Six quarks have been observed(the last discovery was of the top in 1995). Combinations of Up and Down quarks form protons and neutrons while combinations of all six quarks form less stable hadrons. Leptons include the electron, two unstable particles just like it(the muon and tau) and their corresponding neutrinos. The mediators of the weak, strong and electromagnetic forces are the gauge bosons. The Higgs Boson has been predicted by the model but not yet observed.

Experimental particle physics attempts to create these short lived particles in the lab, to explore their properties. This is done by accelerating charged particles(like protons) to very high relativistic energies and colliding them with other stationary or moving particles. The resulting collision

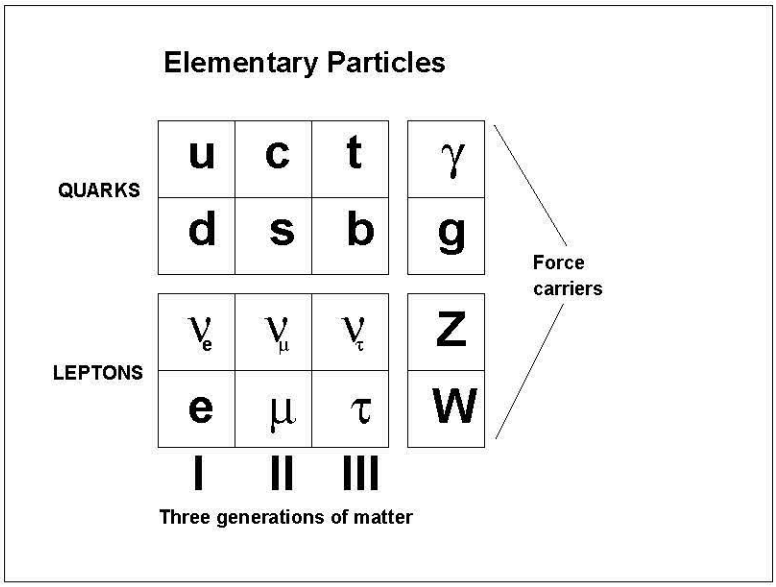

Figure 2.4: The particles according to the Standard Model

obeys basic conservation rules and also produces new particles. Highly specialized detectors are used to measure the production, trajectory and energy of the interesting particles in order to deduce their properties. The search for heavier or exotic particles requires larger accelerators(greater energy). Today's accelerators are typically housed in a dedicated laboratory supported by government research funds. CERN in France, and Fermilab(in IL USA) are examples of laboratories that do particle physics research.

2.3.2 SELEX physics goals

SELEX(Segmented Large X baryon spectrometer) is a fixed target experiment at Fermilab designed to make high statistics studies[11] of charm baryons. Charm baryons are hadrons and contain at least one charm quark. SELEX intends to accumulate more than 10^6 reconstructed charm, half of them baryons, summed over all decay modes and all four stable charm baryons. There is also a set of photon physics topics(Primakoff, Hyperon radiative decays, exotic mesons, hyperon electron scattering etc.), which will be studied parasitically to the main charm data taking.

2.3.3 SELEX Design

SELEX uses a 3 stage magnetic spectrometer and provides good particle identification with a Ring Imaging Cerenkov(RICH), electron TRD(Transition Radiation Detector)[12], and lead glass photon detectors that cover the forward hemisphere in the charm decay frame. The detector has an acceptance of $0.1 < x_F < 1.0$(x_F is the Feynman fraction). The layout of the experiment is shown in Fig 2.5 for the experiment in the Fermilab Hyperon Hall.

Various regions of the spectrometer are designed to perform the following funtions:

- Beam region: A Beam Transition Radiation Detector(BTRD) distinguishes Σ^-/π^- in the beam. Transition radiation is emitted by a charged particle crossing the boundary of dissimilar media. It depends on the γ(Lorentz factor) and hence the particle momentum. Typical TRDs use layers of radiator material to enhance the effect through interference[12] and wire chambers to detect the x-ray radiation.

  8 20μm pitch VLSI readout beam silicon strip detectors provide coverage of the beam region to provide precision tracking for high momentum, small angle tracks. This is important in reconstructing the primary interaction vertex of the charm event.

- Vertex region: A highly redundant 20-plane 4-view silicon strip detector system with VLSI readout covers this region. The 20μm and 25μm readout pitch detectors provide high resolution(4μm)tracking and vertex reconstruction.

- M1 spectrometer: Large acceptance spectrometer with 2.5 GeV/c momentum cut-off. This is designed for soft pions from excited state decays for spectroscopy and soft particles from decay of partner charm for charm pair studies. The Photon I(136×110 cm^2) detector is downstream of the M1 magnet and is composed of 630 lead glass blocks. "Photon" lead glass detectors produce electromagnetic cascades from

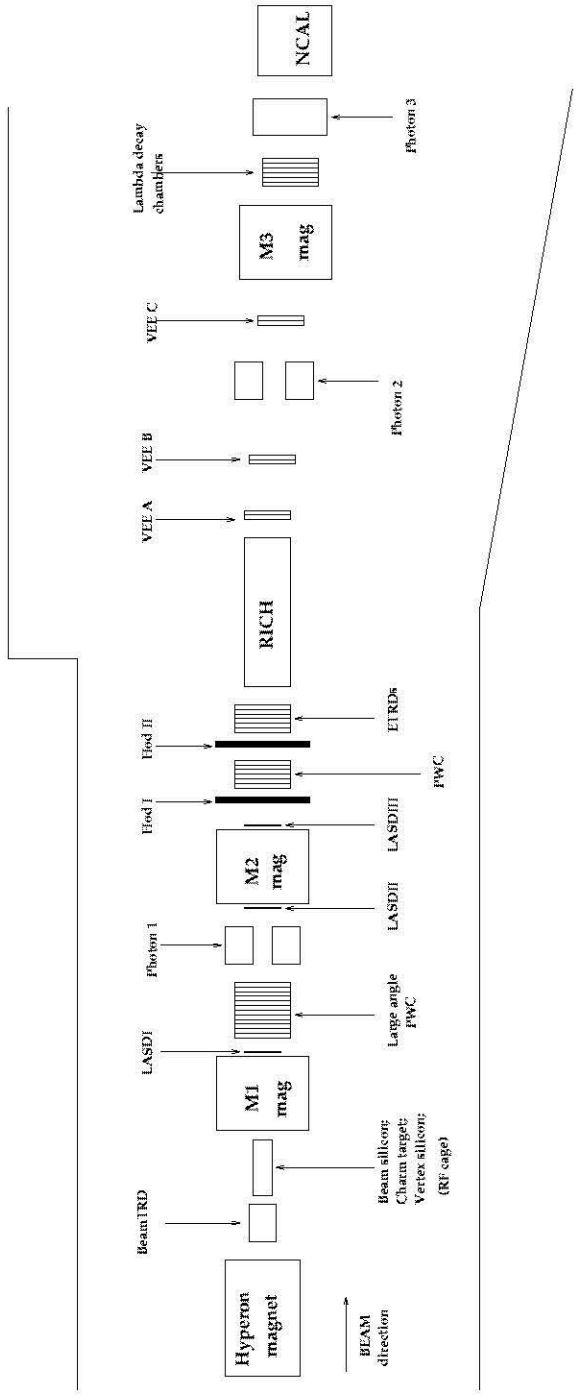

Figure 2.5: Layout of the SELEX spectrometer(not to scale)

high energy photons. These photons are detected by photomultiplier tubes in the detector.

- M2 spectrometer: A forward spectrometer with 15 GeV/c momentum cut-off. This is designed for efficient trigger and large acceptance for charm baryons having $x_F > 0.1$. Tracking is provided by 14 planes of Dual Proportional Wire Chambers(DPWC) downstream of the M2 magnet. Lepton identification is provided via the electron TRD which are 6 PWC planes with polypropylene radiators. In addition, the Ring Imaging Cherenkov(RICH) detector provides (e, μ)separation, useful π/K separation from 20-225 GeV/c, and K/p separation from 40-480 GeV/c. Cherenkov radiation[13] is emitted by a charged particle travelling faster than the phase velocity of light in the medium it is travelling. The RICH is a 11m long, 3m diameter vessel with 15 mirrors and 2800 phototubes as the photon detector. The radiating gas is neon at room temperature and pressure. The Photon II detector has 726 lead glass cells and is $230 \times 110\ cm^2$.

- M3 spectrometer: A final measurement of ultra high mometum charged tracks is done in this spectrometer. Proton momenta are measured from downstream $\Lambda \rightarrow p\pi^-$ decays. The Photon III detector is $80\times\ 61\ cm^2$ and composed of 328 lead glass blocks. The downstream-most detector is a hadron calorimeter

The lead glass photon detector associated with each of the magnetic spectrometer stages is useful for detecting π^os and photons. The choice of this particular x_F is because at higher x_F, tracks have a higher momentum and lower multiple scattering in the vertex region. This improves the vertex resolution and allows a geometrical miss distance based cut. Also, the solid angle to be covered is smaller with high momentum tracks which allows using a RICH detector with a phototube based detector.

2.3.4 SELEX hyperon beam and target

The beam of physics interest to SELEX is a charged hyperon beam in a 100GeV/c narrow band around 650GeV/c. This beam is produced by the interaction of a primary proton beam at 800GeV/c with a 5% interaction length berylium target. A curved tungsten channel in a magnetic field(from the hyperon magnet) is used to provide the momentum selection of the hyperon beam. By changing the polarity of the hyperon magnet, both positive and negative beams of hyperons can be delivered. The negative beam is expected[14] to have a roughly 1:1 composition of Σ^- and π^- while the positive beam is mainly composed of protons with about 1% Σ^+ fraction. There are 5 target foils in the hyperon beam, each about 1.5mm thick and with a 1.5cm spacing between them. The 2 upstream ones are made of Cu and the remaining 3 are diamond(C). All together, they present roughly 5% of an interaction length to the hyperon beam.

2.3.5 SELEX Trigger

Triggering is achieved by the use of scintillation hodoscopes and counters[1] in upstream and downstream areas. The first two levels of trigger are implemented in hardware. The trigger at the beam level (T0) is formed by hits in the beam scintillators and/or the beam TRDs. For charm interactions, the first level(T1) requires at least 2 positive particles in the hodoscopes behind the second magnet, which has an implicit momentum cut of 15GeV/c. A pair of interaction counters directly downstream of the charm targets "counts" the number of MIPs[2] from the interaction and may be used to form the trigger within 150ns after the interaction.

At the second level(T2) correlated hits in the hodoscopes select at least one positive track > 25 GeV/c. A combination of different hodoscopes may be used to implement other physics triggers.

[1] organic or inorganic plastic emitting molecular level optical transitions on the passage of a charged particle

[2] A MIP refers to a Minimum Ionizing Particle

A raw trigger rate of 10KHz is expected for interactions, with an online deadtime $\leq 30\mu s$ per event .

A level three computation intensive online software filter trigger is also designed to enhance the interactions producing charm. This is one of the novel features of this experiment. Charm particles typically decay with a flight path of several mm(in the lab frame). This gives rise to tracks arising from a secondary vertex along with those from the primary vertex. The primary vertex is reconstructed by the trigger algorithm and events with tracks that miss(large χ^2) the primary vertex(i.e. secondary vertex tracks) are selected. This work is described in Chapter 6 of this thesis.

2.3.6 Data Acquisition System

The beam is delivered to the experiment over a 20s spill every minute. It is expected that 100-140K events (average event size $\approx$ 5K) will be acquired over the 20 s spill. A total of 700 MB of data is acquired every spill. Substantial on-line computing ($\approx$ 1000MIPS) running physics algorithms on the raw data in real time, achieves a reduction of a factor of 10 in the volume of data written to EXABYTE tape. The E781 data acquisition system[15, 16] is part of the DART project, a collaboration between the On-Line Systems(OLS) Department of the Fermilab Computing Division and 6 Experiments. This is done in the hope of reducing the manpower needed to set up individual systems for each experiment.

There are 10 parallel streams to readout different detector systems. The front-ends consist of Fastbus SVX Data Accumulators(FSDA) for the Silicon microstrip detectors, Fastbus TDCs for the Drift Chambers, Fastbus ADCs for the photon detectors, the Chamber Readout System(CROS) for the proportional wire chambers, TRDs and RICH, and the Receiver Memory Hybrid(RMH) system for proportional wire chambers. Scalars and latches are readout using CAMAC. These systems are present in the experimental hall and the data in each stream are sent through optical fibers to the "Schoolhouse"(housing the main DAQ hardware) into Dual Ported Memories

sitting in a VME crate. The Silicon and PWC stream data is distributed to 12 filter processes running on an SGI Challenge. After a level three positive decision, a MVME167(68040) CPU module collects the pointers to all fragments of an interesting event and stores them on one of two 9GB hard disks. The data are then constantly written out to EXABYTE tapes for storage. In addition to beam data, interspill calibration and monitoring tasks are constantly being run on the local frontend readout controllers(FSCCs). The interspill data are processed on these FSCCs, which are fully networked computers and the results of the analysis are transferred to the central server via Ethernet.

2.3.7 Need for vertex resolution

As stated earlier, the goal of the experiment is to perform a systematic study of charm particles. These typically have a decay flight path of a few mm after being produced in the primary interaction in the target. The charm decay products form a secondary vertex and a vertex spectrometer is required to observe these vertices in the environment of multiple tracks. The vertex detector should have a track resolution better than 6-7μm to form the vertices with sufficient z resolution to resolve the primary and secondary vertices. The efficiency of such a spectrometer should be high to allow more physics data. With these requirements in mind, a silicon vertex detector was envisioned to be the best choice of hardware to form the vertex spectrometer. The design, construction and evaluation of the vertex detector over the course of 4 years is described in the following chapters.

Chapter 3

Vertex detector construction and testing

3.1 VSSD system components

The Vertex silicon system consists of 20 single sided strip detectors. The plane strip orientations are arranged so that there are 6 "X" views(strips horizontal), 4 "Y" views(strips vertical), 5 "U" views(strips inclined at 45 degrees) and 5 "V" views(strips inclined at 135 degrees)[1]. 4 planes are mounted on a monument block[2] and there are in total, 5 monument blocks. The configuration is shown in Fig 3.1. Fig 3.2 shows the detail of one monument block. The first set of 8 planes(first 2 monument blocks) have a smaller sized detector and are referred to as "5_cm detectors". The remaining 12 planes are larger and are called the "mosaics".

3.1.1 Silicon Detector

The 8 upstream planes on the 5cm detector boards have a strip pitch of 20μm with a total active area of $5.12\times5.00cm^2$. The strip width is 10μm

[1]The last U and V views are oriented at 15 and 165 degrees

[2]a monument block is a 0.75" thick machined Al plate that mechanically supports 4 detector planes

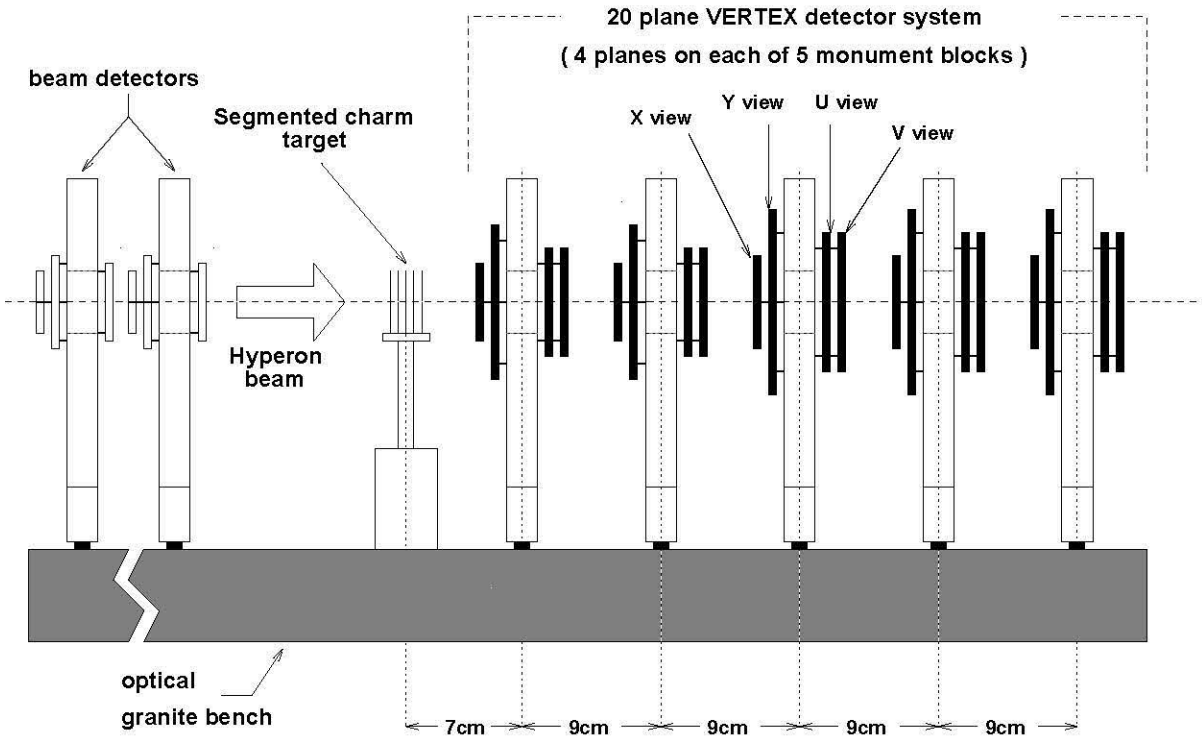

Figure 3.1: The layout of the vertex planes in the vertex region

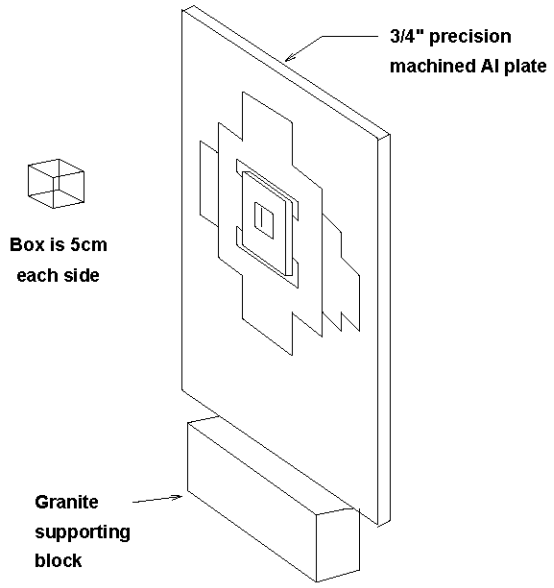

Figure 3.2: A monument block showing 2 detectors on a side

and the strip metallization width is 12μm. The detector is made from 300μm thick n-type Silicon [3]. The strips are processed by p-type ion implantation forming the anodes of the strip diodes. Each diode is connected via a polysilicon bias resistor of value 2.75MΩ to a common bias metallization line(which we wire bonded to ground). A 200nm silicon dioxide layer is formed on the diodes for AC coupling(average capacitance of 22.3pF) of the readout strip metallizations. The Al strip metallizations are fanned out into two double rows of bonding pads on each side, with a pitch of 100μm in each row. The total number of strips is 2560, and in the two outer 512 strip regions, every second strip is metallized on the coupling oxide and read out. There is a 10μm thick Al backing which serves to provide the reverse biasing potential to the detector. A grounded guard ring surrounds the detector to minimize edge effects.

The downstream 12 mosaic planes have a strip pitch of 25μm. The junc-

[3]manufactured by Detection Technology Inc.

tion and strip metallization widths are 12μm and 7μm respectively. Each plane consists of a mosaic of 3 monocrystal silicon detector panels, each $8.3\times3.2cm^2$[4]. Adjacent panels have the long edges butted against each other and all three are connected to the same ground and bias voltage lines. There is a dead space of about 1mm between active end strips on adjacent panels. Strip diode anodes are connected to a grounded line through 6MΩ polysilicon resistors. A grounded guard ring is present to minimize edge effects. There are 1280 strips on each panel. All the strips on the central mosaic panel are read out while the outer panel have every alternate strip read out[5]. The larger size of mosaics reflect the constant angular acceptance(about 100mrad) of the spectrometer.

Both types of detectors show full depletion at a voltage of 35V. They are operated with overvoltage at 65V, provided by a low noise power supply[6]. This voltage was chosen because the signal to noise ratio at this voltage was found to lie on an acceptable plateau(See Fig 3.3). The dark leakage current in the detector was found to be about 2.7nA per channel at 27^oC. The detectors have a protective transparent coating of polyimide. During normal operation, the detectors are in a light tight Al box and continuously flushed with chilled air at 19^oC.

3.1.2 SVX Silicon Readout Chip

The silicon vertex(SVX)[17] chip was designed at Lawrence Berkeley Laboratory in the late eighties for collider beam experiments. It was adapted for fixed target experiments, specifically for SELEX[18]. It is a high density data acquisition Application Specific Integrated Circuit(ASIC) (1.2μm design rules) for reading out data from silicon strip detectors. It has 128 identical channels on a 50μm pitch with two rows of bonding pads to acco-

[4]manufactured by Hamamatsu Photonics

[5]The outer mosaic panels subtend angles greater than 80mrad, where the tracks are expected to be sparser. Also, non-instrumented strips capacitively couple to improve the resolution from that of a 50μm pitch readout

[6]Manufactured by KEPCO

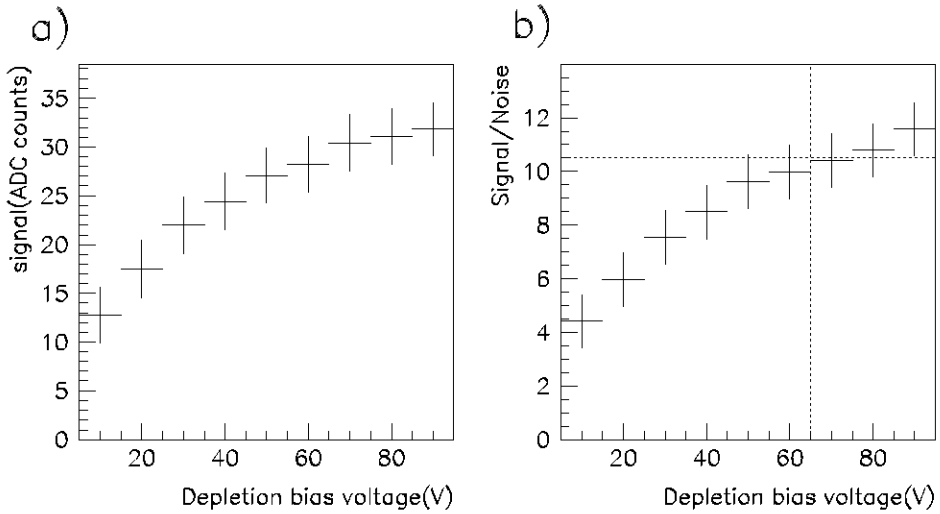

Figure 3.3: a)signal from Back plane pulsing in ADC counts, in a single channel b)The signal to noise ratio for the same channel.(This channel is typical of all channels)

modate wire bonding limitations to $> 60\mu$m spacing. The layout of a single channel is shown in Fig 3.4. The input amplifier connected to the detector strip is a high gain dual cascode inverter with a 0.3pF feedback capacitor. The input point is also coupled to a common calibration line with a 0.06pF capacitor. This is followed by two stages of inverters with a sample and hold capacitor C_{comp} in between. The output from the second comparator is coupled to the latch section. Readout is achieved by controlling the sequence of switching of Ra,Rb,Rs,Rc,Rd and a few more signals. This is done using the SVX Readout Sequencer(SRS) (described later in the section on readout). The charge from the detector strip is integrated and stored on C_{comp}. A known threshold charge input from the calibration line is then subtracted from the signal. The polarity of the summed charge determines the output of the comparator/latch and whether the channel is read out or not, in sparse mode[7]. Each SVX chip draws on the average about 55mA and dissipates

[7]The mode in which fewer than the total number of instrumented channels are read

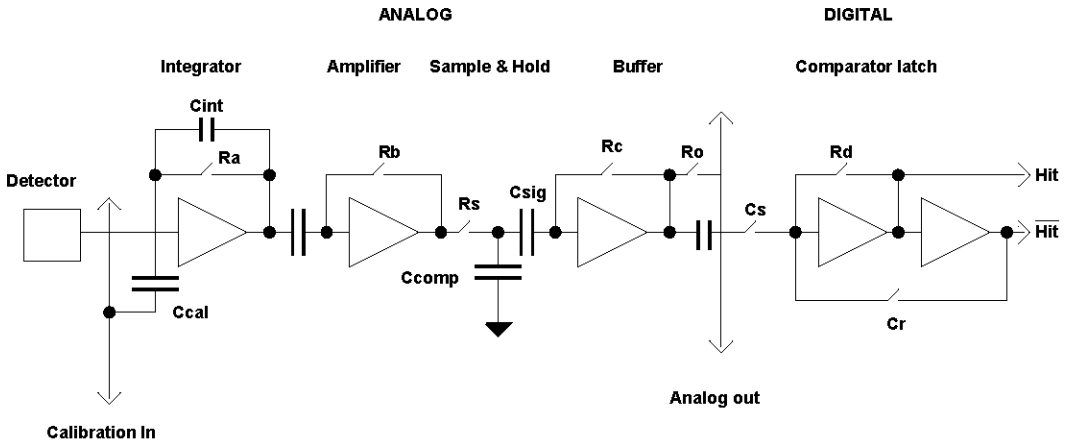

Figure 3.4: Schematic of a single SVX channel

about 260mW. The chips first have to be initialized with a unique 6bit chip address. Up to 64 chips may be daisy chained and read out using a priority token logic. Every readout cycle is 650ns long and identifies a channel by its chip id and 7bit channel address(0-127). The analog output of each channel is a tristated line and is connected to an analog output line common to all chips in a chain.

All the SVXs are connected to the bi-directional SVX bus which is a set of lines carrying analog and digital signals from the SRS.

The SVX chip has to be synchronously controlled for proper read out operation. For this purpose, there is a set of 8 dedicated control lines. A sequenced series of voltage pulses is input on this bus by a sequencer module(SRS, described in 3.1.4). This results in the control of various switches in every SVX channel and hence the proper functionality of the channel as a charge to voltage converter and amplifier. In this sense, the SVX is a programmable device requiring active real-time control.

out. The mode in which all channels are read out is called "latch-all"

3.1.3 Assembly of VSSD planes

Each detector plane is mounted on a G-10 printed circuit board, with support along the edges. Conductive epoxy serves to hold the detector down as well as provide electrical bias contact to the backplane. The SVX chips are epoxied on to the circuit board next to the detector(see Fig 3.5) in two rows on opposite sides of the detector. The strip pads on the detector are wire bonded to the corresponding strip pads on the SVX chip with 30μm Al wire[8]. 1024 channels(for 5_cms) on each read-out side of the detector are wire bonded to 8 SVX chips, each with 128 channels. For mosaics, each read out side has 1280 channels. The circuit board contains 4 layers, designed to carry power, digital and analog readout buses to every readout chip, with adequate grounding in between. Most of the components are surface mounted and 20 and 24 pin connectors are soldered near the corners. The printed circuit board is epoxied on to an 1/8 " thick anodised Al plate, which has mechanical mounting holes and provides overall support to the detector plane. An exploded view of a vertex detector is shown in Fig 3.6. A cover plate is glued on to the circuit board and serves to protect the exposed SVX and wire bond. All the mechanical components have the active area of the detector cut out so that a particle sees only the 300μm thick silicon in its path. When turned on, the SVX chips dissipate about 4-5W, some of which heats up the silicon detector nonuniformly[9]. A study was done on a thermal mock-model of a 2 plane detector system to evaluate this problem. It was found that cutting slots in the cover plate and forced air convective cooling(using a boxer fan) ensured satisfactory thermal dissipation(this design feature is incorporated in the final system).

All detector planes require 4.85V for the SVX power and 65V for the reverse bias depletion voltage. High current capacity, low noise regulated power supplies have been used.

The circuit board on all detectors is laid out as two halves which are mirror

[8]done at PROMEX CA and FERMILAB

[9]when in the vertical position, convection creates hot spots

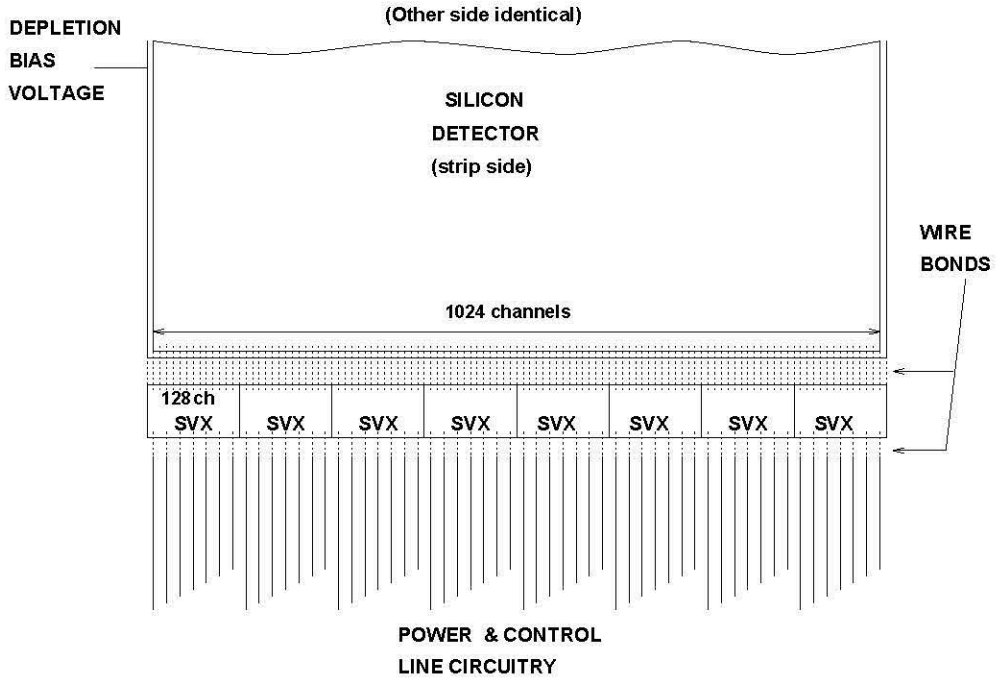

Figure 3.5: Detail of the Detector and SVX chip region

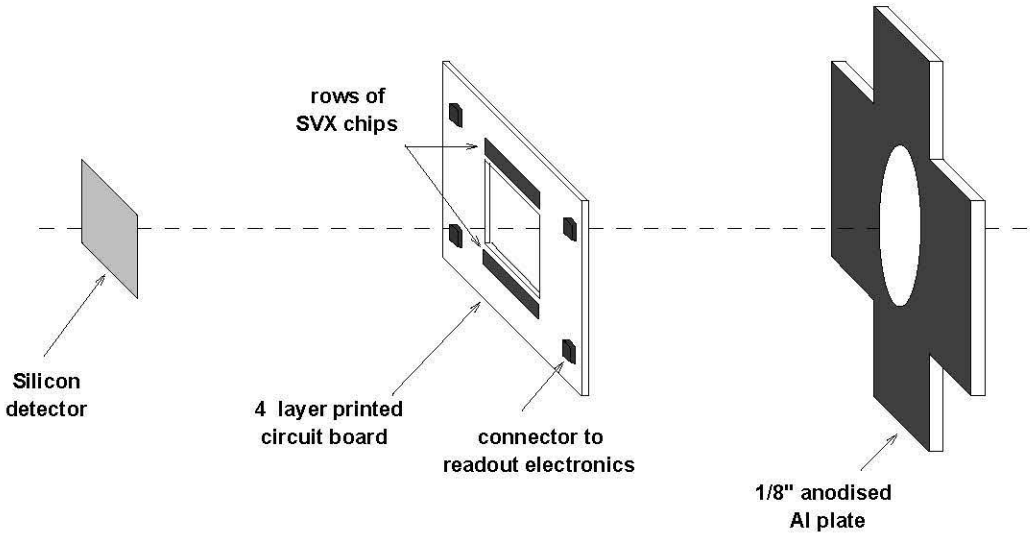

Figure 3.6: Exploded view of a vertex detector

images of each other and only share the same ground plane. Each row of SVX chips is daisy chained and associated with one half of the circuitry. Each half is connected to a bi-directional control bus(24 pin) and a set of calibration lines(20 pin). These signals come in from the DRIVER CARD, on high density flat cable with headers that plug into the connectors on the detector board. As the detector strips are interleaved, the physical order must be re-established in the read-out process. This is a feature of the FSDA(read-out module, described in 3.1.6) architecture.

3.1.4 Silicon Readout Sequencer

The Silicon Readout Sequencer(SRS)[19] which is the master control module, controls the initial programming, reset, calibration and read out of all the SVX chips in the system. It resides in a CAMAC crate about 2m from the silicon detectors. The SRS is a CY7C910[10] based programmable sequencer in a triple width CAMAC module. Fig 3.7 shows the logic diagram of the SRS. Its main functions may be listed as:

- Initialize all SVX chips;
- Interface trigger signals and generate BUSY and LIVE bits;
- Provide a preset sequence of control signals for SVX signal integration;
- Synchonize data read out from the SVX;

The code to perform these functions is an ASCII file called a "pattern". A sample set of lines from a pattern is shown below and the '1's and '0's are the set and reset operations on the readout switches. In this respect the pattern is essentially a low, machine level code. The pattern file is read by a FORTRAN cross compiler which produces code in a CAMAC downloadable

[10]Cyrix manufactured microcontroller

format.

```
*****************************************************
*************Sample of SRS code(pattern)****************
*****************************************************

'line inst labl addr –bottom— ——top——- cc dac clk' comment
 7 cont   0   0  010100000000 1111000101000000 00  00 1;let AR settle
 7 cont   0   0  010100000000 1111000101000000 00  00 1;let AR settle
 7 cjp   22  30  010100000000 1111000101000000 06  00 1;test AR
 7 jmap   0  22  010100000000 1111000101000000 00  00 1;wait if not
 1 cont  30   0  010100000000 1101110101000000 00  00 1;cRabcdCk
 1 push   0  10  010100000000 1101100101000000 00  00 1;
 1 rfct   0   0  010100000000 1111000101000000 00  00 0;Ra clear 1 us
 1 push   0  10  010100000000 0111000101000000 00  00 1;
 1 rfct   0   0  010100000000 0111000101000000 00  00 1;Ra settle 2us
 1 jmap   0  36  010100000000 0111000101000000 00  00 1;jmp to WAIT
 1 cont  32   0  010100000000 0101110101000000 00  00 1;cRbcdCk: MRS
 1 push   0   4  010100000000 0111000101000000 00  00 1;
 1 rfct   0   0  010100000000 0111000101000000 00  00 1;Ra settle 2us
 1 cont   0   0  010100000000 0110000101000000 00  00 0;lasd
 1 cont   0   0  010100000000 0110000101000000 00  00 0;lasd
 1 cont   0   0  010100000000 0110000101000000 00  00 0;lasd
 1 cont   0   0  010100000000 0110000101000000 00  00 0;lasd
 1 cont   0   0  010100000000 0110000101000000 00  00 0;lasd
 1 jmap   0  36  010100000000 0111000101000000 00  00 0;jmp to WAIT
 1 cont  45   0  010100000000 0110000101000000 00  00 0;SRes from T1/noT

   ********************end ****************************************
```

Patterns that synchronize the readout cycle are initially downloaded into the SRS via CAMAC into its 2 banks of 4K RAM. The Micro-sequencer

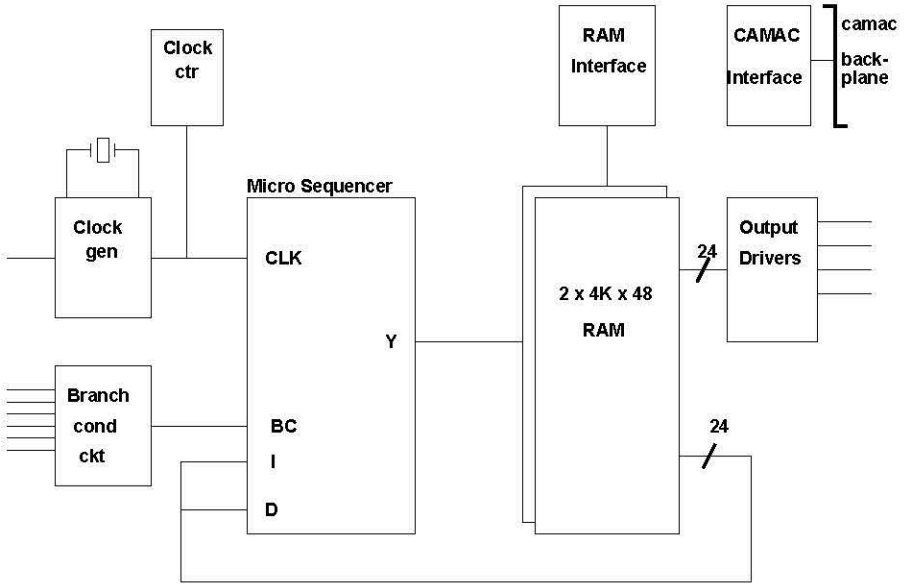

Figure 3.7: Schematic layout of the SRS module

then continuously generates addressess which accesses instructions from the memory. These pre-programmed bits appear as hardware SVX control signals on the output bus of the SRS. The SRS can handle trigger signals from 7 branch condition inputs and generates output Busy signals in order to interface with the rest of the DAQ.

Salient features of the module are:

- Microprogram memory: 2 banks of 4K works each;
- Clock period: 50ns, 200ns, or external(greater than 50ns);
- Output: Four control buses driven in parallel and 7 NIM user defined signals;
- Branch conditional inputs: 4 NIM(LEMO connectors on front panel), 2 differential on the control bus), 1 software(CAMAC controlled);

3.1.5 Driver Card

The Driver card is a 4-layer 20"x7" printed circuit board functioning as an interfacing unit. It sits about 30 cm from the detector boards(one over each monument block), in slots in the cage housing the detectors. Each Driver card serves the following functions:

- Fan out of SRS signals to 4 detector planes, and 2 FSDAs;
- Translate CMOS(to and from SVXs) to differential signals(to and from FSDAs) and vice versa;
- Shift and amplify analog signals from the SVX and differentially transmit them to the FSDAs;
- Perform handshake between the SVX and FSDA using status signals;
- Provide calibration pulses to each SVX under SRS control;
- Perform bypass of the SVX input to evaluate readout performance characteristics;

The control bus from the SRS goes to the chain(containing five) of Driver Cards through a 40pin flat cable with a delay less than 50ns(the clock cycle for the SRS). During the signal integration and triggering phase, the control bus signals are converted to TTL levels by differential receivers. The signals are buffered and converted to CMOS for each silicon plane(SVX chain). During read out, data come over the the bi-directional data bus. These data are buffered, converted to differential levels and delivered to the FSDAs along with SRS-generated strobes. The SVX-issued Priority Out and FSDA-issued Accumulator Ready are important status signals logically processed by the Driver cards to ensure readout synchronisation. Calibration(threshold) DACs on the Driver Cards are loaded through a serial 3-line interface which is part of the Data Bus. The loading is done by the Fastbus Master Module(FSCC), using the FSDAs as an interfacing unit. The DAC output lines are connected to the SVXs over the single ended Calibration Bus.

3.1.6 Fastbus FSDA Data Acquisition

The Fastbus SVX Data Accumulator (FSDA)[20] is a single width FASTBUS module intended to collect and process SVX data. Each FSDA has two identical channels. Each channel handles data from two subplanes-REVERSE and DIRECT. A simplified logical diagram of one FSDA channel is shown in Fig 3.8 The following is a list of the FSDA functions:

- Receives digital and analog data from SVXs (Latch, Digitizer);
- Converts the strip codes into logical strip numbers(Address Converter);
- Checks the correct(monotonic) order of strip numbers;
- Digitizes analog data amplitudes(Digitizer);
- Subtracts preloaded pedestals(individual, for every strip) from the digitizes amplitudes(Pedestal Subtracter);
- Suppresses data with pedestals below preloaded pedestals(Pedestal Subtracter). This prevents the occurrence of strips with negative signal;
- Converts the amplitude codes into 4-bit format to reduce data size(Format Converter);
- Merges data from 2 subplanes into data blocks ordered in terms of the coordinate of the whole plane(Data Merger);
- Forms headers for event data blocks, including event number and word counter(Data Merger);
- Performs FIFO buffering of the outgoing data blocks(Output FIFO buffer);
- Transmits the data to the Fastbus Backplane using Megablock[11] mode;

[11] a high speed multi-module data transfer

- Provides a serial digital interface to load Threshold DACS located on the Driver Card;

Each of two channels on board a FSDA module receives digital strip addresses and analog voltages(proportional to the charge deposited on the strip). The digital addresses are first converted into logical strip numbers and the monotonicity of addresses checked. The analog signal is digitized using a Flash ADC and a preloaded pedestal value is subtracted. Strips with hit amplitude values less than the pedestal as well as pre-determined "noisy" detector channels may be suppressed. Data from DIRECT and REVERSE subplanes are merged and the strip address and amplitude information is packed into a 32-bit word format. This data is then transmitted into the FASTBUS backplane using the Megablock mode.

The output data for an event is a set of 32-bit words read out over the Fastbus backplane. The first word in the block is a Header word and the rest are Data words(arranged as two 16-bit Data words in each Fastbus word). The Header and Data word formats are shown below in Table 3.1 and Table 3.2. The header word gives information on the event number, data word count and the integrity of the event(through error flag status bits). The Data words may be in two formats. The 8-bit Amplitude format is used when all SVX channels are read out without sparsification in the "latch-all" mode. For a chain containing 2 or more SVXs, the 8 bit strip field will contain ambiguous addresses, but this is inconsequential because we know that all channels are serially read out(in one direction). The second format is the one used in normal "sparse" mode data taking. 12 bits of strip addressing uniquely specifies a hit channel in the largest SVX chain in the system(10 chips). The price for this is paid in lower amplitude resolution. However, studies of the expected amplitude dynamic range indicated that it could be represented in 4-bits with very little loss in 1-MIP vs 2-MIP resolution.

10 FSDA modules are required to read out the 20 vertex detector planes. They sit in a standard Fastbus crate. The hard-wired data processing performed in the FSDA modules has been estimated to be 2000MIPS. The mas-

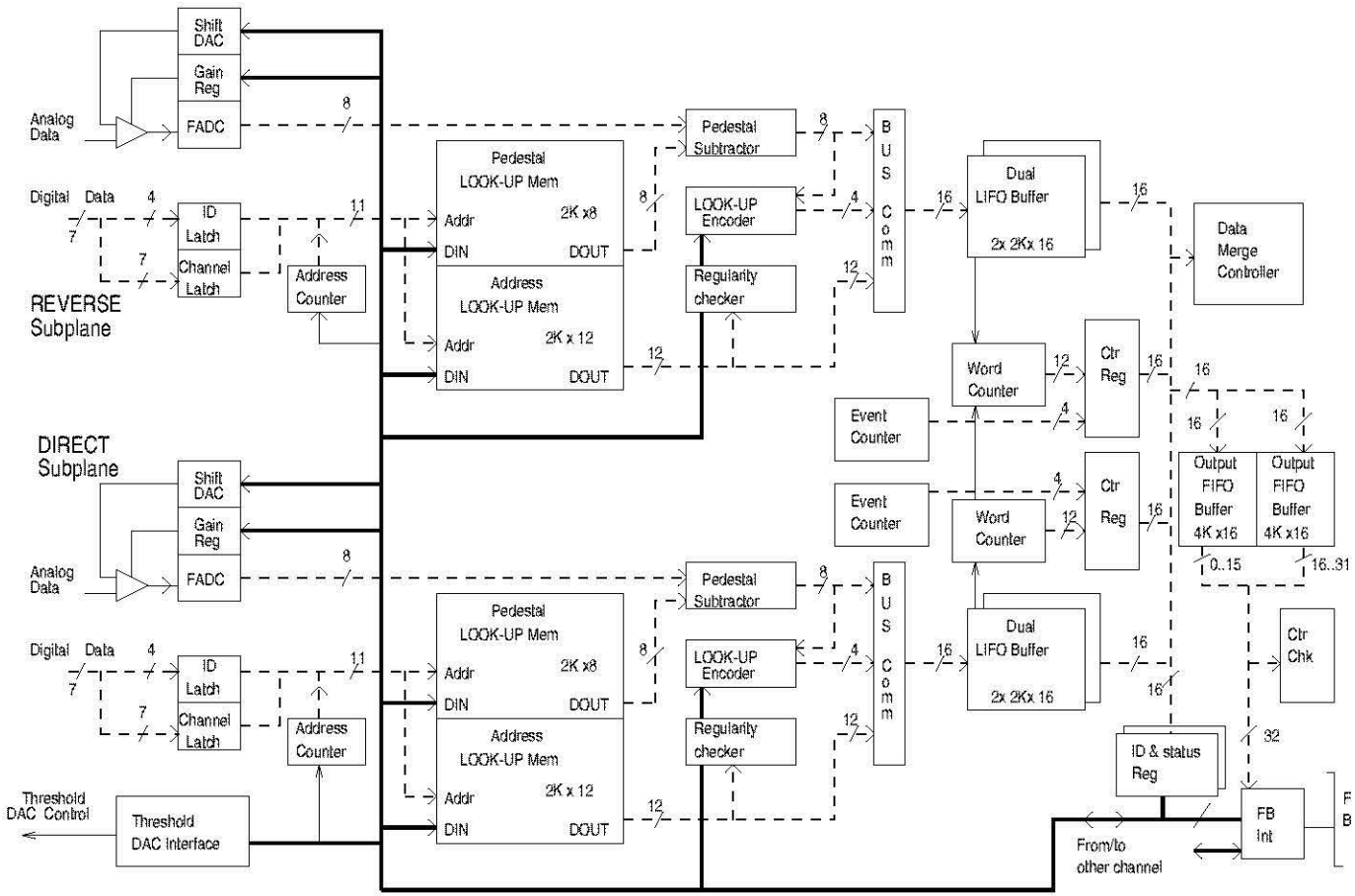

Figure 3.8: Schematic of the channel of the FSDA

15 8	7 0
Strip Number	Amplitude

Table 3.1: 8-bit Amplitude format Data word

15 12	11 0
Amplitude	Strip Number

Table 3.2: Normal format Data word

ter module or crate controller is called the FSCC. This board contains a microprocessesor(MC6802) and performs all Fastbus actions. It also has 4MB of RAM and will perform onboard computation and analysis of data. This feature is used only during off spill data taking[12]. During onspill running, the FSCC only pipes the data from the backplane into its output FIFO in order to be read out. The arrangement of the data flow is shown in Fig 3.9.

Data from the crate is converted into an optical data stream using a Fermilab designed fiber transceiver. The high bandwidth fiber allows efficient transport of all the data over a distance of 100m from the experiment hall to the central computer. The data are then converted back to an electronic bit stream by another optic-electronic transceiver and pushed into Dual Ported Memories(DPM) residing in VME crates. Here streams corresponding to different dectectors in the experiment are merged into the standard E781 data structure. 11 processors in a SGI Challenge[13] unpack, analyze and save events as part of an online level three filter trigger.

3.1.7 Trigger Handling and read out Sequence

The first step in the data taking sequence is initialization. The SRS is initialized with a pattern from the host computer(via CAMAC) and started. The FSDA memories are initialized by the FSCC with pedestal, strip address and adc lookup tables. The threshold DAC levels are loaded and set on the Driver

[12]e.g. pedestal acquisition and monitoring
[13]1200MIPs

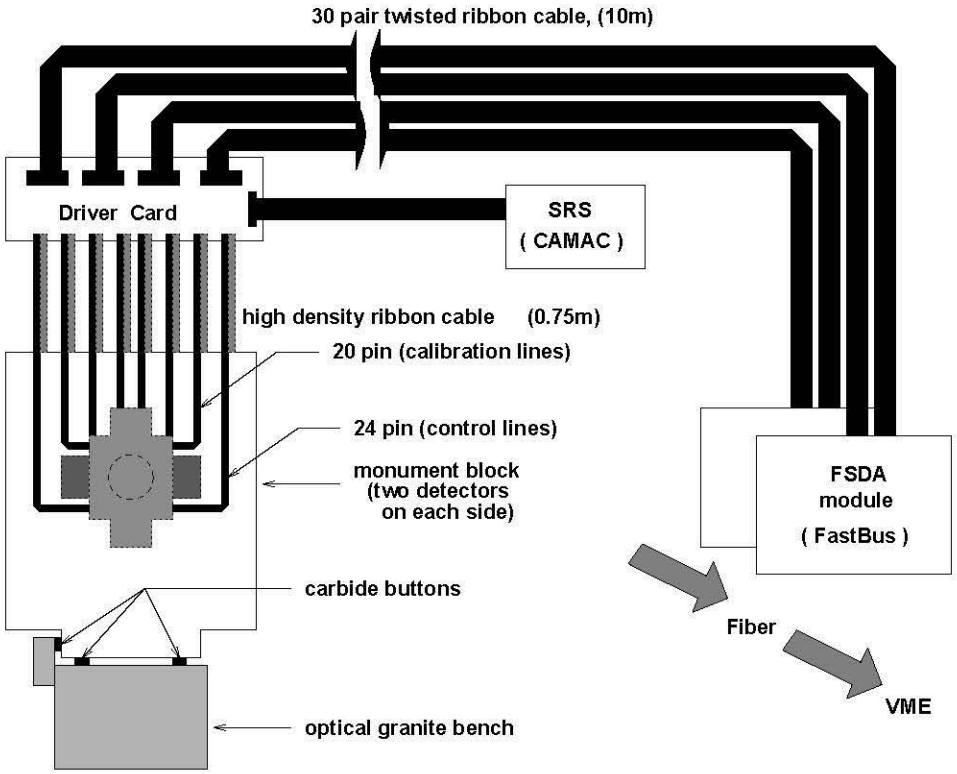

Figure 3.9: Arrangement of data flow in the vertex system

cards. Once all the initialization is complete, the SRS handles trigger signals and controls the system. While waiting for a trigger, the SRS arms the analog stages of the SVX to integrate incoming charge for about 10μs . (Bench tests had shown that the noise due to leakage currents is acceptable(0.35fC) for 10μs but increases steadily for longer integration times.) If no trigger is received in this period, a fast reset erases the charge due to leakage currents and/or beam tracks that do not satisfy the physics trigger. After 100 short resets, a longer and more comprehensive long reset is performed, followed by a short reset. BUSY is asserted when resets are performed and the dead time is less than 5% at a 25kHz readout rate. The reset logic and trigger definition are flexible and changes are easily implemented by changing the SRS pattern.

Fig 3.10 shows a logic flow diagram of the trigger-readout interaction. When a valid first level trigger(T1) occurs, the system looks for a second level trigger(T2) which is a confirmation. If no T2 confirmation is received then a short reset is performed and the system continues to loop, waiting for a T1. If T2 is received then the microcode jumps to the place which allows the injection of a fixed amount of threshold calibration charge[14]. This is followed by readout in the sparse mode. The SVX will latch ON channels with signal charge greater than the calibration threshold(on board SVX sparsification). Each hit channel is read out in about 650ns. As all the detectors are read out in parallel, the duration of the sparse cycle readout is determined by the maximum number of hit channels in a single detector[15]. This read out time is under 30μs (the design spec) and is closer to 20μs. Prior to resetting and waiting for the next trigger, the SVX awaits the Accumulator Ready signal from the FSDA which signals that data has been properly transferred into the FSDA. The FSCC is triggered only at the beginning and end of the spill[16].

[14]In the data run, T2 did not contain any decision and was simply passed

[15]and a few microseconds of initialization overhead

[16]The spill is a periodic time structure dictated by the availability of beam particles in the accelerator rf bucket. During the first 20 seconds(onspill) of every minute, the spill is ON and beam is present. During the remaining 40 seconds(offspill) there is no beam.

At the beginning of spill, the FSCC assigns the Primary Address Cycle to the first FSDA and waits for output FIFO data in MegaBlock mode. The FSCC continues to loop with MegaBlock Transfer Reads, transferring data to the central server, until the end of the spill.

3.2 Software infrastructure development

Every major aspect of the vertex detector system was developed from the ground-up. Once the hardware configuration(FSCC, FSDA, SRS etc.) was finalized, a specific suite of programs were written to readout the newly built detectors. This code covered the following major areas,

- **VxWorks/FastBus libraries:** FastBus FSDA modules acquired and digitized a raw data event. This data then had to be read out observing Fastbus protocol. The FastBus crate controller(FSCC) ran the VxWorks real-time operating system. Libraries(macros) were written for this platform to co-ordinate data transfer in a synchronous manner from the FSDA to the FSCC. These included all the FastBus system calls to operate the FSDA. After analysis in the FSCC, histogrammed results were to be transferred to the host (UNIX) computer. This was all in cross-compiled C code which was then embedded into the FSCC at run-time.

- **System housekeeping:** The readout sequencer(SRS) required assembly code downloading from the host UNIX machine, at run-time. A set of programs, (in FORTRAN and later in C) were written to handle this functionality.

- **Data analysis:** : Once the event data is transferred into the FSCC, it required almost real-time analysis. Applications written in C processed the data to derive statistical information(mean, standard deviation),

This spill structure is available as a modulated rf signal which is used in the trigger and readout

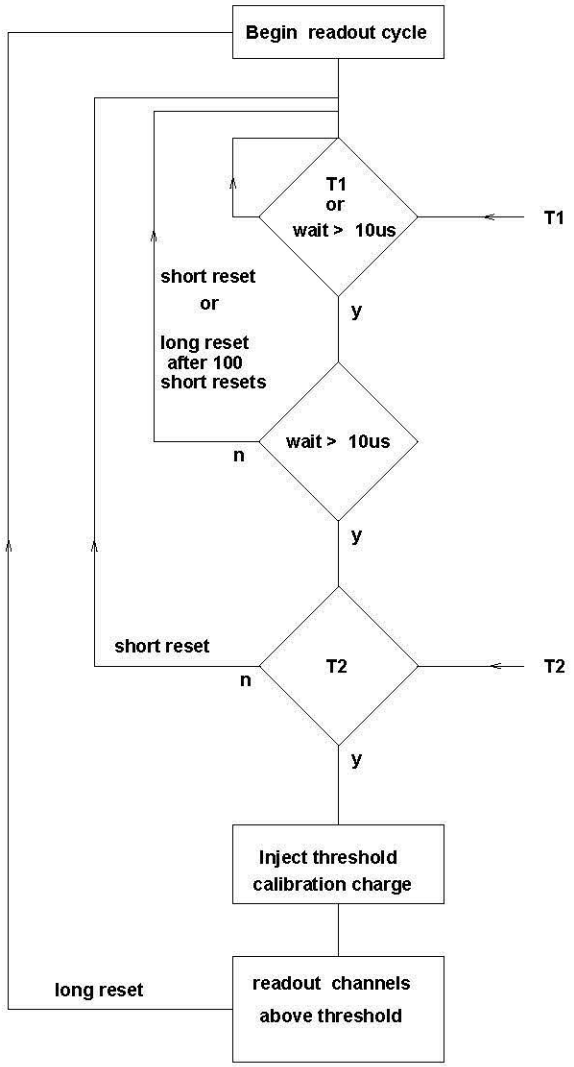

Figure 3.10: Flow chart showing the trigger-readout interaction

signal and other useful analysis data. The code was optimized for speed and a RAM limitation of 4MB in the FSCC. It too was cross-compiled and embedded into the FSCC at run-time.

This set of programs was sufficient to test the the detector hardware completely. It was found to be robust and was very easy to adapt for specific needs. All the tests and results described in this chapter were done using this code package. It served as a prototype for the standard run-time analysis packages which were later developed.

3.3 Bench Testing of VSSD planes

Prototype(and production) detectors went through a series of extensive lab-test techniques. The test set up was designed to be as close to the final operating conditions as possible. The final version of read-out electronics was used. The first step involved bonding SVX chips on the read-out boards and checking the integrity of all digital readout signals. This confirmed that the SVXs were wired correctly and could be read out. Only 0.5%[17] of the chips were found to be defective[18]. The cure involved debonding the offending chip and regluing on another working chip. Next the silicon detector was glued on and all the strips wirebonded to their corresponding pads on the SVXs. The detector plane could then be checked for efficiency and analog integrity.

3.3.1 Pedestal and Noise in planes

Initial check-out consisted of reading out all the channels in the "latch-all" mode. Typical data samples contained 500-1000 events. The mean and rms deviation of the distribution for a single channel, read out in latch-all mode, are seen in Fig 3.11. There is no signal and the pedestal value reflects nominal switching charge injection into the integrating capacitor.

[17] 368 SVXs in total

[18] caused by accidental wire bond footprints accidentally straying into the SVX active substrate area

This charge is expected to be uniform for every event, even when signal is present. The non-uniformity of the pedestal(the rms width) is thus, a measure of the noise in the system. The noise contribution to the analog signal from the bare SVX chip(not wire-bonded to the detector) and all the readout electronics was measured to be 925 electrons. Next the detector was glued on and the interconnections between detector and SVX chip are made using 30μm AlSi wire. The detector has a capacitance of 1.0pF /cm, which raises the noise contribution of the detectors to the value seen in Fig 3.11.

The typical pedestal(and rms deviation or "noise") across the detector strips are shown in Fig 3.12. The conversion from ADC units to electrons is 926 electrons/ADC count[19]. The pedestal is the average charge collected due to quiescient set points of the amplifiers and net switching charge. The noise arises from different sources, both in the detector and in the readout electronics. This rms noise was observed to fall by a factor of 2 to 1850 electrons by lowering the analog supply voltage of the SVX chip from 6.00V to 4.85V. This reason for this phenomenon is not fully understood yet[20]. However, the signal size for induced charge(including beam particles) is not affected, which from 1MIP(after charge sharing between strips is accounted for) is expected to be about 17,500 electrons on one strip.

In about 0.4% of the channels, the analog readout showed a large pedestal variation. This was due to severe field distortion in the region of defects like shorted adjacent channels[21]. These channels were isolated by permanently disconnecting the wire bond to the SVX readout. Such channels are referred to as "plucked" channels and would never be read out.

[19] 1fC $\approx$ 6250 electrons

[20] It is accompanied by a 50% rise in SVX current and related to the PCB anodised Al interface. Bare PCB mounts do not show this phenomenon

[21] these matched a list of channels classified as visual defects, provided by the manufacturer

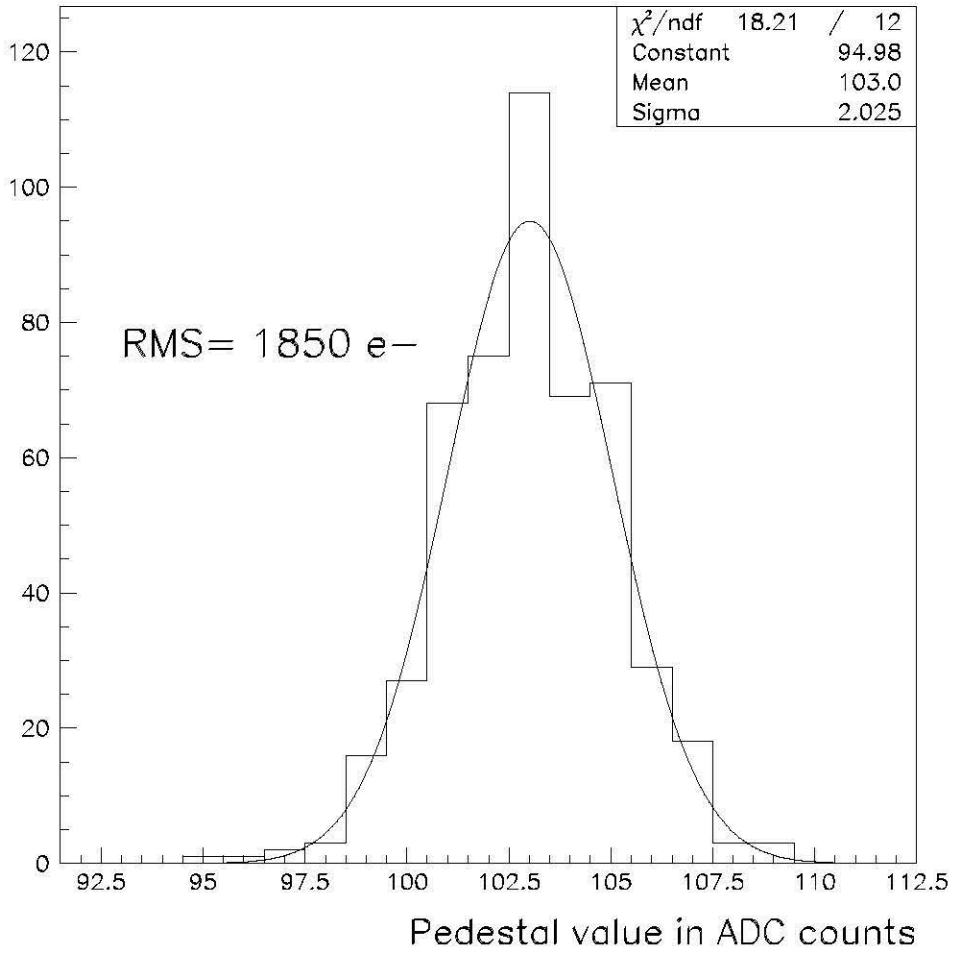

Figure 3.11: The pedestal distribution of a single channel(500events)

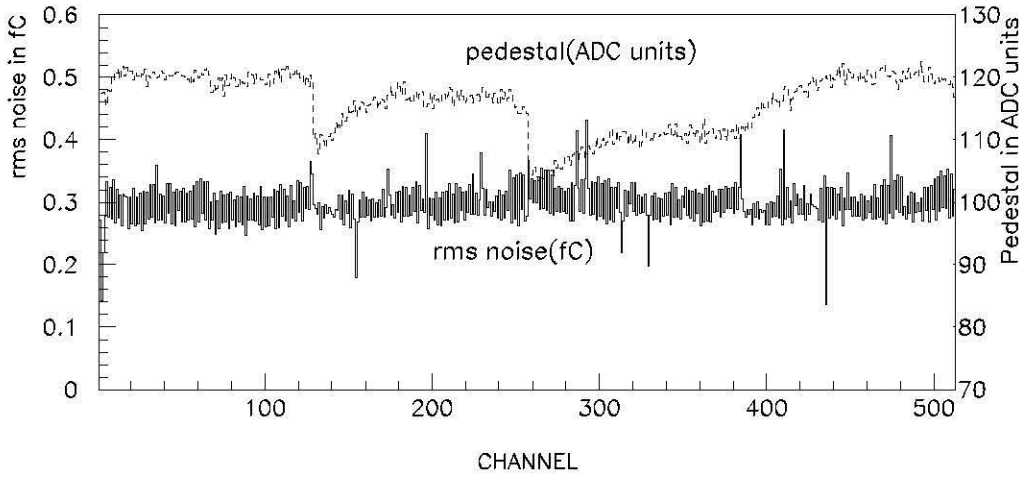

Figure 3.12: Mean pedestal and noise for 512 channels in 4 SVX chips

3.3.2 Sparsification and Calibration

The read-out mode during actual data taking would utilize the sparsification characteristics of the SVX. The calibration capacitor(C_{cal}) on each channel(see Fig 3.4) connected in parallel to the detector, deposits a threshold charge into the summing capacitor. On selecting the proper sign of the charge, this establishes a threshold which must be overcome by signal(or noise) in order for the channel to be read out. This charge is also reflected as a change in average pedestal value.

The detector loaded SVX channels display different probablilities of read-out with varying threshold charge, in the absence of external signals. This firing probability is due to the noise(Johnson, shot, 1/f, switching etc) present in the detector and analog front end of the SVX channel. A "waterfall" plot of the noise occupancy rate as a function of threshold DAC setting is shown in Fig 3.13. The width(10% - 90%) of the waterfall region is related to the

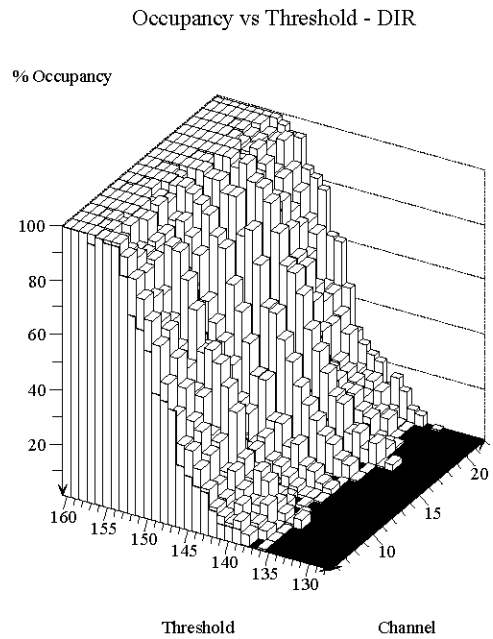

Figure 3.13: The waterfall plot for a typical set of channels. The average noise occupancy is plotted as a function of the threshold setting.

noise and the comparator response function. As seen in Fig 3.13, it is typically 1.65fC for these detectors. Data Acquisition(DAQ) design anticipates about 30 strips to be read out on each detector. At the thresholds used here, the average cluster size for 1 MIP is 1.3 strips. At a typical track multiplicity of 10-12, this means we can read out about 20 signal hits and about 5 noise hits. This requires setting the adjustable SVX threshold so that the noise occupancy in the sparse readout mode is between 0.1% to 0.2%. Due to the fact that the interstrip capacitive coupling is about 0.15pF, SVX chips across from each other have to be calibrated at the same time. An automated DAQ procedure was developed whereby all the chips on a detector were calibrated simultaneously. The algorithm involves scanning the occupancy level over the threshold DAC range until a preset level is reached and then dynamically allowing the thresholds to change until all chips have the desired occupancy. The noise occupancy behaviour in the region of interest is shown for both types of detectors in Fig 3.14.

The sequence of steps followed in readying the detector hardware is as

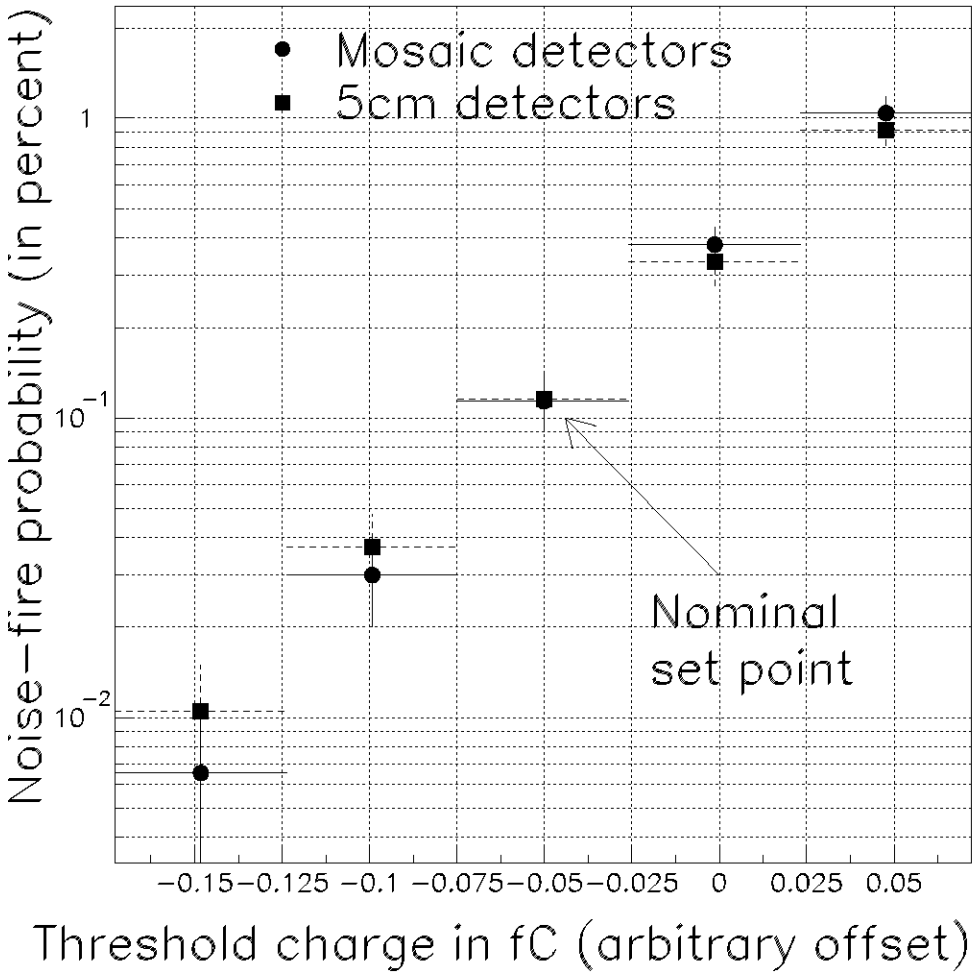

Figure 3.14: Average noise occupancy of 5_cms and mosaic detectors (Note the log scale on the Y axis)

follows. First the calibration program is spawned and this automatically sets the threshold level uniformly on all SVX chips, to the preset level. All channels are read out without any external signal and a mean of the pedestal for each channel is obtained. These pedestals are then downloaded into the FSDA pedestal bank. The detector is now ready to be read out in the sparse mode. Any external signal(charged particle, IR-LED light etc) if strong enough will cause strips to fire. The FSDA digitizes the strip hit on each readout channel and reports it as a hit if the ADC level exceeds its correponding value in the pedestal bank. Thus there are 2 levels of data suppression, one at the SVX and the other at the FSDA level, both of which serve to minimize the load on online and offline computing. The final ouput of the FSDA is the address of the hit strip and the ADC level with 4 bits of resolution.

3.3.3 Calibration Charge Injection

The calibration capacitor(C_{cal}) on each channel connected in parallel to the detector, deposits a threshold charge into the charge collection capacitor. In the absence of an external signal charge(like a particle) the calibration charge can be used to force a readout of the channel[22]. Changing the amount of calibration charge will now shift the pedestal as long as the channel still reads out. By adjusting the polarity of the charge so that the channel always reads out, the response of output pedestal ADC units with threshold charge is a measure of the deposited charge gain of the SVX. This gain plot for a typical SVX chip(averaged over all channels) is shown in Fig 3.15. As seen, the response is quite linear in the expected region of operation of the device. These gain curves were extracted on the test bench for all the SVX chips used in the vertex system. Fig 3.16a,b shows this gain value for 128 channels in each of two SVX chips. The average gain of all(368)chips used is shown in part c of the same figure and is a measure of the uniform analog response

[22]by picking the appropriate polarity of the charge

expected from the system.

When charge is deposited in the detector, the charge signal migrates to the detector strips in about 30ns[23]. The SVX readout channels convert this charge to an output voltage with a characteristic response time determined by the effective RC time constant of the amplifier. This time constant is expected to be about some 100s of nanoseconds. By varying the integration time for a constant calibration induced charge pulse and observing the output ADC counts, the effective risetime/response time of the SVX readout was measured. Fig 3.17 is a plot of the ADC response vs. integration time, for one SVX channel, fitted to an exponential(capacitor-charging) curve. The risetime for a few channels, is found to be 165 $\pm$15 ns.

From an operational standpoint, the hardware trigger readout in conjunction with the SRS allows charge to be integrated for 375ns or about 2.3 lifetimes. This results in a ballistic deficit of about 10% in the digitized output ADC value.

3.3.4 LED testing

To test the response of the strip detectors, a local charge was generated in the sillicon using a high intensity, near-infrared light emitting diode[24]. The schematic of the setup is shown in Fig 3.18. Silicon has a band gap of 1.1eV at 27^oC. IR light from the IR-LED(800-1300nm) may be transported through an optical fiber and shined on to the detector surface in a spot diameter determined by the NA of the fiber. At a wavelength of 1.15μm the e-h pair generation production is expected to be uniform(to within 15%)[21] throughout the depth of the 300μm silicon bulk region.

In order to perform this check, the detector was placed in a light tight box with the optical fiber end at a height of about 5 mm from the detector surface. An electronic LED driver[25] was used to convert a NIM pulse from

[23]hole velocity of 9600m/s and 300μm Si width
[24]HP manufactured AlGaAs LED
[25]built with off the shelf components

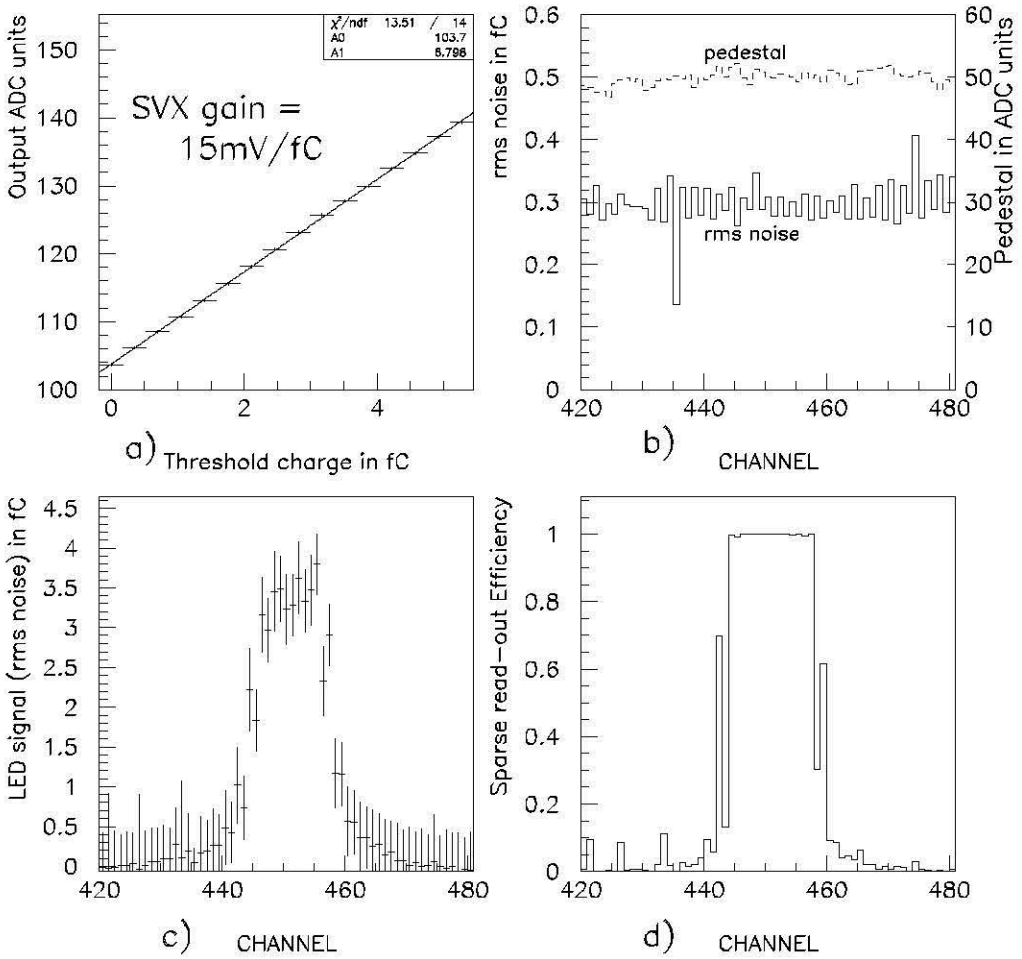

Figure 3.15: a)The gain of the SVX channels is a plot of the output ADC response to the input charge via threshold setting b)pedestal and noise of a few channels illuminated by an LED via a thin fiber c)The signal seen in the detector from an LED pulse d)The sparse occupancy response of the channels(note the full occupancy for a charge above 1.8fC)

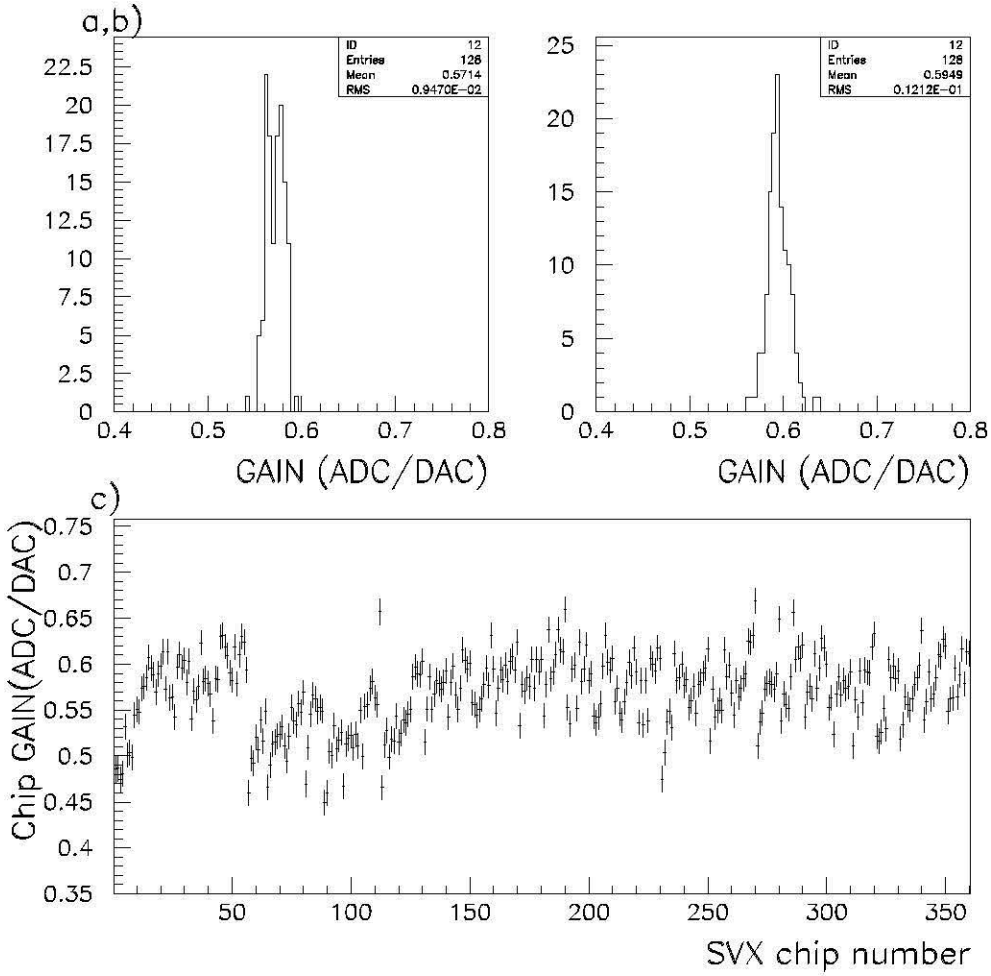

Figure 3.16: a,b) The gains in 128 channels in each of two typical SVX chips c)The gains for all the SVX chips in the vertex system(ADC units/DAC units from calibration signals averaged over all 128 channels in a chip)

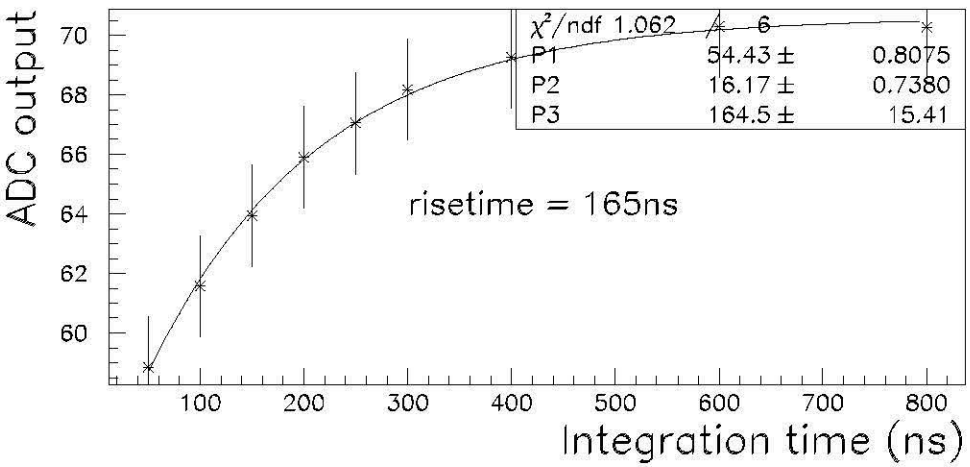

Figure 3.17: ADC output response to the integration time in one SVX channel.(This yields the characteristic risetime of the charge to voltage amplifier)

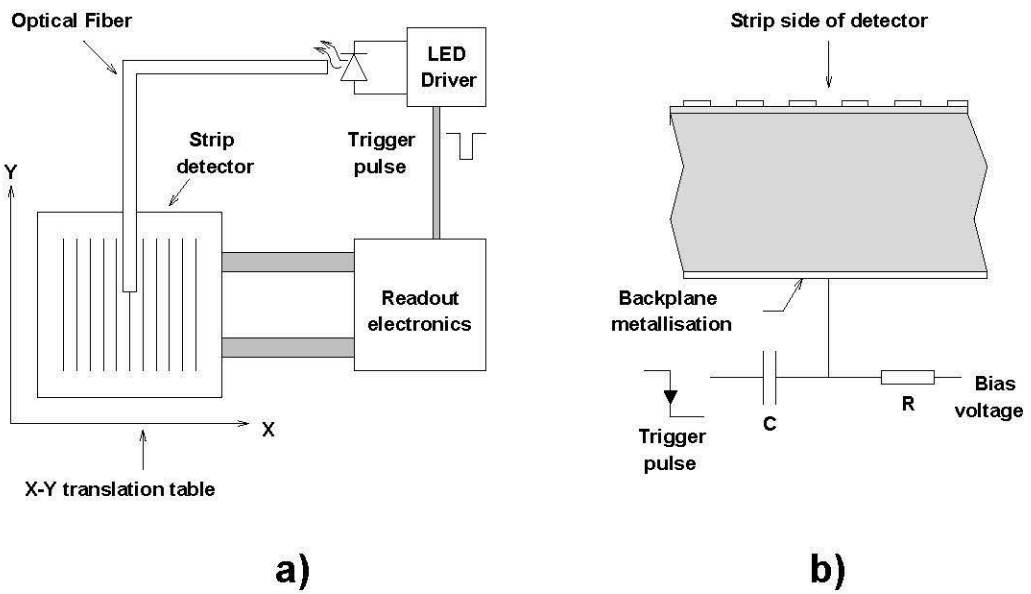

Figure 3.18: a)Schematic of the LED test setup b)Schematic of the Back Plane pulse setup

the readout trigger into a current pulse to drive the LED output. The optical fiber was coupled to the LED using optical grade UV curable epoxy.

The LED light pulse duration could be varied from 100ns to 1μs and the intensity adjusted so that the average ADC response corresponded to about 1 minimum ionizing particle's worth of charge. The fiber was moved relative to the detector using the XY translation table, thus checking strips both across and along their length. At each fiber setting, two 1000 event runs were acquired:- one with the LED on and the other with it off. The LED off run was used for pedestal subtraction from the signal run. Two sizes of fiber were used. A large fiber(1mm dia) illuminated a wider spot allowing quick scans of broad areas. A smaller 100μm core diameter fiber allowed more detailed investigation of an area a few strips wide. All detectors were scanned in this way to verify whether a strip was alive and to quantify its gain. Plucked strips, as expected, showed no response to illumination and its two nearest neighbours picked up an extra 35% charge(from the floating strip capacitively coupling to the neighbours). Fig 3.19 shows the LED light pulse profile and the corresponding readout efficiency of strips on a typical detector with the broad fiber.

3.3.5 Backplane pulsing

Another method used to checkout the detectors was to apply a voltage pulse to the aluminium biasing backplane of the detector with a 10nF capacitor in series(see previous Fig 3.18). This capacitively induces a charge on the detector strips which is quite uniform in magnitude. The slope of the rising edge of the pulse is what determines how much the signal level is. The trigger NIM pulse triggered a gate generator which supplied the required pulse. By adjusting the size of the pulse, the amount of signal induced on the strips could be varied. One of the advantages of this method was that it was simple to perform with very little detector preparation and hookup. All detectors were assembled with a two prong connector to feed in a backplane test pulse. Runs with about 1000 events were acquired from which a mean

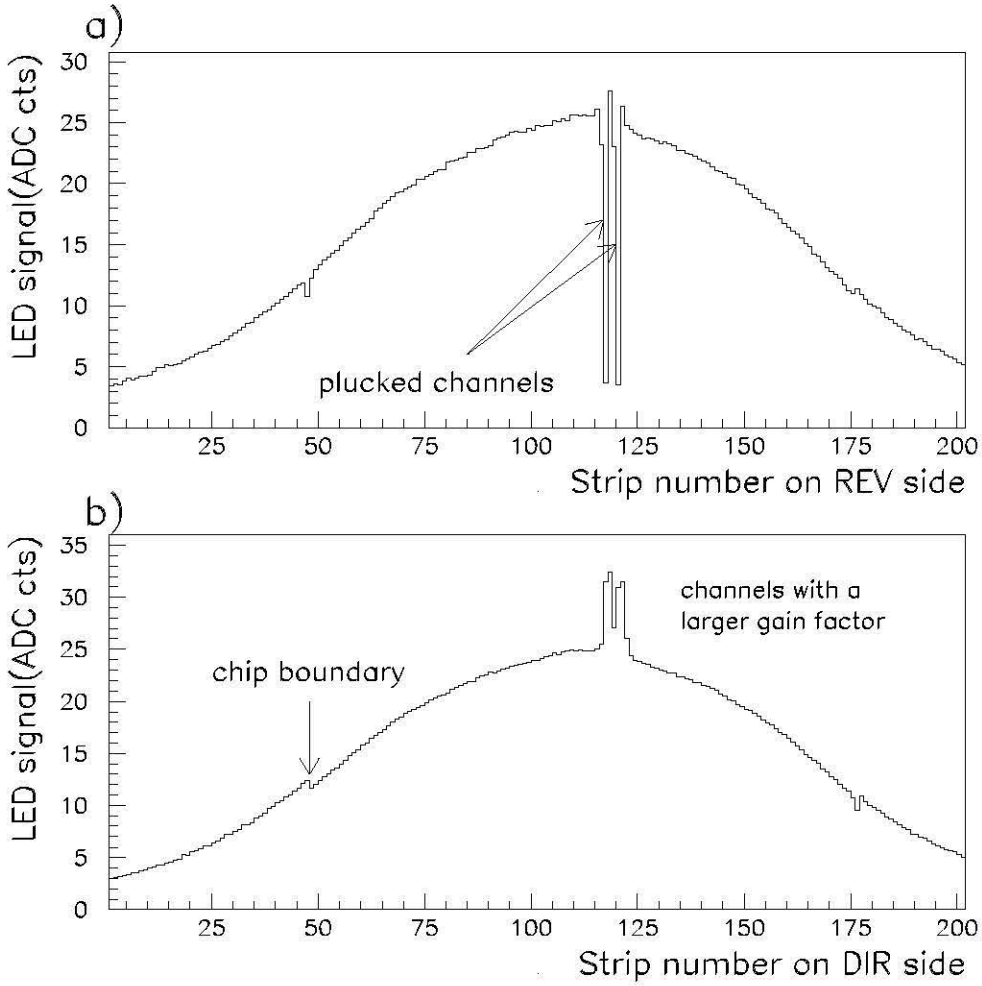

Figure 3.19: a)Mean LED pulse profile with a broad fiber on a mosaic detector(wire map from the REV side only) with plucked channels b) Same profile from the interleaved REV side, showing higher signal gain on channels adjacent to plucked channels.

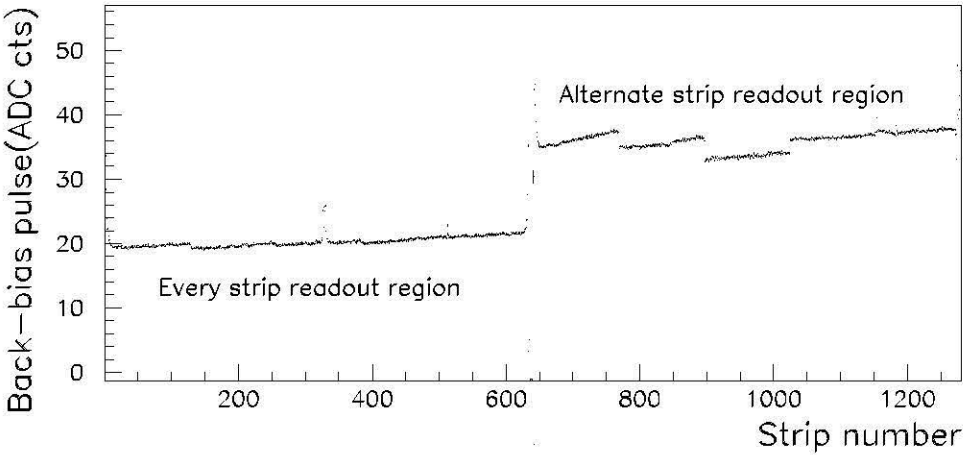

Figure 3.20: The pedestal subtracted signal seen with a back bias pulse to a mosaic detector

pedestal and noise were extracted.

In the region of alternate strip pitch readout, the single strip signal size was approximately 75% above that over the rest of the detector. This was because floating unread strips capacitively shared their charge with the readout strips. This confirmed that charge sharing to improve hit resolution was possible. Once a detector was functional, this method tested all the strips on the detector, all at once. The efficiency of a strip to a given amount of signal size could be determined. Fig 3.20 shows the signal response of a typical detector to a backplane pulse corresponding to a signal charge of 0.75 MIP in the every strip read out region. The detector is seen to be fully efficient at this signal level. The response time for the back bias pulsing method was limited by the RC time constant of the detector and associated series resistance. This does not probe the signal charge migration through the depletion region(which the LED method does).

The gains of all strips were found to be uniform to within 10% of the average except for plucked strips which did not read out. The channels adjacent to plucked channels picked up an extra 35% signal(from capacitive

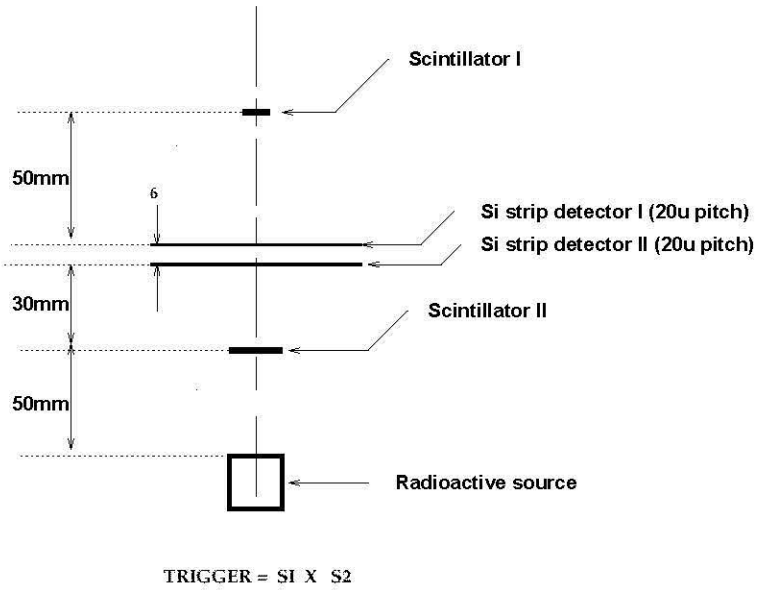

Figure 3.21: Schematic of the radioactive source setup

charge sharing). The deviations of the gains from the average has been recorded and this information may be used to adjust the ADC pulse height in the real run data.

3.3.6 Source testing

Testing of detectors to confirm their responsivity to charged particle radiation could not be conducted before the turn on of beam at Fermilab fixed target. Cosmic ray testing was considered but the small size of detectors gave rise to rate considerations which required long periods of testing(days). Recourse was made to a radioactive source to provide charged particles.

A Ru-106 source was used to introduce charged particles(3.54MeV electrons) through two detector boards placed back to back and read out simultaneously. The schematic of the setup is shown in Fig 3.21. The trigger was a coincidence of 2 scintillators indicating a possible straight through track. A sample of 5000 events were taken with the source in place. The data were

analyzed with a cut requiring hits in both detectors within 4mm of each other. Another run without the source and triggering on a random pulser was taken for comparison. The observed pulse height spectrum obtained is shown in Fig 3.22. This exercise showed that the signal was well above the background in the ADC pulse height and the maximum was about what we expect to see for a MIP on a strip.

3.4 Installation in the experiment hall(PC4)

3.4.1 Hardware Alignment on Monument blocks

The general idea was a 2 part alignment procedure. In the first part, detectors were aligned and mounted on monument block(Al plates). This was done outside the experimental hall. The next part was to precision mount these loaded monument blocks within the experimental hall.

The alignment procedure was carried out on a CORDAX Coordinate Measuring Machine(CMM) at Fermilab(Lab D), with the operational assistance of Mike Roman. The measurement precision on the machine was about 1μ in each of the three orthogonal directions.

Each monument block has a set of carbide "buttons" precisely glued on as shown in Fig 3.23. The buttons are machined to have parallel faces and their spacing with respect to the mounting pins on the monument block was controlled during gluing by a vacuum fixture. The glue layer thickness is expected to be uniform and about 25μm. The two buttons on the bottom rest on the surface of the granite table and the third one butts against a steel plate perpendicular to the granite surface. This orientation defines the origin as the intersection of the lines as shown in Fig 3.23. All positions of detector strips are given with respect to this origin.

To align the detectors, a precise(to within 200μrad) right angle was set up using granite blocks clamped to the CMM table. The granite blocks were at worst, shifted 60μm in 30cm, i.e. a 0.2mrad offset from 90°. In 2 cm, this results in an offset error of 4μ in the position of the origin. The CMM

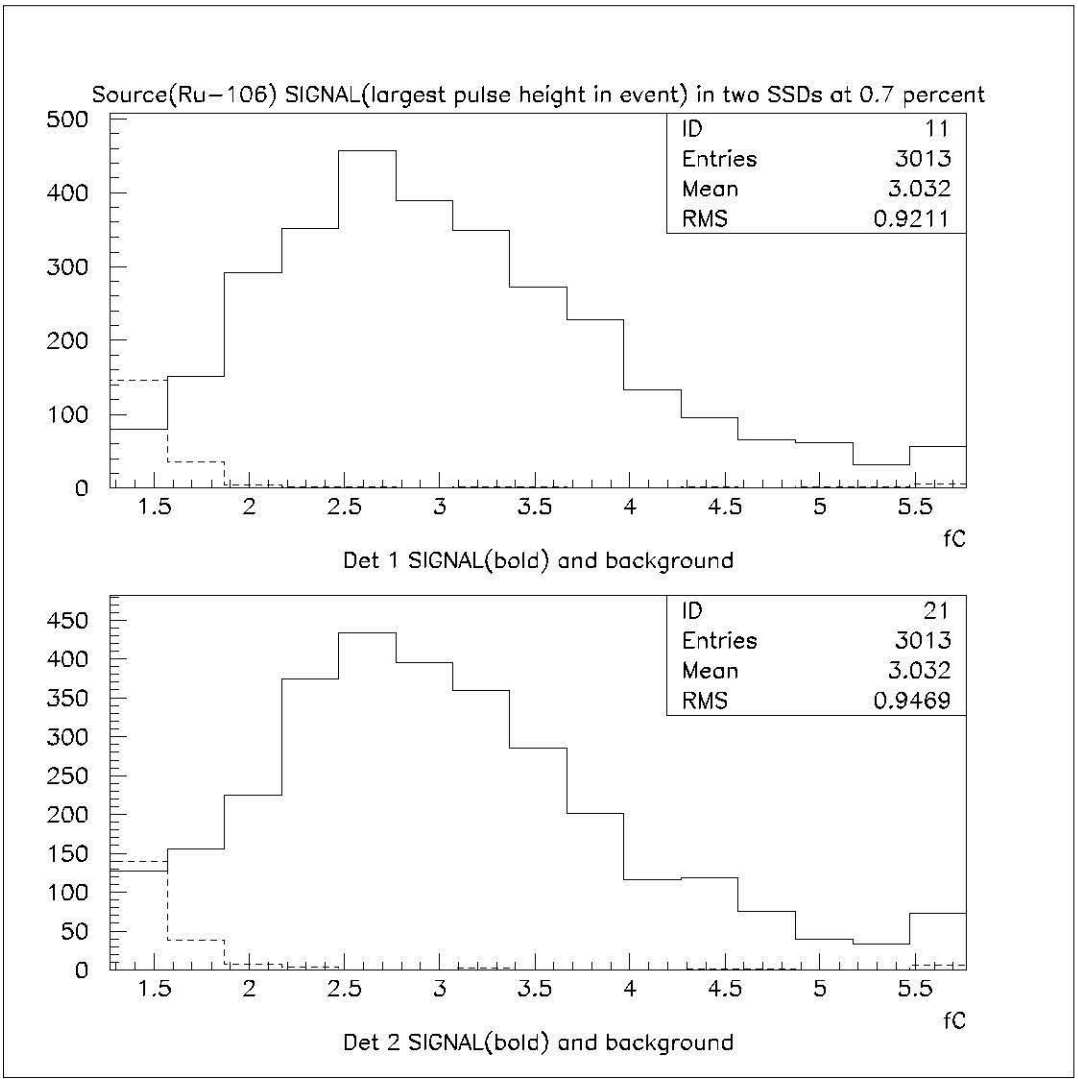

Figure 3.22: The ADC pulse height spectrum in two VSSDs for a Ru radioactive source. Notice the well separated noise background.

recorded the orientations of the "X" and "Y" lines and formed the origin. As this was done in software, it was possible to rotate the axes about the origin, necessary in order to align the "U" and "V" detectors. The monument block was slid and pushed into place and a detector was mounted on the top face of the block. After hand tightening the detector support nuts, the alignment of a detector strip perpendicular to the view sense of the detector, was checked. This consisted of observing the edge of the last strip of the detector and adjusting the detector orientation(by loosening one end support at at time)so that the run-out along its length was $<3\mu$m . In the case of mosaic detectors, the strip 2559(in the central panel) was aligned. Once a detector was aligned and fixed in place, a second detector was mounted on the same side and the alignment procedure repeated. Then the monument block was flipped about the Y axis(with appropriate standoff blocks present) and two detectors were mounted and aligned on this side. This completed the alignment of one monument block. The angular precision depends on the size of the detector. The run-out error of 1-3μrad is divided by twice the strip length. At worst(for 5_cms), it is $3\mu/10$cm => ± 30 μrad. The alignment was very stable. We flipped the monument block, installed back-side detectors, flipped it again and re-checked. The alignment was unchanged. We installed a monument block in PC4, tested detectors, removed and rechecked the alignment. It remained unchanged.

Nomenclature of VSSD planes

The naming scheme of the vertex detectors was based on a global SELEX detector naming scheme. It specified each detector in terms of its spectrometer, the type of detector and its plane number within that detector type. The vertex plane names were of the form "VX_SSD_2X" which meant that it belonged to the vertex spectrometer, it was a single sided detector and it was the second detector with an "X" orientation of measurement. Similarly, "VX_MSD_1V" stood for a vertex spectrometer associated mosaic type detector, and being the first one with the "V" orientation. (Actually for the

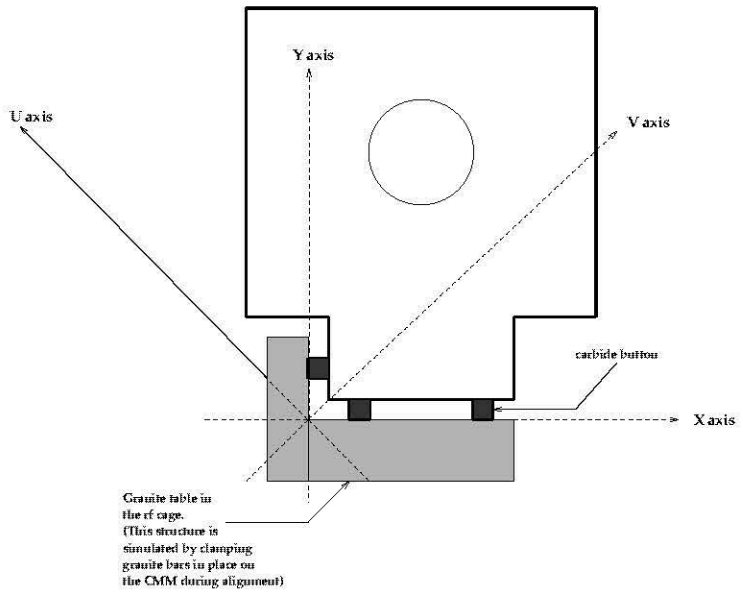

Figure 3.23: Formation of the coodinate origin on a monument block

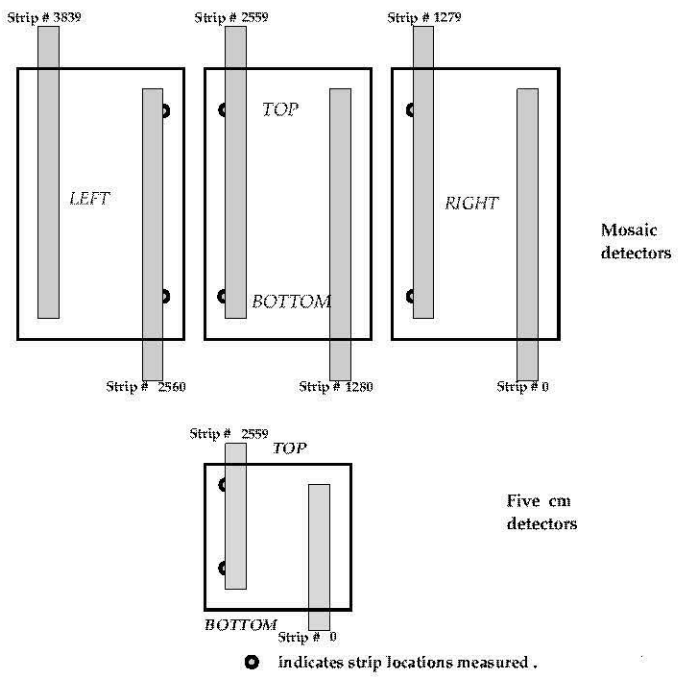

Figure 3.24: Layout of surveyed points on vertex planes

purposes of offline analysis, each mosaic detector is further subdivided into 3 detectors, each corresponding to one of the 3 panels on the mosaic detector(e.g. "VX_MSD_1V1", "VX_MSD_1V2" etc.)).

As described earlier, the upstream 8 5_cm SSDs are on 2 monument blocks and the downstream 12 mosaic MSDs are on the next 3 monument blocks. All monument blocks have the views "X", "Y", "U", "V" going upstream to downstream. The only exception is the fifth monument block which instead, has views "X", "V", "U", "X". Table 3.3 summarizes the names and measurement direction of all the vertex planes(listed from upstream to downstream).

Detector	**readout orientation(deg)**
VX_SSD_1X	0
VX_SSD_1Y	-90
VX_SSD_1U	-135
VX_SSD_1V	135
VX_SSD_2X	0
VX_SSD_2Y	-90
VX_SSD_2U	-135
VX_SSD_2V	135
VX_MSD_1X	0
VX_MSD_1Y	-90
VX_MSD_1U	-135
VX_MSD_1V	135
VX_MSD_2X	0
VX_MSD_2Y	-90
VX_MSD_2U	-135
VX_MSD_2V	135
VX_MSD_3X	0
VX_MSD_3V	-15
VX_MSD_3U	-165
VX_MSD_4X	0

Table 3.3: Nomenclature and readout orientation of the VSSD planes.

Alignment data

Every silicon panel in the vertex detector (3 for each mosaic and 1 for a 5_cm detector) has one strip whose position has been surveyed at two points denoted TOP(T) and BOTTOM(B). Fig 3.24 shows the locations on mosaics and five cm detectors, which were surveyed and measured. "TOP" for all X,U and V detectors refers to the direction of increasing Y,V and U axes respectively. For Y detectors, "TOP" refers to the direction of decreasing X axis. Knowing the width of the strip feature,(10μm for mosaics and 14μm for 5_cms) we calculate the offset of the center of the strip. These numbers are reported in Table 3.4(mosaics) and Table 3.5(5_cms) below. The heights are the coordinates of the point along the length of the detector. This data is useful for calculating the tilt in the detector strip.

Rotations of the vertical plane about the X and Y axes, introduced by machining tolerances on mounting hardware, are estimated at 0.5mrad at worst. These rotations can be completely ignored as their impact on X and Y measurements scales as the cosine of the angular offset.

All X and Y detectors are on upstream faces and all U and V detectors are on downstream faces of monument blocks with the exception of VX_MSD_4X and VX_MSD_3V.

Table 3.6 describes the z positions of the vertex detector planes. In this report the upstream face of the first monument block is chosen to be at the z origin and the z is positive in the downstream direction. This is offset from the E781 z origin.

Points that need to be stressed

- All measurements have been made with respect to **one fixed point** on the monument block(The intersection of lines formed by the fixed buttons), which is also the origin.

- All coordinates in this document are given with respect to the X, Y, U, V axes as defined in Figure 3.23. **These may not necessarily cor-**

respond to the beam coordinates or MC coordinates defined elsewhere.

- The numbers reported in the Tables 1 and 2 are the offsets of the **centers** of strips. The measured positions of edges(in Figure 3.24.) have been used to recalculate the central offset, i.e. the distance from coordinate origin defined in Figure 3.23.

- The height is the coordinate of the measured point, along the axis parallel to the length of the strip. The height can be used to calculate the tilt of the strip.

- Figure 3.24 is **not** a view of detectors looking downstream. It is a view when looking at the strip side of a detector(downstream view for detectors on the upstream side of a monument block and vice versa). The recipe to figure out TOP and BOTTOM of a detector has been described in section 3.4.1.

3.4.2 Power Supply and Wiring layout

Silicon Detector Power

Electrically, each monument block serves as a local power distribution network, supplying +4.85V to each detector plane to power the SVX chips and +65 V (nominal) at very low current to provide the reverse bias to each silicon detector. The +4.85V is distributed from a master power supply to a distribution stand at each monument block. From the terminal blocks on the distribution stand, the +4.85V power goes to the detectors via 14-gauge wiring affixed to the monument block. Near the detector, another terminal strip provides the connection point to the 18-gauge wires running to the detector itself. All wires terminate in spade lugs for attachment. The layout is shown in Figure 3.25 Each detector draws at most 1 A, so the distribution

line is fused at 2 A. The power supply itself has an internal 15 A fuse, suitable for protecting the 14-gauge wire used to bus the supply voltage to the distribution panels.

The 65 V detector bias power comes from a supply with a maximum current of 1 A. The bias voltage is connected in parallel to all detector backplanes. The leakage current in each detector is a few microamperes and hence, no fuses are needed for this system.

Driver Card Power

Signals from the detectors are processed in another set of circuits called Driver Cards. These boards are mounted in slots atop the RF enclosure. Each Driver Card takes about 2 A of +5 V and 1.5 A of -5 V power. The five (5) driver cards needed for the entire system are driven from a common pair of 16A power supplies. The power distribution for them is shown in Figure 3.26. Again, the supply has an internal 15A fuse that limits the maximum current supplied to the 10-gauge/14-gauge wire network that carries current up to the fuse/distribution panel. Each Driver Card has 3 A fuses to limit current in +5 and -5 lines. Power to individual Driver Cards is carried on 18-gauge wires from the fuse/distribution panel to plugs on the Driver Card.

3.4.3 Cooling and shielding

As described earlier, all the monument blocks sit on an optical granite block which is 2m long and 40x40 cm in cross section. The granite block is inside an Al rectangular enclosure,(4'x4'x6') called the "rf cage". The walls of this cage is made of 1/4" thick Al, with removable side panels. Holes in the upstream and downstream end allow for the passage of the beam. The panels are lined with Cu-Be finger contacts, and the frame of the rf cage is grounded to provide electromagnetic shielding for the silicon detectors and fast trigger electronics inside it. There are 3 feedthrough panels to provide

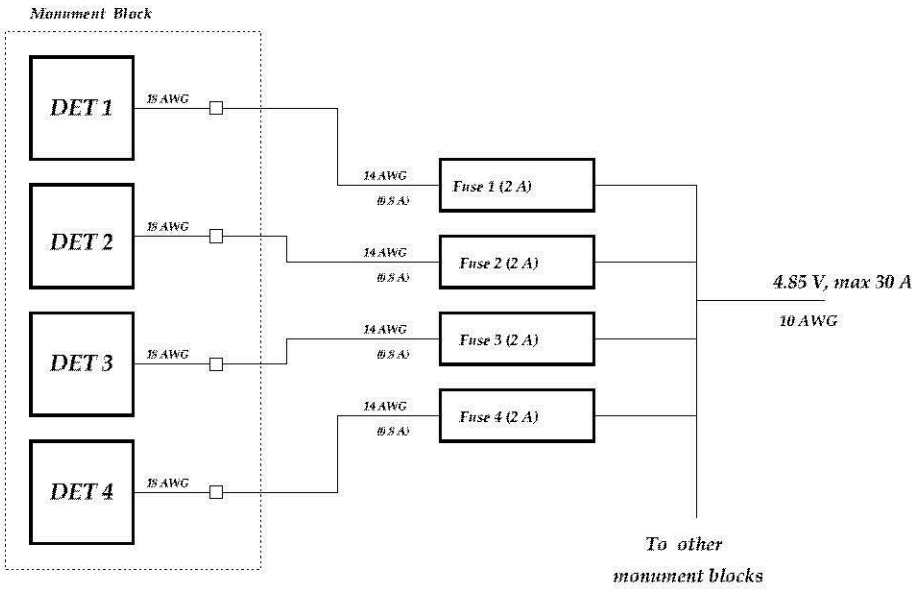

Figure 3.25: Schematic of power supply to the vertex planes

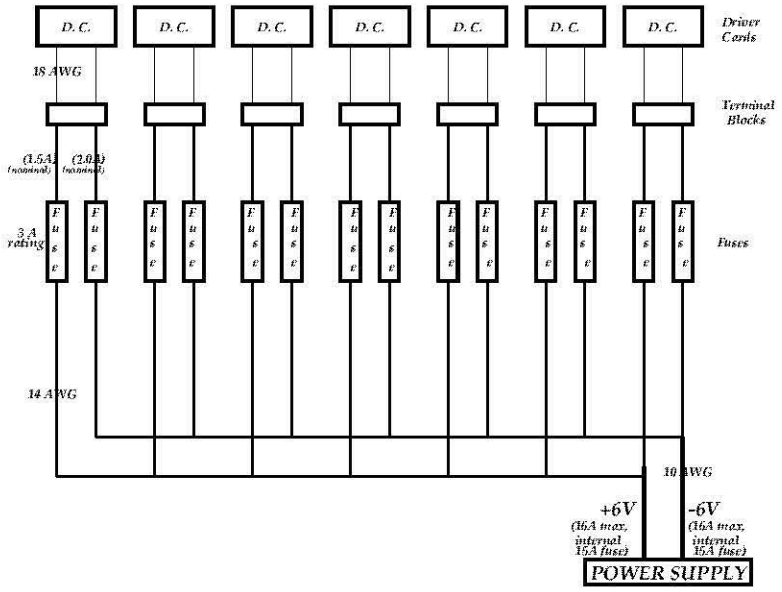

Figure 3.26: Schematic of power supply to the driver cards

power and signal connections to the detector hardware. The Driver Cards sit in slots cut into the roof of the cage, which is light-tight and fairly air-tight.

A blower and chilled water heat exchanger cooling system located nearby continually recirculates cool air at about 19° C through the cage. An array of 5 (12V AC) boxer fans sitting near the edge and aimed in between the monument blocks, help to improve convection and dissipate heat from the detector SVXs more evenly. The temperature inside the rf cage is constantly monitored by the EPICURE system, and has been found to vary between 21 and 23^oC.

3.4.4 Cabling to Fastbus Readout

Signals from the 20 detectors are transmitted on 20 30 pair 0.05" spacing twisted flat cable over a distance of 25 feet. The maximum frequency of the digital signals in the control and data buses is defined by the SRS clock period(50ns). The bandwidth of the analog signals generated by the SVX is about 10MHz. For digital signals, the twisted pair lines are loaded by matching resistors at both ends. Careful labelling and arrangement of all these cables is done so as to prevent any confusion in the readout mapping. The upstream set of 12 detectors are connected into 6 FSDA modules in a Fastbus crate designated FSDA2. The remaining 8 detectors are plugged into 4 FSDA modules in another crate called FSDA1. Table 3.7 summarizes the cabling scheme.

3.5 Final System Checkout

With the detectors aligned and powered up in their final location in the rf cage, some simple checks were conducted to confirm that the system worked as a whole. All the detectors were read out in the latch-all and sparse mode simultaneously to look for any cross-talk betweeen detectors. No cross-talk was found and the pedestal, noise and sparsification characteristics were the same as that for a single detector on the test bench.

Since the space between detectors was insufficient to safely allow a light fiber, resort was made to the back-bias pulsing to verify performance under signal charge. An easily accesible 2 pin connector on the detector was left on the detector for this purpose. Hooking these detector backplanes to a voltage pulse, all detectors were readout and verified to respond as expected. Fig 3.27 shows an example of the backplane pulse output of the detectors as installed. This resulting signal plot contains the relative ADC gain information from all the detectors strips. Once turned on, the system was left on and the detectors were then ready to receive beam.

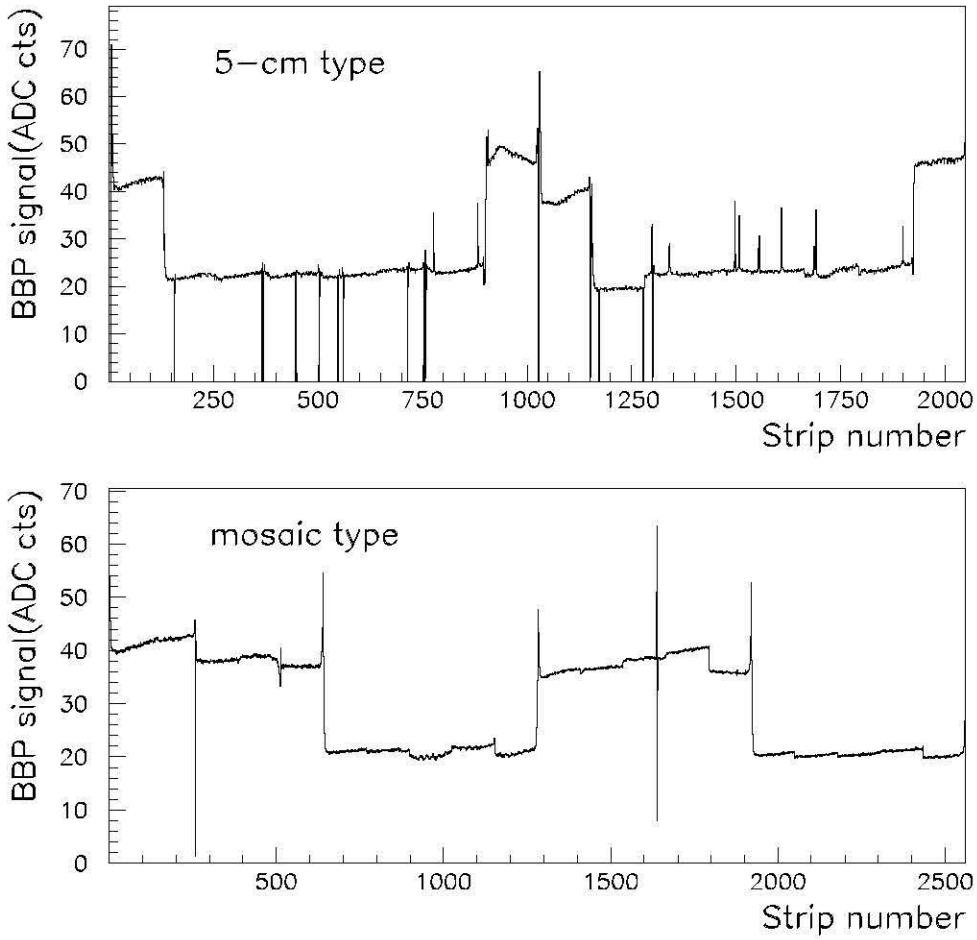

Figure 3.27: Typical Back-bias Pulse(BBP) signals seen in the detectors as installed.(The DAQ pathway was the same as that for runtime conditions)

Detector	strip 1279		strip 2559		strip 2560	
	offset	height	offset	height	offset	height
VX_MSD_1X_T(X3T)	144.035	338.147	110.464	338.190	108.888	338.152
VX_MSD_1X_B(X3B)	144.029	256.960	110.467	256.942	108.875	256.883
VX_MSD_2X_T(X4T)	143.981	338.756	110.442	338.705	108.852	338.631
VX_MSD_2X_B(X4B)	143.986	257.455	110.443	257.468	108.847	256.950
VX_MSD_3X_T(X5T)	143.889	338.959	110.335	338.049	108.751	338.944
VX_MSD_3X_B(X5B)	143.907	257.674	110.337	257.255	108.756	257.674
VX_MSD_4X_T(X6T)	108.910	339.063	142.478	339.099	144.059	339.077
VX_MSD_4X_B(X6B)	108.916	257.817	142.479	257.823	144.059	257.908
VX_MSD_1Y_T(Y3T)	316.119	86.045	282.560	86.053	280.982	86.147
VX_MSD_1Y_B(Y3B)	316.131	167.100	282.563	167.192	280.974	167.291
VX_MSD_2Y_T(Y4T)	316.927	86.267	283.354	86.754	281.771	87.022
VX_MSD_2Y_B(Y4B)	316.925	167.839	283.355	168.021	281.765	167.803
VX_MSD_1U_T(U3T)	139.764	342.038	106.208	342.023	104.624	342.015
VX_MSD_1U_B(U3B)	139.780	260.736	106.208	260.757	104.629	260.742
VX_MSD_2U_T(U4T)	138.495	342.591	104.947	342.488	103.346	342.493
VX_MSD_2U_B(U4B)	138.495	261.675	104.944	261.675	103.358	261.654
VX_MSD_3U_T(U5T)	-27.251	360.309	-60.833	360.264	-62.407	360.671
VX_MSD_3U_B(U5B)	-27.254	280.109	-60.833	280.109	-62.407	280.119
VX_MSD_1V_T(V3T)	283.438	162.848	317.000	162.857	318.576	162.830
VX_MSD_1V_B(V3B)	283.442	81.580	317.001	81.554	318.581	81.618
VX_MSD_2V_T(V4T)	283.127	161.519	316.685	161.393	318.259	161.584
VX_MSD_2V_B(V4B)	283.138	80.714	316.688	80.695	318.270	80.582
VX_MSD_3V_T(V5T)	217.503	296.411	183.945	296.093	182.375	296.177
VX_MSD_3V_B(V5B)	217.520	215.235	183.948	215.170	182.381	215.260

Table 3.4: Aligned Strip locations(in mm) on the Mosaic detectors

Detector	**strip 2559**		**strip 0**
	offset	height	offset
VX_SSD_1X_T(X1T)	101.314	323.532	152.494
VX_SSD_1X_B(X1B)	101.315	273.430	152.495
VX_SSD_2X_T(X2T)	101.800	322.922	152.986
VX_SSD_2X_B(X2B)	101.799	273.394	152.985
VX_SSD_1Y_T(Y1T)	273.109	101.887	324.289
VX_SSD_1Y_B(Y1B)	273.106	151.919	324.286
VX_SSD_2Y_T(Y2T)	272.854	101.792	324.034
VX_SSD_2Y_B(Y2B)	272.853	151.939	324.033
VX_SSD_1U_T(U1T)	95.730	326.256	146.910
VX_SSD_1U_B(U1B)	95.732	276.047	146.912
VX_SSD_2U_T(U2T)	96.319	326.652	147.499
VX_SSD_2U_B(U2B)	96.321	276.489	147.501
VX_SSD_1V_T(V1T)	326.114	145.593	274.934
VX_SSD_1V_B(V1B)	326.113	95.405	274.950
VX_SSD_2V_T(V2T)	326.749	146.774	275.569
VX_SSD_2V_B(V2B)	326.749	96.601	275.569

Table 3.5: Aligned Strip locations(in mm) on the 5_cm detectors

Detector	z postion	z wrt MB**
VX_SSD_1X(X1)	-20.25	-20.25
VX_SSD_1Y(Y1)	-5.46	-5.46
VX_SSD_1U(U1)	24.51	24.51
VX_SSD_1V(V1)	39.30	39.30
VX_SSD_2X(X2)	69.75	-20.25
VX_SSD_2Y(Y2)	84.51	-5.49
VX_SSD_2U(U2)	114.54	24.54
VX_SSD_2V(V2)	129.30	39.30
VX_MSD_1X(X3)	159.75	-20.25
VX_MSD_1Y(Y3)	174.51	-5.49
VX_MSD_1U(U3)	204.54	24.54
VX_MSD_1V(V3)	220.09	40.09
VX_MSD_2X(X4)	248.96	-21.04
VX_MSD_2Y(Y4)	264.51	-5.49
VX_MSD_2U(U4)	294.54	24.54
VX_MSD_2V(V4)	311.68	41.68
VX_MSD_3X(X5)	338.96	-21.04
VX_MSD_3V(V5)	354.51	-5.49
VX_MSD_3U(U5)	384.54	24.54
VX_MSD_4X(X6)	400.09	40.09

Table 3.6: z positions(in mm) for all vertex detector planes.(Origin chosen to be at the upstream face of the first monument block) (** is with origin on the upstream face of that particular monument block.)

Detector	local number	Crate Slot Ch
VX_SSD_1X(X1)	1	FSDA2 19 1
VX_SSD_1Y(Y1)	2	FSDA2 19 2
VX_SSD_1U(U1)	3	FSDA2 20 1
VX_SSD_1V(V1)	4	FSDA2 20 2
VX_SSD_2X(X2)	5	FSDA2 17 1
VX_SSD_2Y(Y2)	6	FSDA2 17 2
VX_SSD_2U(U2)	7	FSDA2 18 1
VX_SSD_2V(V2)	8	FSDA2 18 2
VX_MSD_1X(X3)	9	FSDA2 15 1
VX_MSD_1Y(Y3)	10	FSDA2 15 2
VX_MSD_1U(U3)	11	FSDA2 16 1
VX_MSD_1V(V3)	12	FSDA2 16 2
VX_MSD_2X(X4)	13	FSDA1 10 1
VX_MSD_2Y(Y4)	14	FSDA1 10 2
VX_MSD_2U(U4)	15	FSDA1 11 1
VX_MSD_2V(V4)	16	FSDA1 11 2
VX_MSD_3X(X5)	17	FSDA1 8 1
VX_MSD_3V(V5)	18	FSDA1 8 2
VX_MSD_3U(U5)	19	FSDA1 9 1
VX_MSD_4X(X6)	20	FSDA1 9 2

Table 3.7: Detector hookup to FSDAs

Chapter 4

Analysis of vertex silicon data

Data taken from a run are available almost immediately for offline analysis. Analysis was performed using the SELEX Offline Analysis Package(SOAP) which runs on a UNIX platform(either fn781a or Fermilab's FNALU cluster). The SOAP package is compiled by each user in his/her own area and offers many standard functions like unpacking, clustering, tracking, linking, vertexing etc., controlled by switches in a user owned command file. The user has the option to tailor the analysis by writing a FORTRAN "user" routine which will run in conjunction with the global SOAP analysis. The output could be saved in ASCII files or PAW[1] and Histoscope[2] readable HBOOK files. Thus a very flexible analysis package with useful built in algorithms and the capability to extend the analysis options was used to analyze data from the vertex silicon system.

The raw data is written to EXABYTE tape for future analysis. However, about 10% of the data from each run is sent to the Fermilab Mass Storage System(FMSS). This data is easily accessible in a few minutes by running a simple data retrieval script. 10% of the data from every run(about 60,000 events for a typical BEAM trigger run) was good enough to perform alignment and tracking studies on the vertex system. In order to analyze all

[1]Physics Analysis Workstation

[2]A Fermilab histogramming software package

the events in a run, the EXABYTE tape is ported to the computing center at FERMILAB and read into the Mass Storage System. A standard data retrieval script makes this data available to be analyzed, in a few minutes.

Designed and measured plane information like position and rotational orientation in local coordinates, pitch and detector type are found in the silicon database in the form of Open Constant System(OCS) tables. This information is crucial to the offline code and is read in by SOAP each time it is invoked.

4.1 On-spill and off-spill data

The accelerator proton primary beam is on for 20s out of every minute. During this time, physics data is acquired and this period is referred to as the on-spill. All the various detectors are controlled by the DAQ and read out their data synchronously. The data are packed into a standard data structure containing information from all the detectors. This data is filtered by the online software trigger and interesting events are stored on tape. The remaining 40s out of very minute is called the off-spill/interspill period. DAQ relinquishes some control during this period and different detector systems have a choice between acquiring calibration/monitoring data from their detectors or not doing anything. The standard physics trigger is inactive and some kind of pulser driven software/hardware trigger may be used to exercise individual detectors. The data structure is not critical and small amounts of data may be written to disk and analyzed. Larger sets of data are generally analyzed within the FastBus Crate controller(FSCC) and the results available for viewing over the local ethernet. A special suite of software programs was written to operate the detectors during the interspill period. DAQ control ensured tight coordination between the spill structure timing and interspill programs. Off-spill tasks would be spawned and would "sleep" during the spill if their lifetime spanned several spills. Calibrating the detectors(typically 0.1% noise level occupancy) was an important task

that would automatically seek the optimum operating thresholds(this was described in section 3.3.2). Monitoring occupancy, noise and pedestal levels was also handled by off-spill tasks. These will be described further in section 4.3.

4.2 Hits and Clustering

A strip could be triggered by noise fluctuations or by charge from the passage of a charged particle. At the hardware level, there are two levels of sparsification of the raw data. One is at the SVX chip level, imposed by the calibration threshold level in sparse mode readout. The next is at the FSDA pedestal cut level where channels with ADC less than the preloaded pedestal are ignored. Both cuts help to keep the data bandwidth within the acceptable real-time data taking level(140kB/min). This raw data is stored on disk and tape and is available for more stringent analysis. Each hit strip is characterized by a plane number, strip number and pulse height ADC. The 4-bit pulse height is mapped into a charge value in fC.

In the first layer of analysis, the data are unpacked and a cluster finding algorithm converts the array of hit strips into an array of clusters. Hit strips adjacent to each other are grouped together to form a cluster. A cluster is defined as a group of up to 5 adjacent strips. If the cluster contains more than 5 strips then it is broken up into the lowest 5 plus the rest. The pulse height in a cluster is summed and the position(in spectrometer local coordinates) of the cluster is the charge weighted centroid of the strips composing the cluster. A cluster is required to have at least 0.01MIP(minimum ionizing particle) worth of charge, otherwise it is discarded. Fig 4.1 shows the hit wire-map, cluster size, hit multiplicity and ADC hit pulse height in the raw data. Single strip clusters form the majority. Lowering the calibration threshold increases cluster multiplicity and improves the position resolution. But this also increases the amount of data triggered by noise occupancy. The calibration threshold set is a compromise to optimise speed, efficiency and

resolution.

4.2.1 Tracking and Errors

A tracking algorithm is performed on the clusters found within the vertex spectrometer to find track segments. A spectrometer track segment, is a list of the coordinates in each of the planes of that spectrometer which are believed to belong to one charged track. Missing coordinates may be due to inefficiencies in a plane, software inefficiencies of segment finding algorithm, or that the particle missed the detector.

The TRACK_SEGMENT algorithm is based on the assumptions that tracks are found in 3-dimensional space and each coordinate measurement(hit) will be assigned to at most one track segment. This straight line search agorithm is programmed at a higher level by storing an ordered list of combinations to be run on each spectrometer. An example of such a list is shown below. The "planelist" is the list of detector planes to be included in the fit. The "planeinit" are the initial planes required to start forming combinations and "cuts" are the cuts on the track parameters.

```
**************************************************
********* example track combination listing ***********
**************************************************
comb: vx_comb1
planelist: vx_ssd_ 1x1y1u1v2x2y2u2v
planelist: vx_msd_ 1x1y1u1v2x2y2u2v3x3u3v4x
planeinit: vx_ssd_1u vx_ssd_1v vx_msd_2x vx_msd_2y
! cut names xl xh txl txh yl yh tyl tyh xs ytgt chi2 npl
cuts: 0., 0.,-.025, .025, 0., 0.,-.025, .025, , , 5.0, 12

********************** end ***********************
```

The cut parameters make it possible to define efficient search strategies. The planeinit combination of detectors is used to find all combina-

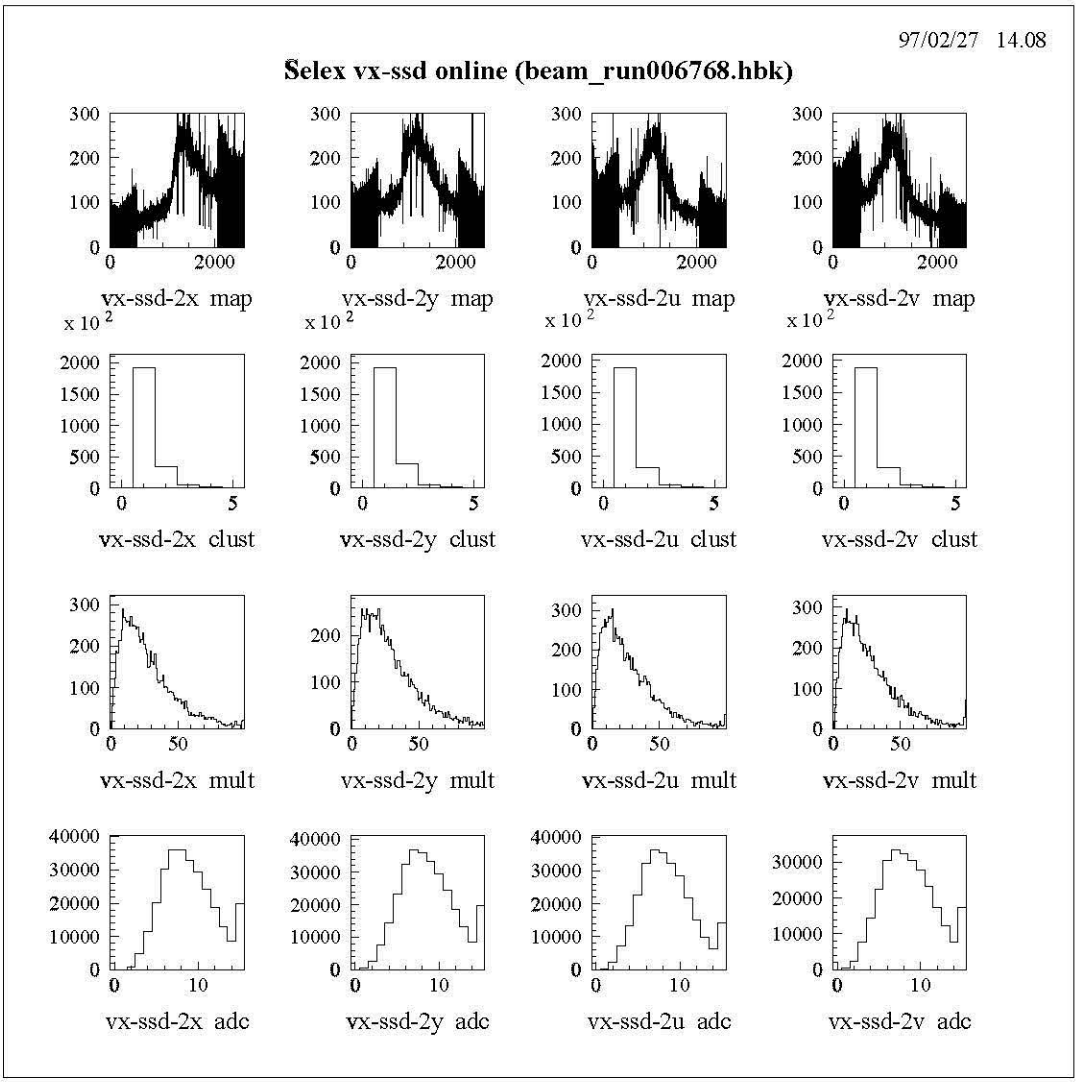

Figure 4.1: Typical histograms showing hit wire maps, cluster size, hit multiplicity and ADC level in the raw data

tions of possible track segments, and hits found on other detectors along the line(constrained by position, angle and χ^2 cuts) are added to the track segment. Hits associated with tracks are removed from the hit list. This is a "layered" pattern recognition approach which optimises efficiency and speed. The user can tune the track segment program in any spectrometer to fulfil certain segment finding criteria. The track segments are found in 3-dimensions and are reported as 4 phase space variables(X and Y intercepts and slopes). Once segments are found in all spectrometers, they could be matched up or "linked" to the same physical track through space. This process is determined by how well segment slopes and intercepts match up in both views as well as the momentum as given by the bends through the spectrometer magnets. Two beam silicon and two vertex planes are designated as reference planes. All shifts and rotations are measured with respect to these planes.

4.2.2 Residuals

Once the track segment programming was functional, it was possible to observe a track segments in the vertex spectrometer. In order to form a track segment, at least 12 vertex planes were required in the fit. The plane hit efficiency could now be calculated and the residuals plotted. To do this, one of the vertex planes was dropped out of the track segment algorithm. A 3-dimensional track segment was found and the dropped out detector is examined in a window about 1-2 strips wide for a hit around the predicted position of the track in that plane. The number of times a hit was found gives the hit efficiency. If the expected position of the track(in the plane view) is x_{track} and x_{hit} is the position coordinate of the hit nearest to the expected track position, then the distribution

$$x_{residual} = x_{track} - x_{hit} \tag{4.1}$$

gives us the "residual" distribution. The plane under investigation must always be dropped out of the fit so that the distribution is unbiased. The

width of the residual distribution is dependent on the errors of the fitted track segment and on the detector measurement errors. This method of finding the residuals for all 20 detector planes is long and tedious as each of the planes have to be dropped out one at a time. To speed up the process, a different approach was taken. Upstream of the vertex detector is a 8 plane(spread over 150cm) Beam Silicon detector whose resolution is comparable to that of the vertex silicon. Track segments were first found in the Beam silicon and then pointed down into the vertex detector. Now the hit nearest to the beam segment could be plotted for all vertex planes all at once. This technique was used with data from a beam triggered run at 650 GeV/c[3].

Fig 4.2 shows some typical residual distributions from a 5_cm detector and a mosaic. The distributions are found to be very close to an ideal Gaussian(normal) distribution indicating that the errors in measurement and fit are almost purely random[4]. The distribution disagrees from the normal fit in the region of the tails, outside 3σ. The mean position of the distribution is very nearly zero as the planes are quite well aligned. These distributions are representative of all the planes in the vertex detector. The larger pitch of the mosaic detectors is evident in their slightly broader residuals.

4.2.3 Hit and plane efficiency

In order to compute the unbiased detector hit efficiency of all the planes, a beam triggered run at approx 650GeV/c was analyzed. The following were the cuts applied on the events

- Only one beam segment was found in the beam spectrometer. This ensured that only one MIP could possibly have gone through the vertex spectrometer;

[3]Multiple Coulomb scattering is negligible at this momentum.

[4]Deviations from Gaussian near the tail is evidence of "delta" knock-on electron production

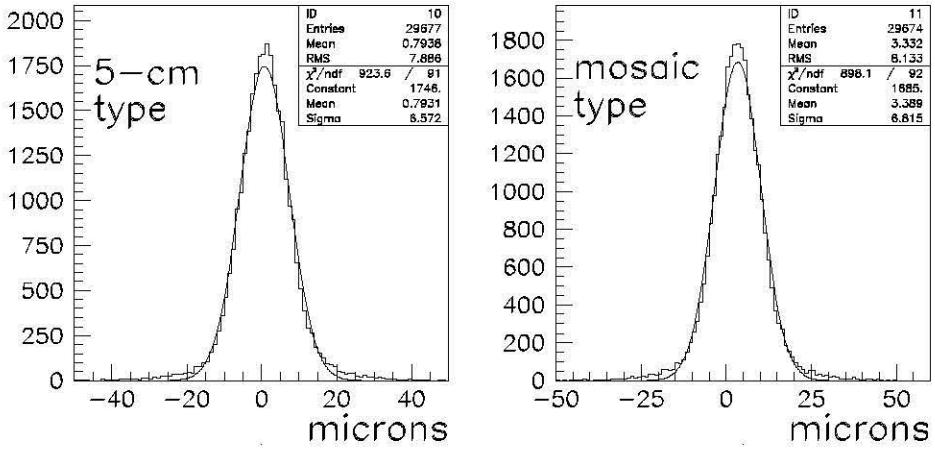

Figure 4.2: Typical residuals in vertex planes

- All 8 beam silicon planes had to participate in finding the beam segment. This minimized the beam segment fit errors;
- Only one segment was found in the M2 spectrometer;
- The single segments found in the beam and M2 spectrometers were linked to the same track;

All these cuts were made to ensure that there was almost certainly one good beam particle which was seen in the beam and M2 spectrometers and therefore had to have passed through the vertex spectrometer. Linking the segments ruled out interactions and large angle scatters within the vertex silicon planes. No special requirement is made on data from the vertex silicon and this makes the investigation of efficiency completely unbiased. About 30,000 events in run 2056 made these cuts and were processed. A window that varied linearly from 40μm at the upstream-most vertex plane to 60μm at the downstream-most vertex plane was selected to look for hits around the expected postion of the extrapolated beam segment. A hit in this window meant that the plane was efficient for that particular event. The cluster associated with this hit was considered the hit cluster left by the MIP. The total

single plane efficiency was the ratio of the number of events that had a hit, to the total number of linked events analyzed. This value for all 20 vertex planes is shown in Fig 4.3. In order to calculate the noise hit contribution to the efficiency, a "fake track" analysis was done on the same events. This consisted of finding hits in the current event corresponding to extrapolation of a track from the previous event. No real track is expected to be found there[5] and any hit seen there must have been from noise.

In an interaction run, there are a number of tracks within the same event and the resolution is dependent on the momentum of the track. The clusterization algorithm which allocates hits to different clusters now becomes important. The detector hit efficiency in the environment of multiple tracks is shown for a couple of typical detectors in Fig 4.4. Fig 4.4a,b show the efficiency of finding hits(on one plane) associated with all reconstructed tracks in an event. Most of the time($> 95\%$) all tracks in an event have nearby hits.

Very early on during the run, vertex plane 1(X view) developed a readout problem with SVX 7 on the Reverse side. As the chip could not pass the readout priority token the entire Reverse side was switched off. This reduced plane 1 to a 40μm read-out pitch detector. As the strips on the switched off reverse side are not floating but grounded through the input to the op-amps on the SVX, charge sharing is not expected to be efficient. Hence the plane is expected to be of slightly worse resolution than a 40μm charge shared-readout detector. As a result this plane shows a larger hit inefficiency(of the order of 25%). The vertex detector has a total of 6 direct and 8 indirect X measurements and as such is highly redundant in this view. Hence it was decided to leave the half working plane so as to not disturb the well understood alignments of all the other planes.

The calibration threshold set on the SVX chips also plays a role in the hit efficiency of the vertex planes. The lower limit of the threshold is set by the acceptable number of words that can be read out by the DAQ. The threshold was varied in the increasing direction and the hit efficiencies of all the planes

[5] The chances of finding consecutive tracks in the same 100μm space is .05%

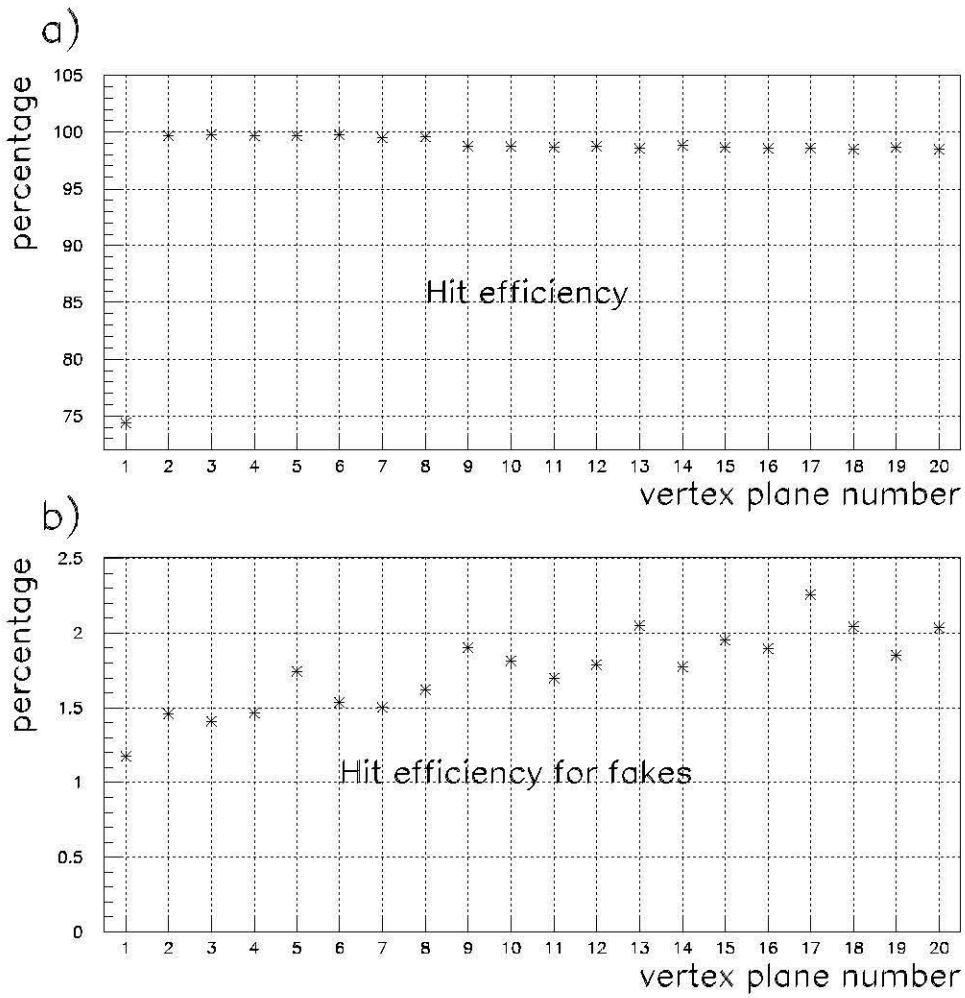

Figure 4.3: Hit efficiency and "fake"(noise) hit efficiency of vertex planes using beam tracks

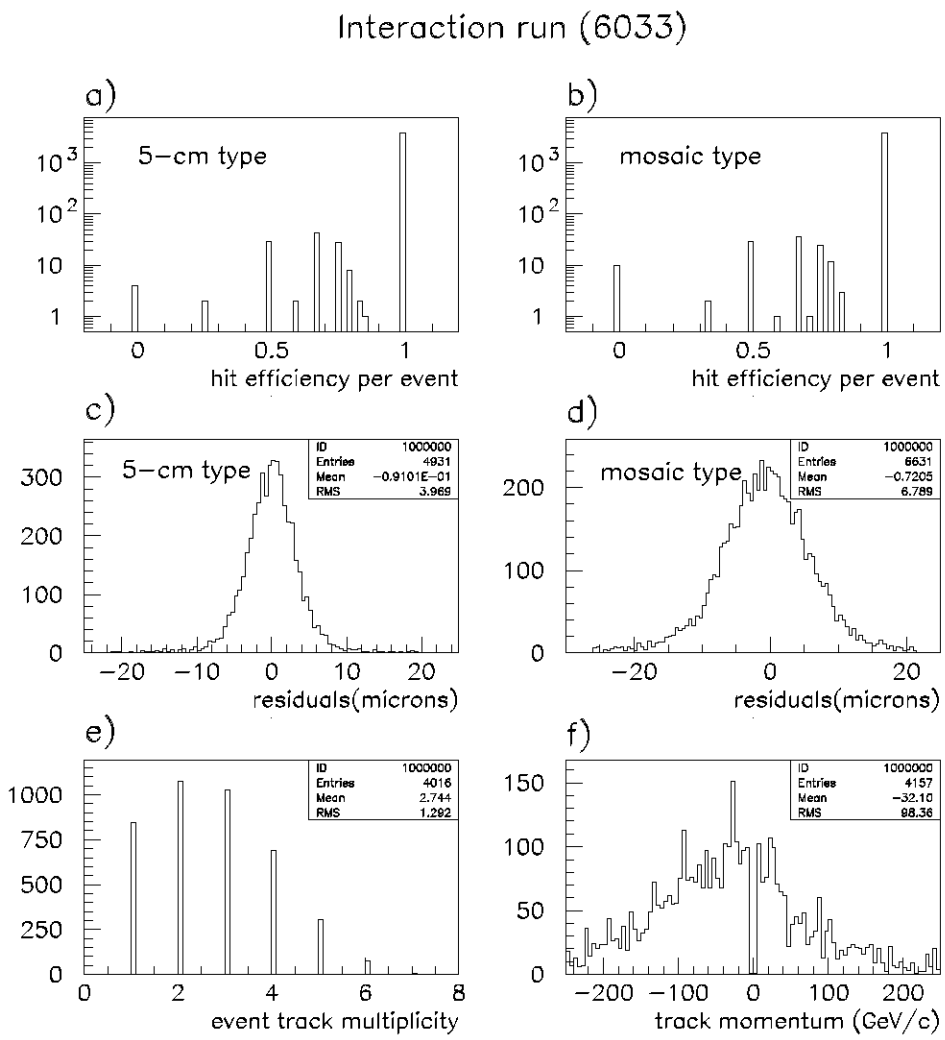

Figure 4.4: a)Efficiency for correctly associating hits to all tracks in an event for a typical 5_cm plane b)The same efficiency for a typical mosaic plane c)The residuals from the correctly assigned hits on a 5_cm plane d)The same residual distribution for a mosaic plane e)The track multiplicity within the events analyzed e)The momentum distribution of the tracks analyzed

computed as before. The results are in Fig 4.5, showing that the current nominal threshold is quite well optimised and that increasing the threshold will cut in to the plane hit efficiency.

4.2.4 Pulse Height ADC

A minimum ionizing particle (MIP) is expected to deposit about 4fC of charge in 300μm of silicon. Following the same analysis to find the hit efficiency, the cluster within the 2 strip window was histogrammed for multiplicity, pulse height ADC, and position. Fig 4.6 shows the relative cluster strip size distribution for all the "beam" clusters for a typical 5_cm detector plane. The same set of plots for a mosaic detector is shown in Fig 4.7. 3-strip clusters make up only about 2.0% of the total number of clusters and don't make a significant impact on the system performance.

The summed pulse height within a cluster is plotted in Figs 4.6b and 4.7b. The analytical form of the energy loss distribution can be approximated by a Vavilov distribution[22]. In the case of the vertex detector planes, this distribution is expected to be convolved with a 0.3fC(18keV) wide Gaussian/normal distribution from noise in the detector and readout electronics. The data are fit to a MC generated Vavilov distribution convolved with a Gaussian and the agreement is quite good. The most probable energy loss agrees with the expected value of 78keV[23] and the mean loss is 110keV. During the data-taking, there was a 1.4fC(27keV or 10ADC count) suppression on the mosaic planes at the hardware level, from ADC output range considerations. This tends to increase the mean and most probable values of energy losses for the mosaic planes by about 8%.

4.2.5 Software Alignment

Using high momentum beam tracks to find the alignment of the detector planes is a powerful and reliable method. Since there is no magnetic field between the Beam and Vertex systems, straight line extrapolations at high

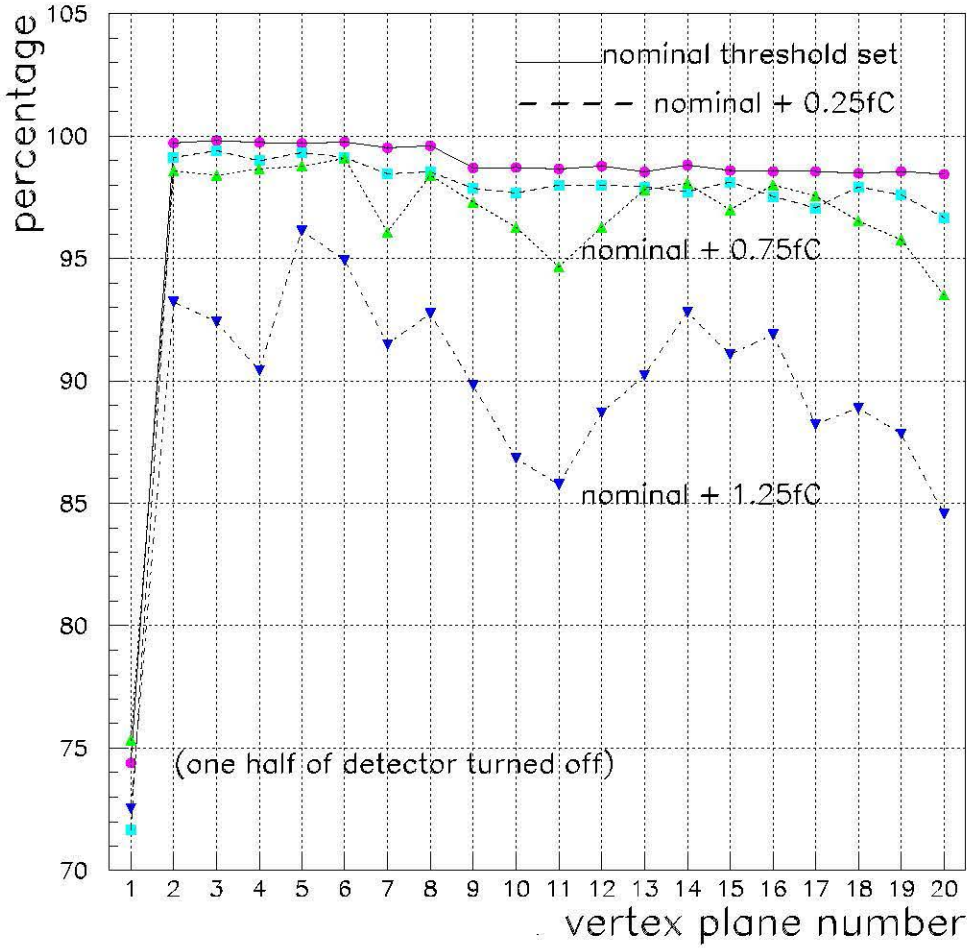

Figure 4.5: Variation of vertex plane hit efficiencies with thresholds

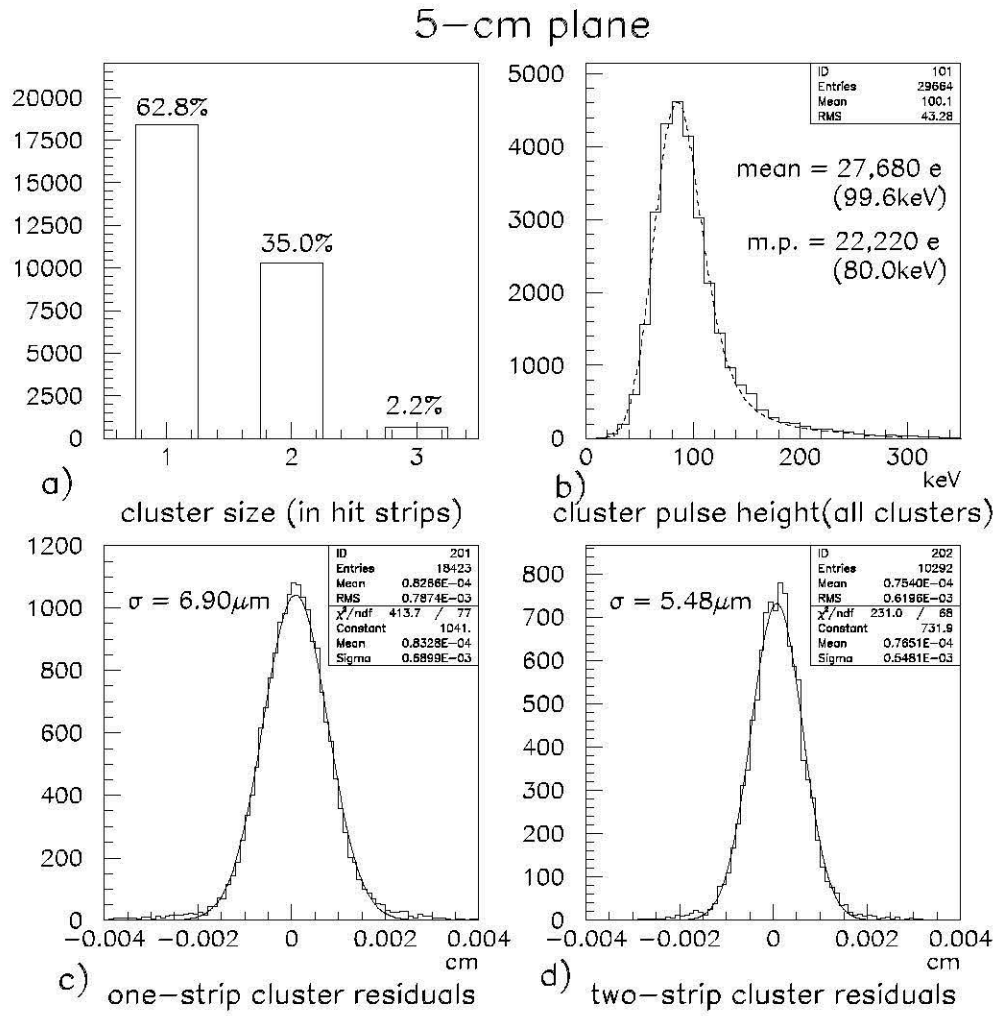

Figure 4.6: a)Relative cluster size distributions, b) Fitted ADC spectrum of cluster charge, c)Single strip cluster residuals, d)Two strip cluster residuals

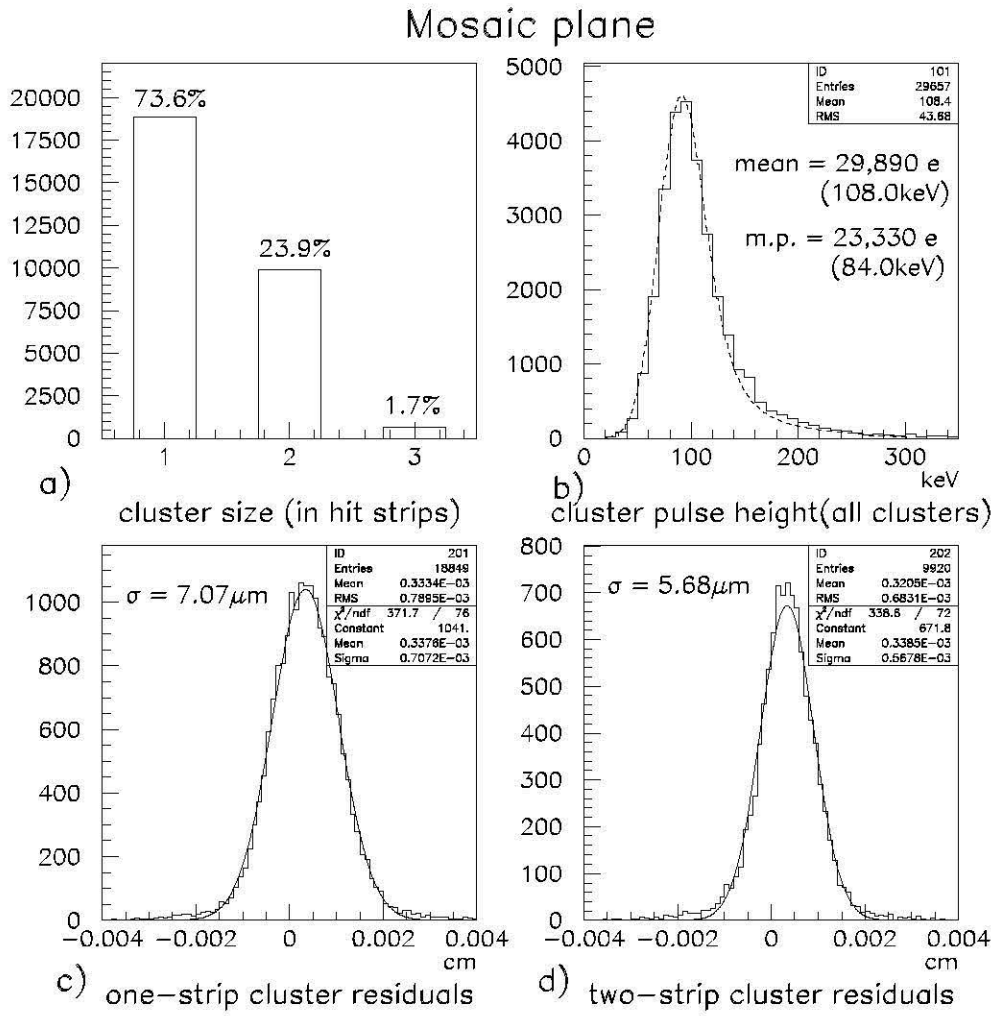

Figure 4.7: a)Relative cluster size distributions, b) Fitted ADC spectrum of cluster charge, c)Single strip cluster residuals, d)Two strip cluster residuals

momentum are quite accurate. Clusters within a window around expected beam track postions in the vertex planes are first found. The charge weighted centroid of the clusters is computed. The signed deviation from the expected position is plotted as the familiar residuals. As seen in earlier figures, the distribution is well described by a Gaussian fit. The mean position of the residuals is a well known quantity[6] and describes the average position of the detector plane with a precision down to a tenth of a micrometer. Any deviation from zero indicates a mis-alignment of the plane and this information can be be fed back to the alignment constants in the SOAP software. The composite system alignment is quite satisfactory after two such iterations. This also provides a tool to monitor any drifts in the alignment with time. The procedure for finding the alignment constants consists of plotting residuals, fitting them to a normal distribution and then reading off the mean of the distribution for each of the 20 planes.

Plane rotations

The vertex planes were installed with their readout along the different views (X,Y,U and V). Using residuals from vertex segments, the rotation of each plane around the z axis was confirmed. A plane is dropped from the track fit and the residuals on this plane plotted against the track position in the orthogonal view. The slope of the systematic correlation seen in this scatter plot(e.g. Fig 4.8a,b) is a measure of the planes deviation from the expected angle. Fig 4.8c shows the mis-alignment in plane rotation for all the 20 planes. These are found to be within the errors expected from the mechanical alignment. The last 4 planes show a mis-alignment by about 1mrad. This is as a result of a coherent supporting monument block mis-rotation. One of the carbide alignment buttons had fallen off from this block and was reattached without the use of the button mounting fixture(see section 3.4.1). An extra 150μm thick layer of epoxy on one button will cause the observed coherent rotation.

[6]with a statistical accuracy that improves with $\sqrt{N}$ where N is the number of events

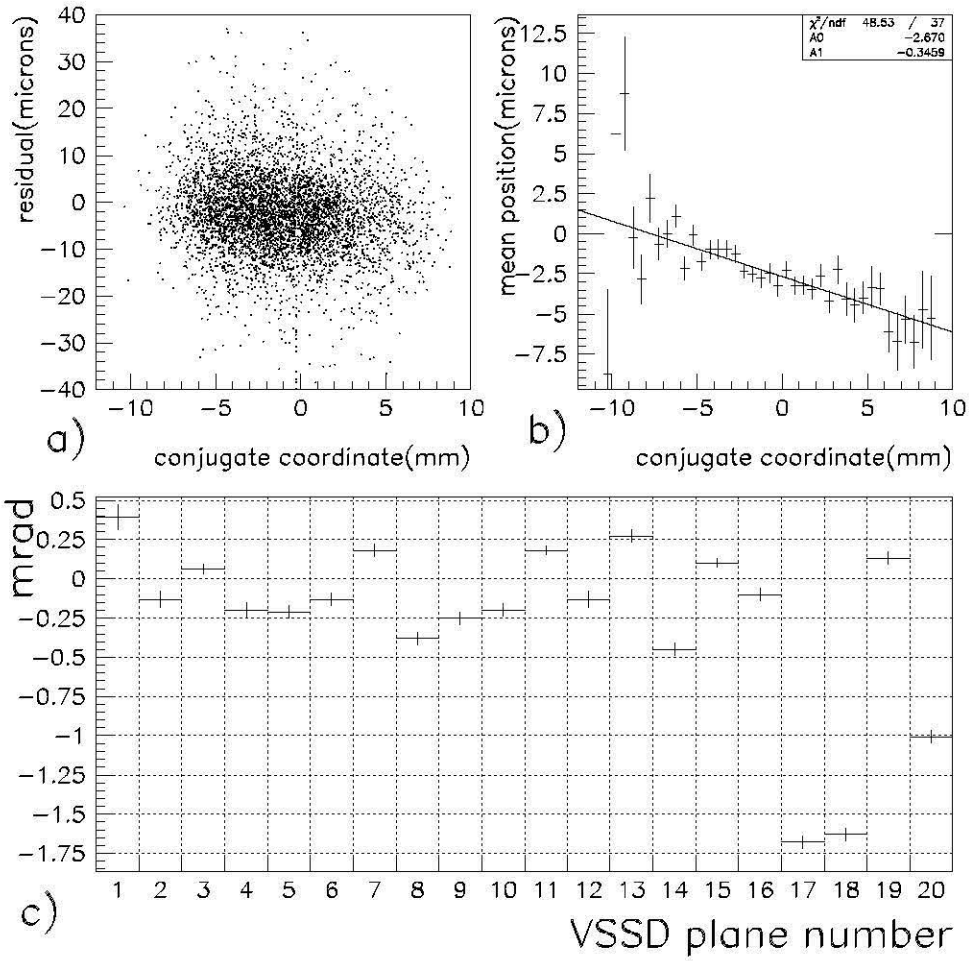

Figure 4.8: Illustration of the determination of angular mis-alignments a)Scatter plot of residuals with coordinate of track position in the orthogonal view, for a typical detector, b)linear fit to the mean of the same distribution, c)Observed mis-rotations of all vertex planes

Rotations of planes about the x and y axes affect track measurement precision by changing the effective pitch of the plane as the cosine of the angle of deviation. During installation, the planes were all made parallel to each other to within 1mrad. Using interaction track residuals, no mis-rotations were seen to within 2mrad, which was the precision of the method.

Plane z positions

The z positions of the planes during installation, were determined with a precision of 0.5mm. By scatter plotting the residuals in a plane with the track angle, the systematic z shifts of the plane can be determined from correlations. This plot was made for each plane(eg Fig 4.9a,b) and the z positions systematically varied(in software) until the residuals and track angles were uncorrelated. Deviations on the planes were all within 1mm(see Fig 4.9c)from design. The pattern of shifts for detectors on the same block shows some degree of coherency which is indicative of a mis-measured Al monument block thickness(by about 0.3-0.5mm) Other deviations are possibly due to uncertainties in epoxy layer thicknesses and slight bowing of the silicon detector crystals. The accuracy of this method was 0.1mm, with a silicon detector thickness being 0.3mm.

All these software alignment exercises returned deviations in various parameters from the currently known value and this process was done iteratively. This yielded a self consistent set of alignment parameters as shown in Table 4.1. Deviations from design in the hardware alignment were tolerable as long as they were small and could be precisely determined through software alignment.

4.2.6 Detector plane resolution

When the residual distribution is plotted, the width of the distribution $\sigma_{residuals}$ is a function of the random statistical errors involved. These arise from a detector measurement contribution σ_{det} and a track fit error contri-

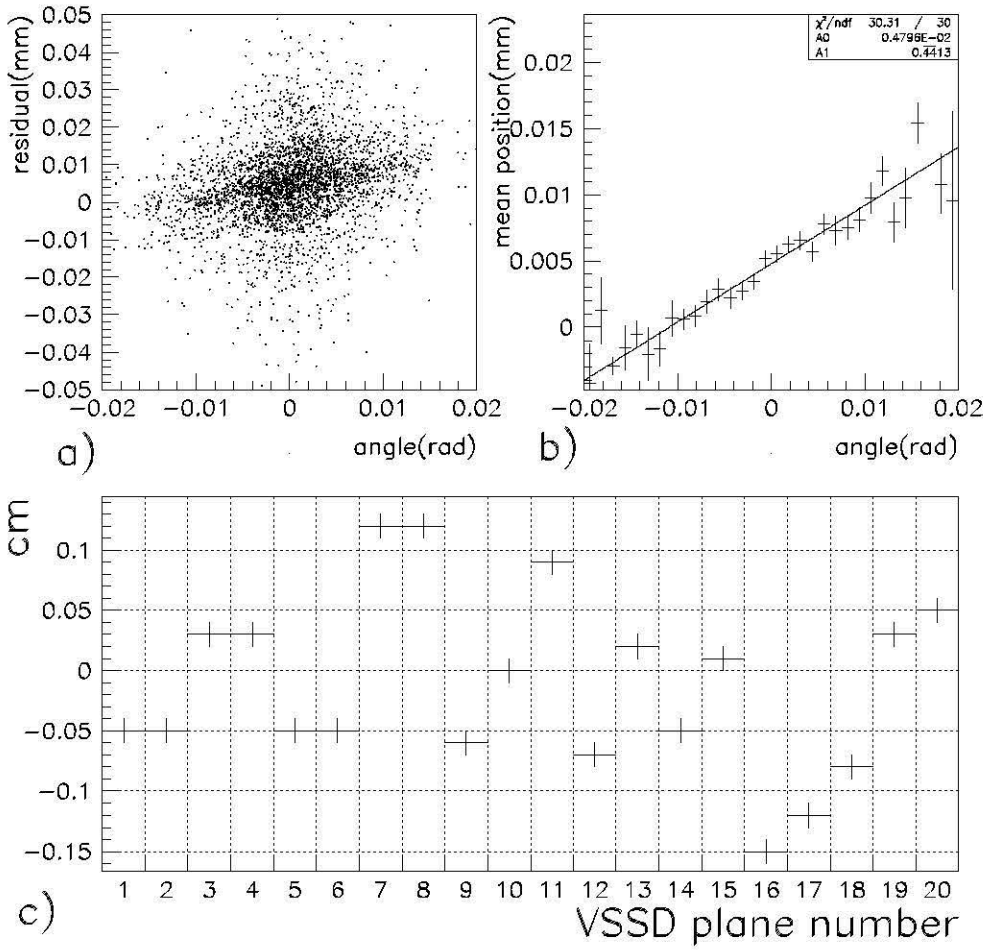

Figure 4.9: Illustration of the determination of z position shifts a)Scatter plot of residuals with the angle of the track for a typical detector, b)linear fit to the mean of the same distribution, c)Observed z position deviation of all vertex planes

No.	Detector	readout position (μm)	readout angle (mrad)	position along z (mm)
1	VX_SSD_1X	24±1.0	0.32±0.1	-0.50±0.1
2	VX_SSD_1Y	174±1.0	-0.20±0.1	-0.50±0.1
3	VX_SSD_1U	94±1.0	-0.01±0.1	0.30±0.1
4	VX_SSD_1V	23±1.0	-0.27±0.1	0.30±0.1
5	VX_SSD_2X	-106±1.0	-0.28±0.1	-0.50±0.1
6	VX_SSD_2Y	11±1.0	-0.20±0.1	-0.50±0.1
7	VX_SSD_2U	102±1.0	0.11±0.1	1.20±0.1
8	VX_SSD_2V	78±1.0	-0.45±0.1	1.50±0.1
9	VX_MSD_1X	73±1.0	-0.32±0.1	-0.60±0.1
10	VX_MSD_1Y	-75±1.0	-0.27±0.1	0.00±0.1
11	VX_MSD_1U	-81±1.0	0.11±0.1	0.90±0.1
12	VX_MSD_1V	-34±1.0	-0.20±0.1	-0.70±0.1
13	VX_MSD_2X	-99±1.0	0.20±0.1	0.20±0.1
14	VX_MSD_2Y	-143±1.0	-0.52±0.1	-0.50±0.1
15	VX_MSD_2U	-100±1.0	0.03±0.1	0.10±0.1
16	VX_MSD_2V	-18±1.0	-0.17±0.1	-1.50±0.1
17	VX_MSD_3X	502±1.0	-1.75±0.1	-1.20±0.1
18	VX_MSD_3V	455±1.0	-1.70±0.1	-0.80±0.1
19	VX_MSD_3U	-109±1.0	0.06±0.1	0.30±0.1
20	VX_MSD_4X	-217±1.0	-1.08±0.1	0.50±0.1

Table 4.1: Alignment deviations from the expected positions

bution σ_{fit}. Both these errors are expected to be normal in distribution as is their character and there is no dominant systematics in the analysis. Thus residuals are a result of the convolution of the detector measurement and fit errors. For normal distributions these errors add in quadrature. Knowing the error of the fit, we have a method to calculate the detector resolution as

$$\sigma_{det}^2 = \sigma_{residuals}^2 - \sigma_{fit}^2 \tag{4.2}$$

The fit errors are calculated from knowing the 4x4 error matrix E_{fit} generated as a result of fitting a track segment in the beam spectrometer.

This error matrix is reported at the origin of Beam spectrometer at the downstream-most target. To propagate this error matrix to the z positions corresponding to the different vertex detectors, we need to matrix multiply out the following

$$\sigma^2_{fit} = Z^T(E_{fit})Z \tag{4.3}$$

where Z is the column matrix of plane geometry. For the ith plane,

$$\mathrm{Z} = \begin{pmatrix} cos(\theta_i) \\ z_i \times cos(\theta_i) \\ sin(\theta_i) \\ z_i \times sin(\theta_i) \end{pmatrix}$$

where θ_i is the orientation angle of the ith plane. There is a correction to this value of the computed fit error. The Beam segment error matrix is calculated using a certain value of the Beam detector plane measurement error squared(nominally pitch/$\sqrt{12}$), entering into the χ^2/dof of the fit. Since the observed[7] χ^2/dof is 0.8, this must be factored into the σ^2_{fit} calculation multiplicatively. Table 4.2 lists the σ_{fit} found at the 20 vertex planes.

Now we are ready to calculate the detector measurement error. To do this we plot the residual distribution at each plane for 1-strip clusters and 2-strip clusters and fit all of the distributions to a Gaussian. For the class of 1 strip clusters, one expects from rectangular statistics that the statistical measurement uncertainty is given by pitch/$\sqrt{12}$. What is observed is a systematically better(by about 5-10%) resolution for 1-strip clusters. This is because 2-strip clusters occur for tracks passing near the edges of the strips, thus decreasing the effective 1-strip pitch. For 2 strip clusters, ADC charge weighting of the strips will yield a more precise centroid than if the weights on both strips were the same. Fig 4.10 is a plot of the observed distance to the predicted distance(by ADC weighting) of a track from the nearest strip center. The strong correlation of the plot indicates that ADC charge weighting improves the resolution of a track in over 90% of the interstrip distance. Fig 4.11 and Table 4.3 summarizes the resolutions of the vertex planes for

[7]for run 2048

Plane number	Detector	Fit error(μm)
1	VX_SSD_1X	4.96
2	VX_SSD_1Y	5.10
3	VX_SSD_1U	4.46
4	VX_SSD_1V	5.94
5	VX_SSD_2X	5.39
6	VX_SSD_2Y	5.53
7	VX_SSD_2U	4.86
8	VX_SSD_2V	6.42
9	VX_MSD_1X	5.84
10	VX_MSD_1Y	5.98
11	VX_MSD_1U	5.27
12	VX_MSD_1V	6.91
13	VX_MSD_2X	6.29
14	VX_MSD_2Y	6.43
15	VX_MSD_2U	5.69
16	VX_MSD_2V	7.42
17	VX_MSD_3X	6.75
18	VX_MSD_3V	7.24
19	VX_MSD_3U	6.55
20	VX_MSD_4X	7.07

Table 4.2: Beam segment fit error(μm) at vertex planes

different cluster sizes and ADC information.

Charge Sharing region analysis

The outer mosaic planes have every other strip connected to the readout channel. Alternate detector strips are floating and it is expected that the particle deposited charge will be capacitively coupled to adjacent strips. This charge sharing phenomenon will improve the measurement resolution to better than simply a detector with twice the wire-spacing. An unfiltered interaction run was selected and residuals from the outer and middle panels of a mosaic detector was compared. Only about 1-2% of all tracks lay in an

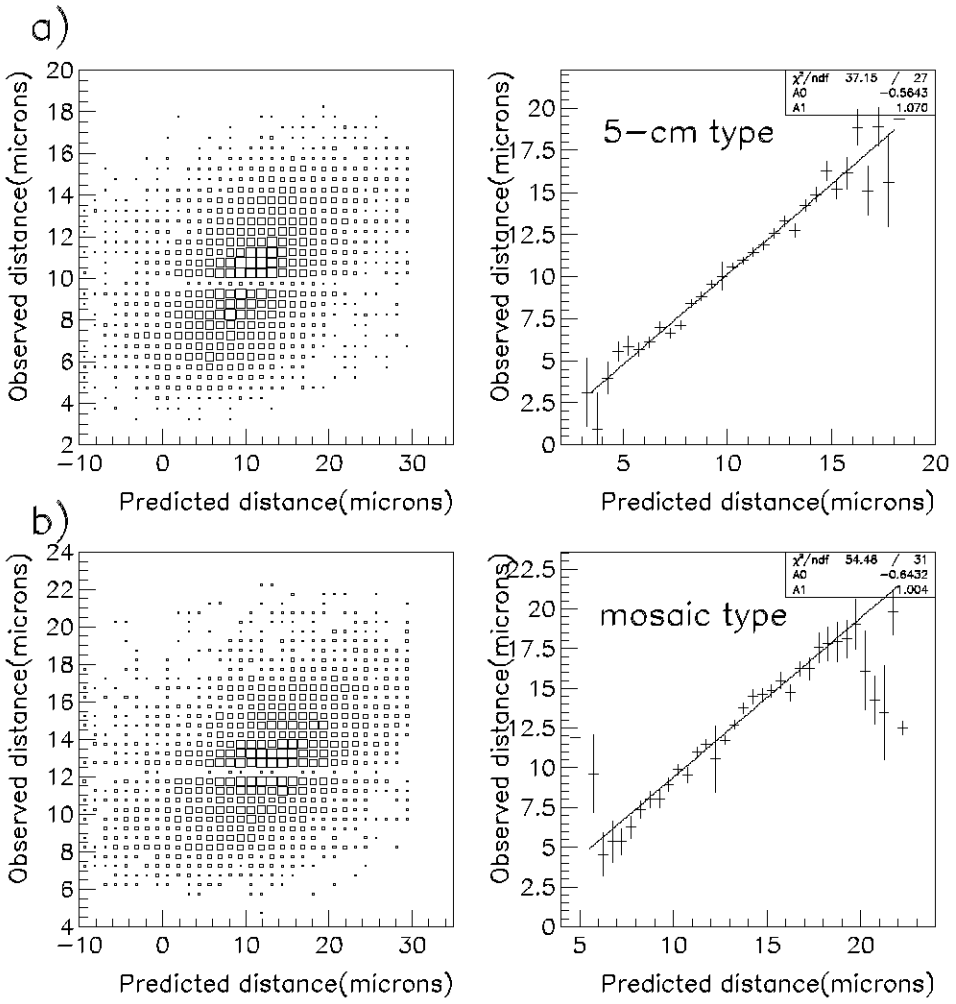

Figure 4.10: a)Scatter plot of the observed and predicted(from ADC charge weighting) positions of tracks, from a strip center for a 20μm pitch 5_cm detector, b) The same plot for a 25μm pitch mosaic detector

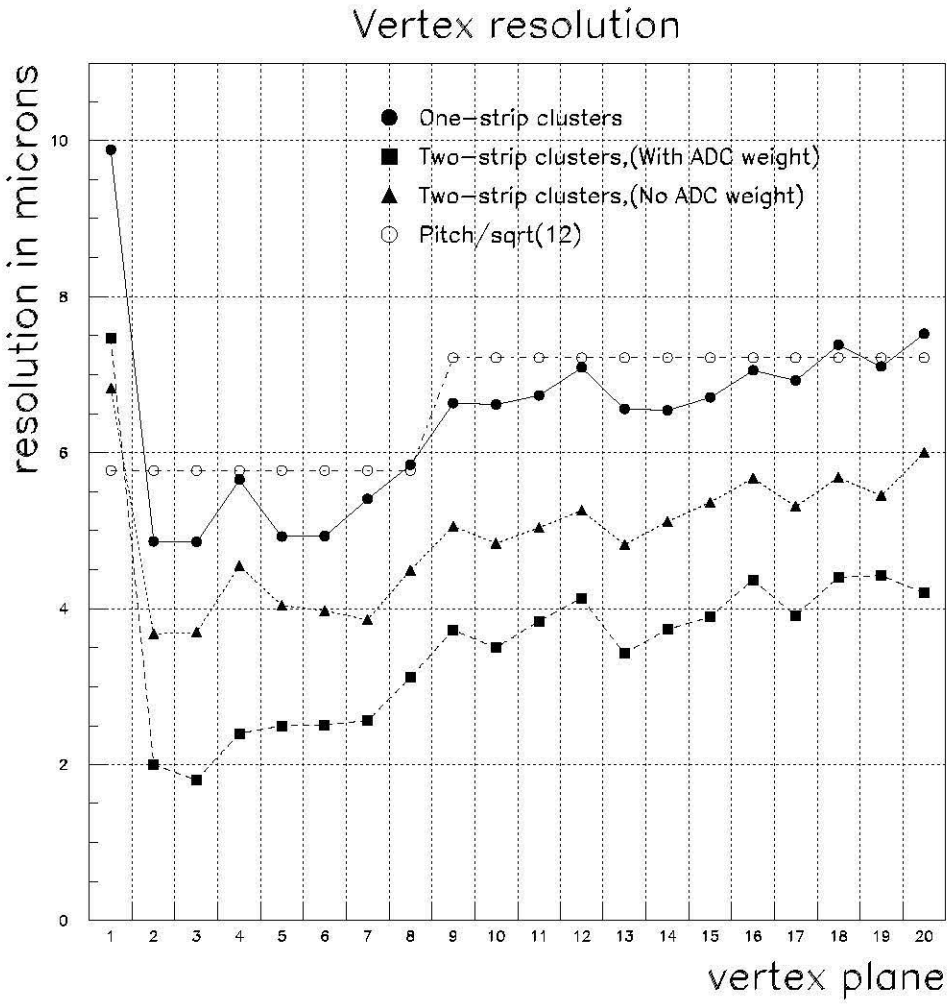

Figure 4.11: Resolutions of all the vertex plane(Errors are $\pm 1\mu$m).

No.	Detector	1-strip (exp)	1-strip (obs)	2-strip (w/o ADC)	2-strip (w ADC)
1	VX_SSD_1X	5.77	9.89±1.0	6.83±1.0	7.46±1.0
2	VX_SSD_1Y	5.77	4.87±1.0	3.68±1.0	2.00±1.0
3	VX_SSD_1U	5.77	4.86±1.0	3.70±1.0	1.80±1.0
4	VX_SSD_1V	5.77	5.66±1.0	4.54±1.0	2.40±1.0
5	VX_SSD_2X	5.77	4.92±1.0	4.04±1.0	2.49±1.0
6	VX_SSD_2Y	5.77	4.93±1.0	3.98±1.0	2.51±1.0
7	VX_SSD_2U	5.77	5.41±1.0	3.86±1.0	2.57±1.0
8	VX_SSD_2V	5.77	5.85±1.0	4.49±1.0	3.11±1.0
9	VX_MSD_1X	7.22	6.63±1.0	4.05±1.0	3.72±1.0
10	VX_MSD_1Y	7.22	6.62±1.0	4.84±1.0	3.50±1.0
11	VX_MSD_1U	7.22	6.74±1.0	4.04±1.0	3.84±1.0
12	VX_MSD_1V	7.22	7.09±1.0	4.26±1.0	4.14±1.0
13	VX_MSD_2X	7.22	6.56±1.0	4.82±1.0	3.42±1.0
14	VX_MSD_2Y	7.22	6.55±1.0	5.12±1.0	3.73±1.0
15	VX_MSD_2U	7.22	6.71±1.0	5.37±1.0	3.89±1.0
16	VX_MSD_2V	7.22	7.06±1.0	5.67±1.0	4.37±1.0
17	VX_MSD_3X	7.22	6.93±1.0	5.31±1.0	3.91±1.0
18	VX_MSD_3V	7.22	7.38±1.0	5.68±1.0	4.40±1.0
19	VX_MSD_3U	7.22	7.11±1.0	5.45±1.0	4.43±1.0
20	VX_MSD_4X	7.22	7.53±1.0	6.00±1.0	4.20±1.0

Table 4.3: Position resolution(μm) at vertex planes

outer panel. Residuals from these tracks and tracks in the outer 2mm of a central mosaic panel are shown in Fig 4.12. As seen from this figure, the outer panels have a residual distribution only 55% broader for a wire spacing twice as broad as the inner panel. This confirms that charge sharing occurs in the vertex detectors which have alternately read-out strips. The momentum distribution of the tracks used in the residual distribution is also seen in Fig 4.12a. The residual distributions appear broader than those for a beam run because of multiple scattering in the low momentum distribution with a significant relative spread.

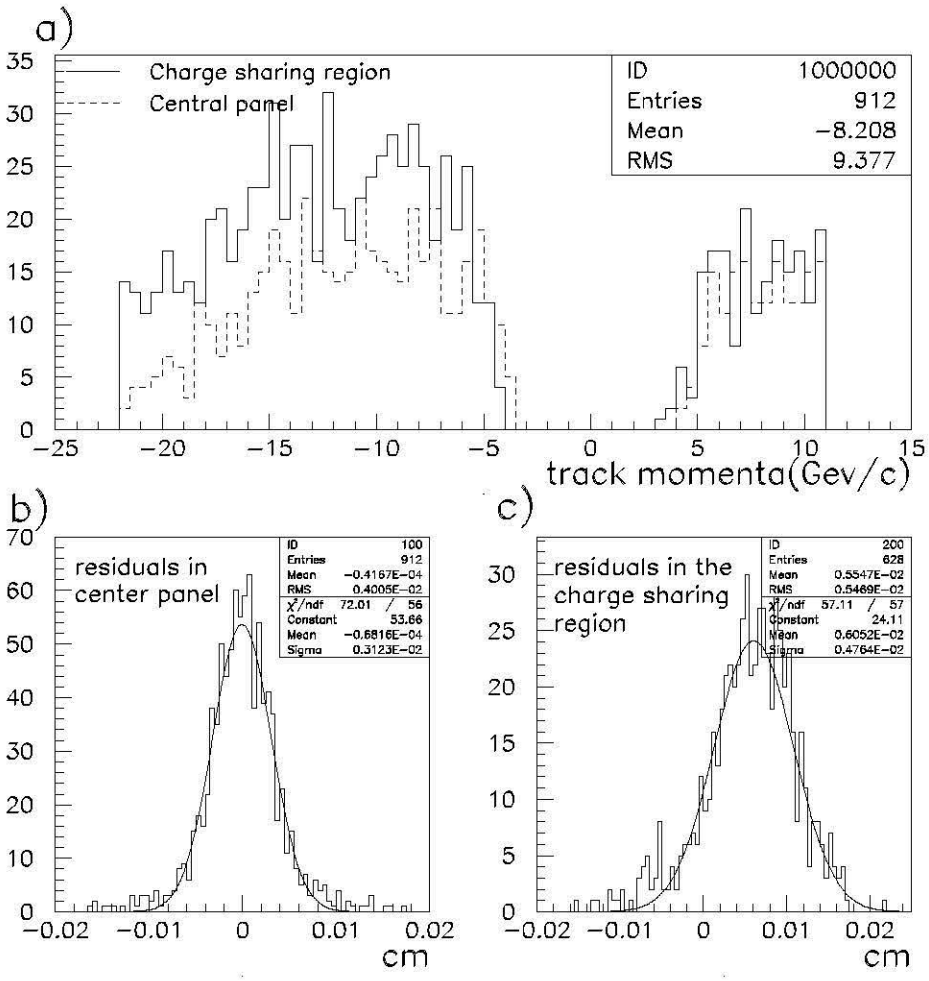

Figure 4.12: a)Momentum spectrum of sample of large angle tracks in the vertex b)Residuals seen in the central(every strip read out region)panel c)Residuals in the outer(alternate strip read out region)panels

The systematics of measurement have been accounted for and the errors well understood. The detector resolutions are slightly better than what would be expected from the design criteria. The stability of these quantities have been studied (see section 4.4) and found to be quite stable.

4.3 Momentum dependent Multiple Coulomb Scattering

The previous analysis utilized beam tracks with momentum around 650GeV/c. The effects of Multiple Coulomb scattering start to become evident at momenta of 100GeV/c and lower. A charged particle traversing a medium is deflected by many small-angle scatters, mostly due to Coulomb scattering from nucleii. The Coulomb scattering distribution is well represented by the theory of Moliere as roughly Gaussian for small angles. The width of the distribution may be described by θ_{ms} given by[24],

$$\theta_{ms} = \frac{13.6Mev}{\beta cp} z\sqrt{x/X_o}[1 + 0.038ln(x/X_o)] \tag{4.4}$$

where p, βc, and z are the momentum, velocity and charge number of the incident particle and x/X_0 is the thickness of the scattering medium in radiation lengths. There are 20 planes of 300μm silicon in the vertex detector and this material corresponds to a total of 6% of a radiation length, which is not negligible at low momentum. The effect gets progressively worse as the particle travels downstream through more vertex planes. At 50 Gev/c, the error due to multiple scattering is comparable with the detector plane error. A study of the effects of multiple scattering in the vertex detector was conducted to be able to compensate for the varying position resolution at various planes for track fitting.

4.3.1 A model for scattering in the VSSD

As the charged particle traverses through the vertex detector, it is successively scattered by planes it passes through. The effect is cumulative(i.e. it increases with more planes that it goes through), but it does not simply add in quadrature. The multiple scattering error can be parametrized by forming an error matrix E^{MS}. This is a 20×20, symmetric square matrix, whose dimension is determined by the number of planes which make measurements. Each of the detector planes measures the particle trajectory in a particular view and so there will be non-zero correlation terms in the multiple scattering matrix due to U and V measurements which correlate the X and Y views. The i_{th} diagonal elements may be written as

$$E_{ii}^{MS} = \left(\sigma_i^{plane}\right)^2 + \sum_{k=1}^{k<i} \theta_{ms}^2 \times (z_i - z_k)^2 \tag{4.5}$$

where the z's are the z positions of the planes and θ_{ms} is the multiple scattering angle as defined in previous subsection(Eqn. 4.4, same for all the planes). For the cross terms in the matrix, we have

$$E_{ij}^{MS}(i < j) = \sum_{k=1}^{k<i} \theta_{ms}^2 \times (z_i - z_k)(z_j - z_k) \tag{4.6}$$

The effect of scatterers between two planes i and j are cancelled out in the ij^{th} term of the matrix. This formulation can be extended in a straight forward manner to include passive scattering objects like interaction counters and targets in the path of the beam, before the vertex detector as follows

$$E_{ij}^{MS} = E_{ij}^{MS} + \sum_{obj=first\ object,\ last\ object} \theta_{ms,obj}^2 \times (z_i - z_{obj})(z_j - z_{obj}) \tag{4.7}$$

where $\theta_{ms,obj}$ is the multiple scattering angle in the object material. There is a multiplicative factor expressing the projection of each plane on the other as

$$E_{ij}^{MS} = E_{ij}^{MS} \times cos(\phi_i - \phi_j) \tag{4.8}$$

where the ϕs are the readout orientation of the dectector planes.

The origin is chosen to be the point where the errors due to multiple scattering are to be evaluated, which was usually the target at which an interaction took place and the track in the vertex detector began. The error evaluation is done in the X-Y coordinate system. The errors are defined as a matrix of errors E^{Err}, which is a 4×4 symmetric matrix. The diagonal terms are the squared errors in $X_{intercept}$, X_{slope}, $Y_{intercept}$, Y_{slope} and the cross-terms are the correlations between these quantities. To use the error matrix E^{MS} to yield the matrix of errors E^{Err}, we need to formulate a 20×4 matrix D. The D matrix contains the geometrical constants of the 20 detector planes in position and rotational orientation. Each row of the D matrix represents each of 20 detectors in the vertex system. It is written down as

$$D = \begin{pmatrix} cos(\phi_1) & z_1 \times cos(\phi_1) & sin(\phi_1) & z_1 \times sin(\phi_1) \\ cos(\phi_2) & z_2 \times cos(\phi_2) & sin(\phi_2) & z_2 \times sin(\phi_2) \\ cos(\phi_3) & z_3 \times cos(\phi_3) & sin(\phi_3) & z_3 \times sin(\phi_3) \\ ... & ... & ... & ... \end{pmatrix} \tag{4.9}$$

With all these pieces in hand, we can calculate

$$E^{Err} = \left(D^T \left(E^{MS}\right)^{-1} D\right)^{-1} \tag{4.10}$$

This gives us the error in a track parameters due to the effects of multiple Coulomb scattering in elements before and in the vertex detector. The momentum dependence of the track error comes in from the definition of the θ_{ms} in the error matrix terms. For the limit of large momentum, $\theta_{ms} \rightarrow 0$. The error matrix E^{MS} becomes diagonal with the elements being the plane resolution terms. The dependence on momentum disappears and the problem reduces to a least squares fit to measurements with fixed uncertainty.

4.3.2 Simulation and Parametrizing scattering

A FORTRAN routine was coded which followed the multiple Coulomb scattering model described above. Table 4.4 describes the relevant parameters in the system.

All calculations were done using double precision accuracy in order to minimize rounding off errors. The input to the program was in the form of a file describing the entire system in terms of material properties and geometry. This made the analysis flexible with respect to different detector scattering configurations. A target where the interaction occured could be specified, and the program computed the error due to scattering in all objects downstream of that target. The error matrix is calculated at specified increments of momentum in GeV/c in a momentum range.

4.3.3 Agreement of Model with data

In order to test the accuracy of this model, it was checked against real interaction data acquired during the run. Within the SOAP analysis software is an algorithm called SILMATCH which takes M2 found segments and looks for the corresponding track segment in the vertex detector. Having found a track in a road through the vertex detector, it assigns a χ^2/dof to the track. This χ^2/dof will is sensitive to the plane measurement error or "weights" associated with each detector plane. At high momentum, these plane errors are constant and given by roughly pitch/$\sqrt{12}$. The χ^2/dof for these tracks have been verified to have the expected χ^2 distribution with a mean of unity. For low momentum tracks, the plane errors increase with lower momentum and start to depend on multiple scattering through previous material. Naively using the high momentum weights distorts the χ^2/dof distribution and changes its mean value.

The Multiple Coulomb Scattering Model developed earlier, is able to predict the the plane error quantity as a function of momentum. The test of the model now boils down to using the model predicted weights in the χ^2/dof calculation and observing their distribution. If the distribution stays χ^2 like with a mean of unity, independent of momentum, then the scattering model is credible.

Such a test was conducted on interaction runs 2891, 3150-3153. The momentum of the track is given by the bend measurement in the M2 magnet.

The Multiple scattering error program was run on vertex configuration consisting of just the 20 silicon vertex planes. The error matrix was propagated down to the positions of the vertex planes and the errors expected at various momentum are as shown in Fig 4.13. The errors(pl_error_n on the nth plane) were then parametrized as a function of 1/p and the vertex plane number n(ranging from 1-20), in the momentum(p) range 2-100 Gev/c. It was described by the functional form

$$pl_error_n = -23.449 \times p^{-1} + 33.784 \times p^{-1} \times n \tag{4.11}$$

The weight associated with the nth plane for the χ^2/dof calculation was then computed as

$$weight^{-1} = pl_error_n^2 + \left(\sigma_n^{det}\right)^2 \tag{4.12}$$

where σ_n^{det} is the detector measurement error for the nth plane.

Using these modified weights, we plot the resulting χ^2/dof in various momentum bins, in Fig 4.14. All the distributions have uniform χ^2/dofs as should be expected when the error parametrization is correct. The momentum of the tracks in the sample is shown in Fig 4.15. A comparison of the same χ^2/dof distributions with constant momentum independent errors is shown in Fig 4.16.

The track resolution at the vertex is a quantity which will depend on the momentum(described in the next section) roughly like 1/p. The use of the multiple scattering model to estimate the momentum dependent track fit weights is summarized in Fig 4.17. We observe that that the mean χ^2/dof is relatively unchanged while the vertex track resolution displays the expected behaviour.

4.3.4 Track resolution at the vertex

Having verified that the error description by the multiple scattering model is adequate to give correct χ^2/dof distributions, we can now use the model to estimate the transverse resolution at the vertex region for tracks passing

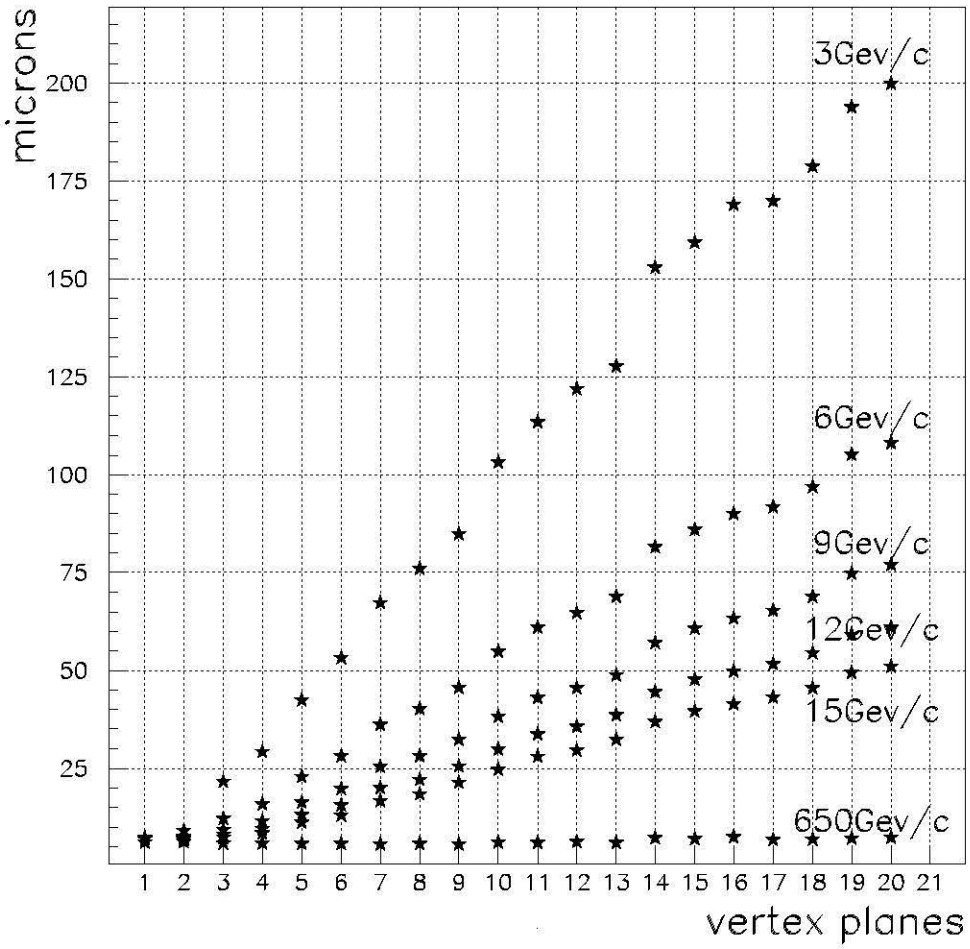

Figure 4.13: The simulation model predicted error on each vertex plane from multiple scattering

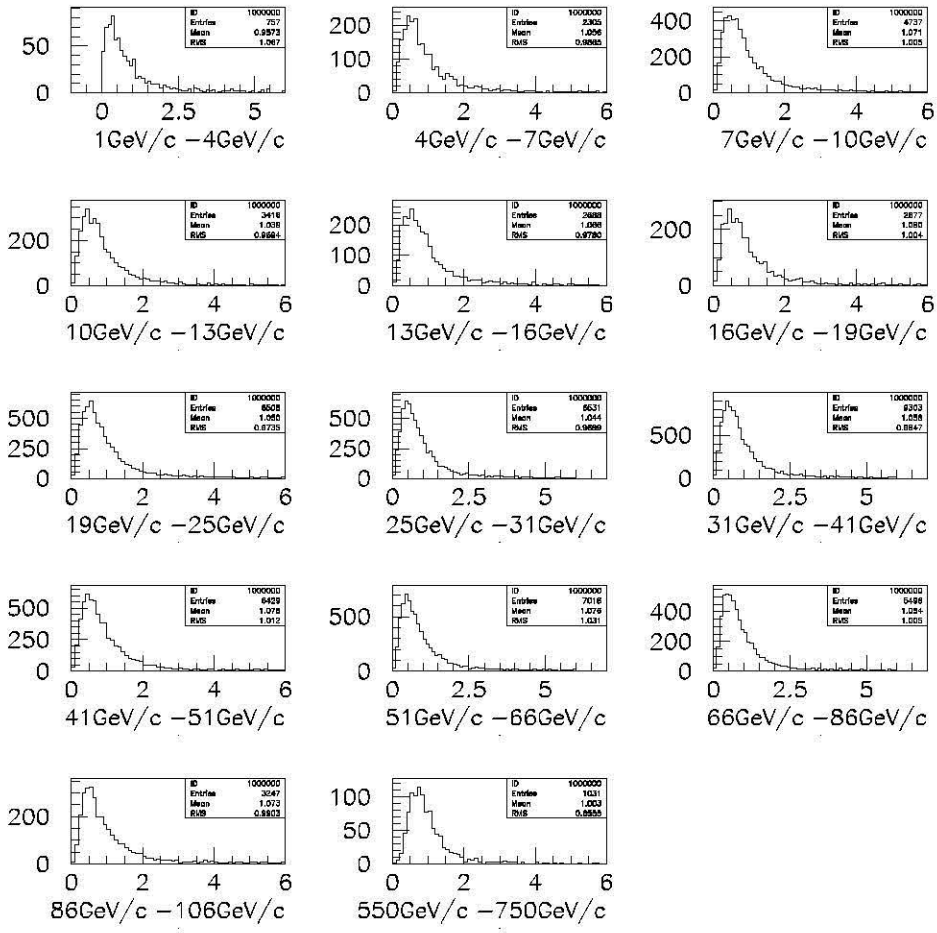

Figure 4.14: χ^2/dof of fitted tracks in various momentum bins using the multiple scattering model predicted plane weights

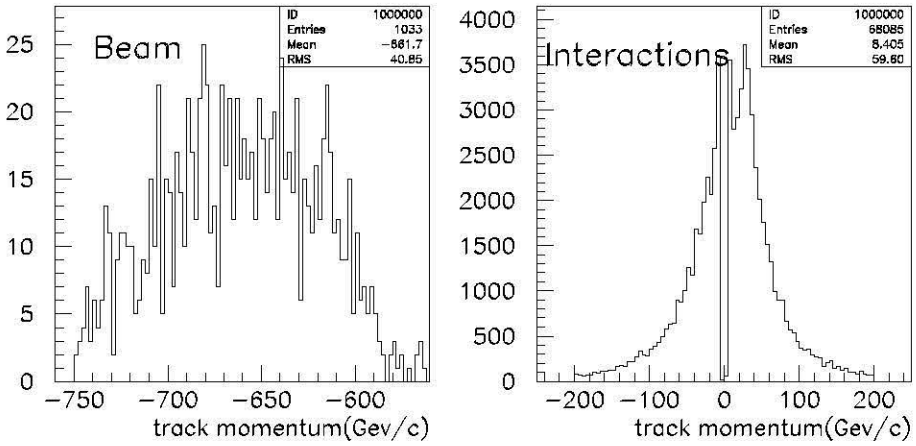

Figure 4.15: The momentum distribution of tracks that were fitted a)high momentum beam b)low momentum interactions

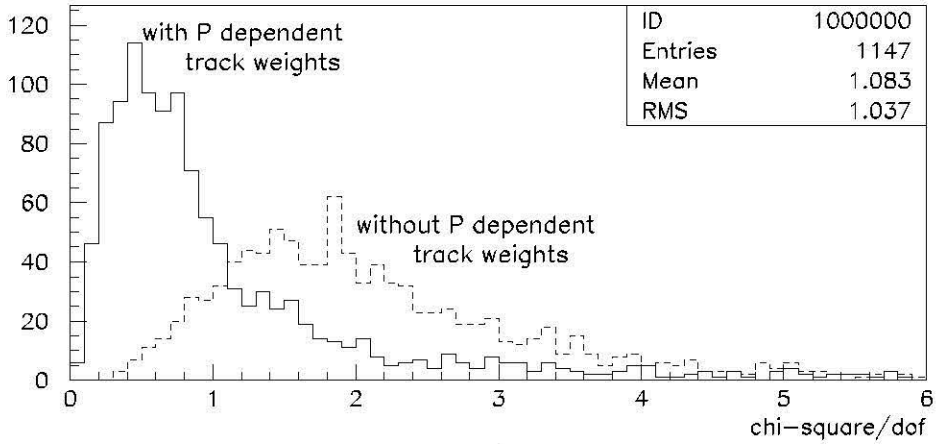

Figure 4.16: A comparison of the χ^2/dof distributions for momentum dependent and momentum independent track weights

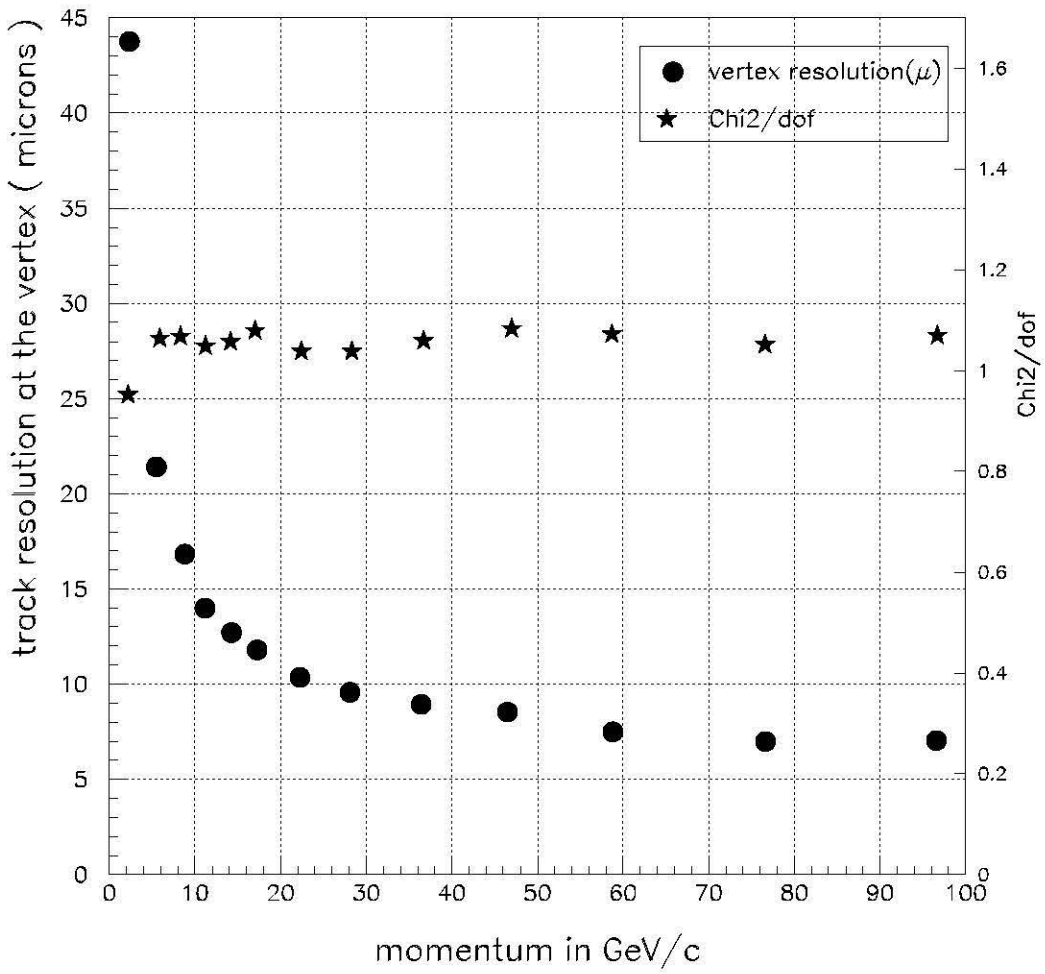

Figure 4.17: Mean χ^2/dof and vertex track resolution at different momenta

through targets and detected in the vertex spectrometer[8]. Below is a sample output for the simulation of a track error matrix at the most downstream charm target. We can clearly see the 1/p like dependence of the errors on the momentum. Scattering now occurs in half the diamond target thickness, two interaction counters and 20 planes of vertex silicon. The error matrix is expressed in the XY coordinate system. The units are in cm(x,y) and radians(θ_x, θ_y) and the form of the error matrix is as follows.

$$E^{Err} = \begin{pmatrix} \sigma_x^2 & cov(x,\theta_x) & cov(x,y) & cov(x,\theta_y) \\ cov(\theta_x,x) & \sigma_{\theta_x}^2 & cov(\theta_x,y) & cov(\theta_x,\theta_y) \\ cov(y,x) & cov(y,\theta_x) & \sigma_y^2 & cov(y,\theta_y) \\ cov(\theta_y,x) & cov(\theta_y,\theta_x) & cov(\theta_y,y) & \sigma_{\theta_y}^2 \end{pmatrix} \tag{4.13}$$

****

Track slope-intercept error matrix for 2.0GeV/c

$$\begin{pmatrix} 0.2190E-04 & -0.6502E-05 & 0.5468E-07 & -0.8496E-08 \\ -0.6502E-05 & 0.2294E-05 & 0.5783E-08 & -0.1957E-08 \\ 0.5468E-07 & 0.5783E-08 & 0.2440E-04 & -0.6975E-05 \\ -0.8496E-08 & -0.1957E-08 & -0.6975E-05 & 0.2368E-05 \end{pmatrix}$$

The transverse error at origin at 2GeV/c = 68.040 μm

Track slope-intercept error matrix for 20GeV/c/c

$$\begin{pmatrix} 0.1004E-05 & -0.1273E-06 & -0.3315E-07 & 0.1907E-08 \\ -0.1273E-06 & 0.2879E-07 & 0.1983E-08 & -0.1020E-09 \\ -0.3315E-07 & 0.1983E-08 & 0.7269E-06 & -0.1095E-06 \\ 0.1907E-08 & -0.1020E-09 & -0.1095E-06 & 0.2767E-07 \end{pmatrix}$$

The transverse error at origin at 20GeV/c = 13.155μm

Track slope-intercept error matrix for 100GeV/c

[8]the momentum is given by track bending in M1 and M2 spectrometer magnets

$$\begin{pmatrix} 0.2470E-06 & -0.1304E-07 & -0.1441E-07 & 0.7505E-09 \\ -0.1304E-07 & 0.1563E-08 & 0.6667E-09 & -0.3552E-10 \\ -0.1441E-07 & 0.6667E-09 & 0.2249E-06 & -0.1324E-07 \\ 0.7505E-09 & -0.3552E-10 & -0.1324E-07 & 0.1639E-08 \end{pmatrix}$$

The transverse error at origin at 100GeV/c = 6.870μm

Track slope-intercept error matrix for 650GeV/c

$$\begin{pmatrix} 0.1811E-06 & -0.5702E-08 & -0.1439E-07 & 0.8016E-09 \\ -0.5702E-08 & 0.2464E-09 & 0.6704E-09 & -0.4040E-10 \\ -0.1439E-07 & 0.6704E-09 & 0.1921E-06 & -0.8128E-08 \\ 0.8016E-09 & -0.4040E-10 & -0.8128E-08 & 0.4634E-09 \end{pmatrix}$$

The transverse error at origin at 650GeV/c = 6.109μm

****

The transverse track resolution is given by

$$\rho = \sqrt{\sigma_x^2 + \sigma_y^2 + 2cov(x,y)} = \sqrt{E_{11}^{Err} + E_{33}^{Err} + 2E_{13}^{Err}} \qquad (4.14)$$

(The observed correlation is $\leq 5\%$.)

During the runtime analysis of data from the vertex detector, the momentum dependent matrix of errors is required to calculate the vertexing resolution. Computing the matrix during the analysis is a time consuming and CPU wasteful procedure. Hence, it was decided to parametrize the 10 independent matrix elements as a function of momentum(or 1/p) and use the parametrized form to recompute the matrix. For tracks arising in the downstream-most target, the 10 independent elements are plotted in Fig 4.18 for the momentum range 3-100 GeV/c at 0.5GeV/c intervals. As we can see most of the drastic effects of multiple scattering occur for momentum below 100GeV/c. These functions were normalized to their value at 650GeV/c and broken into 5 intervals for the purposes of parametrization. They ranged from 2-6 GeV/c, 5-30 GeV/c, 25-70 GeV/c, 50-290 GeV/c and 250-700 GeV/c. The functions were fitted to a third order polynomial fit in the variable 1/p to an accuracy of better than 3.0%. The overlapping intervals ensured a

smooth transition between bins. An example of these polynomial fits and the errors are shown in Fig 4.19 for the (1,1) diagonal element(the X error term squared). The fit parameters are stored in an ASCII file or as data statements and a simple FORTRAN routine can quickly recompute the matrix of errors for a desired momentum. This momentum parametrization was performed for matrices for tracks beginning in each of the 5 different charm targets. The software to carry out this procedure is largely automated and can be run in a relatively short time if the detector configuration is modified.

4.4 Stability of the vertex detector

There are some crucial parameters which determine the performance of the vertex detector system. Foremost among these are the threshold calibration setting which determines event size and the pedestal and noise in the SVX which determines the resolution through ADC pulse height. These and other quantities are regularly monitored to verify the integrity of the data.

4.4.1 Monitoring detector performance

Monitoring is done on online beam data as well as offspill data. During the offspill period, interspill jobs are spawned on the FSCC. These acquire both sparse and latch-all mode data using a pulser as the trigger. Latch-all data yields the pedestal value(typically 200 events) and the rms noise associated with it. This is compared with the existing pedestal data loaded into the FSDA pedestal banks. An example of the output histograms from an offspill latch-all job is shown in Fig 4.20. The offspill sparse jobs give us the average occupancy(in a 1000 events) of a channel in all detectors. This parameter is very critical as it determines the event read-out time. A large event multiplicity means that a read-out imposed time limit of $30\mu s$ limits the number of read-out channels and thus, the physics information. Too few read-out channels(high threshold) means that the hit efficiency is being limited. Based on the output of the sparse job monitoring, the threshold

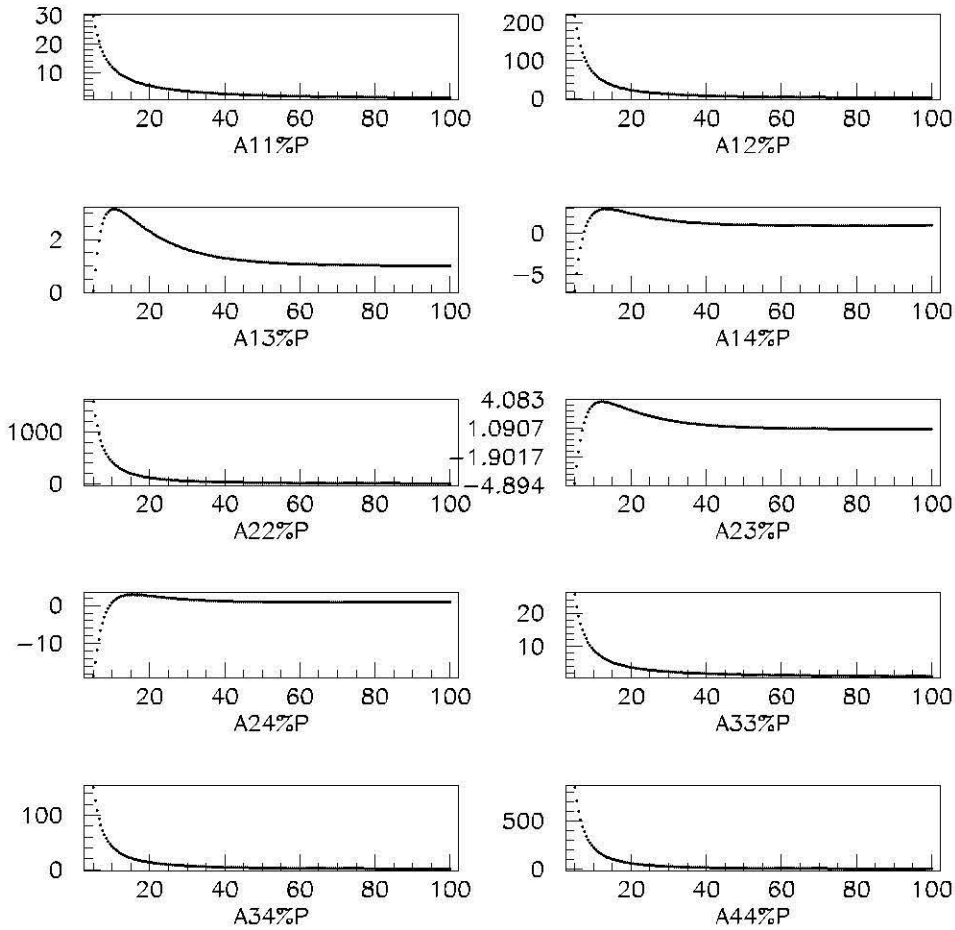

Figure 4.18: Variation of the 10 independent terms of the matrix of errors due to multiple scattering, with momentum

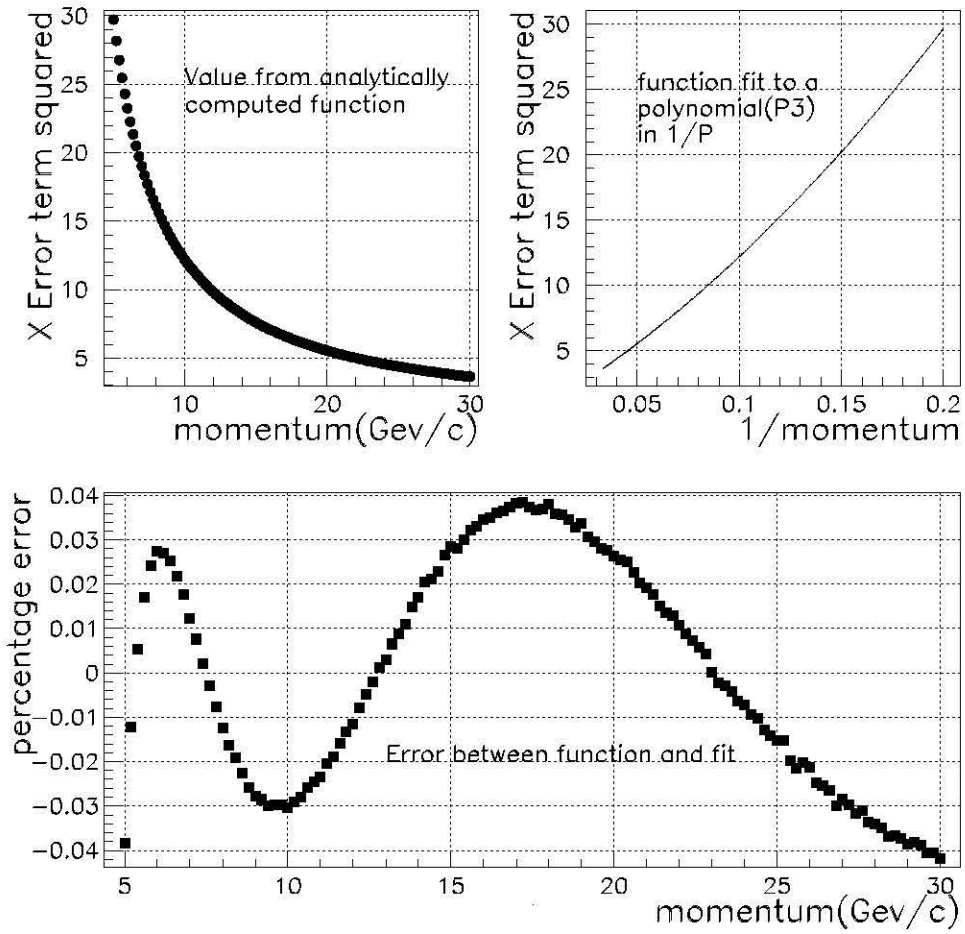

Figure 4.19: A example of the fit of the ER(1,1) term(i.e. the squared error in the X intercept) a)the computed value in 0.2Gev/c bins, b) fit to a third order polynomial in 1/p, c)relative error between the function and the fit (Note: The function values are displayed with a multiplicative factor)

can be adjusted to keep the occupancy at a desired level, uniform across all channels on all the detectors. A sample output from a sparse job is shown in Fig 4.21.

During the onspill data taking, an automatic offline analysis job is spawned on SOAP. The first 10,000 events of every online run is analyzed. Each detector has histograms like the wire-map, cluster size, ADC pulse height and event multiplicity produced and stored in an HBOOK file. These are available after about 10 minutes after a run has started. An example of these monitoring histograms for an interaction run is shown in Fig 4.22. This near-online monitoring output along with a reference set of histograms, is scanned by the shift crew ensuring that the data being written to tape is reasonable. Single events can also be plotted using the SEED(Single Event Display)package. Fig 4.23 shows a single beam event plotted in the vertex spectrometer in 2(X and Y) out of 4 possible views. A typical interaction event during normal charm data taking is shown in Fig 4.24.

4.4.2 Stability of operating parameters

The detectors were powered since the beginning of June 1996. Based on offspill sparse mode monitoring, the calibration job is spawned on an average of once every 10 weeks. The calibration threshold and the pedestals are quite stable during this period. To document the stability of the vertex system, performance data was acquired over a period of about 8 weeks and stored in a database. Fig 4.25 shows the pedestal variation for a particular channel and the same quantity averaged over one SVX chip of a typical detector. The variations are well within the rms noise of the distribution implying good stability. Fig 4.26 shows the observed hit efficiency variations in beam data for typical detectors. They are all consistently above 99%. An indicator of the efficiency of the threshold setting is the ratio of 2-strip clusters to 1-strip clusters in beam data. The time variation of this quantity is shown in Fig 4.27 for some typical detectors.

Fig 4.28a shows the alignment variations of some sample detectors with

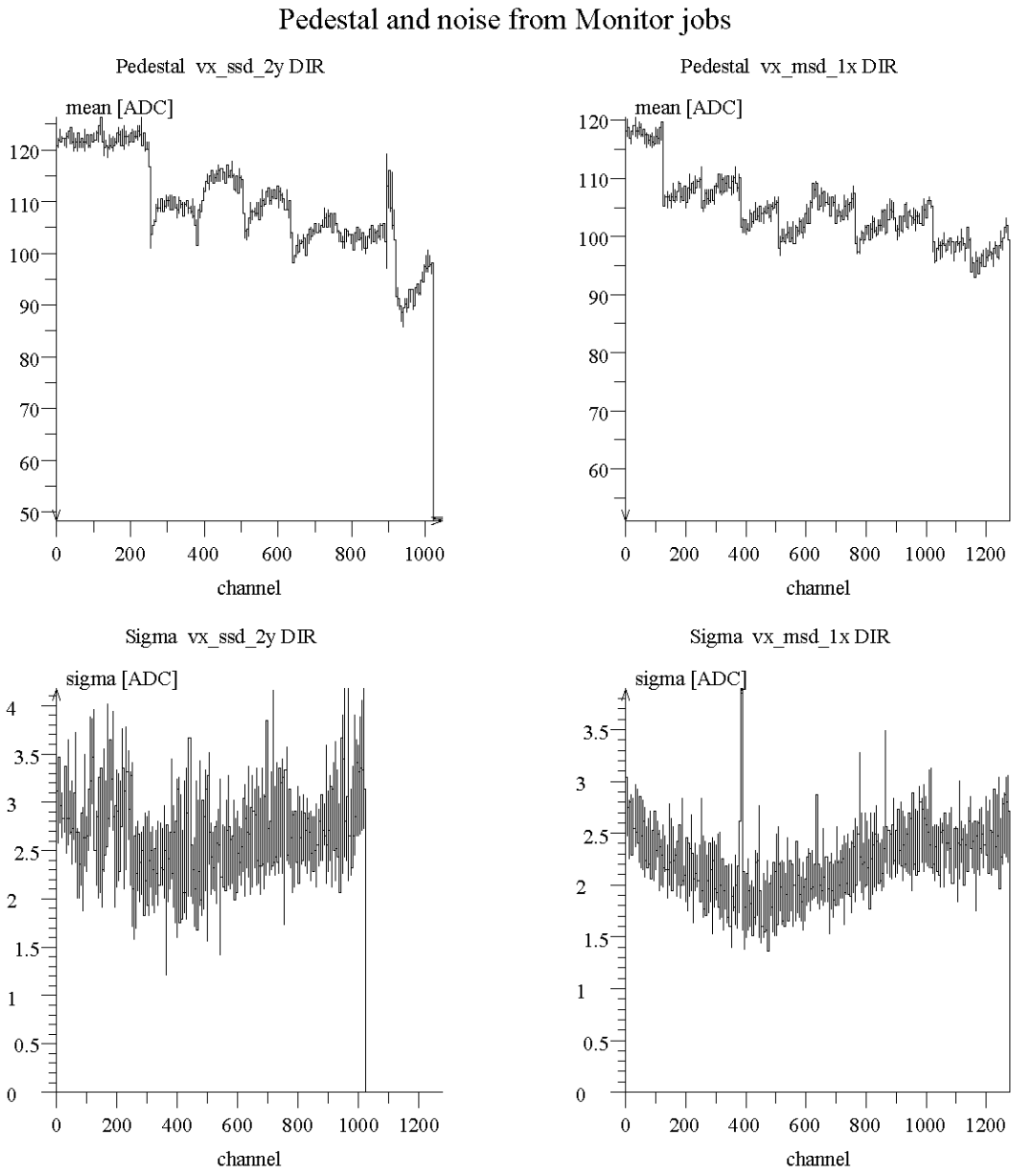

Figure 4.20: Pedestal and rms deviation output from an offspill monitoring job. Displayed are the direct sides of a 5_cm(vx_ssd_2y) and mosaic(vx_msd_1x) detectors

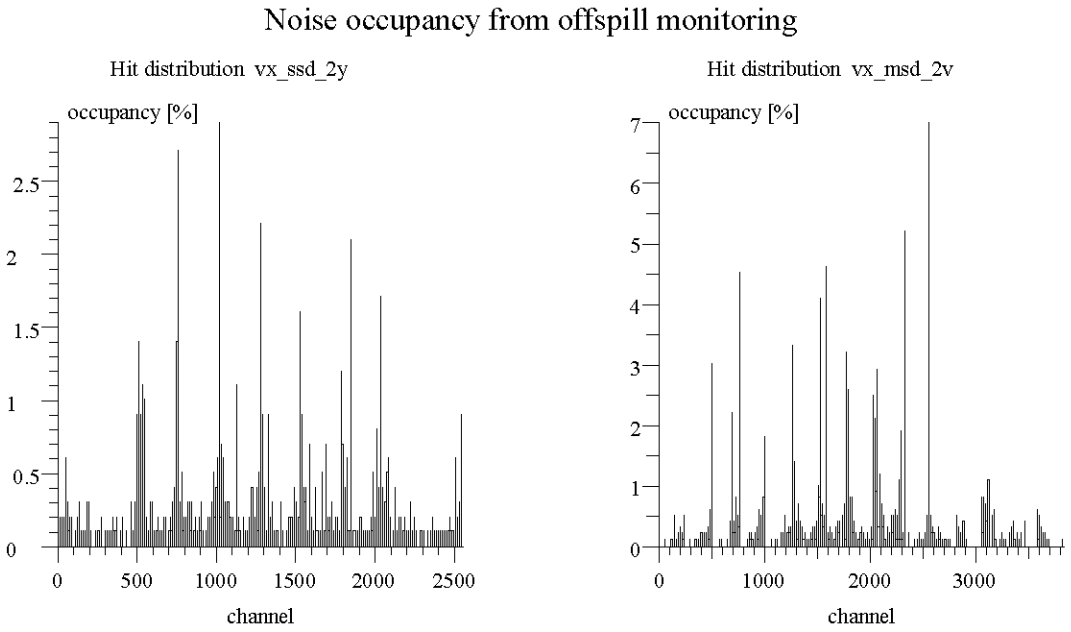

Figure 4.21: The sparse noise occupancy output from an offspill monitoring job. Displayed are a 5_cm(vx_ssd_2y) and mosaic(vx_msd_2v) detector

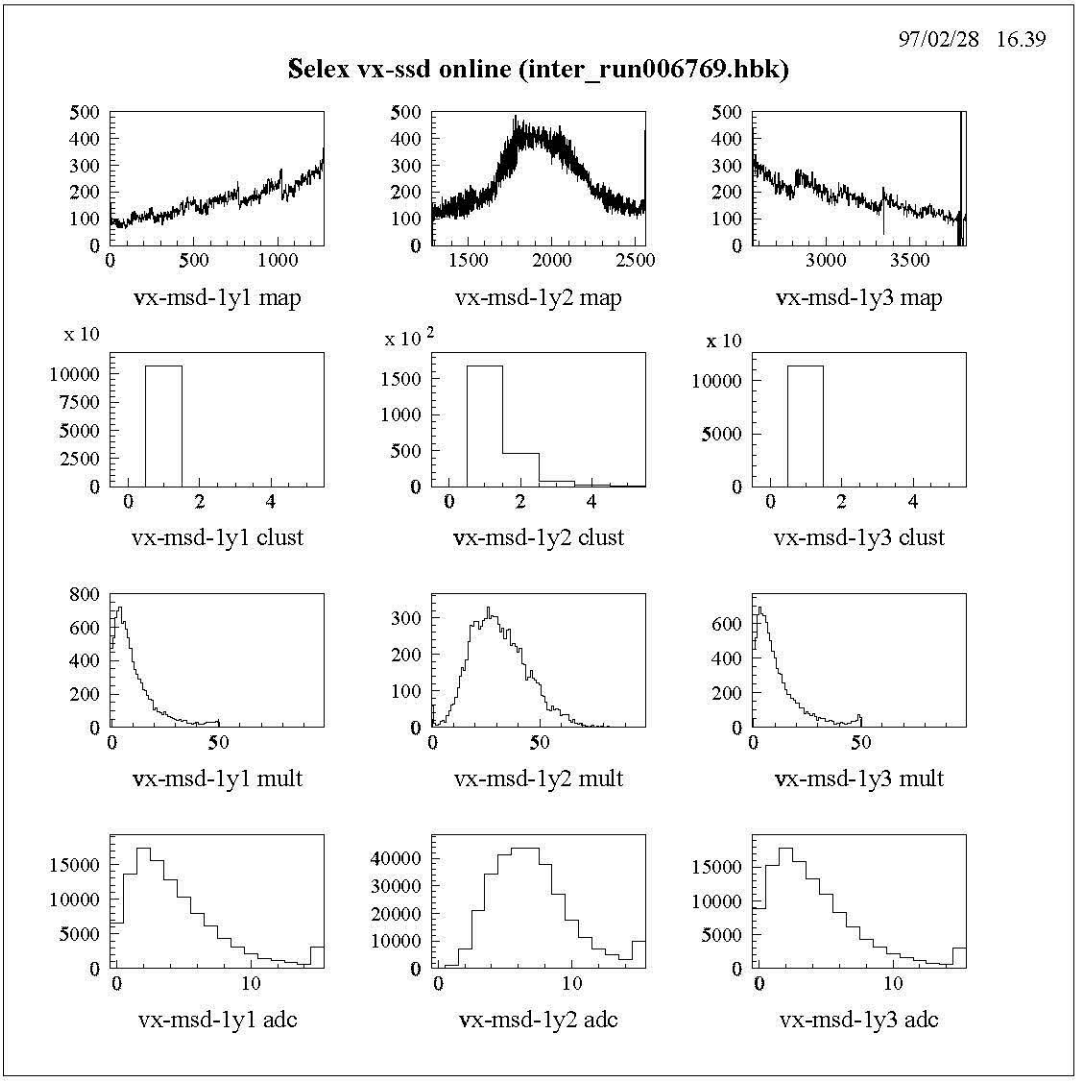

Figure 4.22: The output from the onspill monitoring job for a mosaic detector

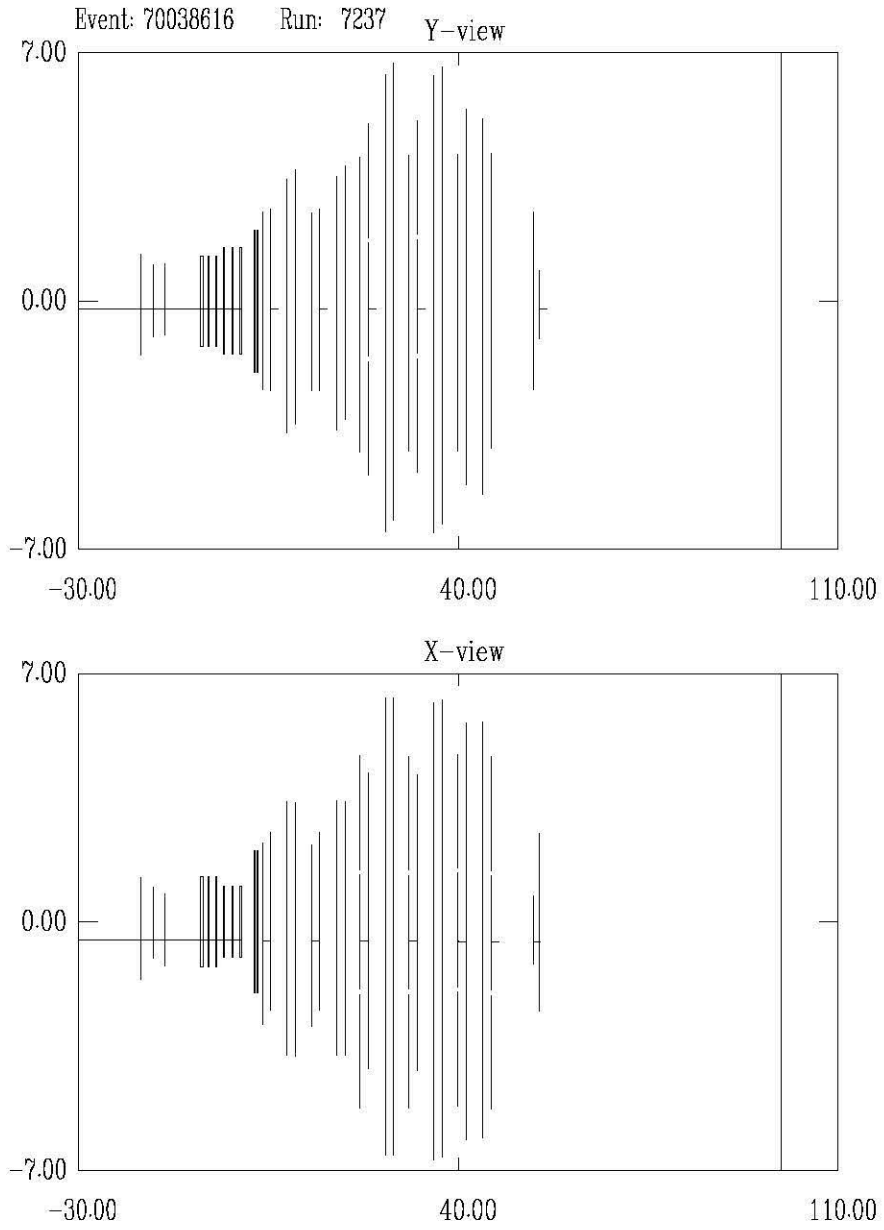

Figure 4.23: A single beam event display using the SEED package (Corresponding U and V views are not shown, but similar)

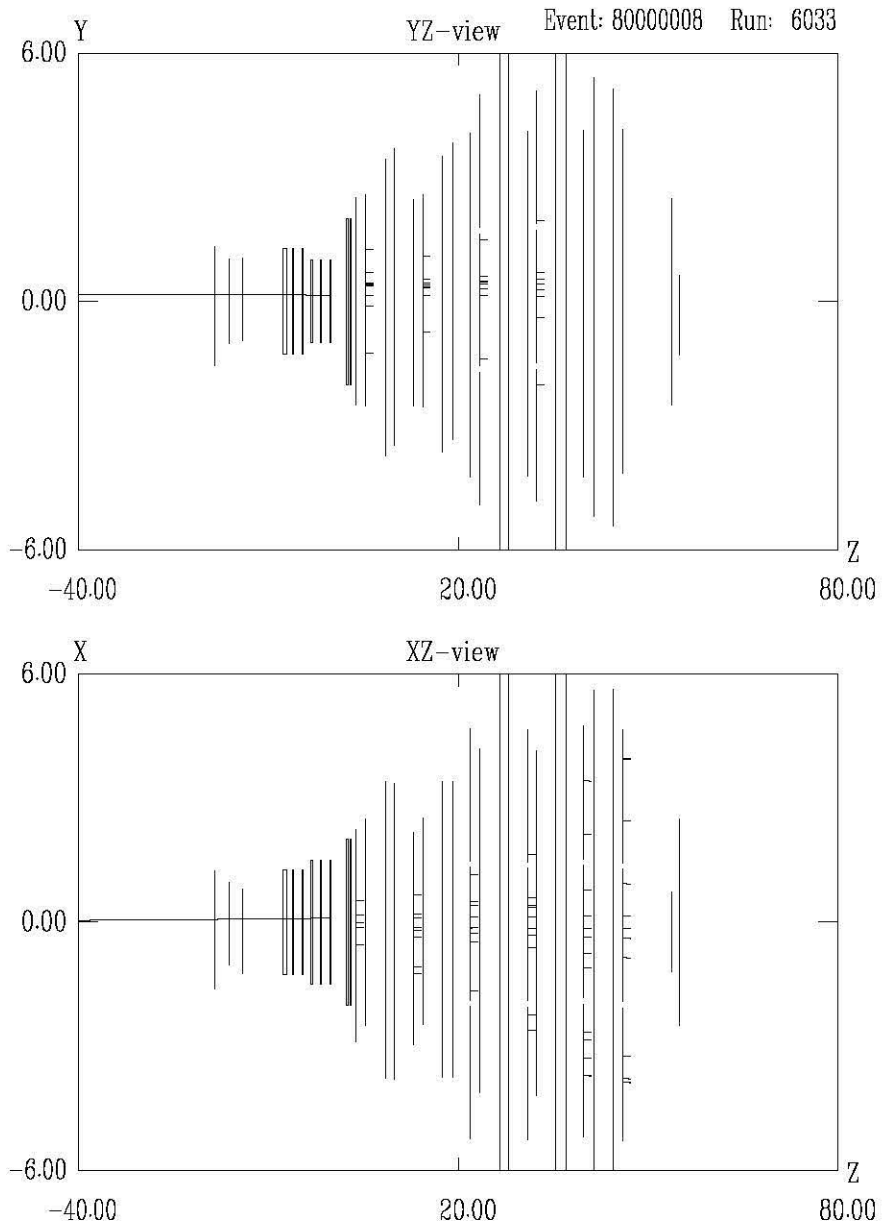

Figure 4.24: A typical interaction event (using the SEED display package) (Corresponding U and V views are not shown, but similar)

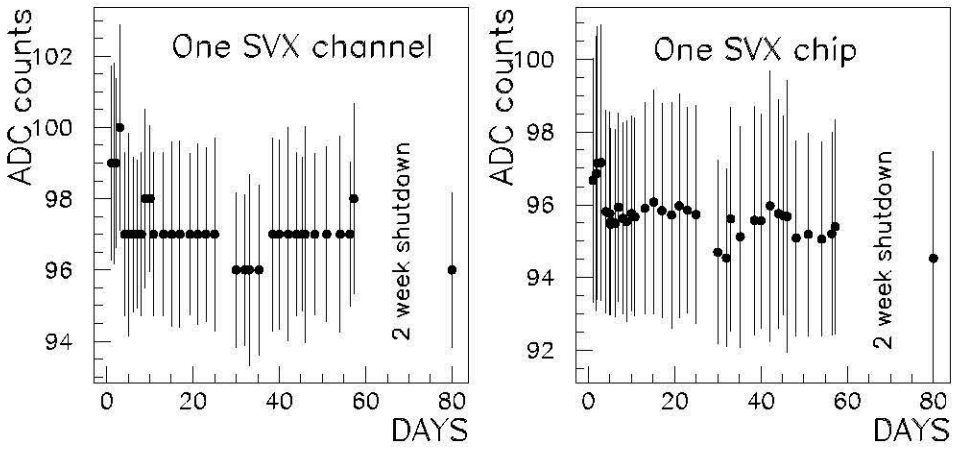

Figure 4.25: Pedestal(and noise) variation of a single channel and average over an SVX chip, over 9 weeks

respect to the experiments origin. However the alignment variation of the detectors with respect to the alignment of one fixed vertex plane is shown in 4.28b. This demonstrates that the vertex system has an internal alignment stability of better than 2μm. Fig 4.29 shows the noise occupancy time variation for a couple of typical detectors. The automated calibration routine was initially programmed to set all the thresholds to a 0.2% occupancy level. The resolution variation of some detectors is shown in Fig 4.30.

All these quantities display stability over a period of weeks. Re-calibration was performed only when a new SRS pattern implemented affected the occupancy. Overall, the vertex detector performance was as designed.

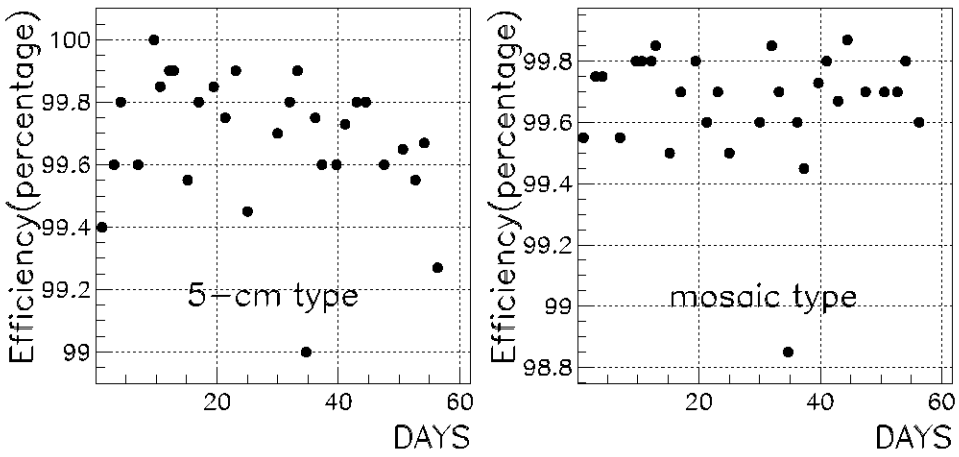

Figure 4.26: Typical hit efficiencies for 5_cm and mosaic detectors over 9 weeks

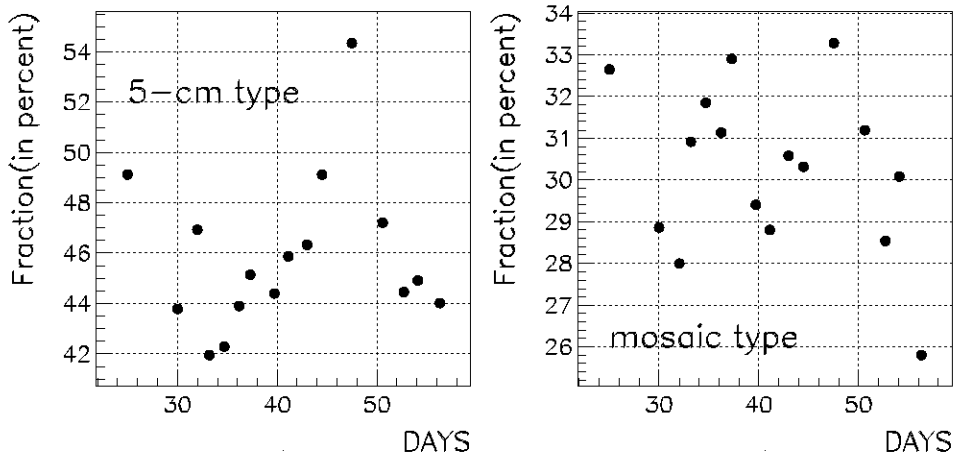

Figure 4.27: The ratio of two-strip to one-strip clusters in typical 5_cm and mosaic planes

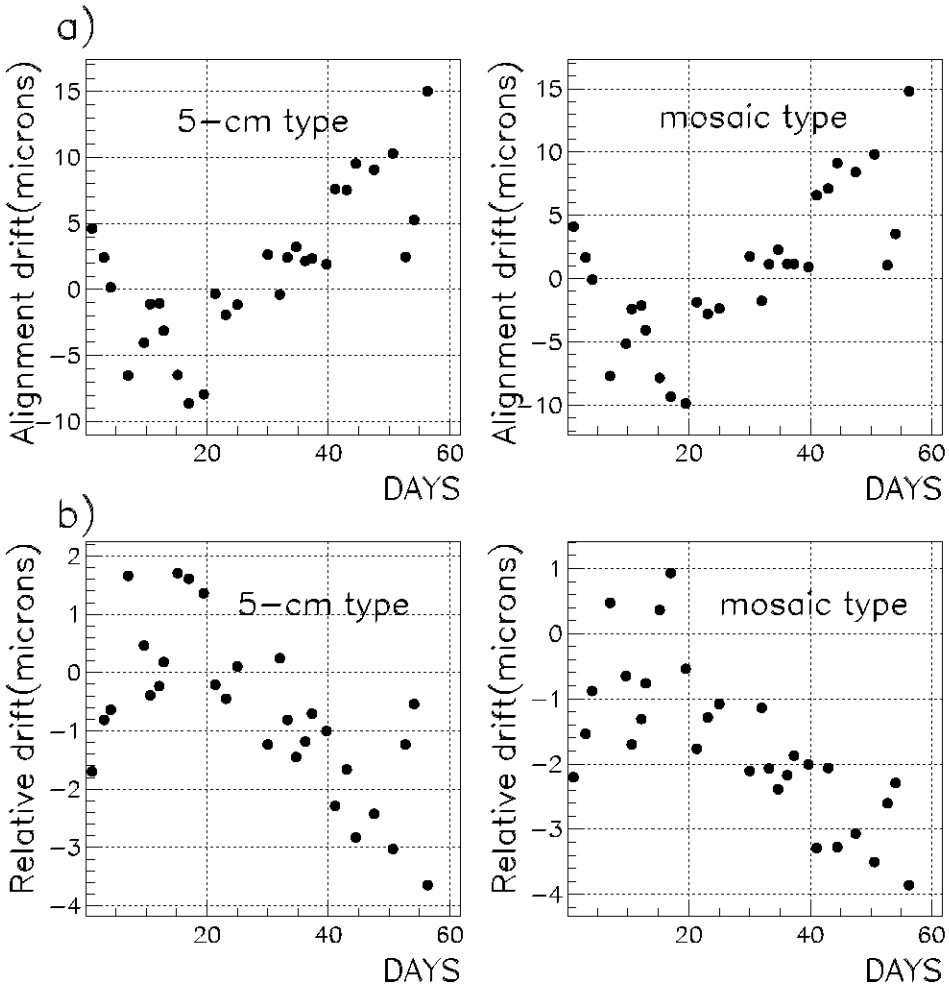

Figure 4.28: a)The typical alignment drifts of 5_cm and mosaic planes w.r.t. the SELEX alignment reference(This reference contains points outside of the vertex system) b)The same alignment drift w.r.t. a reference within the vertex system.

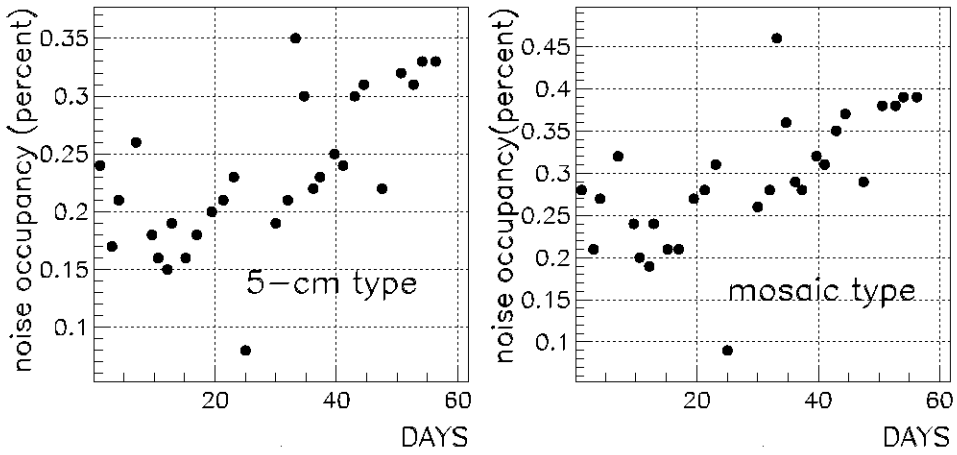

Figure 4.29: The typical noise level in beam runs for 5_cm and mosaic planes seen over a period of 9 weeks

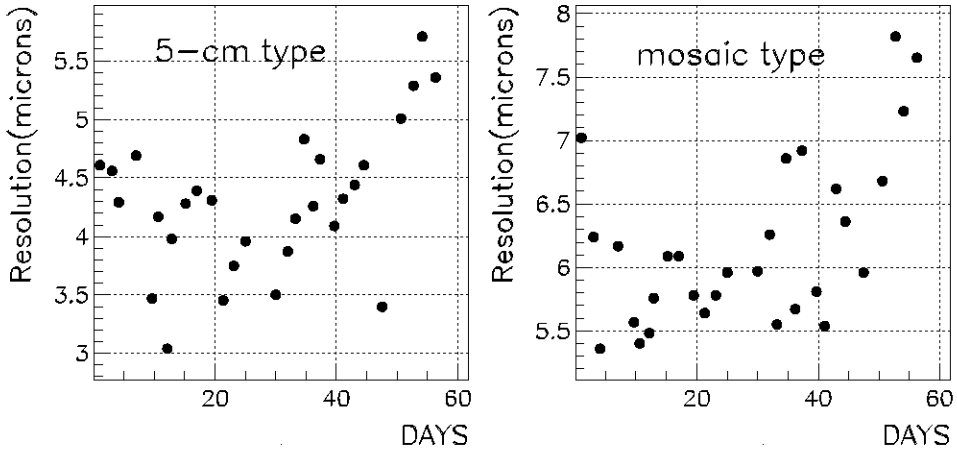

Figure 4.30: The typical resolution seen in beam runs for 5_cm and mosaic planes seen over a period of 9 weeks

Object	material	z(cm)	x/X_0
Target	copper	-10.055	0.1119
Target	copper	-8.526	0.0710
Target	diamond	-7.085	0.0117
Target	diamond	-5.585	0.0117
Target	diamond	-4.085	0.0117
Int counter	silicon	-3.000	0.0048
Int counter	silicon	-2.500	0.0048
VX_SSD_1X	silicon	0.000	0.0032
VX_SSD_1Y	silicon	1.970	0.0032
VX_SSD_1U	silicon	4.476	0.0032
VX_SSD_1V	silicon	5.955	0.0032
VX_SSD_2X	silicon	9.000	0.0032
VX_SSD_2Y	silicon	10.476	0.0032
VX_SSD_2U	silicon	13.479	0.0032
VX_SSD_2V	silicon	14.955	0.0032
VX_MSD_1X	silicon	18.000	0.0032
VX_MSD_1Y	silicon	19.476	0.0032
VX_MSD_1U	silicon	22.479	0.0032
VX_MSD_1V	silicon	24.034	0.0032
VX_MSD_2X	silicon	26.921	0.0032
VX_MSD_2Y	silicon	28.476	0.0032
VX_MSD_2U	silicon	31.479	0.0032
VX_MSD_2V	silicon	33.193	0.0032
VX_MSD_3X	silicon	35.921	0.0032
VX_MSD_3V	silicon	37.476	0.0032
VX_MSD_3U	silicon	40.479	0.0032
VX_MSD_4X	silicon	42.034	0.0032

Table 4.4: Description of material associated with multiple scattering simulations.

Chapter 5

Hyperon mass resolution

Having evaluated the hardware performance of the vertex detector, we now investigate the impact of silicon detector resolution on physics quantities. For this, we reconstruct beam hyperon masses and relate errors in mass with errors in track measurements using silicon detectors. SELEX utilizes a charged hyperon beam(positive or negative) interacting with a set of targets for the purpose of charm production studies. The hyperon beam itself is derived by the interaction of a primary proton beam at 800GeV/c with a Be(or Cu) target.

5.1 Apparatus description

5.1.1 Hyperon beam

The primary beam is a beam of protons on a 30x0.2x0.1cm^3 Berylium target. The primary beam has an angular divergence of 0.33mrad full width at half maximum(FWHM), with a spot size of less than 1mm FWHM at the target. The charged secondary beam is defined by a curved tungsten channel[25] with a radius of curvature of 700m turning the secondary beam through 11mrad. The rectangular aperture of the channel varies along its length and is $0.6 \times 0.2cm^2$ at its downstream end. It narrows to an aperture about 1mm wide in the X view at its center. It is made of 350 blocks of tungsten, each

about 15cm long. The upstream end of the channel has the target nearby and also serves as a beam dump for the non interacting primary beam. The target and channel are both inside the field region of a 7.3m long magnet called the hyperon magnet. The layout is shown in Fig 5.1. The resulting secondary beam has a full width momentum spread of dp/p $=\pm 8\%$ and a solid angle of 0.5μsr. The momentum of the secondary beam can be changed by changing the magnetic field in the hyperon magnet. The transverse momentum of the secondaries is varied by changing the angle of the incident proton beam relative to that defined by the channel, using an angle-varying bend magnet system. The primary beam intensity can be varied, depending on experiment demands from 1×10^{10} to 1×10^{12} protons /cycle. This cycle(on-spill) is 20 sec long and occurs every minute. The spill has a moderate time structure($\approx$ 30% modulation) due to accelerator features.

5.1.2 Beam silicon

Within the PC4 experimental hall, the relevant detection apparatus layout is as shown in Fig 5.2. The beam silicon comprises eight planes of single sided silicon microstrip detectors with a 20μm pitch, and an active area of $2\times$ 2 cm^2. They are oriented so that there are 3 'X', 3 'Y' and 2 'U' views of an incoming beam track. They are placed between 2.5m to 4.0m from the exit of the hyperon magnet. These planes are read out using FSDAs in a setup almost identical to that of the vertex silicon readout. The hit efficiency of these planes is close to 99% and beam track segment reconstruction efficiency is better than 95%. This spectrometer defines the trajectory of the incoming hyperon. Extrapolating a beam track upstream through the hyperon magnet and having it originate in the hyperon target(of known position) yields the momentum of the beam track with a resolution better than 1%.

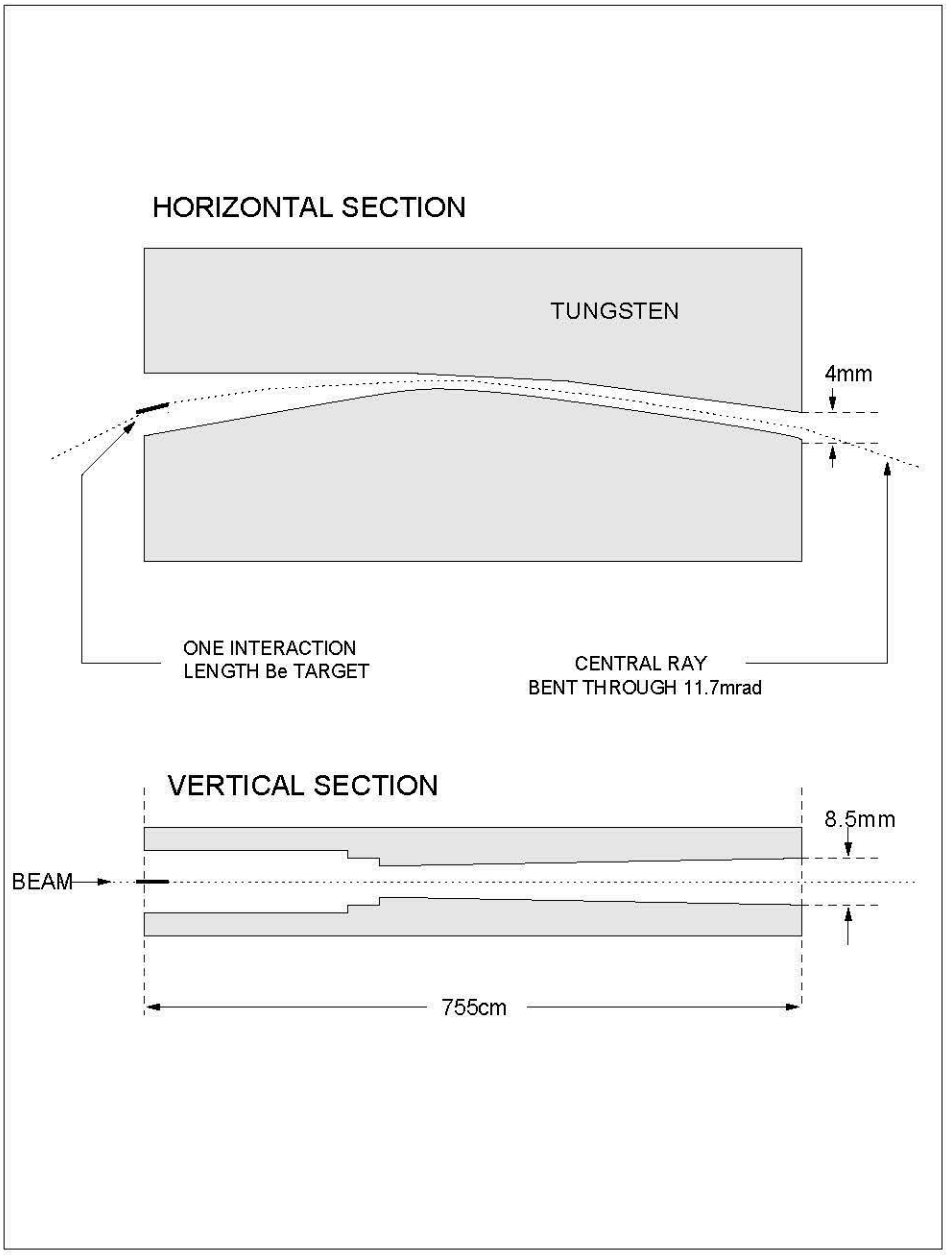

Figure 5.1: Hyperon target and momentum selecting tungsten channel and target

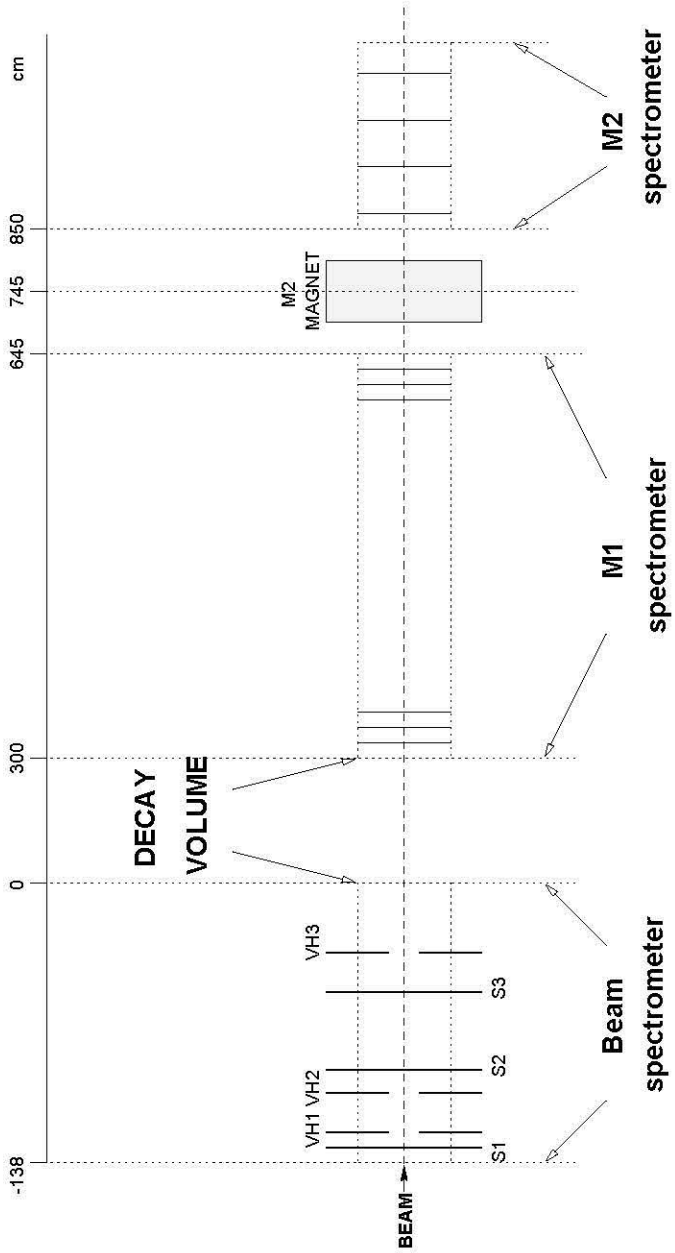

Figure 5.2: Layout of the detector apparatus(as relevant to hyperon reconstruction)

5.1.3 M1 magnet chambers

The M1 spectrometer chambers used are a set of large aperture single and double sided silicon strip detectors(LASDs). They are arranged in a set of two stations, each consisting of 2 "X", 2 "Y", a "U" and a "V" view. The first station is immediately downstream of the M1 magnet and the second station is just upstream of the M2 magnet. These planes have a 50μm strip pitch and are also read out using the FSDA readout system. The hit efficiency of these planes is about 97% with a track reconstruction efficiency of 94%.

5.1.4 M2 magnet chambers

The M2 magnet is about 7.5m from the experiment origin. The chambers used comprise one LASD station (similar to the ones used in the M1 spectrometer) and a set of 7 proportional wire chambers (PWCs) distributed into 4 'X', 4 'Y', 3 'U' and 3 'V' views. The strip pitch of the PWCs is 2mm and they have a hit efficiency of about 92% and a track reconstruction efficiency of 95%. These chambers have a gas mixture of 73% Ar, 27% Isobutane Argon, and 0.15% Fr13B1(freon) and are operated at a high voltage between 2750V and 2950V.

5.1.5 Analyzing Magnets

The relevant analyzing magnets in the experiment are denoted "Hyperon", "M1", and "M2" magnets. The bend planes of all these magnets are aligned so that the magnet bending is seen in only the experiment's X view. Table 5.1 lists the nominal(surveyed and/or from past experiments) characteristics of the magnets.(The origin is at the downstream face of the last charm target foil.)

Magnet	z of bend plane(cm)	current(A)	ptkick(T.m)
Hyperon	-755	3250	7.5750
M1	191	2200	0.7332
M2	745	2675	0.8421

Table 5.1: Analyzing magnet characteristics

5.1.6 Trigger

The "Beam" trigger is designed to select uninteracting hyperons(or pions) that go straight through the system. This trigger is derived from the "T0" level trigger and operates with information from the Beam Scintillators(S). These are a set of plastic scintillators with its active area in the beam. There is another set of "veto halo" scintillators(VH) which are large scintilltors with the active plastic cut out in the region defining the beam. All these scintillators are coupled to photomultiplier tubes. The raw beam trigger is formed by ANDing the signals from S_1,S_2,S_3,$\overline{VH_1}$, $\overline{VH_2}$, and $\overline{VH_3}$(Here, $\overline{V}$ stands for the inverted signal). It also accepts signals from the Beam Gate(In-spill/off-spill), Accelerator Radio Frequency and a test prompt from several test signals. T0 interacts with the Silicon Readout Sequencer to synchronize with the SVX clears and then produce a prescaled level 2 "T2" output which is the desired beam trigger. A normal spill lasting 20s produces about 80K triggers written to tape.

5.1.7 Incoming beam profiles

The Beam spectrometer is used to characterize the incoming beam phase space. This is shown in Fig 5.3 which shows the same beam position profiles when extrapolated back to the exit of the hyperon channel. The tungsten channel exit is evident as the sharp cutoff in beam position and it has the expected width of 0.4cm in X and 0.85cm in Y. As seen the beam is distributed quite symmetrically in the experiments XY coordinate system and has a divergence of less than 1mrad.

The momentum of these beam particles can be calculated using the bend plane approximation and knowing the hyperon magnet ptkick[1] and the hyperon target position(known to a surveyed precision of $\pm$1mm). Fig 5.4 shows the beam momentum profiles for negative and positive incoming beam particles. The highest positive beam momentum is typically 20% lower in the positive beam because of proton beam targeting angles limitations imposed by radiation safety. Using beam TRD detectors, a hyperon vs. pion identification can be made. There is no assymetry in beam phase space with respect to particle type.

5.2 Two-body hyperon decays

The typical dominant two-body hyperon decay has the topology shown in Fig 5.5. Typical hyperon decay lengths within the experiment's coordinate frame are 10-20m. The neutral secondary may decay immediately($\Sigma^+ \rightarrow p + \pi^o; \pi^o \rightarrow 2\gamma$), may live a few lifetimes longer than the parent($\Xi^- \rightarrow \Lambda + \pi^-; \Lambda \rightarrow p + \pi^-$) or not decay at all($\Sigma^+ \rightarrow n + \pi^+$)[26]. The secondary charged particle($\pi^\pm$,$K^\pm$,p) does not decay within the experimental apparatus. In general we would expect to see only one track through the experiment and the primary decay would be distinctly resolved as a kink within a suitable decay volume(shown in Fig 5.2). The Beam and M1 spectrometers are used to determine the two arms of the kink. The M2 spectrometer is used only to provide a momentum value for the charged daughter particle.

The choice of the decay volume in the experimental apparatus was made in order to obtain the best resolution possible. The silicon detectors are the most accurate position measuring devices in the experiment. The mass resolution is related to how well we can measure the trajectories of the incoming and outgoing particles. The Beam spectrometer and the M1 large aperture silicon planes provide good angular resolution(5-10μrad) by virtue

[1]In the small angle approximation, it is the bend angle produced by the field on a charged particle with unit momentum

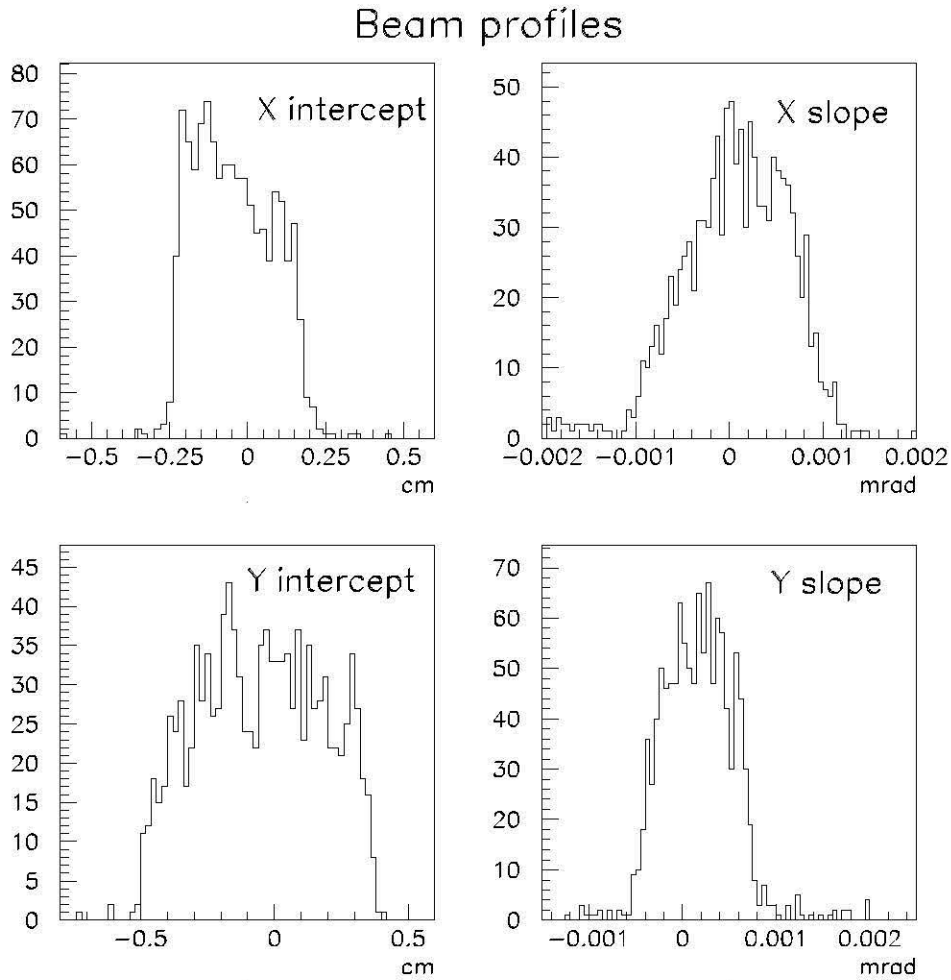

Figure 5.3: Beam phase space in X and Y views at the exit of the hyperon channel

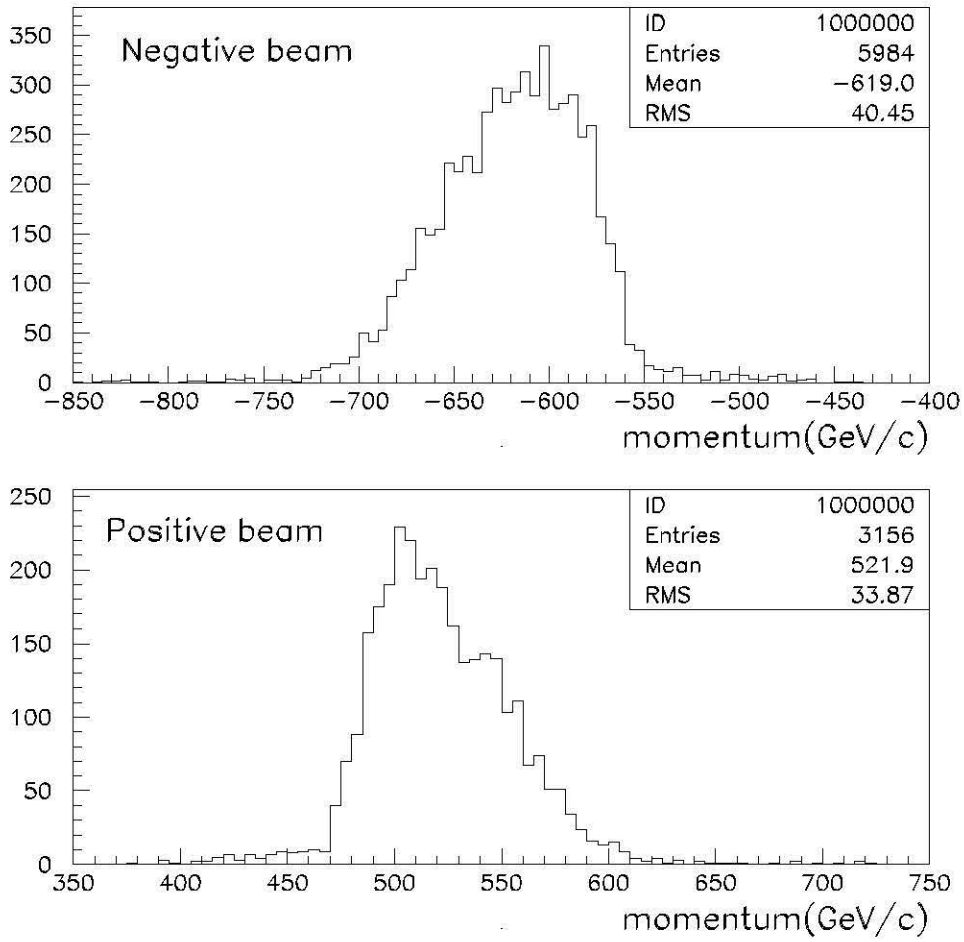

Figure 5.4: Beam momentum for positive and negative beam

of being 6μm measurements distributed over z distances exceeding a meter. The choice of Beam and M1 spectrometers to detect the 2 arms of the kink means that the kink can be reconstructed only in the 3m between the two spectrometers. The upstream 0.6m of this 3.0m space has the 20 vertex detectors and a 3mm wide scintillation counter. As the mass reconstruction is dependent on the instantaneous vectors at the decay point, any multiple scattering before and after the decay point will become important. Multiple scattering in the vertex+scintillator setup of the beam, is less than that for the secondary particle because of the higher momentum. Hence only the downstream 2.4m between the Beam and M1 spectrometers are included in the decay volume.

Other regions of the experimental apparatus could be used as the decay volume, but they all suffered from the lack of precision in some of the momentum and trajectory measurements. The 2.4m of selected decay volume had the best overall optimized measurement precisions.

5.2.1 Missing mass reconstruction

The reconstruction of a hyperon is based on the missing mass of the unobserved secondary daughter particle. The momentum vectors of the incoming parent hyperon and the outgoing secondary are measured using Beam, M1 and M2 spectrometers . Depending on the decay mode, an assumption of the identities(and hence rest masses) of the outgoing secondaries is hypothesized. Using conservation of momentum and energy in the decay, we have,

$$\overline{p}_{hyp} = \overline{p}_{charged} + \overline{p}_{neutral} \tag{5.1}$$

and

$$E_{hyperon} = E_{charged} + E_{neutral} \tag{5.2}$$

These equations are sufficient to calculate the rest mass of the hyperon. A correct assumption of the decay products will produce a plot which has a

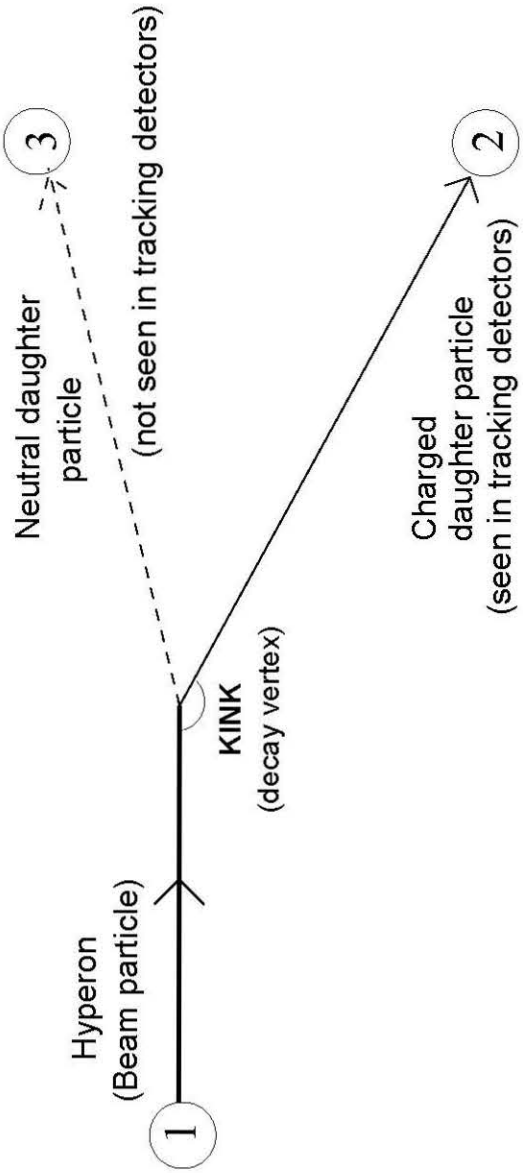

Figure 5.5: Typical dominant hyperon decay topology

reasonable width at the correct mass while a wrong assumption produces a broad "mass reflection" in the mass plot.

5.2.2 Tracking and reconstruction code

The tracking program is implemented within Selex Offline Analysis Package(SOAP). A least squares fit of a 3-dimensional track in each of the Beam, M1 and M2 spectrometers is made to a set of hits on individual planes. Each track segment found is reported as a 4 element vector containing X,Y slopes and intercepts. The hyperon reconstruction code requires at least one track segment be found in a spectrometer. It loops over combinations of found segments in the 3 spectrometers. For each combination, various decay modes are hypothesized and the hyperon mass plotted. All of the relevant parameters for each event are saved in a multiple field data structure referred to as ntuples. [2]

5.3 Reconstructed Hyperon decays

Fig 5.6, Fig 5.7, Fig 5.8, show the reconstructed mass plots for a few of the dominant hyperon decay modes. Table 5.2 lists the salient features of the reconstructed masses. Fig 5.9 shows the so called R-θ plot(kink angle versus secondary momentum fraction) in the positive beams. The two dominant decays of the Σ^+ are well separated in the product momentum space.

Using the mean lifetime of the Σ^+ at a mean momentum of 520GeV/c, the mean decay length is 1049.3cm. Fitting the z distribution of the observed decay points to an exponential function(Fig 5.10) we see a mean decay length of 935.5 $\pm$ 327.9 cm. As seen from the fit, the errors on this fit are large and sensitive to the region included in the fit. This is due to the limitation of fitting the exponential in a region which is small compared to its decay

[2] The ntuple is generated using PAW(Physics Analysis Workstation) and is in the form of a n$\times$n array. Each row is an event and each column is an attribute. Arithmetical and logical manipulations of the ntuple are possible.

length, with the available statistics. This is hardly a precise measurement of the Σ^+ lifetime but rather a check that the sample of decay events are consistent with the hypothesis that they are Σ^+ decays.

Rough estimates for the yields of identified hyperons are as seen in table 5.2.(Positive beam run 7237(+3mrad targeting angle) and negative beam run 5729(+2mrad targeting angle) were used.)

Decay mode	**triggers (K)**	**momentum (GeV/c)**	**Reconstructed events**	**mass width (MeV/c^2)**
$\Sigma^+ \rightarrow \pi^+ + \mathrm{n}$	883	520	1879±51	2.722±0.075
$\Sigma^+ \rightarrow \pi^o + \mathrm{p}$	883	520	706±40	5.962±0.25
$\Sigma^- \rightarrow \pi^- + \mathrm{n}$	655	-620	18092±691	3.128±0.43
$\Xi^- \rightarrow \pi^- + \Lambda$	655	-620	527±57	3.408±0.78

Table 5.2: Reconstructed hyperons

The $\Sigma^+ \rightarrow \pi^+ + \mathrm{n}$ and $\Sigma^+ \rightarrow \pi^o + \mathrm{p}$ have branching ratios of 48.31±0.3 % and 51.57±0.3 % respectively. The reconstructed data are seen to differ from these ratios. This is due to the difference in the relative acceptance of the spectrometer for the two modes. The heavier secondary particle(p) makes smaller kink angles which are harder to resolve in the spectrometer. Similarly, the smaller kink angle and secondary momentum fraction for the Ξ^- decay is different from that of the Σ^- decay, making the acceptances different. We cannot conclude relative production statistics simply from the numbers in the table above. Also, they are not a measure of the absolute production statistics as the reabsorption in the 30cm long target and other factors have not been taken into account.

5.3.1 Discussion of the mass resolution

Some cuts are applied to the data in the mass ntuples in order to produce the mass plots shown. They mostly help to suppress the background and comprise the following.

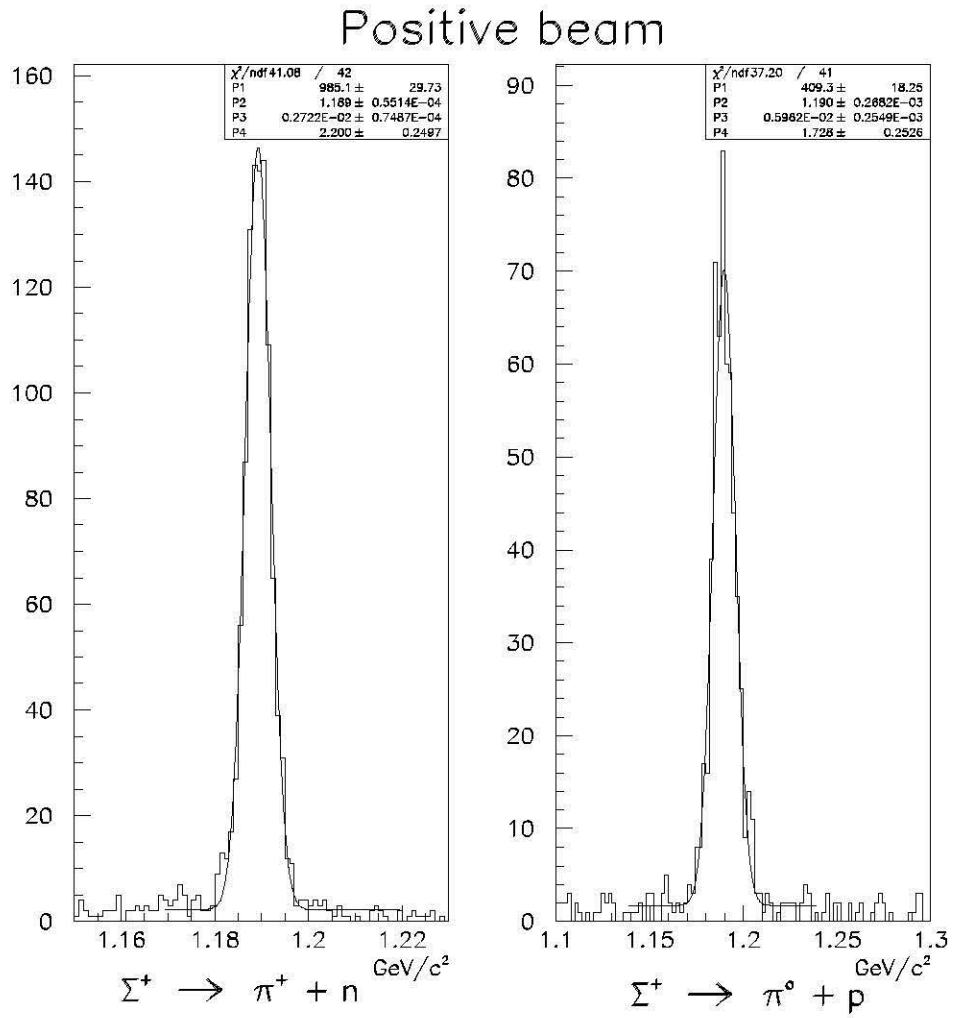

Figure 5.6: Σ^+ mass plots from positive beam data

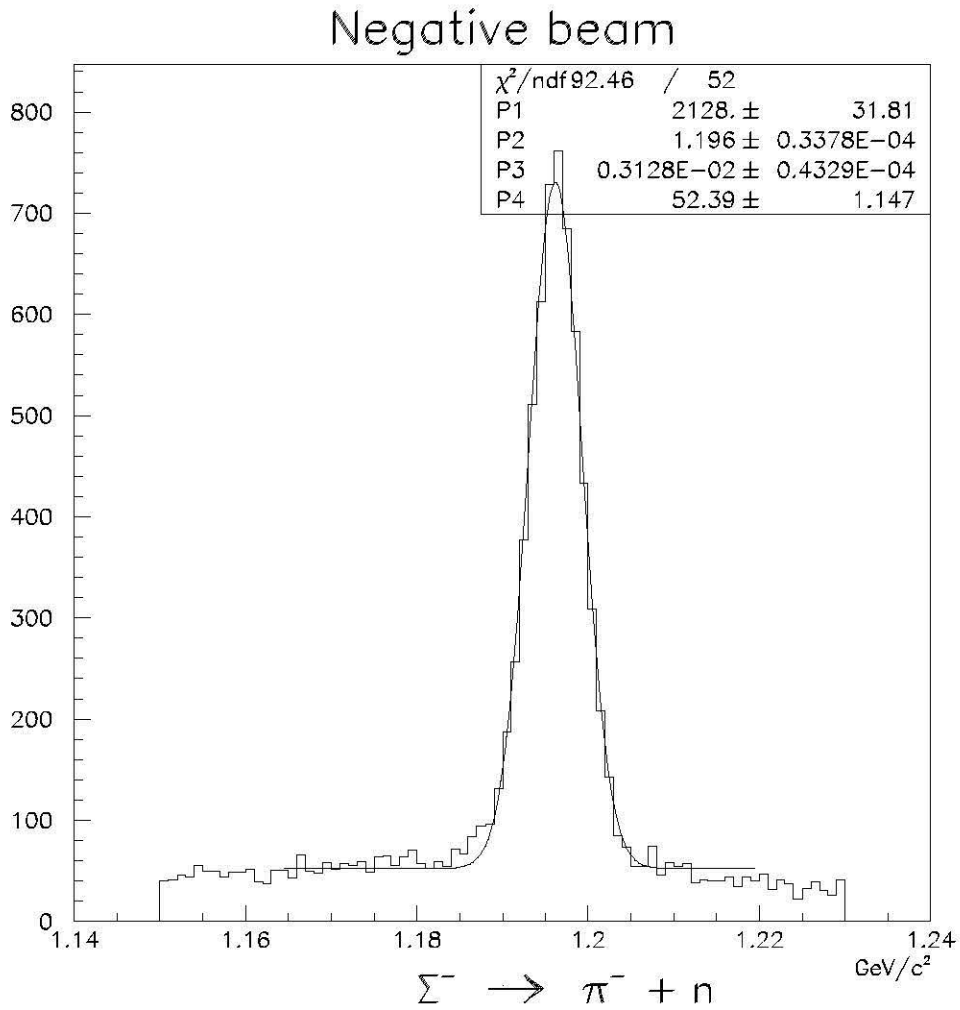

Figure 5.7: Σ^- mass plot from negative beam data

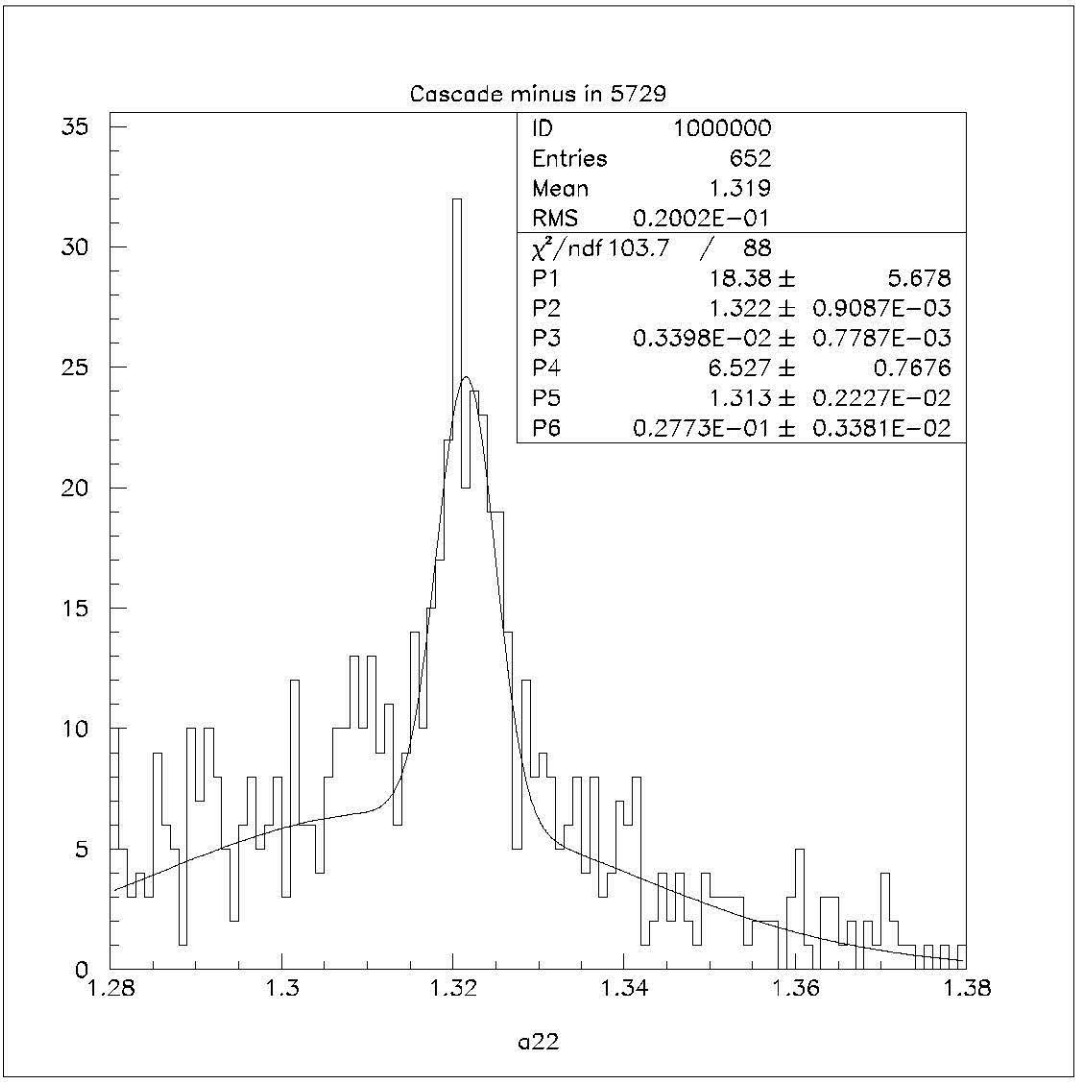

Figure 5.8: Ξ^- mass from the negative beam data ($\Xi^- \rightarrow \Lambda + \pi^-$)

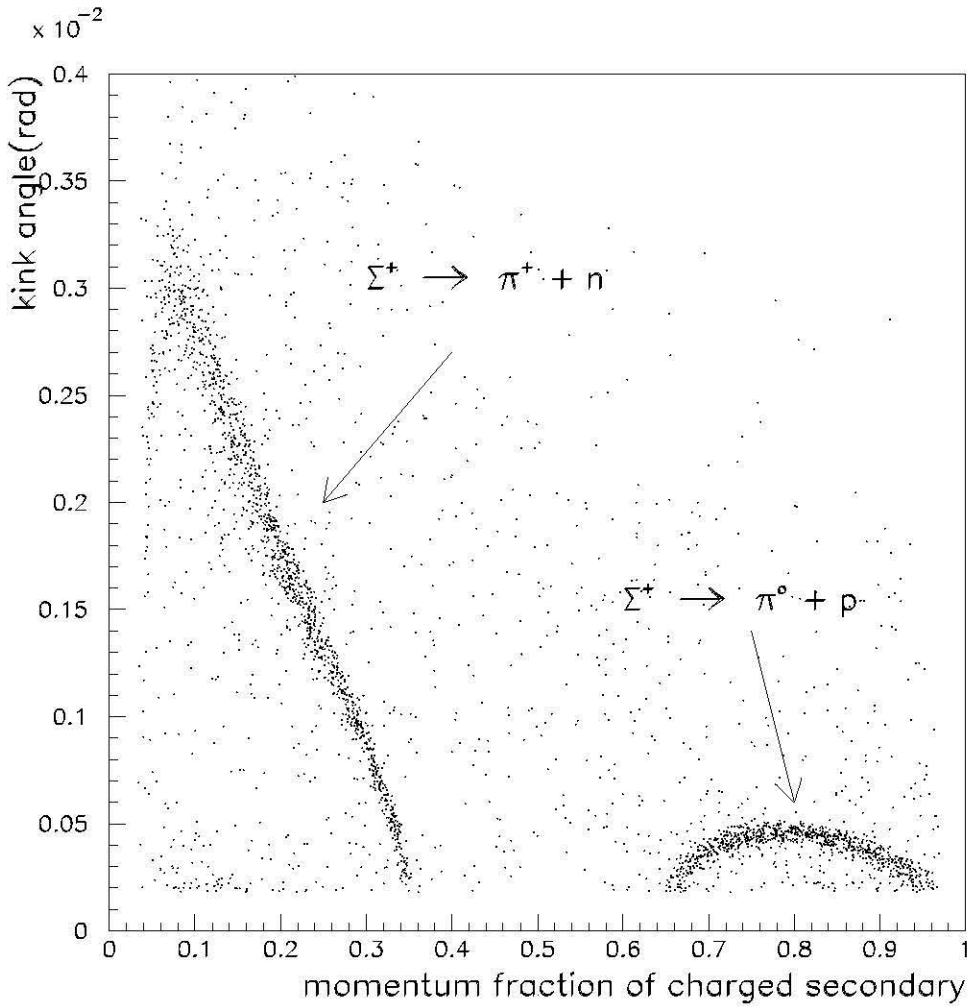

Figure 5.9: R-Θ plot for the positive hyperon reconstruction.(The angle of the kink at the hyperon decay plotted against the momentum fraction of the secondary daughter to the beam)

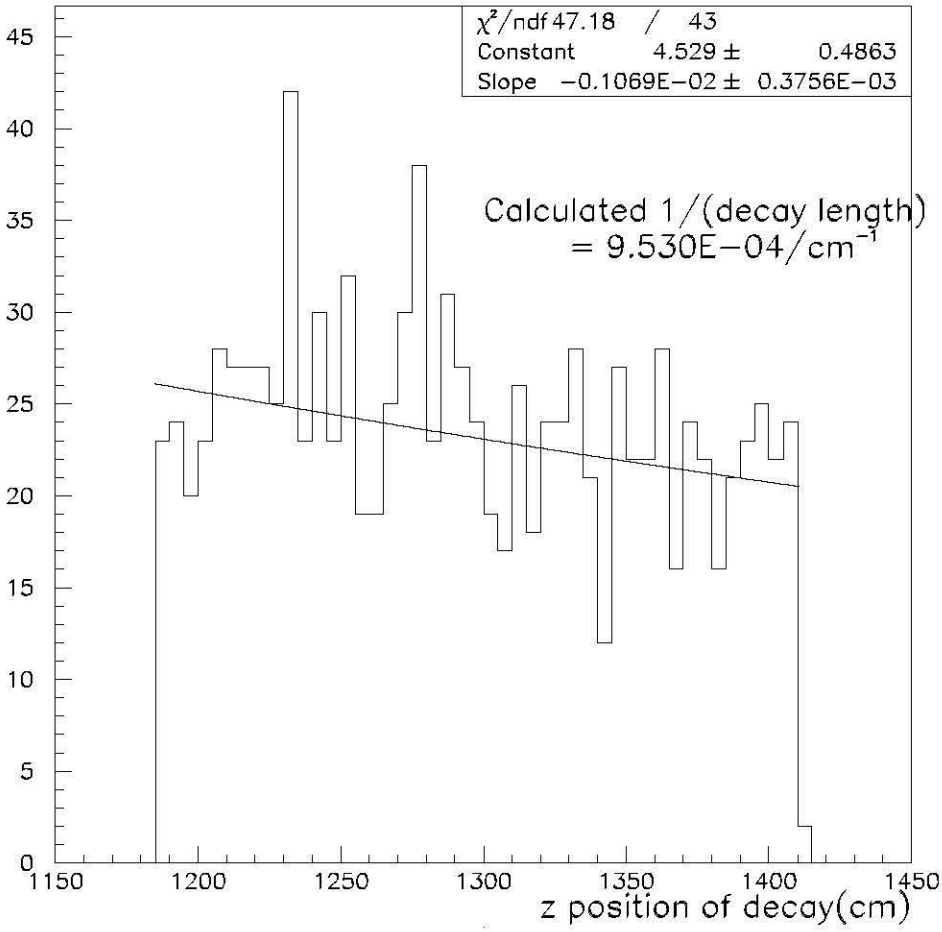

Figure 5.10: An exponential fit to the z distribution of the hyperon decay point. (The expected and observed decay lengths(1/slopes) are within one sigma)

- A kink angle cut of 90μrad. This eliminates events with low angle hyperon scatters.

- The kink position is restricted to the area downstream of the vertex silicon and just upstream of the first LASD station. Choosing a region with no material for multiple scattering improves the resolution.

- All the silicon detectors could integrate up to 3 beam track hits before a valid trigger. This is a feature of the trigger. Finding the beam track which caused the trigger reduces the combinatorial background. A 50μm pitch "hardware scatter" silicon detector[3] is read out with a time gate narrow enough to capture only the triggering beam particle. This plane is about 20 cm from the beam spectrometer and is utilized to find the "in time" track.

- A cut on the number of tracks seen in the downstream M2 spectrometer is imposed. There will generally be only one track from the charged daughter in M2.

The alignment of all the planes used in the system was a factor in improving the mass resolution. All silicon planes were aligned up to precision of better than 1μm using TRD tagged non-decaying pion beam tracks. This procedure removed systematic angular offsets between various detector subsystems. Care was also taken to do a slope-point momentum calculation of the track undergoing bending in the M2 magnetic field. Systematic uncertainties in the average positions of the hyperon target and all the magnet bend planes all primarily affected the mean value of the mass peak and not its width(to first order).

It is possible to estimate the error contributions arising from each of the factors that enter the mass calculation. To do this, we write down the expression for the squared mass of the hyperon as

[3]The "hardware scatter" trigger emplys a set of 6 50μm pitch silicon detectors to conduct a parasitic hyperon scattering experiment

$$m_1^2 = m_3^2 - m_2^2 + 2(E_1E_2 - \overline{p_1}.\overline{p_2}) \tag{5.3}$$

Since $E_i = \sqrt{|\overline{p_i}|^2 + m_i^2}$, under the approximation $|\overline{p_i}|^2 \gg m_i^2$, the above expression becomes

$$m_1^2 = m_3^2 - m_2^2 + 2(|\overline{p_1}||\overline{p_2}| - \overline{p_1}.\overline{p_2}) \tag{5.4}$$

where m_1,m_2,m_3 are the hyperon, charged daughter and neutral daughter particle rest masses, and $\overline{p_1}$, $\overline{p_2}$ are the hyperon and charged particle momentum vectors.

Denoting the angles made by the momentum vector in the x,y and z axes by $\theta_{x,yetc}$, we may rewrite eqn 5.3 as

$$m_1^2 = m_3^2 - m_2^2 + 2p_1p_2(1 - \frac{1 + \theta_{x_1}\theta_{x_2} + \theta_{y_1}\theta_{y_2}}{\sqrt{1 + \theta_{x_1}^2 + \theta_{y_1}^2}\sqrt{1 + \theta_{x_2}^2 + \theta_{y_2}^2}}) \tag{5.5}$$

Taking the partial derivatives of the squared mass with respect to each of the variables, we have

$$\frac{\partial m_1^2}{\partial p_1} = 2p_2(1 - \frac{1 + \theta_{x_1}\theta_{x_2} + \theta_{y_1}\theta_{y_2}}{n_1n_2}) \tag{5.6}$$

$$\frac{\partial m_1^2}{\partial p_2} = 2p_1(1 - \frac{1 + \theta_{x_1}\theta_{x_2} + \theta_{y_1}\theta_{y_2}}{n_1n_2}) \tag{5.7}$$

$$\frac{\partial m_1^2}{\partial \theta_{x_1}} = 2p_1p_2(\frac{\theta_{x_2}}{n_1n_2} - \frac{\theta_{x_1}}{n_1^3n_2}) \tag{5.8}$$

$$\frac{\partial m_1^2}{\partial \theta_{x_2}} = 2p_1p_2(\frac{\theta_{x_1}}{n_1n_2} - \frac{\theta_{x_2}}{n_2^3n_1}) \tag{5.9}$$

$$\frac{\partial m_1^2}{\partial \theta_{y_1}} = 2p_1p_2(\frac{\theta_{y_2}}{n_1n_2} - \frac{\theta_{y_1}}{n_1^3n_2}) \tag{5.10}$$

$$\frac{\partial m_1^2}{\partial \theta_{y_2}} = 2p_1p_2(\frac{\theta_{y_1}}{n_1n_2} - \frac{\theta_{y_2}}{n_2^3n_1}) \tag{5.11}$$

where $n_1 = \sqrt{1+\theta_{x_1}^2+\theta_{y_1}^2}$ and $n_2 = \sqrt{1+\theta_{x_2}^2+\theta_{y_2}^2}$

These quantities are also calculated and stored in the ntuple for real beam data. The contribution from each of these terms to the mass error is assumed to be independent of each other and the total error is given by

$$\sigma^2_{hyperon\ mass} = \sum_{i=all\ variables} \left(\frac{\partial m_1}{\partial x_i}\right)^2 \sigma^2_{x_i} \tag{5.12}$$

where we have used

$$\frac{\partial m_1}{\partial x_i} = \frac{1}{2m_1}\frac{\partial m_1^2}{\partial x_i} \tag{5.13}$$

The errors in the variables themselves may be listed as follows

- The beam momentum resolution is limited by the finite width(1mm) of the hyperon target. This results in a 0.75% error at a beam momentum of 550GeV/c.

- The outgoing daughter particle momentum resolution depends on the fractional angular resolution of the bend angle in the M2 magnet(i.e. $\Delta\theta/\theta = \Delta p/p$). At the current setting of the M2 magnet this resolution is a function of p_2^2.

- The incoming beam angular resolution depends on the resolution of the beam spectrometer. This is typically about 6-8 μrad.

- The outgoing daughter particles angular resolution is given by the sum of the M1 detectors angular resolution which is about 5μrad. Added to this is a 1/p like momentum dependent term(from multiple coulomb scattering in the upstream LASD stations). The errors are the same in both X and Y views.

Using these errors and the calculated partial derivatives, the width contribution to the hyperon mass from each of the momentum and angle variables is shown in Fig 5.11. The error is plotted against a ballistic variable, chosen to be the momentum of the daughter particle. Fig 5.12 shows the total calculated width of the hyperon mass and the observed width. Good agreement is

seen between the expected and observed errors. This indicates that we have an accurate($\approx$ 5%) quantitative estimation of silicon detector measurement errors which dominate the resolution of physics quantities like particle mass.

5.3.2 Embedded Monte Carlo

In order to investigate the effect of tracking algorithm efficiencies a "pseudo" Monte Carlo "embedding" approach was employed. Data from a beam run was first analyzed to select events with a well identified straight through beam track through all the spectrometers. Hits corresponding to this track were removed in software and a ray trace Monte-Carlo generated hyperon decay event was overlaid on it. This embedding was done purely in software and takes into account multiple coulomb scattering and detector hit efficiencies. The modified event was then reanalyzed to determine tracking code efficiencies and errors. This method has the advantage of retaining the realistic noise background. For each hyperon decay mode under study, 2000 ray-trace Monte Carlo events were embedded into a standard beam run and reanalyzed. Fig 5.13 shows mass plots from Monte-Carlo embedded data runs.

The software efficiencies and the mass widths found with the embedded MC data were consistent with the real data results seen in Table 5.2. This suggests that the MC model used is very reasonable.

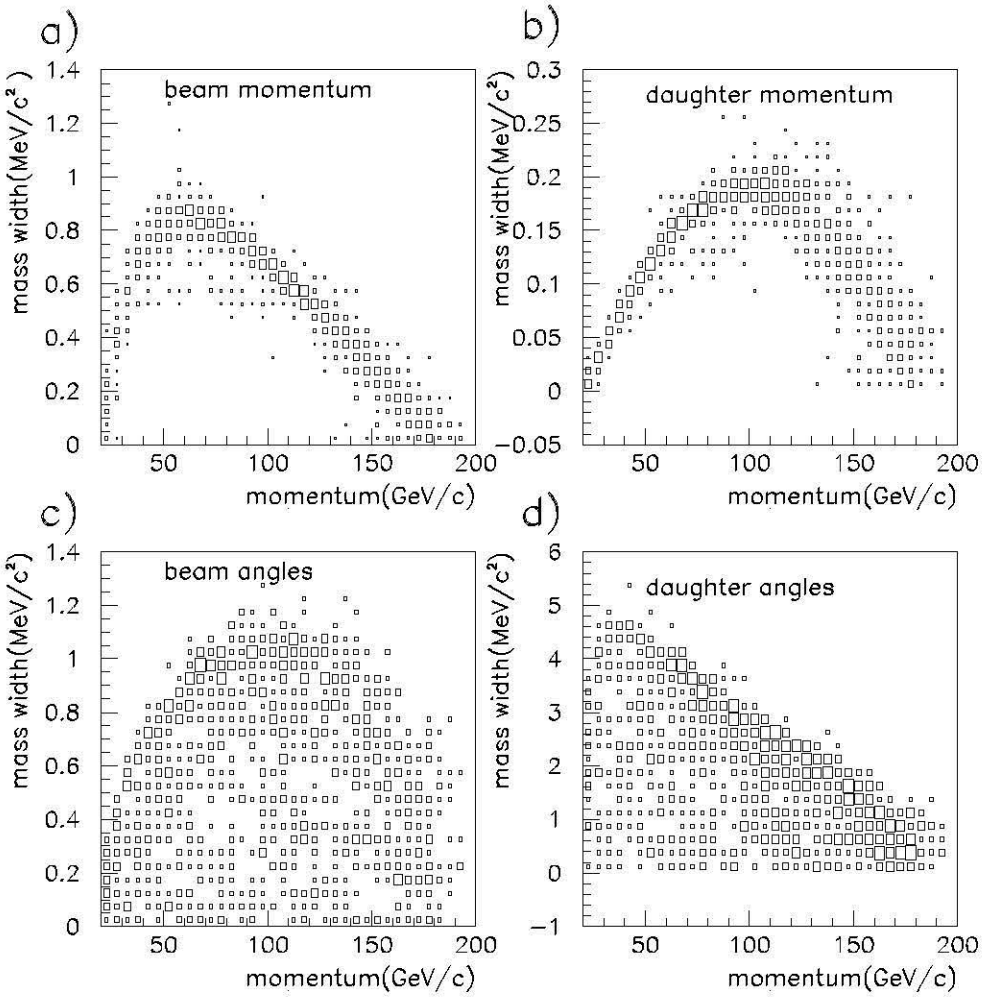

Figure 5.11: The contribution to the total hyperon mass width vs. the secondary momentum from a) The beam momentum magnitude, b)The secondary particle momentum, c) The beam angular resolution(in 3-D) d) The secondary particle angular resolution(in 3-D)

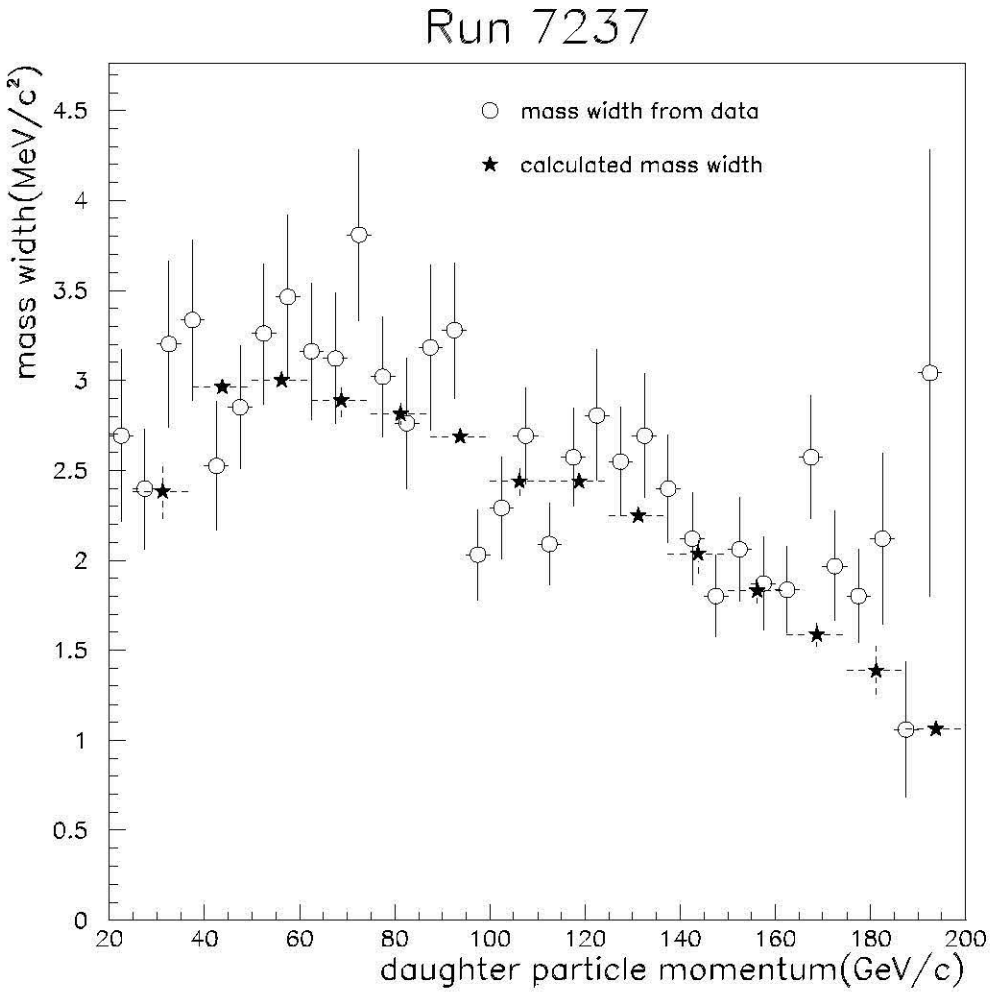

Figure 5.12: Comparision of the estimated mass width and the actual mass width seen in the data (both plotted against the secondary momentum)

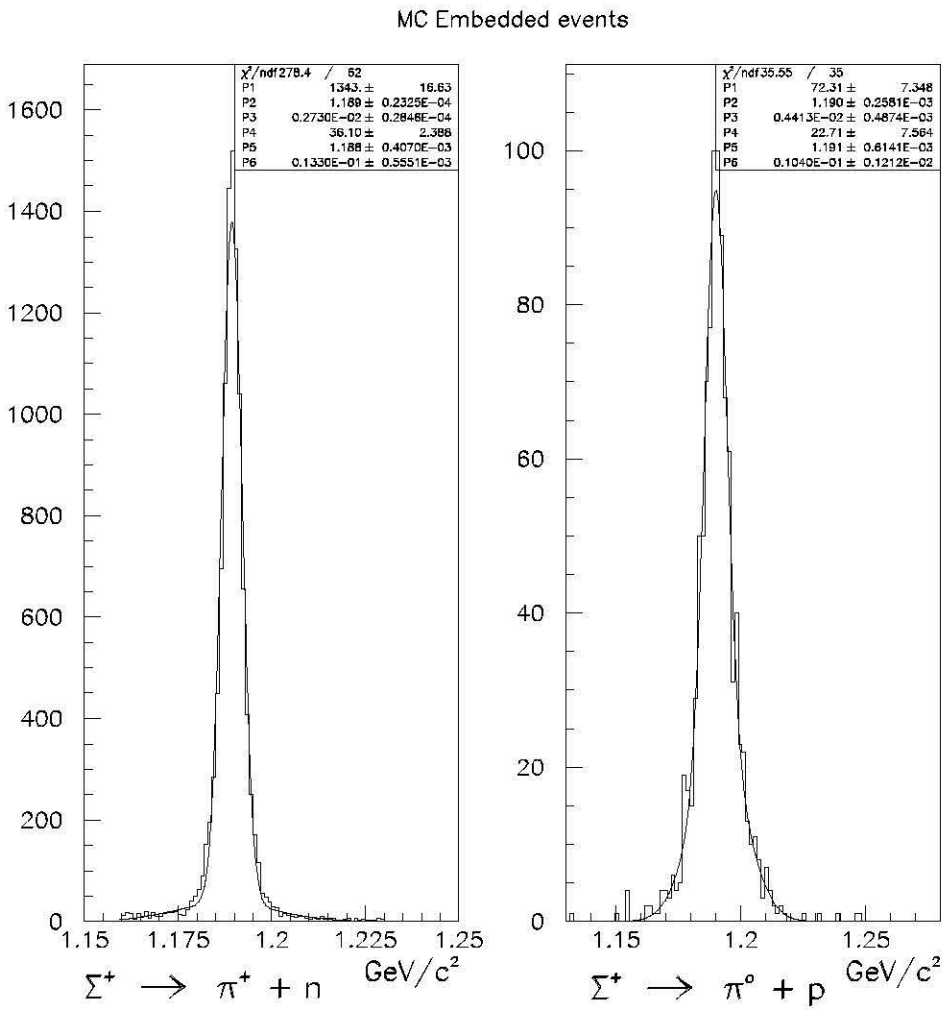

Figure 5.13: Monte-Carlo embedded data mass plots for the Σ^+ decay modes

Chapter 6

Vertex finding with the silicon vertex detector

6.1 Introduction

The silicon vertex detector is designed to resolve multiple-track primary and secondary vertices. So far we have seen how single beam tracks are resolved in the vertex spectrometer. We will now look into the problem of extrapolating multiple(1-7) vertex track segments and a beam segment to form a primary interaction vertex. The goal is to demonstrate that the vertexing resolution of the detector is as per design and that the errors are well understood.

The products of the primary interaction in one of the charm targets typically have much lower momenta(< 300GeV/c) than beam tracks. The effect of Multiple Coulomb Scattering(MCS) in the target and detector material is significant and must be corrected for. In sections 4.3 we have developed the MCS included track error matrix formulation which we shall make use of in the vertexing problem.

The vertex finding procedure is critical to SELEX because the online software filter utilizes it while trying to select charm events.

6.2 Silicon-M2 matched vertex segments

In trying to find individual track segments in the vertex detector, a brute force hit combination method is not used because it would take too long to be of use in the online filter. Instead, we resort to finding tracks by "matching" them to tracks in another spectrometer where they are found more easily. The SELEX apparatus has a RICH spectrometer about 15m downstream of the vertex detector and its particle ID is necessary for the charm analysis. A track which is seen by the RICH counter must make it past the M2 tracking spectrometer and hence the M2 spectrometer is the best candidate for finding the the set of tracks which can be matched into the vertex spectrometer. Low momentum tracks(<15GeV/c) do not make it past the M1 magnet and are neither seen in the M2 chambers nor in the RICH counter(they can be reconstructed in the vertex spectrometer during later offline analysis).

All the interaction and decay products with a momentum >15 GeV/c are expected to be seen in the downstream M2 spectrometer. These tracks are then assumed to originate from the midpoint of the segmented charm targets. Knowing the position and magnetic field of the M1 and M2 magnets in between, a momentum is assigned to these tracks. They are then extrapolated upstream into the vertex planes(after bending in M1 and M2 magnets) and each plane is searched for hits within a search window around the extrapolated track position. This search window is consistent with the detector and momentum dependent MCS errors. Once a set of hits corresponding to a track is found, they are then fit to a track within the vertex spectrometer. Depending on the charge ADC value of a hit, tracks may or may not share the same hit. As seen previously in section 4.3.3, the χ^2/dof[1] of the segment fit is quite independent of the momentum of the track. The overall χ^2/dof of typical interaction tracks is shown in Fig 6.1.

[1]dof refers to the degrees of freedom in the fit

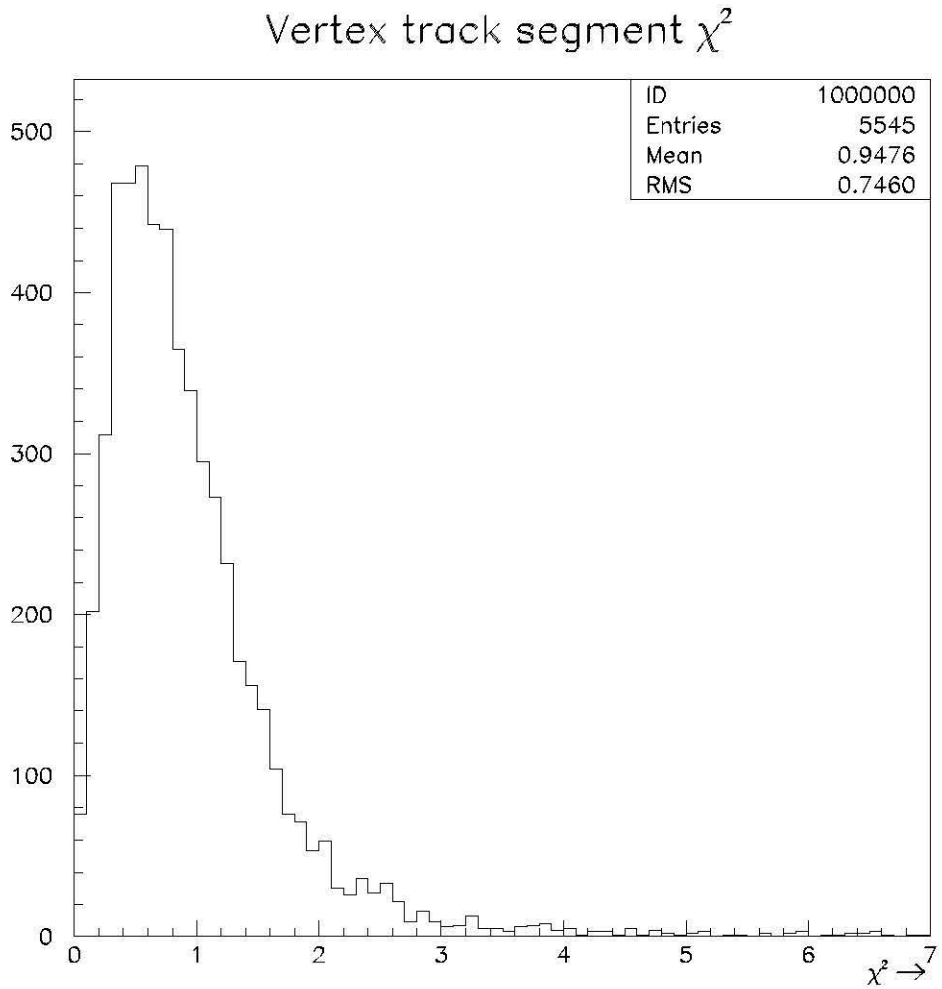

Figure 6.1: χ^2 for reconstructed vertex tracks

6.3 Vertexing algorithm

A layout of the vertexing region is shown in Fig 6.2. Hits in the individual vertex planes have been fit to separate tracks and now these tracks must be fit to a vertex. Barring hyperon decays, the z position of the vertex is expected to be in the region of interaction material i.e. the segmented targets. The interaction counters and the S4 scintillator may also produce interactions. Table 6.1 lists the properties of the material relevant to both interactions and multiple scattering. The vertex spectrometer design attempts to minimize the distance between the vertex and the center of gravity of the measured hits on the planes. This is done by putting the lower pitch 20μm planes as well as the whole detector as close as possible to the vertex point. Angular errors from multiple coulomb scattering are allowed as small a lever arm as is possible.

Object	**z position (cm)**	**thickness (cm)**	**% of rad length**	**% of int length**
Target 1(Cu)	-6.080	0.1600	0.1119	1.063
Target 2(Cu)	-4.551	0.1016	0.0710	0.675
Target 3(C)	-3.110	0.2200	0.0117	0.577
Target 4(C)	-1.610	0.2200	0.0117	0.577
Target 5(C)	-0.110	0.2200	0.0117	0.577
Int ctr 1(plastic)	2.500	0.200	0.0048	0.252
Int ctr 2(plastic)	2.800	0.200	0.0048	0.252

Table 6.1: Properties of the segmented charm targets and other scattering material

6.3.1 The general idea

The algorithm employs an iterative(Newton-Raphson)[27] method to converge to the vertex point in 3-D space. A vertex seed in 3-D is initially estimated and the requirement of χ^2 minimization(derivatives = 0) yields a set of corrections on the initial estimate. This process is successively repeated

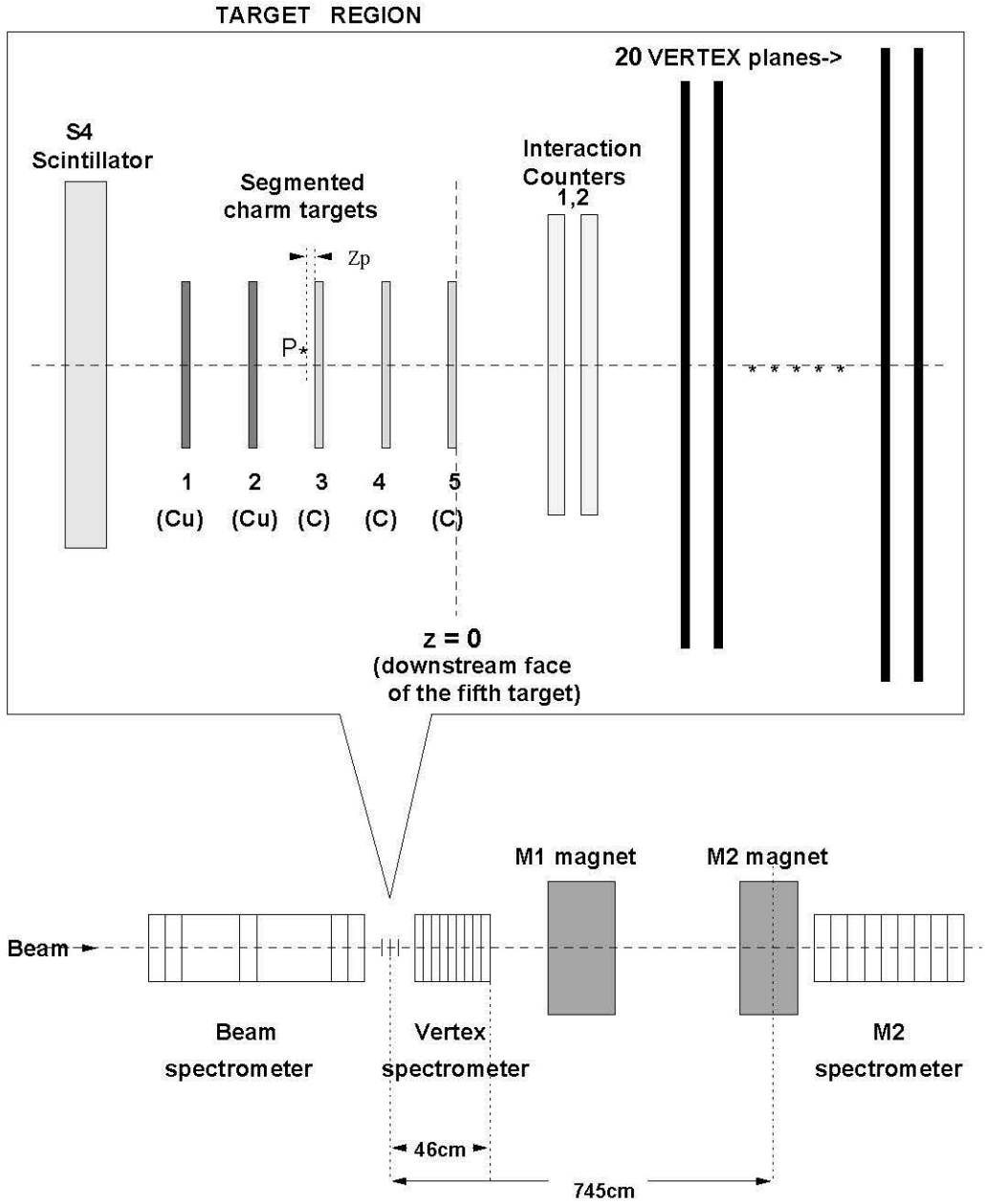

Figure 6.2: General layout of the apparatus appropriate to the charm vertex reconstruction. The target area is shown in greater detail(fig not to scale).

until the correction terms are less than 12.5% of the error in the method(i.e. the derivatives are sufficiently close to zero).

6.3.2 The initial seed vertex

Each vertex is required to contain one beam track segment. This is the track that presumably caused the interaction. The beam spectrometer may contain up to 2 more non interacting tracks because of the data memory feature of the readout. The choice of the "correct" beam track is made by finding the beam which was "in time" with a detector system(hardware scatter silicon) with a short time gate. Having decided on the beam track, the z positions of the Distance of Closest Approach(dca) of this track and all vertex tracks are computed. The most upstream z position of the distance of closest approach is selected. As the interaction is expected to happen in one of the segmented targets, the intial z position is chosen to lie at the center of the nearest target foil. The x and y positions of the initial vertex are the x and y coordinates of the beam track intersecting the selected z plane.

6.3.3 Track error matrix

As seen in section 4.3, we have prescribed a formulation to evaluate the momentum dependent track error matrix. This is a 4×4 error matrix(X,Y intercepts and slopes), complete with correlation between the different terms. The detector measurement error and the Multiple Coulomb Scattering in the individual vertex planes are accounted for. If we know the momentum of a track then we can describe its errors in terms of this error matrix. We need to extend this formulation into the region of the segmented targets because that is where the vertex is located. In a region without scattering centers, the error matrix can be propagated by a linear transformation. However when a scattering center. e.g. a charm target foil, is crossed then the error matrix has to be recalculated with the new material configuration. To do this we first write the n×n error matrix as in Eqns 4.5 and 4.6.

Any passive scattering object is included in as a correlation term.

$$E_{ij}^{MS} = E_{ij}^{MS} + \sum_{obj=first\ object,\ last\ object} \theta_{obj}^2 \times (z_i - z_{obj})(z_j - z_{obj}) \qquad (6.1)$$

We then proceed in the same manner as in section 4.3.1 and use the geometry and angular views of the system to realize the momentum dependent error matrix for tracks in orthogonal X and Y views. Since we are interested in tracks that form vertices at the position of the segmented targets, the track error matrices are evaluated at the center of each of the 5 targets separately. At each target, we include scattering from one half the thickness of that target and all the material downstream of it. This includes the interaction counters seen in Fig 6.2, as well.

6.3.4 Track errors and weights

Each track that makes up the fit to a vertex is not a perfectly measured line. Its transverse errors along its length are described by its error matrix. However we are interested in the transverse errors at a certain z position, namely the z position of the vertex. This can be derived by projecting the matrix on to a certain z position. This will fold both intercept and angular errors into spatial X and Y errors with correlations at the desired z.

For example, to find the transverse error matrix associated with the point P in fig 6.2, we take the 4×4 track error matrix corresponding to target 3. Then, the 2×2 transverse error matrix (E_{tr}) at the point z_p is given by

$$E_{tr} = \begin{pmatrix} 1 & z_p & 0 & 0 \\ 0 & 0 & 1 & z_p \end{pmatrix} \begin{pmatrix} e_{11} & e_{12} & e_{13} & e_{14} \\ e_{21} & e_{22} & e_{23} & e_{24} \\ e_{31} & e_{32} & e_{33} & e_{34} \\ e_{41} & e_{42} & e_{43} & e_{44} \end{pmatrix} \begin{pmatrix} 1 & 0 \\ z_p & 0 \\ 0 & 1 \\ 0 & z_p \end{pmatrix} \qquad (6.2)$$

We can define a "weight" matrix W_{tr} to be the inverse of the transverse error matrix, i.e.,

$$[W_{tr}] = [E_{tr}]^{-1} \qquad (6.3)$$

The transverse error and weight matrices are distinct for tracks with different momenta and at different z positions.

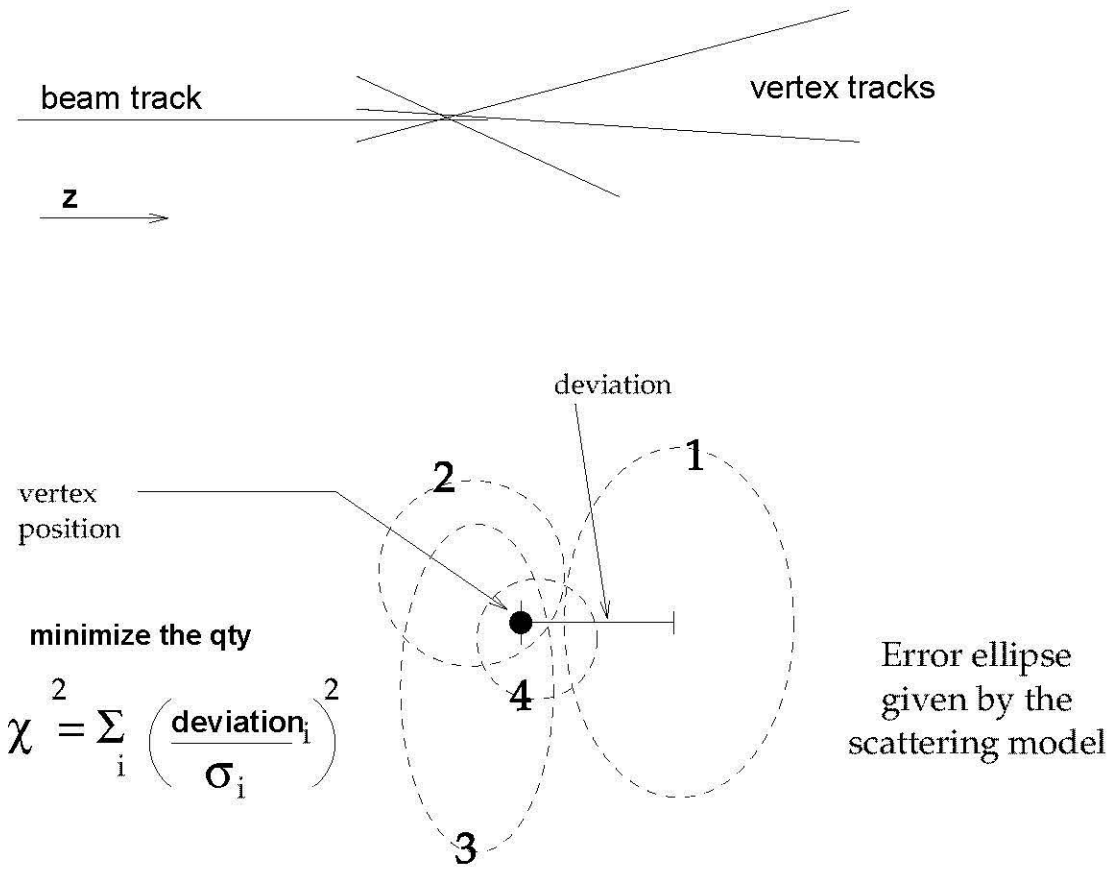

Figure 6.3: A transverse slice at a fixed z of the primary vertex region.

6.3.5 A definition of a vertex χ^2

We can also define a χ^2 quantity for the vertex fit. Shown in Fig 6.3 is the region near the primary interaction vertex. A standard χ^2 is given by the squared ratio of the deviation to a characteristic error. In this case, we choose the deviation to be the perpendicular distance of the fitted vertex point to the track. The characteristic error is given by the error(weight) matrix. The total χ^2 is obtained by summing over all the tracks.

In forming the χ^2, we need the shortest distance from the vertex point to track line. As all the vertex tracks make an angle of no more than 30mrad

with the z axis(average = 7mrad), we approximate the shortest distance with the transverse distance at a particular z. The deviation from the true distance in this approximation is of the order of a $\sin(\theta)$ factor where θ is the angle of the track w.r.t. the z axis. This is an error of about 1% which is smaller than other errors(measurement etc) in the system. In this approximation, with the X and Y views correlated, the χ^2 is given by,

$$\chi^2_{track} = [\delta x \delta y] \begin{bmatrix} W_{xx} & W_{xy} \\ W_{xy} & W_{yy} \end{bmatrix} \begin{bmatrix} \delta x \\ \delta y \end{bmatrix} \tag{6.4}$$

$$= W_{xx}\delta_x^2 + 2 \times W_{xy}\delta_x\delta_y + W_{yy}\delta_y^2 \tag{6.5}$$

6.3.6 Successive iteration to find the vertex

The property of any general "best fit"(at $\overline{V} = (X_V, Y_V, Z_V)$), is that the χ^2 quantity is minimized w.r.t. the vertex variables $\overline{v} = (x_v, y_v, z_v)$ i.e.,

$$\frac{\partial \chi^2(\overline{v})}{\partial \overline{v}} = 0 \qquad (at\ \overline{v} = \overline{V}) \tag{6.6}$$

We can also form a Taylor series expansion of the first derivative of χ^2, up to the first order(linear expansion), as

$$\frac{\partial \chi^2}{\partial v_i} = \frac{\partial \chi^2(\overline{v}_{n-1})}{\partial v_i} + \sum_j \frac{\partial}{\partial v_j} \frac{\partial \chi^2(\overline{v}_{n-1})}{\partial v_i} (\overline{v_n} - \overline{v_{n-1}}) \tag{6.7}$$

From equations 6.6 and 6.7, each successive iteration yields a correction term

$$(\overline{v_n} - \overline{v_{n-1}})_n = -\frac{\partial}{\partial v_i} \frac{\partial \chi^2(\overline{v}_{n-1})}{\partial v_j} \frac{\partial \chi^2(\overline{v}_{n-1})}{\partial v_j} \tag{6.8}$$

As a practical matter, the first and second vector derivatives w.r.t. the vertex location are evaluated at the point from a previous iteration. Using these values in the matrix equation 6.6, we obtain a set of corrections with which we modify the current vertex estimate. This procedure is then repeated until the desired precision. The error matrix for the corrections themselves

are given by E = $(\frac{1}{2}R)^{-1}$ where

$$R_{ij} = \frac{\partial^2 \chi^2}{\partial v_i \partial v_j} \tag{6.9}$$

The z error on the correction is given by $\sqrt{E_{3,3}}$ and when the z correction for a particular iteration exceeds 12.5% this value, the procedure is deemed to have converged and then stopped.

6.3.7 Vertex refining using χ^2 criterion

This is a good place to put the purpose of the vertexing routine in perspective. The goal of SELEX is to identify weak decays from charm baryons produced in the primary interaction at a target. Under this topology, an interesting event is one in which most of the tracks fit to a primary vertex and some of them miss it. Tracks that miss the primary vertex may be due to interesting charm decay products but may also include scattered and mis-measured tracks. Forming the χ^2 of the track is a way of quantifying the degree of association with a primary vertex. Based on the χ^2, a choice to include or exclude the track in the vertex may be made. The vertex is first fit with the identified beam track and all the available vertex track segments, at the center of the selected target. The algorithm requires that the χ^2 contribution of each of the tracks be below a certain cut(3σ like criterion). After the first iterative fit of a vertex, tracks with high χ^2 contributions(above 22.0) are pruned from the track list. The remaining tracks are then refit(iteratively) to a vertex and once again pruned of tracks with χ^2s above 11.5. This vertex fit χ^2/dof is also required to be below 10.0. Table 6.2 summarizes the upper bound χ^2 selection criterion used.

criterion	χ^2
Track χ^2 after 1st pass	22.0
Track χ^2 after 2nd pass	11.5
Track χ^2 after 3rd pass	10.0

Table 6.2: Criterion used to select the vertex

6.4 Vertex chi squares and the definition of an outlier

10K interaction data events were processed by the vertex finding routine. The track multiplicity distribution, the total χ^2/dof, the χ^2/dof at each target and the reconstructed z position of the vertex are shown in Fig 6.4 shows the observed χ^2/dof for all the reconstruced vertices. The track multiplicity distribution, χ^2/dof at each target and the reconstructed z position of the vertex are seen in Fig 6.5.

The purpose behind finding a good primary vertex is to be able to define an outlier which is an indication of a secondary decay(a secondary decay track extrapolated to the primary vertex z will miss it). There are a number of "tests of an outlier" that may be applied to identify a track that does not belong to the vertex. One such test is Chauvenet's criterion[29] which says that data that are so far from the mean (as judged by the sample standard deviation) that one would expect less than 1/2 an occurence in the whole experiment, are to be rejected. This is not a hard and fast rule and we may modify this criterion into χ^2 space to exclude events tracks with a χ^2 contribution >11.5(> 3.4σ away). The χ^2 contribution from each track forming a vertex will have two degrees of freedom. In Fig 6.6 we plot a normal a χ^2 distribution with two degrees of freedom and observe that events with $\chi^2 > 11.5$ are only 0.31% of the total number of events. We consider this background small enough to be acceptable. This is a reasonable criterion to define an outlier. The presence of such an outlier in real data makes the event of interest(possible charm decay) and hence will be selected to be stored on

tape by the online filter.

6.5 Vertex reconstruction from embedded events

As discussed in section 5.3.2, embedding is the procedure by which we can artificially implant a ray trace Monte Carlo event into a real data event. For the purposes of verifying the vertex finding code, a ray trace Monte Carlo event with 5 tracks(4 vertex tracks + 1 beam) was first generated. Next a beam trigger data file was chosen and analyzed to find the beam track. The ray trace Monte Carlo event was then attached to the original beam track(with the appropriate rotations to conserve p_T), at one of the targets. Downstream hits from the original beam track were removed. Hits corresponding to multiple Coulomb scattered trajectories of the embedded vertex tracks and convolved with observed detector efficiencies, were put into the hit bank. The event was then reanalyzed to find the multiple track "interaction" vertex. Interaction tracks with the parameters found in Table 6.3 were embedded into a standard beam triggered data file. The χ^2/dof for the vertex is shown in Fig 6.7. A plot of χ^2/dof versus vertex z position and the z distribution of the reconstructed vertices is shown in Fig 6.8. The efficiency of finding a vertex was 99.4% with the vertex being found at the correct target foil(as embedded) in 95.9% of these cases. 66.5% of the vertices reported back all the 4 embedded tracks and 26.1% had one missing vertex track. This is consistent with what we know about the M2 and vertex matching efficiencies. The M2 spectrometer has an track finding efficiency of 91.6% and after the matching routine is executed, 90.5% of the tracks survive. The probability of 4/4 surviving tracks is then 0.905^4=0.67, which is about what we observe in the reconstruction.

Conclusions from this exercise have to be drawn carefully. The χ^2 criterion compares the observed deviations with the expected errors. The observed deviations are based on a plane by plane random multiple scattering which we have simulated through embedding. The expected errors are cal-

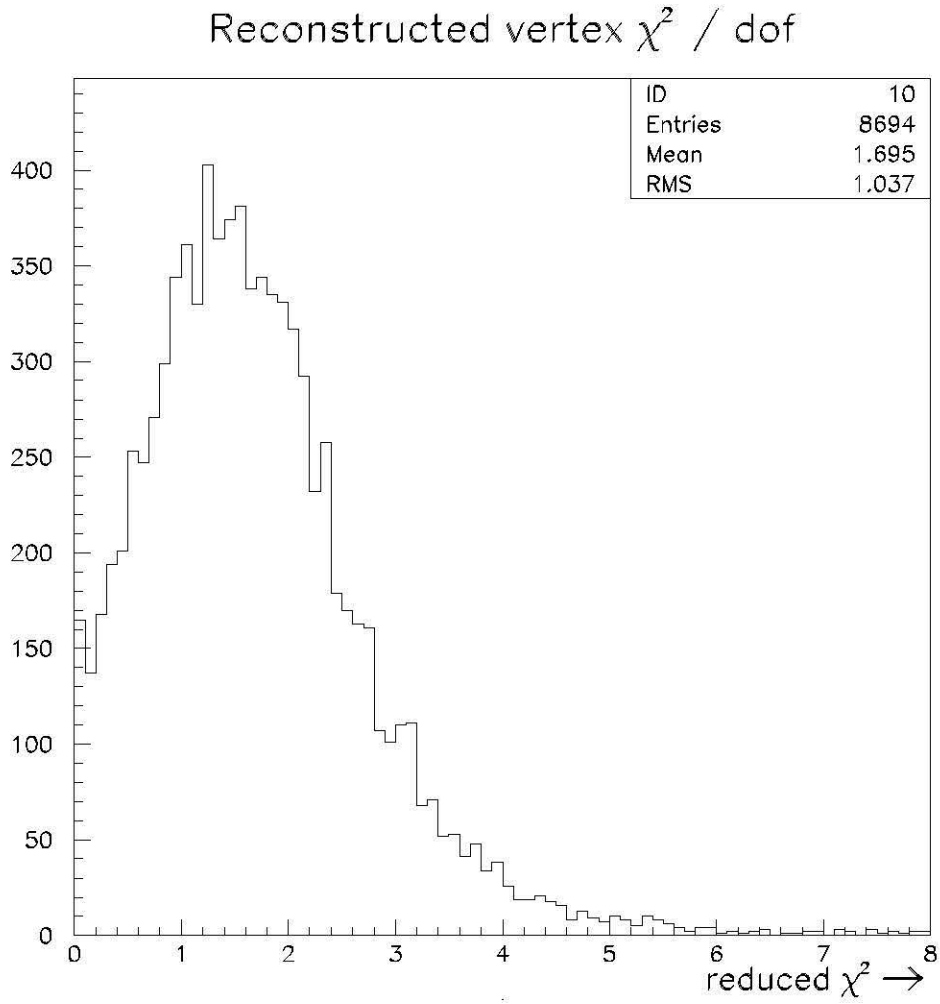

Figure 6.4: Overall χ^2/dof for vertex reconstructed data.

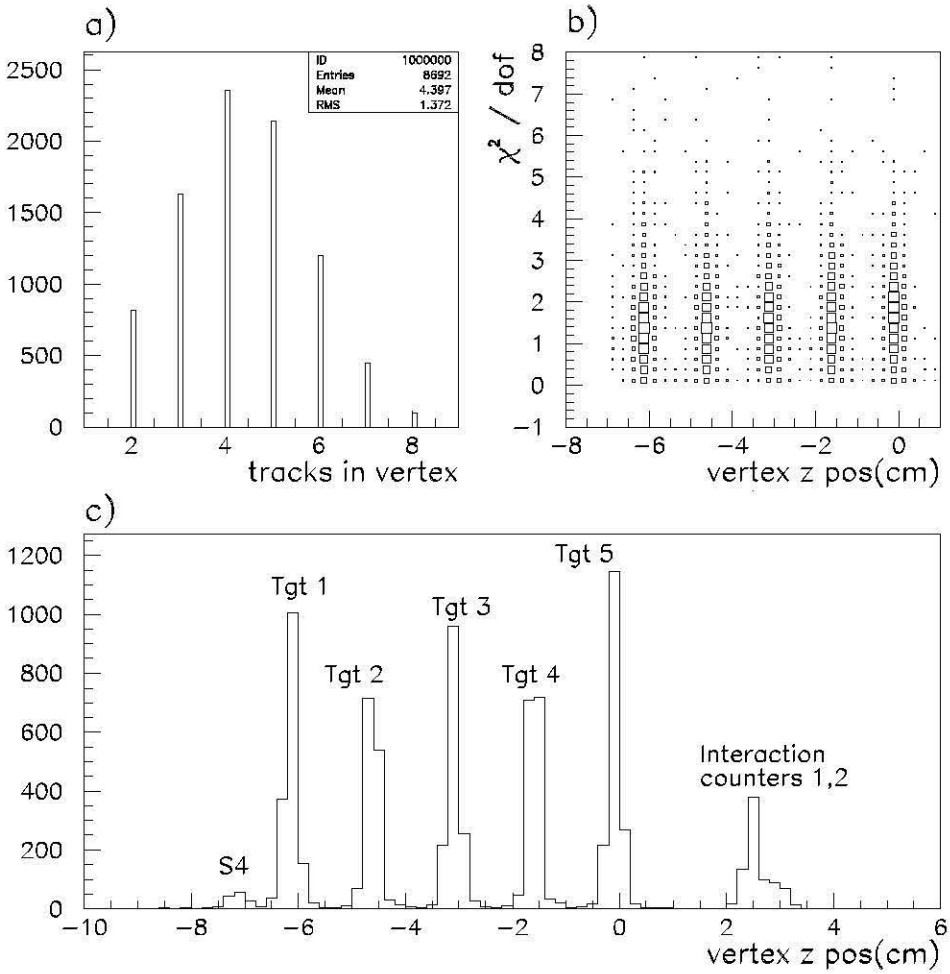

Figure 6.5: a)track multiplicity distribution, b)χ^2/dof versus vertex z position, and c) the reconstructed z position of the vertex for the interaction data

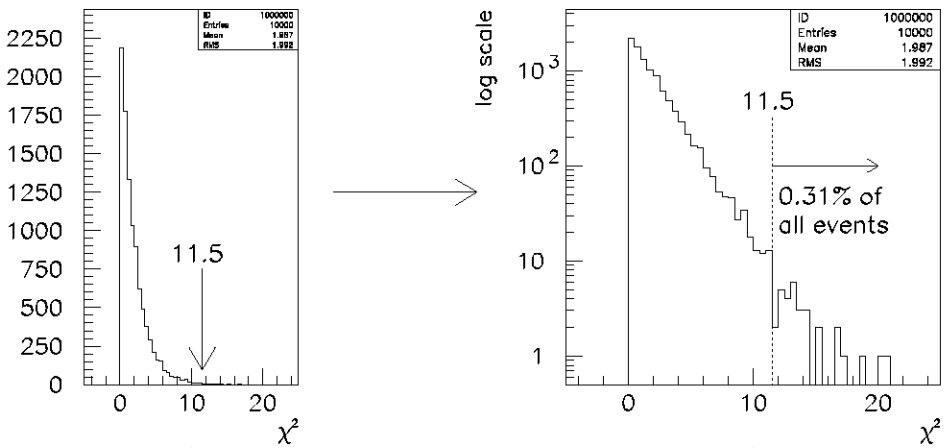

Figure 6.6: Illustration of a "modified" Chauvenet's criterion. Occurences with $\chi^2 > 11.5$ in a 2-dof distribution are considered outliers.

Track number	**X slope (cm)**	**Y slope (mrad)**	**momentum (GeV/c)**
1	0.00418	-0.00150	185.07
2	0.01565	-0.00590	63.94
3	-0.00188	0.00083	121.11
4	0.00183	0.00347	115.07

Table 6.3: Embedded vertex track characteristics

culated from the error matrix formulation which is also based on the same multiple scattering model. Both the numerator and denominator in the χ^2 term are in essence based on the same model. That they are comparable(the χ^2/dof is about unity) means that mechanical details of our vertex finding algorithm and embedding routines are correct(we have not made silly mistakes by factors of 2 etc.). This is not a proof that the model itself is correct.

The accuracy of the model can be gauged only by analyzing real data.

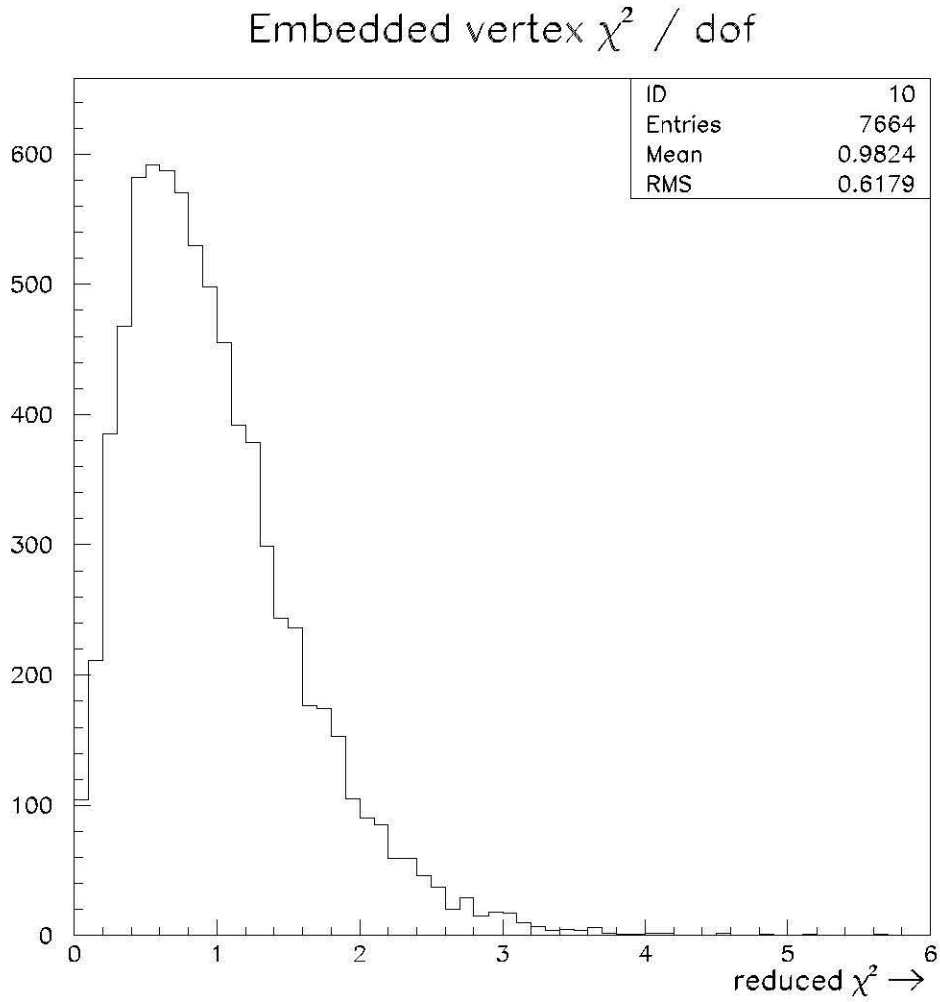

Figure 6.7: Overall χ^2/dof in reconstructed embedded data.

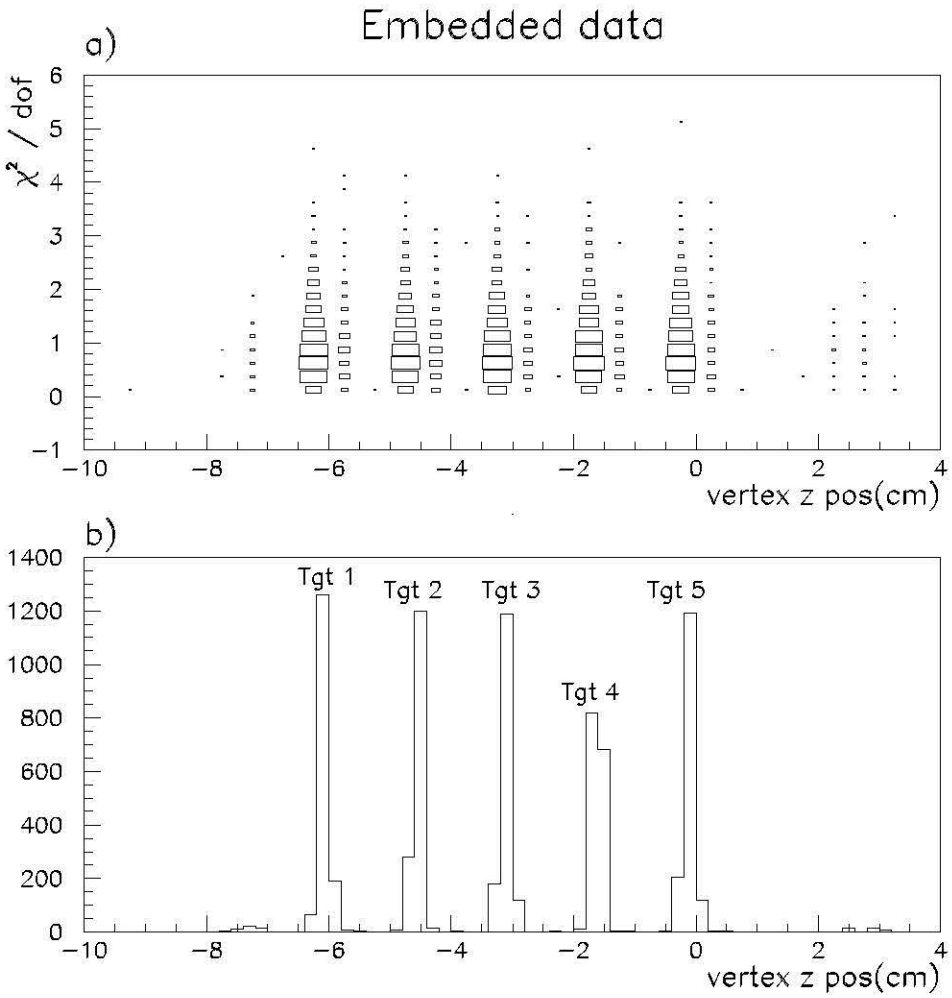

Figure 6.8: a) χ^2/dof versus vertex z position and b) reconstructed vertex z position in embedded data.

6.6 Discussion of χ^2 in real data

The previous section on the exercise of embedding Monte Carlo data revealed a consistent picture of our simulation and reconstruction models. However this simulated system differs from real data in many ways. For example, embedding assumes a perfectly aligned system while in real life there may be alignment errors. Moreover the detailed noise background for embedded and real data is different. In order to explain the observed deviation of the mean χ^2/dof from unity, a number of variables and procedures were checked. The following discussion summarizes the method and conclusions from these checks.

6.6.1 Detector and target alignments

The actual z positions of the 20 vertex planes were derived by using an iterative procedure as described in section 4.2.5. The precision on this method was about 100μm while the detectors themselves are 300μm thick. The transverse detector alignments are done with respect to a straight line passing through 2 chosen points in space. One of these points is defined by the centers of a pair of orthogonal beam silicon detectors and the other by a pair of vertex silicon detectors. A check of this transverse alignment was done by extrapolating beam track segments into the vertex planes and observing the mean of the residuals. The means did not exceed 4.0μm on any plane and showed no particular pattern. As an extended precision alignment, these new offsets were also loaded into the alignment table and the next iteration showed deviations of the mean residuals by less than 1.0μm. The beam system was also internally aligned to better than 1.0μm precision and checked. The reduced vertexing χ^2 for the standard system alignment was 1.690 and the more precise alignment showed a χ^2/dof of 1.691. This shows that the system is well aligned and the vertexing χ^2 is not particularly sensitive to the alignments.

It was also checked that the axes of the Beam and Vertex spectrometers

were colinear. To confirm this, offsets in the transverse position and angles were introduced and the χ^2/dof computed for the same sample of data. Table 6.4 and Table 6.5 summarize the results of scanning over systematic offsets.

ΔX (μm)\ ΔY (μm)	-6	-3	0	3	6
-6	1.95	1.84	1.84	1.79	1.84
-3	1.86	1.76	1.74	1.72	1.78
0	1.83	1.74	1.69	1.71	1.78
3	1.86	1.76	1.71	1.75	1.83
6	1.93	1.84	1.83	1.84	1.92

Table 6.4: χ^2/dof dependence on transverse BM-VX system alignment offsets

ΔX (μrad)\ ΔY (μrad)	-100	0	100
-100	1.78	1.74	1.77
0	1.74	1.69	1.73
100	1.77	1.73	1.78

Table 6.5: χ^2/dof dependence on BM-VX system angular alignment offsets

The alignments of the segmented target positions were also checked. The reconstruction code uses the target positions as surveyed. To verify the actual positions of the targets, the z positions of the reconstructed vertices were plotted. The mean positions of the targets deviated from the surveyed positions by less than 0.05cm as seen in Table 6.6. Using the new target positions in the reconstruction code, the χ^2/dof was found to be 1.683. This shows that the χ^2/dof is quite insensitive to greater alignment precision than that which already exists.

The momentum of the tracks that are being fit are calculated by assuming that downstream tracks have bent through the magnets and begin at the center of the target stack. The maximum momentum estimation error possible(and observed) in this method is $< 5\%$. This rules out any incorrect momentum assignment as the cause for the larger reduced χ^2.

target #	surveyed pos(cm)	calculated pos(cm)
1	-6.080	-6.1185 ±0.0015
2	-4.550	-4.5992 ±0.0014
3	-3.110	-3.0952 ±0.0015
4	-1.610	-1.6053 ±0.0015
5	-0.110	-0.0996 ±0.0013

Table 6.6: Segmented target positions as surveyed and calculated from vertexing

6.6.2 Vertex plane combinations and track fitting

As described in Chapter 3, there are 20 vertex planes distributed into 5 groups(monument blocks). The 4 detectors on the first 4 groups are laid out in identical X, Y, U and V views, while the last group has its 4 detectors in X or almost all X views. In the online vertexing code it is somewhat simpler to loop over similar arrangements of views and so only the first 16 planes are used in the fit to determine vertex track segments. Besides, the system with 20 planes is quite redundant and data from all planes can be used in offline code.

In order to check the fitted vertex segments, we can extrapolate them into the last four detectors and plot the residuals. These are seen in Fig 6.9. The residuals have the expected mean position and width for this set of tracks with varying momenta. The efficiency of finding a hit within two strips from the expected position is 99%. This shows that the tracks found using the first 16 planes are quite real and are confirmed by corresponding hits in the last 4 planes.

It is also possible to remove detectors from the list used to fit the vertex track segments. This is readily done in groups of 4. Table 6.7 shows the effect of using 12 out of a possible 20 detectors in the fit. We see from the data that the choice and number of detectors used to fit the vertex affect the χ^2/dof somewhat but only at the level $< 18\%$.

There was some concern that the first detector on which half the readout

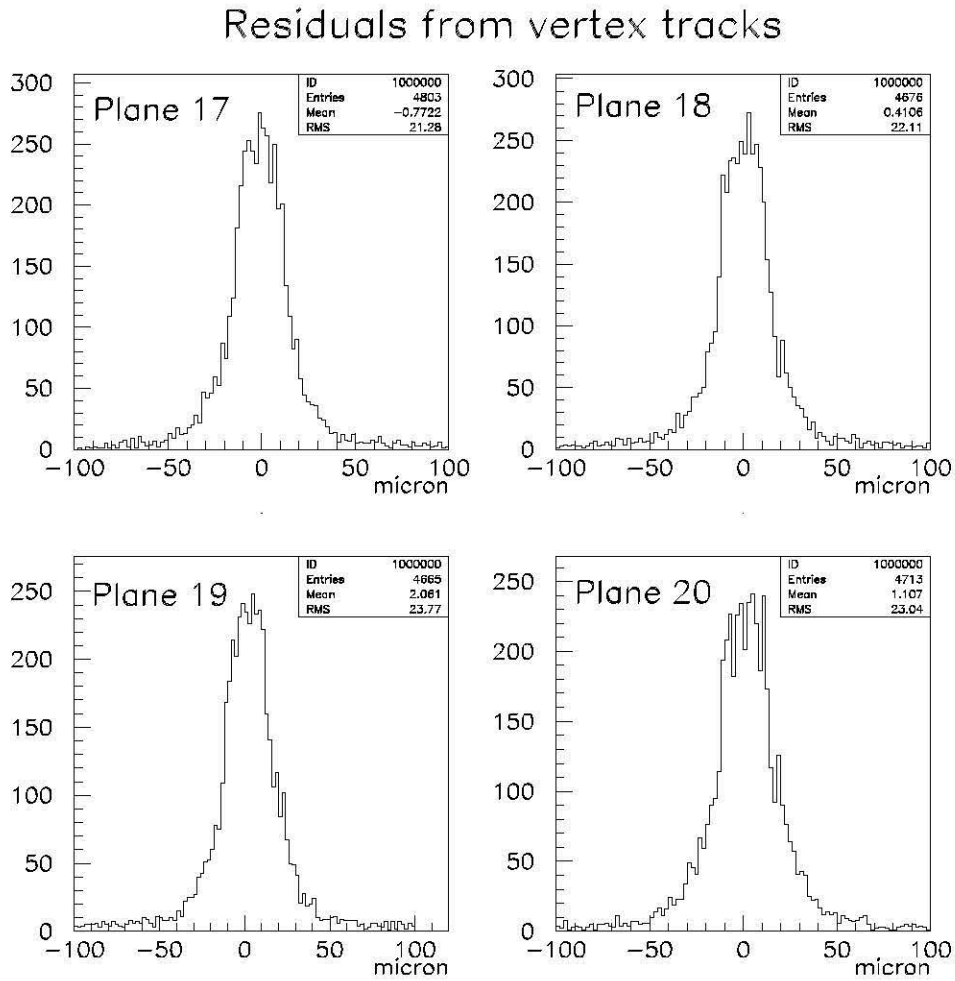

Figure 6.9: Residuals plotted in the last 4 vertex detectors(These planes are not used in the track fit).

Block removed	vertex χ^2/dof
First	2.001
Second	1.784
Third	1.690
Fourth	1.831

Table 6.7: Vertexing χ^2/dof after removing detectors(in sets of 4).

is inoperative[2], was affecting the χ^2. To test for this, vertexing was done with this plane out of the fit and the change in χ^2/dof was seen to be $\approx$ 0.5%. This eliminates the first plane as the source of any large systematic error.

As described earlier, the standard algorithm fits tracks along the extrapolated tracjectory of downstream found tracks. A different algorithm which fitted tracks through pure hit combinations in the vertex spectrometer(and hence slower) was run on the same data sample. Fig 6.10 shows the difference in the track parameters as found by the two different algorithms. The small width and almost negligible mean on the difference argues that the standard track finding algorithm does not have any systematic bias(pulls in the mean).

6.6.3 Degrees of freedom in the vertex fit

In the process of vertexing, we are fitting n tracks to a common vertex point. From our definition of the χ^2, (Eqn 6.5) each track contributes two independent variables into the sum. We are also extracting 3 parameters(the x, y and z position of the vertex from the problem). Hence the number of degrees of freedom is (2n - 3) where n is the number of tracks in the vertex fit. The least possible degrees of freedom is 1. This is from a two track vertex fit(there is no 1 track vertex fit.) Fig 6.11 a-f show the χ^2 distribution for 2, 3, 4, 5 and 6 track vertices. We observe that the shapes follow the expected χ^2

[2]see section 4.2.3

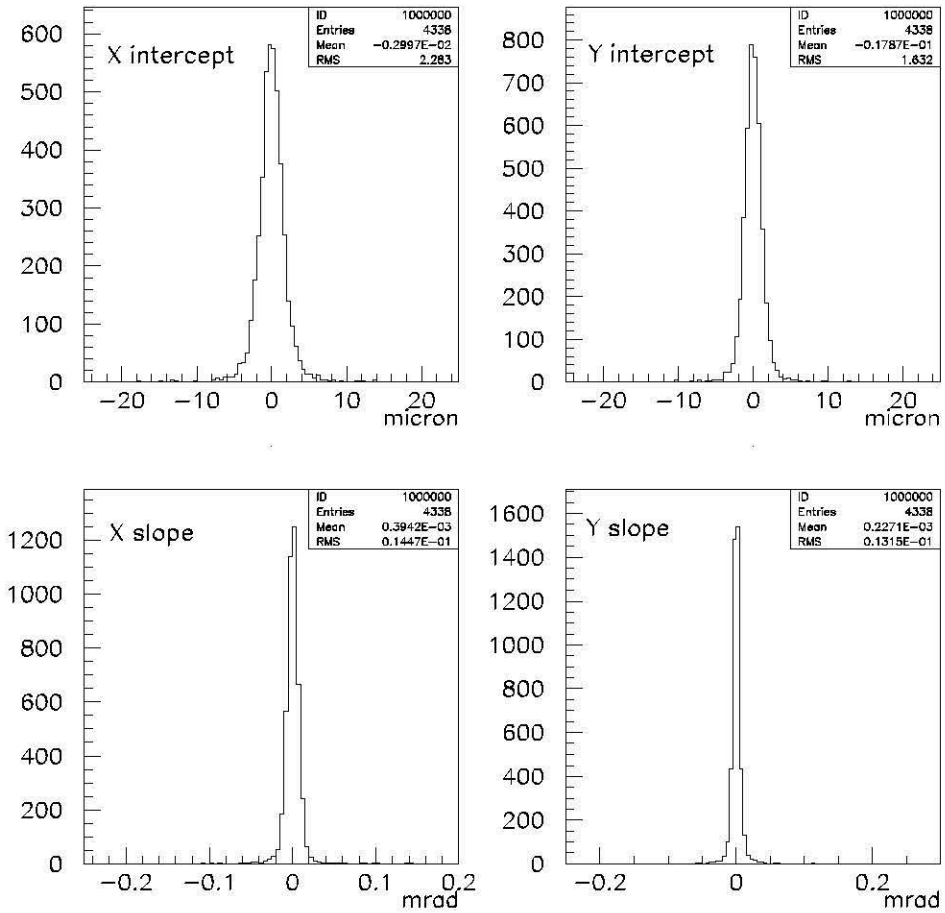

Figure 6.10: Track parameter differences between two different track fitting packages.

distributions for the degrees of freedom. For the case of 1 degree of freedom, the probability density $\mathbf{P}(\chi^2)$ is large at $\chi^2 = 0$ and tends to 0 for large χ^2. For the dof ≥ 3, $\mathbf{P}(\chi^2)$ is zero for $\chi^2 = 0$ and asymptotically tends to zero for large χ^2. These distributions also peak at the mean - 2σ. The χ^2/dof for all degrees of freedom are about the same. These plots show that the degrees of freedom are being counted correctly.

6.6.4 Different vertexing algorithm

The standard algorithm fits the vertex point by minimizing the χ^2 for the fit quantity and uses the MS model predicted errors. A different algorithm in which the minimum distances from the vertex point to all the tracks is minimized and the actual track fit matrix errors is used, was also tried. This method yielded a reduced χ^2 which was lower by about 3-5%.

6.7 Discrepancies from a purely normal distribution

The assumption all throughout is that all points on a track have been correctly assigned and they lie distributed randomly about the mean track position. Perfect track reconstruction would show this pure normal behaviour but in our case, tracking mistakes are possible. A clue to this is seen in Fig 6.12 The same plot is shown on log scale in Fig 6.13. As we can see, real data has more outliers and a longer non-gaussian tail. These are the signs of mis-assignment of hits to a track in the track reconstruction algorithm. They occur at the level of 1-5% of the time.

6.8 Interpretation of the observed χ^2/dof

It is observed that the reduced χ^2 is ≈ 1.69. An explanation for the larger than expected mean of the reduced χ^2 distributions is that the transverse

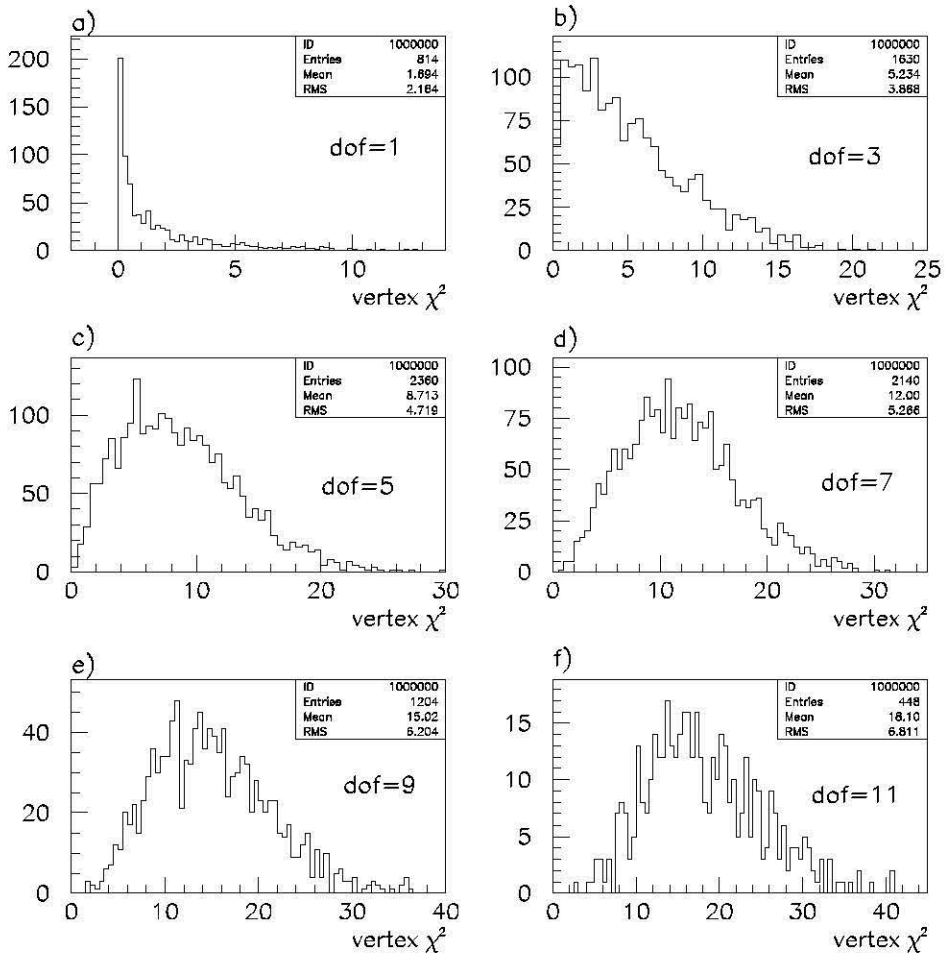

Figure 6.11: The χ^2 distributions for different degrees of freedom in interaction data.

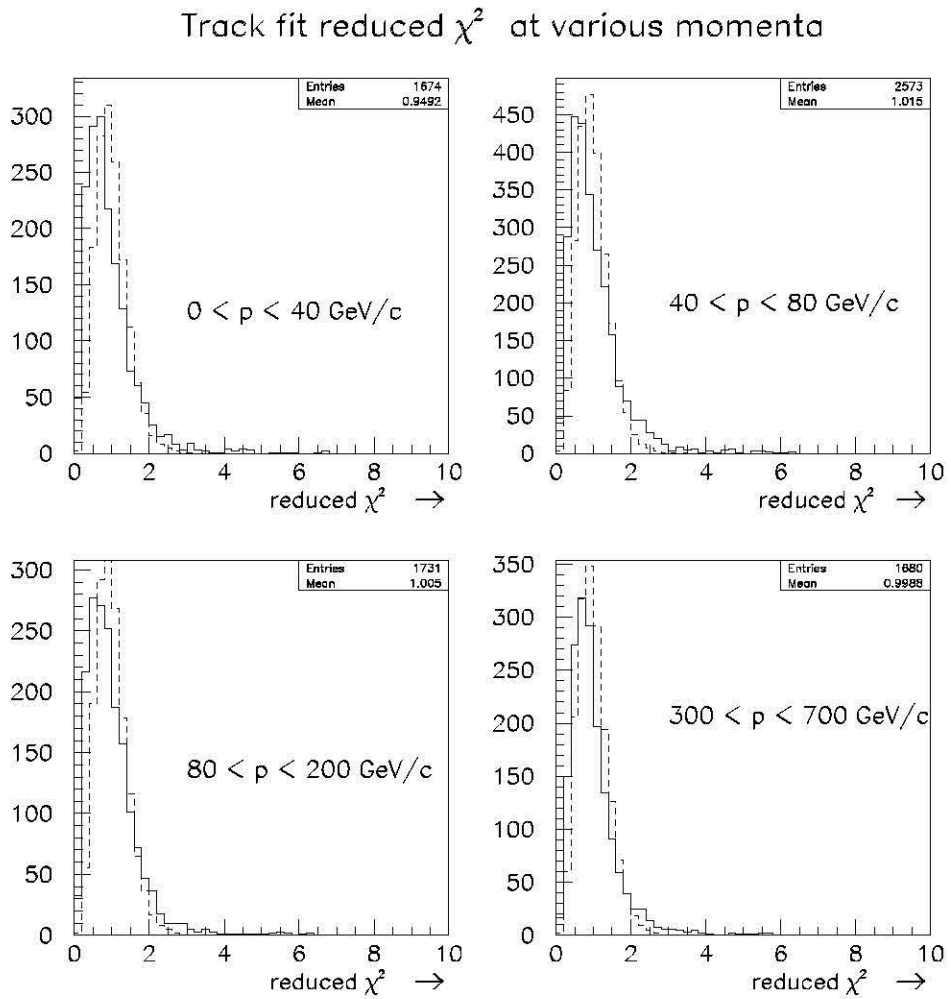

Figure 6.12: Track χ^2/dof distributions. (The bold curve is real data and the dashed curve is from purely normal simulated data)

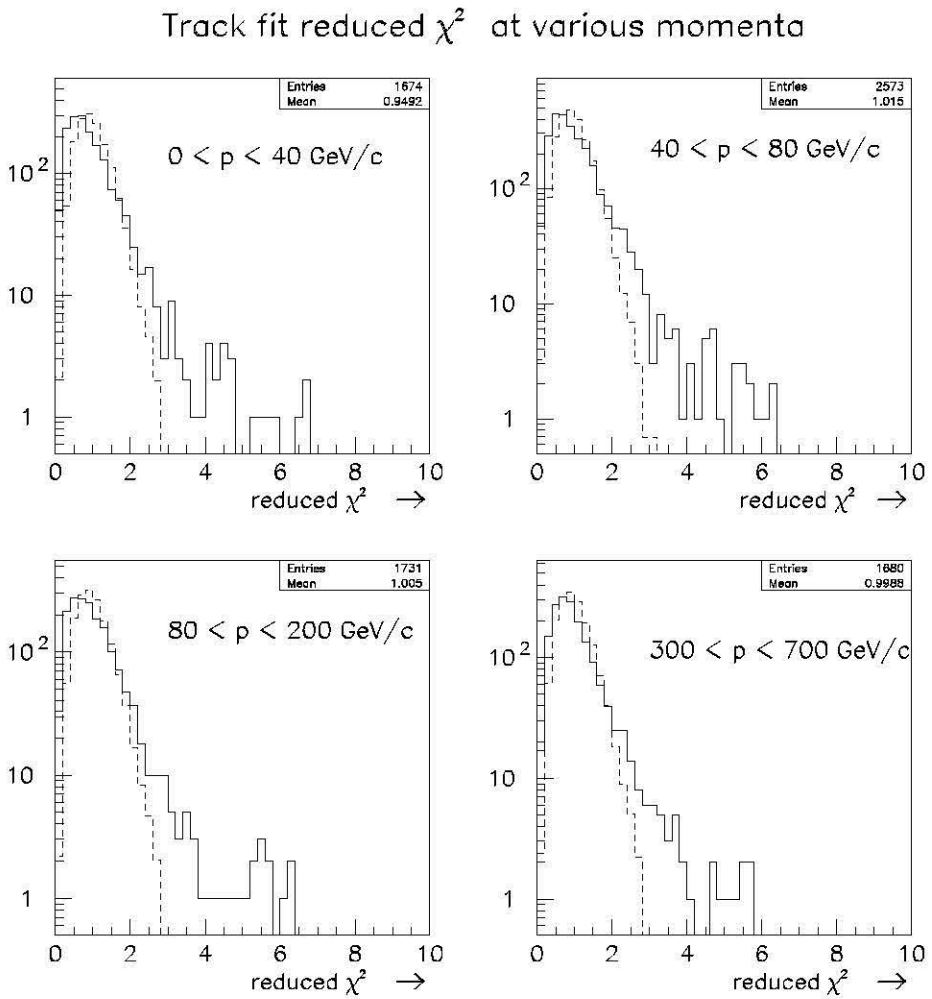

Figure 6.13: Track χ^2/dof distributions(log y scale). (The bold curve is real data and the dashed curve is from purely normal simulated data)

errors themselves have been underestimated by 30%. There are two arguments against this possibility. One is that the χ^2 distributions with errors derived from the actual fit itself show a similar behaviour. Next, the track fit χ^2s(obtained by using the same model), show an expected mean of unity. We attribute this increased χ^2 to incorrect hits being assigned to the tracks forming the vertex. The tracks are formed in a multiple track, many hit environment. It is likely that some of these hits are mistakenly attached on the track by the algorithm. This is not as big an effect on the track χ^2 which stays relatively close to the expected value. However, the small random pull on the track parameters introduces extra "noise" of the order of 70% into the vertex χ^2 term. We believe we understand what is happening and hence it is not particularly worrisome. With the average transverse error being 6μm for a typical interaction track, the uncertainty on this is 1.8μm which is less than half a transverse track sigma. As we have seen, all the χ^2s have the expected shapes which indicates that the error is only a scale factor. Embedding does not show this increased χ^2 because the underlying beam triggered event does not have the same noise hit background as an interaction track.

Chapter 7

Conclusions

We had set out to construct a vertex finding device based on the requirements of charm baryon detection for the fixed target experiment 781(SELEX) at Fermilab. The detector was to be capable of distinguishing secondary decay vertices from primary interactions in a multiple(8-10) track environment. The scale of the longitudinal resolution had to match the mm scale flight path of charm particles and the transverse resolution had to be $\approx 6\mu$m. Added to this were numerous constraints on size, assembly, readout speed, alignment, long-term stability etc. of the detector.

7.1 Hardware performance and evaluation

In the course of this thesis, we have examined the considerations that go into the design of a large, micron-scale resolution vertex detector based on silicon microstrip detectors. A 20 plane detector system, with 20μm and 25μm pitch detectors arranged in 4 views was planned. After extensive prototyping, 31 individual detector planes were fabricated, including spares. The charge sensitivity of these planes was rigorously tested and characterized with LED pulses, backplane charge injection and radioactive sources. The SVX chip based readout was integrated into the data acquisition consistent with the design readout speed of less than 30μs per event. The noise in the detectors

was 0.3fC and a minimum ionizing particle(MIP) detection gave a S/N $\geq$ 10.

Mounting the detector planes into the composite vertex unit was achieved with micron level control on the relative alignment. This was done using precision stainless steel fixtures and custom hardware. Polished granite surfaces were used to transfer the alignment to individual planes relative to a common granite block. This procedure was robust and precise on the scale of a few(3-5)μm and has been stable(<4μm drift) over a period of months. Using beam tracks, the alignment of the system was rigorously checked by studying the residual distribution in individual planes. A statistically limited transverse alignment < 1.0um was possible in the planes. Mis-alignments in the plane rotations were < 500μrad. The longitudinal positions of the 300μm thick detector planes were determined to within 100μm. All aspects of the alignment were understood and found to be extremely stable. A 2 month scan of the alignment was shown in Chapter 4(fig 4.28) and Fig 7.1 and Fig 7.2 show plots over 4 months of the alignment for typical detector planes.

The power distribution and cabling of the detector was optimized to reduce noise pickup and all components were designed to fail-safe. The detector unit was installed in a RF shielding Al box, with a forced nitrogen gas cooling system. This provided a light tight, thermally stable(21-24°C) environment which was important for the overall stability of all operating parameters.

The track resolution of the vertex planes was studied and showed that single strip clusters had the statistically limited(pitch/$\sqrt{12}$)[1] resolution. Multiple strip clusters(mostly 2-strip), with the ADC weighted information improved this resolution by about a factor of two. The hit efficiency was seen to be better than 98%.

The design of the vertex detector was really a "first of its kind" type, with regard to active strip density, size, complexity, resolution and tight tolerances. The hardware performed according to design. Thus, the major goal of this thesis was achieved.

[1]from rectangular statistics

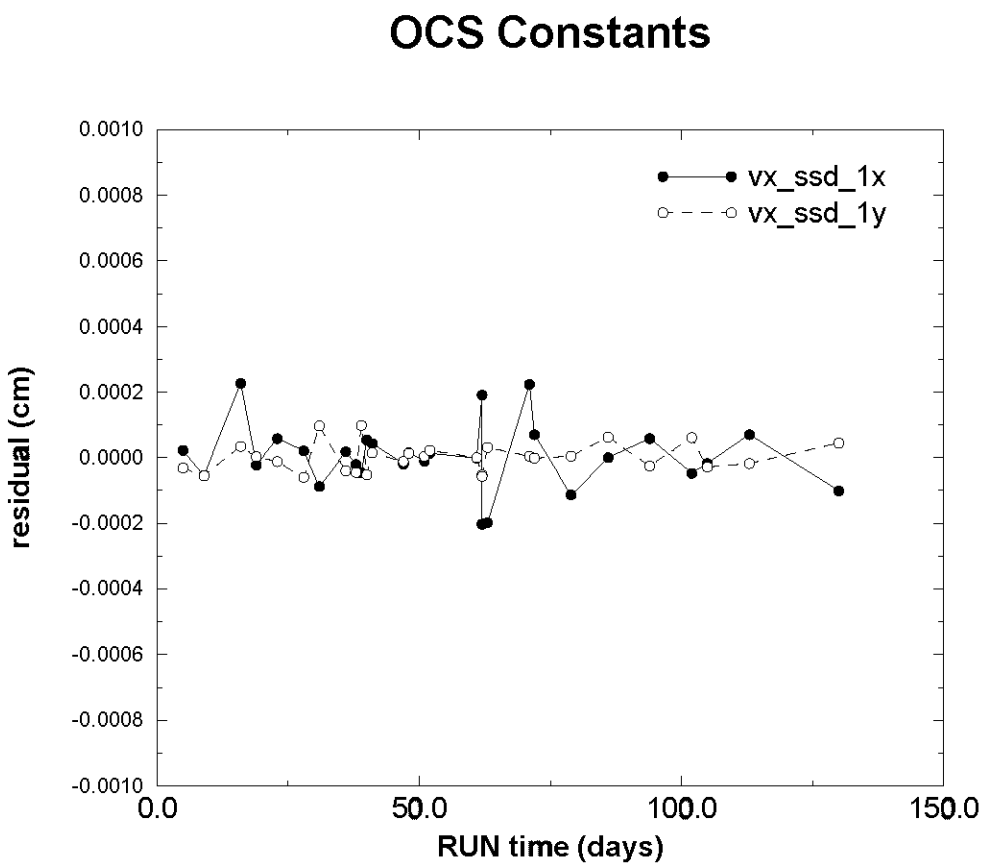

Figure 7.1: The long term alignment stability seen in typical 5_cm detectors.

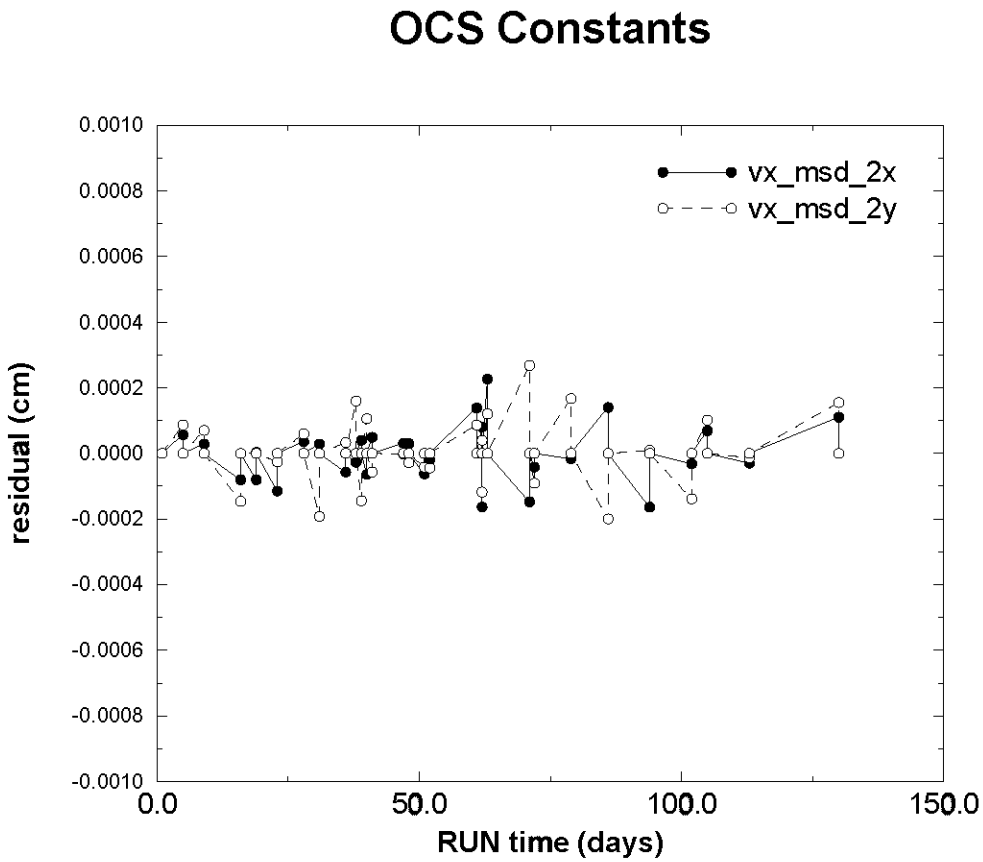

Figure 7.2: The long term alignment stability seen in typical mosaic detectors.

7.2 Tracking errors in silicon detectors

Building a new detector also required us to understand its impact on useful physics data. Chapter 5 illustrated the study of the optimal hyperon(Σ^+, Σ^-, Ξ^- produced at 540-640GeV/c and x_F=0.72-0.78) reconstructed mass resolution achievable using silicon detectors. Consideration of the tracking errors contributing to the mass width demonstrated that single track behaviour in a clean software environment(as is the case with beam decays), was well understood. Experience gained from this exercise was directly applied to fitting interaction tracks in the vertex detector. Multiple Coulomb Scattering(MCS) of particles in the 20 silicon vertex planes produces errors in the track fitting if it is not accounted for. Hence, an error matrix model including MCS was developed to predict momentum-dependent track error matrices. Using these errors to form the χ^2 for track fit, we obtained the expected unit mean χ^2 distribution, independent of momenta(Chapter 4, fig 4.17). Shown in Fig 7.3 is a plot of the function

$$P(\chi^2) = \frac{(\chi^2)^{(dof/2-1)} e^{-\chi^2/2}}{2^{(dof/2)}\Gamma(dof/2)} \tag{7.1}$$

for tracks fitted in the vertex detector, over different momentum bins. "dof" refers to the degrees of freedom in the track fit. The dominant features are those which might be expected from a normally distributed sample. The small peak at low probability represents a deviation from true random behaviour, i.e. a tracking mistake. These occur at the level of 5%. This is not surprising for the online version of the primary vertex reconstruction code, which has been optimized for speed rather than precision. An understanding of the multiple scattering errors was crucial to the high precision track reconstruction required for a precise vertex determination.

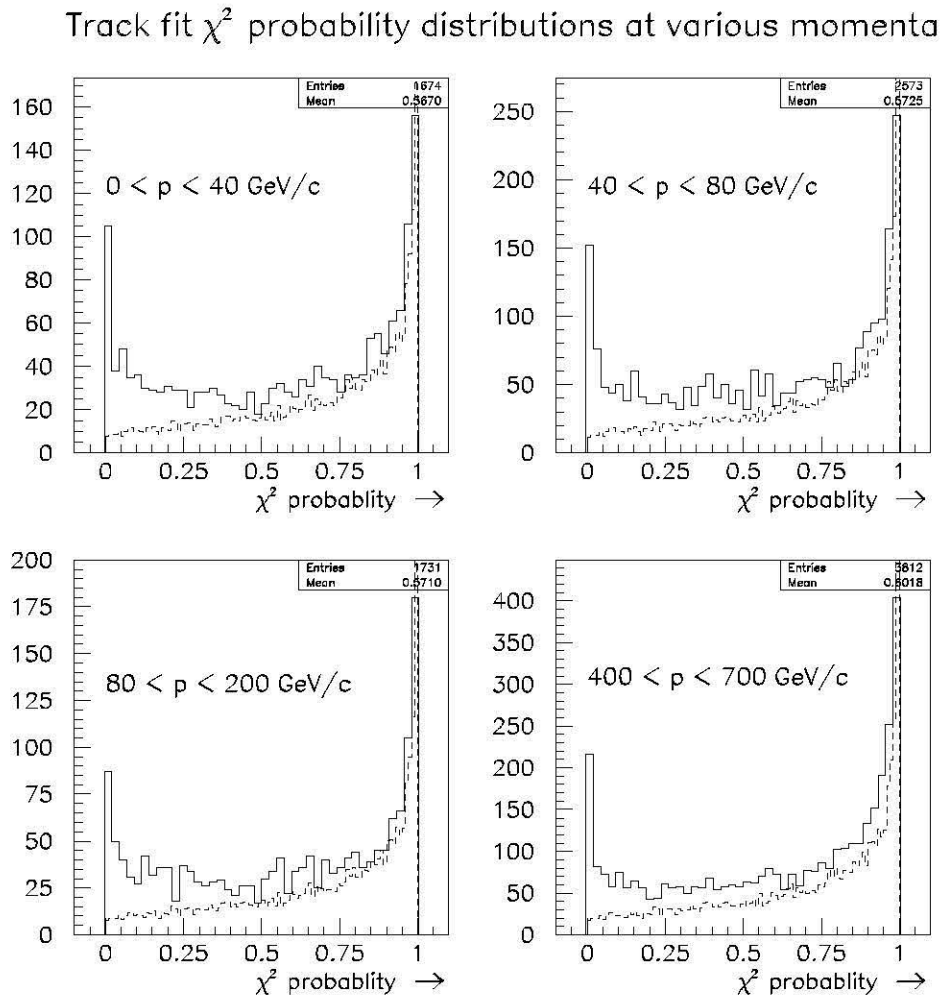

Figure 7.3: The track χ^2 probability distributions(bold) seen over different momentum bins. (The dotted histogram is the same for a pure normal distribution)

7.3 Vertex reconstruction

With a grasp on the limits of track resolution in the vertex detector, we considered the problem of vertex reconstruction. The philosophy of charm identification was to identify tracks that do not fit to a single vertex as evidence for a weak decay. This meant that the vertexing algorithm had to first find a "good" primary vertex. A vertex was fit by seeking the minimum vertex χ^2 configuration and the "goodness" of the vertex was based on the χ^2 consistency with a standard χ^2 distribution. As discussed in Chapter 6, we observe reasonable vertex χ^2 distributions. The distribution of typical track distance to the vertex position is shown in Fig 7.4. A most probable value of around 6μm and a mean of $<8\mu$m shows that the vertex hardware measured up to the claimed vertex resolution.

These real physics observations are a direct statement about the successful design and implementation of the vertex detector. Alongside the actual detector itself, there are a number of support systems. A variety of software programs written during the development stage allow us to control and monitor the detector and all these subsystems. Our experience with the vertex detector over the past 14 months has been that all the pieces have demonstrated consistent long-term stability and reliability. One of the new aspects of the experiment SELEX has been the inclusion of this high precision vertex information at the software trigger level for online enhancement of the signal sample. This online trigger response has been quite uniform over the last year of operation. Fig 7.5 shows the filter trigger response(expressed as a rejection ratio) over a period of 7 weeks. These and all the other aspects described in this thesis demonstrate a successful integration of precision detector hardware and tracking software into usable physics data.

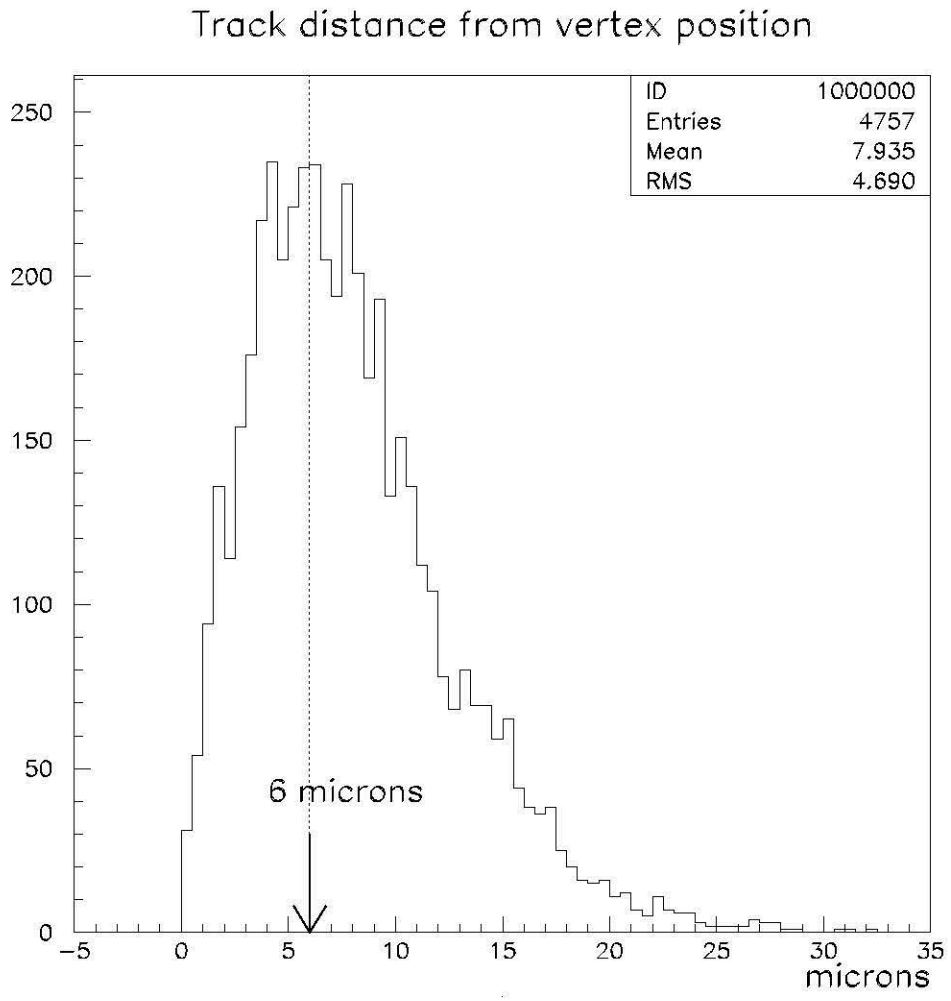

Figure 7.4: The distance from tracks in a vertex to the fitted vertex position

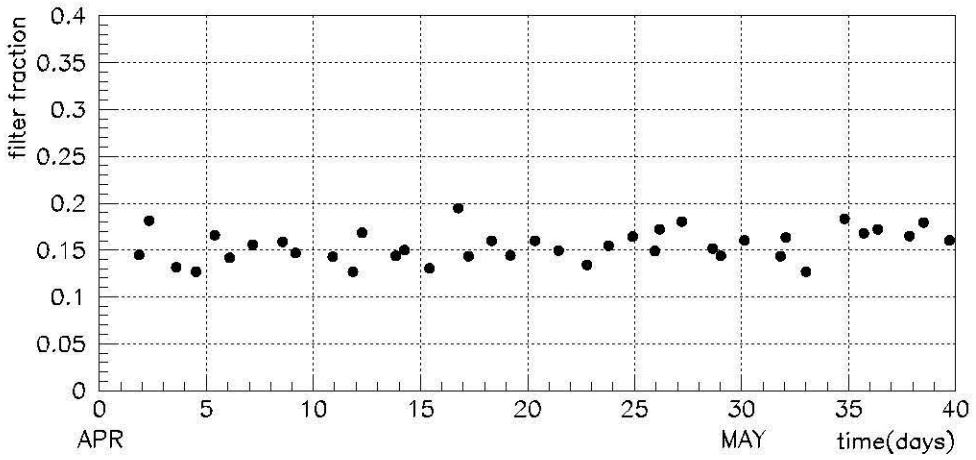

Figure 7.5: The online filter data-rejection fraction seen over 7 weeks of operation. This uses the vertex detector information.

7.4 Future developments

The silicon vertex detector on SELEX has been one of the largest silicon strip detectors($\approx$ 47K read out channels) known to be successfully operating,(at the time of this writing). Future advances may include bigger detectors and use of other radiation hard detector materials including diamond detectors. The development of pixel detectors will be a big step toward simpler track reconstruction geometries. It is certain that all these efforts will benefit from the experience gleaned from the long term operation of this vertex detector.

Bibliography

[1] K.G. McKay, Phys. Rev. 84(1951)829.

[2] J.Kemmer, Nucl Instr. and Meth. 169(1980)499.

[3] V. Radeka, Nucl Instr. and Meth. A 226(1984)209.

[4] P.F. Manfredi, F. Ragusa, Nucl Instr. and Meth. A 252(1986)208.

[5] W. Bruckner et al., Nucl Instr. and Meth. A 357(1995)274.

[6] J. Walter, Encyclopedia of Applied Physics, Vol 4, 513.

[7] W.R. Leo , Techniques for Nuclear and Particle Physics Experiments, Ch 10.

[8] A. Peisert et al, Nucl Instrum. and Meth. A 326(1993)189.

[9] E781 Collaboration: Carnegie Mellon University, Fermilab, University of Iowa, University of Rochester, University of Washington, Petersburg Nuclear Physics Institute, ITEP(Moscow), IHEP(Protvino), Moscow State University, University of Sao Paulo, Centro Brasileiro de Pesquisas Fisicas, Universidade Federale de Paraiba, IHEP(Beijing), University of Bristol, Tel Aviv University, Max-Planck-Institut fur Kernphysik(Heidelberg), Universidad Autonoma de San Luis Potosi.

[10] D. Perkins, Introduction to High Energy Physics.

[11] Charm Baryon Physics - Present and Future; J. Russ. Talk at the CHARM2000 Workshop, Fermilab, June 7-9, 1994.

[12] D. Goyne et al., Phys. Rev. D 54(1996)144.

[13] Particle Data Group, Phys. Rev. D 54(1996)138.

[14] J. Langland, H-693, SELEX Internal H-Note.

[15] J. Engelfried, P. Cooper, and D. Mao, H-643, SELEX Internal H-Note.

[16] The E781 Trigger and Data Acquisition System; J. Engelfried. Talk at the CHARM2000 Workshop, Fermilab, June 7-9, 1994.

[17] S.A. Kleinfelder et al; Lawrence Berkeley Laboratory Note.

[18] J.S. Russ et al., IEEE Trans. Nucl. Sci., NS-36(1989)471.

[19] M. Svoiski, SVX Readout Sequencer - E781 Version, SELEX Internal H-Note

[20] P.Neoustroev et al; FASTBUS SVX Data Accumulator (FSDA) - Technical Reference, SELEX Internal H-Note

[21] Y. Tomita et al., Nucl Instr. and Meth. A 270(1988)403.

[22] S.Hancock et al., Phys. Rev. A 28(1983)615.

[23] Review of Particle Physics, Phys Letters B 239(1990).

[24] Particle Data Group, Phys. Rev. D 54(1996)134.

[25] T.R. Cardello et al., Phys. Rev. D 32(1985)1.

[26] Particle Data Group, Phys. Rev. D 54(1996)636-639.

[27] E.R. Kreyszig, Advanced Engineering Mathematics, Ch 19.

[28] L. Lyons, Statistics for Nuclear and Particle Physics, 136-137.

[29] J. R. Taylor, An Introduction to Error Analysis, The Study of Uncertainties in Physical Measurements, Ch 6.